Title
Investigation of Aerosol Sources, Lifetime and Radiative Forcing through Multi-Instrument Data Assimilation

Author
Rubin, Juli Irene

Publication Date
2012

Investigation of Aerosol Sources, Lifetime and Radiative Forcing through Multi-Instrument Data Assimilation

by

Juli Irene Rubin

A dissertation submitted in partial satisfaction of the
requirements for the degree of
Doctor of Philosophy

in

Engineering - Civil and Environmental Engineering

in the

Graduate Division

of the

University of California, Berkeley

Committee in charge:

Professor William D. Collins, Chair
Professor Robert Harley, Co-chair
Professor Inez Fung
Professor Fotini Chow

Fall 2012

Investigation of Aerosol Sources, Lifetime and Radiative Forcing through Multi-Instrument Data Assimilation

Abstract

Investigation of Aerosol Sources, Lifetime and Radiative Forcing through Multi-Instrument Data Assimilation

by

Juli Irene Rubin

Doctor of Philosophy in Engineering - Civil and Environmental Engineering

University of California, Berkeley

Professor William D. Collins, Chair

Professor Robert Harley, Co-chair

Global-scale atmospheric models play an important role in predicting atmospheric aerosol and the corresponding radiative forcing. Although atmospheric models are important tools, there is large uncertainty associated with aerosol predictions due to uncertainty in aerosol representation within the models. As a result, aerosols and their influence on the Earth's energy balance are considered one of the largest uncertainties in understanding climate change [84]. Given the importance of simulating aerosol for understanding global climate change, it is evident that alternative methods are needed to reduce the effect of the uncertainties associated with aerosol representation and enhance the fidelity of the aerosol models. The goal of this research is to produce aerosol fields with reduced uncertainty by constraining model predictions with observations, using a technique known as data assimilation. The results from the aerosol assimilation are used to investigate aerosol sources, lifetime, and shortwave radiative forcing.

Two new aerosol data assimilations are presented as part of this work with both assimilations making use of an Ensemble Kalman Filter (EnKF) and the National Center for Atmospheric Research's (NCAR) community atmosphere model (CAM) with 60 ensemble members. The first assimilation involves the joint adjustment of the amount of atmospheric aerosol and the relative amount of fine and coarse aerosol using observations of aerosol optical depth (AOD) and angstrom exponent (α) from NASA's Moderate Resolution Imaging Spectroradiometer (MODIS). Both the amount and relative contribution of fine and coarse aerosol were identified as key parameters for determining aerosol radiative forcing and, therefore, accurately determining these parameters is desirable. The second assimilation presented as part of this work is similar to the first with the addition of a vertical redistribution of coarse aerosol using vertical extinction observations from NASA's Cloud-Aerosol LIDAR and Infrared Pathfinder Satellite Observations (CALIPSO) satellite. Studies have shown that the atmospheric lifetime of aerosol is tightly coupled to the vertical profile, therefore, it is expected that vertical adjustments will further reduce aerosol uncertainty, especially

in coarse aerosol. Similar to aerosol amount and size, lifetime is important for properly quantifying radiative forcing as it determines the time an aerosol has to impact the climate and influences the horizontal distribution of aerosol that is highly heterogenous in space and time.

The two presented assimilations are run for the year 2007 and results are compared against a control run simulation as well observations of AOD, angstrom exponent, and fine aerosol contributions from MODIS and NASA's Aerosol Robotic Network (AERONET). Through the comparison, it is demonstrated that the presented assimilations are able to reduce the model bias with an increase in the predicted aerosol optical depth. The globally averaged control run AOD prediction for 2007 is 0.086(±0.06). The globally average AOD predictions for the amount and size assimilation and vertical assimilation are 0.115(±0.05), 0.140(±0.05), respectively. This is compared to globally averaged MODIS observations of 0.161(±0.09). Over-ocean averaged angstrom exponent predictions from the control run are 0.65(±0.35) while the size and amount and vertical assimilation predictions are 0.68 (±0.15) and 0.66 (±0.15), respectively. This is compared to globally averaged MODIS observations of 0.65(±0.30). While it is difficult to determine improvements in angstrom exponent predictions based on the global average, clear reductions in regional biases were observed. Aerosol predictions are also compared to ground-based AERONET observations by site category, including desert dust, biomass burning, rural, industrial pollution, polluted marine, and dirty pollution. While the rural sites have statistically similar averaged AOD values across simulations, improvements are found for the other site categories in the assimilation runs with higher average AOD values and greater temporal variability. In addition to AOD comparison, the predicted amount of AOD due to fine aerosol is compared to AERONET observations by site category. The greatest reduction in bias is observed for polluted marine sites with the assimilation runs predicting a smaller fine aerosol contribution than the control simulation. Size-related observations are concentrated over ocean regions, therefore, the greatest impact of the assimilation with respect to size is expected for marine sites. Additionally, the positive bias in fine aerosol contribution predicted at dusty sites is reduced the most in the vertical assimilation with dust being mostly coarse in size. The adjustments to the vertical profile of coarse aerosol in the vertical assimilation further reduce bias for coarse dominated sites.

The results of the assimilation are used to quantify the contribution of anthropogenic aerosol to AOD. Globally averaged, the anthropogenic contribution to AOD is 38.8% for the control simulation, 47.6% for the amount and size assimilation and 49.5% from the vertical assimilation. These results are comparable to previously published anthropogenic AOD percentages which range from 41 to 72% [84]. Additionally, aerosol loss processes and lifetime are analyzed. The dominant loss processes are condensational growth for nucleation mode aerosol (fine, $<0.1\mu$m), activation and wet deposition for accumulation mode aerosol (fine, 0.1-1μm), and dry deposition and activation for coarse mode aerosol ($>1\mu$m). The longest aerosol lifetimes are found in the vertical assimilation with most aerosol species showing better comparison to reported AEROCOM lifetimes, except for sulfate. In particular, the lifetimes of coarse mode dust and sea salt increased in the vertical adjustment assimilation, reducing the negative aerosol optical depth bias, especially in dusty regions. The predicted sulfate lifetime is double the reported AEROCOM value and may be the cause of some positive AOD bias regions in the Northern hemisphere predicted in the model runs.

The solar direct radiative forcing (DRE) is calculated using the predicted aerosol fields with the DRE including the effects of both anthropogenic and natural aerosol. Uncertainties in DRE for the assimilation runs are determined using the 60 member ensemble spread. Globally averaged DRE values are -1.9 W/m^2, -5.2(±0.51) W/m^2, and -7.2(±0.94) W/m^2, for the control, amount and size and vertical assimilation, respectively. The predicted DRE from the amount and size assimilation compares the best to previously published estimates. Additionally, the calculated anthropogenic contribution to AOD is used in conjunction with the DRE estimates to calculate shortwave anthropogenic direct radiative forcing estimates with predicted values of -0.77, -2.3(±0.64) and -3.2(±0.7) W/m^2 for the control, amount and size assimilation and vertical assimilation, respectively.

I would like to dedicate this doctoral dissertation to my parents, Bill and Cherie Rubin.
Without their endless support and encouragement, I wouldn't be where I am today.

Contents

List of Figures

List of Tables

Acknowledgments

I would like to express my deep appreciation and gratitude to my advisor, Dr. Bill Collins, for the patient guidance and mentorship he provided during my time at Berkeley. I learned a great deal from our work together over the last four years and I was very fortunate to have this opportunity. I would also like to thank my co-advisor, Dr. Rob Harley, for being a great mentor and influence throughout the many years I have known him. I would like to give a special thanks to Dr. Inez Fung and Dr. John Chiang. I learned a great deal from our interactions. I would also like to thank Dr. Tina Chow for her helpful thoughts on my research.

I would like to acknowledge the NASA ROSES program for providing funding for this research.

My years at Berkeley wouldn't have been the same without my research group members, Lara, Dan, Daniele, Kyle, and Lindsey, as well as my officemates, Andrew, Yuwei and Ivana.

A special thanks to the Berkeley girls (Garmay, Beth, Ann, Teresa, Elaine and Lyn) for being great friends through good and bad. Garmay, you are the best friend anyone could ask for and I will miss you always.

Most importantly, I would like to thank my family for always supporting me. Thanks to my husband, Gabriel, for putting up with the long hours and stress of completing my dissertation. I'm very lucky to have the love and support of all the Rubins (my parents, Leah, Ryan, Mike, Renee, Nina, Jack, and Henry) and the Benabous (Lisa, Abner, Azar, Sandi, Isaac, Candi, Tom, Linda, Jacob, Sam, Max, Aliyah, Rebecca, Nathan, Matthew, Oren, Avi, Zac, Josh and Hannah).

Chapter 1

Introduction

The Earth's climate is controlled by the energy balance between incoming solar shortwave radiation and outgoing longwave radiation at the top of the Earth's atmosphere (TOA). As radiation from the sun propagates through the atmosphere, it can be scattered, absorbed or reflected due to interactions with aerosols, gas molecules, clouds, and the Earth's surface. As a result, changes in the composition of the atmosphere or surface properties can affect the amount of shortwave radiation entering the system. Likewise, emitted terrestrial radiation or longwave radiation can be absorbed and reemitted, affecting the amount of radiation leaving the Earth's system.

The effect of aerosols on the Earth's climate is considered one of the largest uncertainties in understanding climate change (Figure 1.1) [84]. Aerosols can affect the Earth's climate directly by scattering and absorbing both shortwave and longwave radiation (direct effects) or indirectly by altering the microphysical and hence radiative properties of clouds (indirect effects) (Figure 1.2). There are several mechanisms by which aerosols can influence clouds, however, the most studied is the first indirect effect or cloud albedo effect which describes a change in cloud albedo due to an increase in cloud condensation nuclei under fixed liquid water content [84]. The effect of aerosols and other drivers such as CO_2 on climate are described using the concept of radiative forcing. This is defined as the change in net (down minus up) radiation at the tropopause, after allowing for the stratospheric temperatures to readjust to radiative equilibrium but with surface and tropospheric state held fixed at unperturbed values. A positive value indicates a warming of the atmosphere and a negative value indicates a cooling. Current estimates of aerosol direct radiative forcing for all aerosol types combined are -0.5±0.4 W/m^2 for the direct effect and -0.7 W/m^2 with a range of -1.8 to -0.3 W/m^2 for the first indirect effect (cloud albedo effect). According to climate models, the radiative forcing of aerosols has helped to offset some of the warming by greenhouse gases (GHG) with radiative forcing estimates for CO_2 at 1.66 W/m^2 (1.49-1.83 W/m^2).

There are several key parameters for determining the aerosol direct radiative forcing. This includes the amount of atmospheric aerosol and the associated optical properties (extinction coefficient, single scattering albedo, scattering phase function) with the optical properties being a strong function of the wavelength of the incident radiation and the size and composition of the aerosol. Additionally, aerosols have a short lifetime and are therefore, highly heterogeneous in space and time. As a result, the horizontal and vertical distribution of aerosol in the atmosphere are required for radiative forcing calculations. In direct radiative forcing estimates, it is also necessary to separate the influence of anthropogenic and natural aerosols since only anthropogenic aerosols can be considered an external cause of climate change [14]. Anthropogenic and natural aerosols have different proportions of fine and coarse aerosols with urban and industrial pollution being composed of mainly fine aerosol and dust and marine aerosol dominated by coarse aerosol with a significant fine aerosol fraction [43]. As a result, aerosol size can be used to approximate the anthropogenic contribution of aerosols. Key parameters for determining the aerosol first indirect effect are the effectiveness of an aerosol to act as a cloud condensation nucleus, which is a function of size, composition, and ambient conditions [84] [20].

Global-scale atmospheric models, which predict the transport and evolution of aerosols in space and time, play an important role in assessing the radiative forcing of aerosols [84]. For global simulations, models are run with much coarser resolution than processes important for aerosol predictions. As a result, aerosol processes must be parameterized. There is significant diversity in how aerosols are treated across the available atmospheric models [92]. This includes the representation of the size and mass of aerosols within the model (bulk versus modal treatment), the chemical state of aerosols (internal versus external mixtures) and the microphysical processes (nucleation, condensation, coagulation, aging, activation). In addition, emissions of primary aerosol and precursor gases for secondary aerosol formation and model chemistry vary. The vertical transport of aerosols and the removal of aerosols by precipitation is particularly uncertain. This combination of factors leads to a large spread in aerosol predictions and a large uncertainty in aerosol radiative forcing calculations [92].

Given the importance of simulating aerosols for understanding global climate change, it is apparent that new techniques are needed for reducing uncertainty in aerosol predictions and their associated radiative forcing. While climate models such as the National Center for Atmospheric Research's (NCAR) community atmosphere model (CAM) simulate aerosols at high spatial and temporal resolution, the predictions are uncertain. On the other hand, observations of aerosols from satellite-based instruments such as NASA's Moderate Resolution Imaging Spectroradiometer (MODIS) [81] [48] and ground-based networks such as NASA's Aerosol Robotic Network (AERONET) [32] provide accurate information at the expense of resolution. Weaknesses in both simulations and observations motivate the development of a system that takes the information from both approaches and merges them together with a goal of producing accurate aerosol fields at high spatial and temporal resolutions. The goal of this research is to investigate aerosols and their effect on the energy budget of the climate system, or radiative forcing, using data assimilation, a technique that uses observational data to constrain model forecasts.

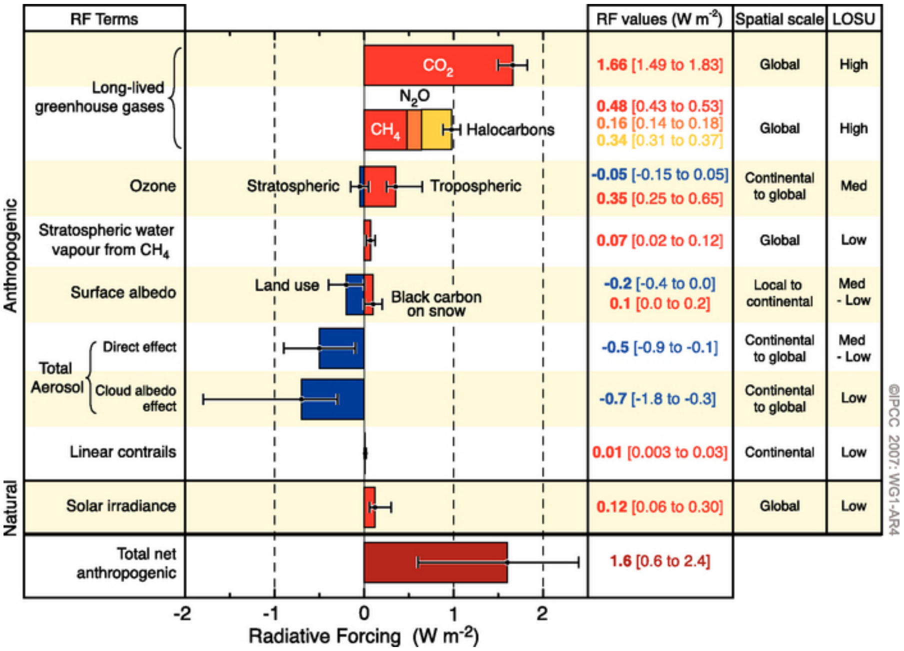

Figure 1.1: Global average radiative forcing (RF) estimates and their associated ranges in 2005 for various climate drivers including aerosol. The level of scientific understanding (LOSU) is also presented. [84]

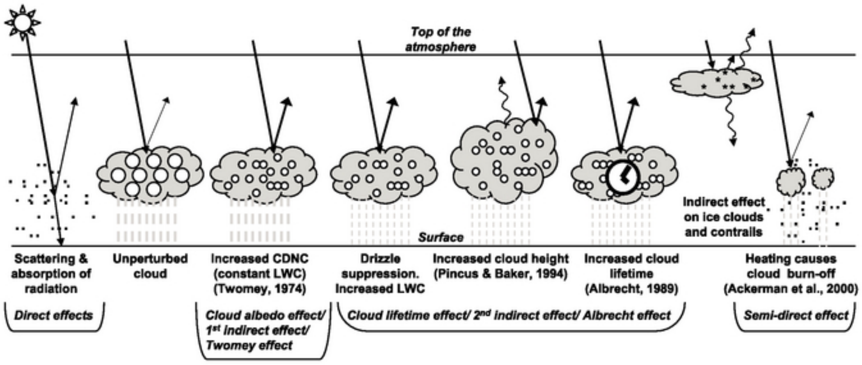

Figure 1.2: Schematic diagram of the various radiative mechanims associated with aerosol indirect effects on clouds. The small black dots represent aerosols while the larger open circles represent cloud droplets. Straight lines represent incident and reflected shortwave radiation and wavy lines represent longwave radiation. CDNC stands for cloud droplet number concentration. The unperturbed cloud contains larger droplets while the perturbed cloud contains a greater number of small cloud droplets. [84]

1.1 Research Objectives

There are three objectives associated with this work. The first is the prediction of the amount of fine and coarse atmospheric aerosol through the assimilation of observations of total aerosol amount and size from NASA's MODIS and AERONET instruments. Both aerosol amount and size are important factors in determining radiative forcing. Additionally, assessing the effect of aerosols on Earth's climate requires distinguishing natural from anthropogenic aerosol since only anthropogenic aerosol can be considered as an external cause of climate change [14]. Satellite data and aerosol transport models show that plumes of smoke and regional pollution have large concentrations of fine aerosols, less than one micron in size [44]. In contrast, natural aerosol plumes are concentrated with coarse particles, greater than one micron in size [46] [88]. As a result, size-assimilated aerosol fields can be used to quantify anthropogenic and natural aerosol components.

The second objective is the inclusion of aerosol vertical profile observations from NASA's Cloud-Aerosol LIDAR and Infrared Pathfinder Satellite Observations (CALIPSO) satellite [102] in the aerosol assimilation. The atmospheric lifetime of aerosols (ie. the timescale over which aerosols can influence the Earth's energy balance) is determined by the vertical profile. Wet scavenging, an important removal process, becomes increasingly less significant when aerosols reach altitudes where the clouds exhibit decreased precipitation efficiency [60]. For small particles in which wet deposition is the main removal mechanism, the altitude can have a significant impact on residence time in the atmosphere [92]. An aerosol tracer study conducted by Balkanski et al. (1993) showed that aerosols in the lower atmosphere have a residence time that is on average four times shorter than aerosols in the upper atmosphere [8]. The resulting aerosol fields from the second assimilation will be used to assess aerosol lifetime in the atmosphere.

The final objective of this research is to investigate the impact of the size assimilation and the vertical profile assimilation on the solar direct radiative effect (DRE) which is the direct forcing from both anthropogenic and natural aerosol. Additionally, the anthropogenic shortwave radiative forcing will be investigated. Aerosol size is an important factor for both the direct and indirect radiative effects given that the scattering and absorbing properties of aerosols and the effectiveness of a particle to serve as cloud condensation nuclei are dependent on aerosol size [84]. The vertical distribution is also expected to have an impact on the radiative forcing since the profile controls atmospheric lifetime, determining the time an aerosol has to impact the climate. Additionally, the lifetime controls the horizontal dispersal in the atmosphere, which is important in determining where the forcing occurs given the heterogenous nature of aerosol.

1.2 Introduction to Aerosols

Aerosols are tiny particles suspended in the Earth's atmosphere. They arise from natural sources such as windborne dust, sea spray and volcanoes and from anthropogenic activities such as combustion of fuels and the burning of vegetation to clear land for agriculture [82]. Aerosols can be directly emitted into the atmosphere as primary aerosol or formed secondarily through gas-to-particle conversion (nucleation) processes with atmospheric aerosols generally existing in the size range from a few nanometers to tens of micrometers [82]. Particles greater than one micron (μm) in diameter are referred to as coarse aerosol and those less than one μm in diameter as fine aerosol with additional divisions into nucleation mode ($<0.1\mu$m) and accumulation mode (0.1 to 1 μm).

Fine and coarse aerosols, in general, have different sources and sinks as well as composition and, therefore, the distinction is important [82]. Fine aerosols are mainly formed from gaseous precursors and include sulfate and carbonaceous particles (black and organic carbon). Fine aerosols are generally associated with anthropogenic sources, with studies showing that urban and industrial pollution and smoke from vegetation burning contain mostly fine particles [88] [46]. Coarse aerosols, on the other hand, are generated through mechanical processes, usually by strong winds, and include dust and sea-salt particles, which are mostly natural in origin [88] [46]. Coarse aerosols are removed from the atmosphere through gravitational settling and scavenging by cloud droplets and precipitation. Fine aerosols are too small to have significant settling velocities and wet deposition is the main removal pathway [82].

Satellite instruments such as MODIS and ground-based networks such as AERONET measure the attenuation of sunlight by a column of aerosol, or aerosol optical depth (AOD, τ), which serves as a measure of aerosol column concentration [58]. In addition to measuring the spatial patterns of τ, these instruments have the ability to distinguish between fine and coarse aerosol [43]. This ability has been exploited to separate natural and anthropogenic aerosol, both regionally and globally. An analysis was conducted as part of the Indian Ocean Experiment (INDOEX), a study aimed at understanding springtime Asian brown clouds in the Indian Ocean region, showing that the haze contains as much as 80(±10)% anthropogenic aerosol [74]. Analysis of AERONET data from select sites has shown that anthropogenic aerosols have a fine aerosol contribution to AOD of 83(±5)% while natural aerosols have a much lower fine aerosol contribution of 35(±5)%. Contributions that fall in between indicate a mixture of natural and anthropogenic aerosol [10]. From an analysis of two years of MODIS data, Kaufman et al 2005 showed that 21(±7)% of AOD over oceans is anthropogenic in origin [43]. Global analyses of anthropogenic contributions to AOD have been conducted in several modeling studies with results ranging from 11 to 50% [84]. The average across all models was 29(±13)% [84]. While some work has been done to investigate anthropogenic and natural aerosol contributions, the large range in results indicate the need to further quantify the anthropogenic aerosol component.

Aerosols typically reside in the troposphere, the lowest layer of the atmosphere, which is characterized by decreasing temperature with height and rapid vertical mixing. Estimates of the residence time of aerosols in the troposphere range from 4 to 60 days [8]. Aerosols with lifetimes on the order of a day are confined to their region of origin while at the upper end they may be transported over large distances, as is the case with aerosol plumes from Africa or Asia reaching America [44]. Aerosol lifetime is dependent on removal mechanisms, which include wet and dry deposition processes. Wet deposition is the transport of aerosols to the surface through scavenging by atmospheric hydrometeors, including cloud and fog drops, rain and snow [82]. Dry deposition is the transport of aerosols from the atmosphere to the surface in the absence of precipitation and includes processes such as gravitational settling and delivery to the surface via turbulence [82]. The rate of deposition for a particle is dependent on several factors, including the size and composition and regional frequency of precipitation [8] [28] [40]. Accumulation mode particles have the slowest deposition rates while coarse aerosols settle out quickly due to gravitational settling [82]. Nucleation mode particles are removed through Brownian motion [82]. For wet deposition, the composition of the aerosol is especially important as this influences its solubility [92]. Sulfate and sea salt aerosols are very soluble and can easily be scavenged unlike dust and freshly emitted black carbon. Wet and dry deposition serve as important sinks of aerosol in the atmosphere and aerosol lifetime is dependent on these processes.

The model-predicted lifetimes of various aerosol species were analyzed as part of AEROCOM, an international effort aiming to compare aerosol predictions across atmospheric models and against observations [92]. The lifetime of an aerosol is defined as:

$$lifetime = \frac{burden}{sinks} \tag{1.1}$$

where the burden is the mass of aerosol in the atmosphere and the sinks are the removal rates due to wet and dry deposition. Averaged across approximately 16 models, the residence time of sea salt was found to be the shortest at 0.48(±0.28) days, followed by sulfate (4.12±0.74 days), dust (4.14±1.78 days), primary organic carbon(6.54±1.76 days), and black carbon (7.12±2.35 days) [92]. Species solubility was found to be the controlling factor in determining the wet deposition rate, which was the main removal process for sulfate, black carbon and primary organic carbon aerosols [92]. Little agreement was found for sea salt and dust removal pathways across models. Large differences also existed in aerosol dispersal across models, both in the vertical and horizontal [92]. While no correlation was found between the degree of dispersal for dust and sea salt and residence time, a relationship was found between vertical dispersal and residence time for sulfate, black carbon and primary organic carbon particles, indicating the importance of the vertical profile for aerosol species, especially those in the fine mode [92].

During their suspension in the atmosphere, aerosols undergo many processes that affect their size, composition and lifetime including growth by condensation and coagulation and activation to form cloud droplets [82]. The ability of an aerosol to go from an interstitial state, or unattached state, to an activated cloud droplet is governed by Kohler theory. Kohler theory states that a particle must reach a critical size after which activation occurs [79]. The critical size is dependent on the saturation of the ambient air, the initial size and the composition of the particle. The ability of aerosols to interact with clouds and form cloud droplets is important as it affects the hydrological cycle, through changes in cloud cover, cloud properties and precipitation [44]. Cloud and aerosol interactions are also important for the Earth's energy budget as clouds reflect solar radiation and trap outgoing radiation emitted from the Earth's surface [84]. Clouds cover approximately sixty percent of the Earth's surface and on a global average cool the Earth-atmosphere system [59]. Aerosols also directly influence the Earth's energy balance through their ability to scatter and absorb both solar and terrestrial radiation, affecting the radiative heating of the atmosphere and the surface [84]. The redistribution of heat can impact atmospheric circulation and the hydrological cycle through changes in evaporation and condensation [80] [18].

1.3 Introduction to Radiative Forcing

The Earth's energy balance requires the flux of incoming solar energy to be balanced by an equal flux of outgoing longwave radiation. Any perturbation to the incoming or outgoing radiation drives the climate to a new warmer or cooler equilibrium state in order for an energy balance to be achieved. While greenhouse gases such as carbon dioxide reduce outgoing radiation and force the atmosphere to a warmer equilibrium state, aerosols can influence both sides of the energy balance. Aerosols that effectively scatter solar radiation, such as sulfate, reduce incoming energy by reflecting radiation back out to space, driving the atmosphere to a cooler state [84]. On the other hand, aerosols that absorb shortwave radiation, such as black carbon and dust, can reduce outgoing radiation and warm the atmosphere if they exist above bright surfaces such as ice, desert or clouds [84]. Additionally, a warming of the atmosphere can occur through absorption of outgoing longwave radiation by dust aerosol [89]. The influence of aerosols on the Earth's energy balance through scattering and absorption of radiation is known as the aerosol direct effect [84]. Aerosols can also modify the energy balance through interactions with cloud microphysics and therefore, cloud radiative properties. This is referred to as aerosol indirect effects [84]. There are several ways that aerosols can influence cloud properties, but the most studied is the first indirect effect or the cloud albedo effect, describing the influence of aerosols on cloud droplet size. The introduction of aerosols, which serve as cloud condensation nuclei, results in smaller cloud droplets under fixed liquid water content due to the distribution of water over greater surface area [84]. This has been confirmed in observations of increased cloud droplet number concentration due to heavy smoke from forest fires [76] [6] [64] and in ship tracks influenced by aerosol [25] [24] [71]. The consequence of decreased droplet size is an increase in the reflective properties of the cloud or cloud albedo and an associated cooling influence.

The effect of aerosols or any other driver of climate change on the energy budget is quantified using radiative forcing (RF). The term has been used to denote an externally imposed perturbation in the radiative budget of the Earth's climate system and is defined in the Intergovernmental Panel on Climate Change's third assessment report as the change in net (down minus up) irradiance (solar plus longwave in W/m^2) at the tropopause after allowing for stratospheric temperatures to readjust to radiative equilibrium, but with surface and tropospheric temperatures and state held fixed at the unperturbed values. For aerosol RF, estimates are most often made in the shortwave since the longwave direct RF is only substantial if the aerosol particles are large and occur in considerable concentrations at higher latitudes [89]. Aerosol RF estimates are also determined at the top of the atmosphere (TOA) instead of the tropopause since shortwave radiative transfer calculations have shown a negligible difference between the two [30]. A positive RF value indicates a warming while a negative RF value indicates a cooling.

The source of energy for the climate system is the sun. The radiative flux from the sun or total solar irradiance at the mean earth-sun distance has been measured by sun-observing satellites and is estimated to be $F_o = 1361 W/m^2$ (Solar Radiation and Climate Experiement (SORCE) [53]). F_o is the amount of electromagnetic radiation that passes through a plane perpendicular to the direction of solar incidence. The globally averaged radiation normal to Earth's surface is equal to F_o multiplied by the ratio of the Earth's cross-sectional area to its surface area or $\frac{1}{4}$. The amount of solar, or shortwave, energy that is absorbed by the climate system is the net flux at the TOA (F_{sw}^{TOA}), calculated as the difference between the downward and upward fluxes (Equation 1.2). This can also be expressed in terms of the shortwave albedo α_{sw}, the fraction of downward incident flux that is reflected upwards. The shortwave albedo is a combination of reflection from the gaseous medium, clouds and aerosols if present and can be represented as the combination of clear-sky (α_o) and cloudy-sky albedos (α_c) with A_c as the fraction of sky covered by clouds (Equation 1.3). For shortwave RF, the quantity of interest is the difference in the solar energy absorbed by the climate system (ΔF_{sw}^{TOA}) when a forcing agent is introduced as expressed in Equation 1.4.

$$F_{sw}^{TOA} = F_{sw}^{-TOA} - F_{sw}^{+TOA} = \frac{F_o}{4}(1 - \alpha_{sw}) \tag{1.2}$$

$$\alpha_{sw} = A_c \alpha_c + (1 - A_c)\alpha_o \tag{1.3}$$

$$\Delta F_{sw}^{TOA} = F_{sw}^{TOA}(aerosol) - F_{sw}^{TOA}(noaerosol) \tag{1.4}$$

Determining direct radiative forcing requires information about three key aerosol optical properties: the extinction coefficient k_{ext}, single-scattering albedo ω, and the backscatter ratio β. The extinction coefficient [km^{-1}] describes the reduction in radiant intensity (I) ($Wm^{-2}sr^{-1}$) over a depth z by both scattering and absorption. This relationship is expressed in the Beer-Lambert law, which can also be written in terms of aerosol optical depth τ (AOD) (Equations 1.5 and 1.6).

$$k_{ext} = k_{scat} + k_{abs} \tag{1.5}$$

$$\frac{I}{I_o} = exp(-k_{ext} * z) = exp(-\tau) \tag{1.6}$$

Aerosol optical depth τ, an important measurable quantity related to the amount of atmospheric aerosol, is the integral of $k_{ext}dz$ over a total depth z (Equation 1.6). While k_{ext} expresses the total loss of photons, the single scattering albedo ω is the fraction of extinction that is due to scattering alone (Equation 1.7).

$$\omega = \frac{k_{scat}}{k_{ext}} \tag{1.7}$$

Additionally, we are interested in the amount of shortwave radiation reflected back out to space and, therefore, need to know about the angular distribution of scattered radiation. The angular distribution of radiation intensity scattered by an aerosol at a given wavelength is called the scattering phase function P(θ) where θ is the angle into which the radiation is scattered. In particular, the amount of radiation reflected back out to space is quantified by the backscatter ratio β, an integral of the phase function representing the fraction of scattered intensity that is redirected into the backward hemisphere of the scattering particle (Equation 1.8).

$$\beta = \frac{\int_{\frac{\pi}{2}}^{\pi} P(\theta) sin(\theta) d\theta}{\int_{0}^{\pi} P(\theta) sin(\theta) d\theta} \tag{1.8}$$

Another measure of the distribution of scattered intensity is the asymmetry parameter σ, which is defined as the intensity-weighted average of the cosine of the scattering angle. For σ, a value of one means light is scattered completely at θ =0° (forward direction) while a value of negative one indicates light is scattered completely at θ =180° (backward direction). A value of zero is for a particle that scatters light isotropically (same in all directions).

All three optical parameters discussed are controlled by the wavelength of the incident radiation(λ), the size of the particle (r), and the complex index of refraction (n-ik) which describes the aerosol optical properties relative to the medium. The refractive index is wavelength dependent with the real and imaginary parts representing the non-absorbing and absorbing components, respectively.

Using the key aerosol optical properties, the radiative transfer equation must be solved to determine the change in flux at the TOA. The basic equation of radiative transfer is shown in Equation 1.9 where -I(λ) represents the loss of radiant intensity due to scattering and absorption and J(λ) is the source function at a given wavelength.

$$\frac{dI(\lambda)}{k_{ext}(\lambda) dz} = -I(\lambda) + J(\lambda) \tag{1.9}$$

For the case where emission contributions from the earth-atmosphere system can be neglected (shortwave range, 0.2 to 5μm) [58] as well as the diffuse radiation produced by multiple scattering, Equation 1.9 reduces to Equation 1.10.

$$\frac{dI(\lambda)}{k_{ext}(\lambda) dz} = -I(\lambda) \tag{1.10}$$

The integration of Equation 1.10 results in the Beer-Lambert law (Equation 1.6), which describes a decrease in radiant intensity through a simple exponential function. Since the Beer-Lambert law has no directional dependence, it is applicable to the radiant intensity (Wm^{-2}sr^{-1}) as well as the flux (Wm^{-2}).

In many applications of the radiative transfer, it is appropriate to assume the atmosphere is plane-parallel such that variations in the intensity and atmospheric parameters only occur in the vertical. For the case where multiple scattering cannot be neglected, the plane parallel assumption is used [58]. In this case, it is convenient to measure linear distances in the normal direction and the general equation for radiative transfer becomes

$$cos(\theta)\frac{dI(z;\theta,\phi)}{k_{ext}dz} = -I(z;\theta,\phi) + J(z;\theta,\phi) \tag{1.11}$$

where θ is the zenith angle (angle between sun and local zenith or normal direction) and ϕ is the azimuth angle (angle between a point of interest projected perpendicularly on the horizontal plane and a reference vector). Since the integral of the extinction coefficient multiplied by dz is equal to the optical depth, Equation 1.11 can also be written in terms of τ.

$$\mu\frac{dI(\tau;\mu,\phi)}{d\tau} = I(\tau;\mu,\phi) - J(\tau;\mu,\phi) \tag{1.12}$$

In this case, μ is the cosine of the zenith angle. This is the basic equation for multiple scattering in a plane-parallel atmosphere. For the problem of radiative forcing, the outgoing radiant intensity is of particular interest. Equation 1.12 can be solved for the upward intensity of an atmosphere bounded by τ=0 at the TOA and τ=τ^* at the surface.

$$I(\tau;\mu,\phi) = I(\tau^*;\mu,\phi)e^{-(\tau^*-\tau)/\mu)} + \int_{\tau}^{\tau^*} J(\tau';\mu,\phi)e^{-(\tau'-\tau)/\mu}\frac{d\tau'}{\mu}(1 \geq \mu{>}1) \tag{1.13}$$

By setting τ=0, Equation 1.13 gives the upward intensity at the TOA.

$$I(0;\mu,\phi) = I(\tau^*;\mu,\phi)e^{-\tau^*/\mu} + \int_{\tau}^{\tau^*} J(\tau';\mu,\phi)e^{-\tau'/\mu}\frac{d\tau'}{\mu} \tag{1.14}$$

In the case where the optical depth is small ($\tau \ll 1$), scattering events are dominated by single scattering of the direct solar beam [58]. The source function J under conditions of small optical depth is expressed in Equation 1.15.

$$J(\tau;\mu,\phi) \cong \frac{\omega}{4\pi}F_oP(\mu,\phi;-\mu_o,\phi_o)e^{-\tau/\mu_o} \tag{1.15}$$

For a black surface (no reflection) such that I(τ^*;μ,ϕ)=0, the upward intensity at the TOA is Equation 1.16.

$$\begin{aligned} I(0;\mu,\phi) = \int_0^{\tau^*} & J(\tau';\mu,\phi)e^{-\tau'/\mu}\frac{d\tau'}{\mu} \\ & = \frac{\mu_oF_o}{\pi}\frac{\omega}{4(\mu+\mu_o)}P(\mu,\phi;-\mu_o,\phi_o)\left(1 - exp\left[-\tau * \left(\frac{1}{\mu} + \frac{1}{\mu_o}\right)\right]\right) \end{aligned} \tag{1.16}$$

and the reflectance is: [58]

$$R(\mu,\phi;\mu_o,\phi_o) = \frac{\pi I(0;\mu,\phi)}{\mu_oF_o} = \tau\frac{\omega}{4\mu\mu_o}P(\mu,\phi;-\mu_o,\phi_o) \tag{1.17}$$

The reflectance is particularly important for satellite measurements, which will be discussed. The intensities have directional dependence under conditions of a plane-parallel atmosphere or the single-scattering approximation. To obtain the outgoing flux, the intensity must be integrated over the solid angle Ω (for a sphere, Ω=4π or 2π for a hemisphere).

$$F(\lambda) = \int I(\lambda) cos\theta d\Omega = \int_o^{2\pi} \int_0^{\pi/2} I(\theta, \phi) cos\theta sin\theta d\theta d\phi \tag{1.18}$$

The total shortwave flux is then obtained by integrating the flux from approximately 0.2 to 5μm.

Charlson et al 1992 [14] calculated the globally averaged direct aerosol RF for scattering aerosols using the single-scattering approximation. The resulting expression is shown in Equation 1.19 where T$_{atm}$ is the transmittance of the atmosphere above the aerosol layer, α is the albedo of the underlying surface, and τ_{scat} is the aerosol layer scattering optical depth. T^2_{atm} reduces the incident solar flux and the reflected flux by the transmittance of the atmosphere above the aerosol layer, (1-A_c) comes from the assumption that albedo changes due to aerosol are only important in cloud free atmosphere, and (1-α)$^2 2\beta\tau_{scat}$ represents the albedo increase due to a scattering aerosol layer. The negative sign represents a cooling tendency.

$$\Delta F^{TOA}_{sw} = -\frac{F_o}{4} T^2_{atm}(1 - A_c)(1 - \alpha)^2 2\beta\tau_{scat} \tag{1.19}$$

Chylek and Wong 1995 [15] took this a step further, including the effects of absorbing aerosol (Equation 1.20). The scattering and absorbing optical depths can be written in terms of the single scattering albedo, resulting in the final Equation 1.21. For a non-absorbing aerosol (τ_{abs}=0,ω=1), Equations 1.20 and 1.21 reduce to the equation used by Charlson et al (1992)[14].

$$\Delta F^{TOA}_{sw} = -\frac{F_o}{4} T^2_{atm}(1 - A_c)[(1 - \alpha)^2 2\beta\tau_{scat} - 4\alpha\tau_{abs}] \tag{1.20}$$

$$\Delta F^{TOA}_{sw} = -\frac{F_o}{4} T^2_{atm}(1 - A_c)[(1 - \alpha)^2 2\beta\tau_{scat} - 4\alpha(1 - \omega)\tau] \tag{1.21}$$

The equations by Charlson et al [14] and Chylek and Wong [15] are for globally averaged radiative forcing and are useful in estimating the magnitude of the effect as well as illustrating some of the key physical factors expected to be important in more complicated calculations. The globally averaged aerosol optical depth is $\tau \sim 0.15$, a typical backscatter ratio is $\beta \sim 0.1$ and the transmission through the air $T_{atm} \sim 0.75$. The globally averaged fractional cloud cover has been observed to be approximately A_c= 0.65 (International Satellite Cloud Climatology Project (ISCCP) at http://isccp.giss.nasa.gov/). Using a global mean surface albedo α ~0.15 and a typical single scattering albedo ω ~0.98, an estimate of the globally averaged aerosol direct radiative forcing is ΔF^{TOA}_{sw}=-1.30 Wm^{-2}. This estimate of aerosol forcing increases with the scattering optical depth as well as the backscatter ratio and decreases as absorption becomes more important. For a dominantly scattering aerosol, the RF scales with the optical depth ($\Delta F^{TOA}_{sw} \propto \beta\tau$). Estimates of aerosol direct radiative forcing from modeling studies and analysis of satellite observations give estimates of aerosol direct radiative forcing at -0.5 ± 0.4 Wm^{-2} [84]. It should be noted that these estimates include anthropogenic aerosol only. The sum of the direct effects due to anthropogenic and natural aerosol is referred to as the solar direct radiative effect (DRE) [84]. The average clear-sky estimate of DRE from various studies is -5.4 Wm^{-2} with a standard deviation of 0.9 Wm^{-2} [84], a much larger cooling influence than anthropogenic aerosol alone. According to climate models, the direct radiative forcing of aerosols has helped to offset some of the warming by greenhouse gases (GHG) with radiative forcing estimates for carbon dioxide at 1.66 Wm^{-2} (1.49-1.83 Wm^{-2}) [84].

For the aerosol indirect effect, the key parameter is the effectiveness of an aerosol to act as a cloud condensation nucleus [20]. Aerosols that become activated to grow to fog or cloud droplets in the presence of water vapor supersaturation are called cloud condensation nuclei (CCN). There is a critical ambient water vapor supersaturation below which particles exist in a stable state and above which it spontaneously grows to become a cloud droplet (activated). The critical supersaturation depends on the size and chemical composition of the aerosol and the ambient conditions. Feingold et al 2003 [24] estimated that the relationship between aerosol and cloud droplet number concentration is nonlinear and described by Equation 1.22 where N_d is the cloud drop number density and N_a is the aerosol number concentration. The parameter b can vary with values ranging from 0.06 to 0.48 [24]. Low b values correspond to aerosols with low hygroscopicity such as nucleation mode black carbon whereas high b values correspond to aerosols that uptake water easily such as accumulation mode sulfate. The change in cloud albedo α_c with a change in N_d can be represented through cloud susceptibility, $(d\alpha_c)/(dN_d)$ [95]. For a given change in N_d, the cloud susceptibility can be used to predict the change in cloud albedo: $\Delta\alpha_c = (\frac{d\alpha_c}{dN_d} * \Delta N_d)$ [2]. By restricting the wavelengths to the broadband visible range (0.3-0.7μm) and considering only cloud droplets and not aerosols, the scattering can be treated as conservative (no absorption) and the asymmetry parameter as constant. This assumption was used by Ackerman et al 2000[2] to define cloud susceptibility using Equation 1.23. The RF due to the cloud-albedo effect depends on the change in α_c.

$$N_d = (N_a)^b \tag{1.22}$$

$$\frac{d\alpha_c}{dN_d} = \frac{d\alpha_c}{d\tau}\frac{d\tau}{dN_d} = \frac{\alpha_c(1-\alpha_c)}{3N_d} \tag{1.23}$$

The first indirect or cloud-albedo RF is the difference in the net shortwave flux at the TOA with the cloud/aerosol interaction and without this effect (Equation 1.24). Using Equations 1.2 and 1.3, the TOA RF is written in terms of fractional cloud cover and cloud albedo (Equation 1.25). The only interaction that is accounted for in the cloud-albedo effect is the change in α_c, therefore, Equation 1.25 can be reduced to Equation 1.26. The cloud susceptibility is then used to calculate the change in α_c, writing the cloud droplet number in terms of aerosol number concentration from Equation 1.22. The result is an estimate of the RF for the aerosol first indirect or cloud-albedo effect (Equation 1.28). For a cloud cover of A_c=0.65 and an initial α_c=0.38 (this is consistent with α_{sw}=0.30 and α_o=0.15), a twenty percent increase in aerosol number concentration results in a cloud-albedo forcing between -0.3 and -2.5 Wm^{-2}, depending on the value of b. The magnitude estimate using Equation 1.28 indicates that the forcing increases with the percent increase in aerosol number concentration and hygroscopicity. Estimates of the aerosol first indirect radiative forcing from modeling studies and analysis of satellite observations give an estimate of -0.7 Wm^{-2} with a range of -1.8 to -0.3 Wm^{-2}. The large range in both the direct and indirect radiative forcing values indicate the high degree of uncertainty associated with these estimates.

$$\Delta F_{sw}^{TOA} = \Delta F_{sw}^{TOA}(aer/cloud.effect) - \Delta F_{sw}^{TOA}(no.effect) \tag{1.24}$$

$$\Delta F_{sw}^{TOA} = \left[\frac{F_o}{4}(1-(A_c\alpha_c+(1-A_c)\alpha_o\right)_{aer/cloud} - \left[\frac{F_o}{4}(1-(A_c\alpha_c+(1-A_c)\alpha_o\right)_{noaer/cloud} \tag{1.25}$$

$$\Delta F_{sw}^{TOA} = -\frac{F_o}{4}A_c(\alpha_{c_{aer/cloud}} - \alpha_{c_{noaer/cloud}}) = -\frac{F_o}{4}A_c\Delta\alpha_c \tag{1.26}$$

$$\Delta F_{sw}^{TOA} = -\frac{F_o}{4}A_c\frac{\alpha_c(1-\alpha_c)}{3}\frac{\Delta N_d}{N_d} \tag{1.27}$$

$$\Delta F_{sw}^{TOA} = -\frac{F_o}{4}A_c\frac{\alpha_c(1-\alpha_c)}{3}\frac{\Delta N_a^b}{N_a^b} \tag{1.28}$$

1.4 Aerosol Measurements

An important method for characterizing tropospheric aerosols is ground-based and satellite-based remote sensing. Remote sensing involves the interpretation and inversion of electromagnetic radiance measurements where the radiation is characterized by a specific wavelength that is sensitive to the object of interest. Understanding the measurements through interpretation and inversion requires the use of radiative transfer theory and the fundamentals of light scattering. If T and S denote the target and measured signal respectively, then a relationship between the two can be written as S=F(T) where F is a function that describes radiation transfer through the atmosphere and involves processes such as scattering and absorption.

For aerosols in particular, determining the amount of aerosol (T) that produces the electromagnetic radiance signal (S) measured by the instrument requires inverting a radiative transfer model that must make assumptions about the types of aerosol present and their optical properties, the surface and its reflective properties (for satellite-based instruments) and the vertical atmospheric profile including absorbing gases. These assumptions allow a separation of the measured aerosol signal from other atmospheric components, and the surface. Additionally, inversion algorithms must have a method for distinguishing cloudy and clear-sky scenes since the presence of clouds obscures atmospheric aerosol. The optimal wavelength range for measuring tropospheric aerosol falls within the solar shortwave spectrum, from approximately 0.3μm to 2μm. The wavelength bands must be narrow enough to avoid the water vapor absorption bands, as an overlap would require additional information about the amount of highly variable atmospheric water vapor.

There are two main types of remote sensing instruments, passive and active. Passive instruments utilize natural radiation sources such as the sun and measure the intensity of the radiation emitted or reflected by an object of interest. Satellite-based instruments such as MODIS and ground-based instruments including AERONET radiometers are passive. MODIS and AERONET radiometers measure column-integrated aerosol optical depth (τ) in the shortwave and information about aerosol size. On the other hand, active instruments emit radiation, often using pulses from a laser at a specific wavelength, and measure the radiation that is reflected or backscattered from a target. Cloud-Aerosol LIdar with Orthogonal Polarization (CALIOP), the space-based instrument onboard NASA's CALIPSO satellite, is an example of active instrumentation and are used for measured aerosol vertical profile. Aerosol observations from MODIS, AERONET, and CALIOP are used for constraining aerosol model predictions in this research. Since these instruments measure aerosol in the shortwave, the focus of this research will be the influence of aerosols in the shortwave. Additionally, AERONET is used as an independent dataset for validation of the model runs. These instruments are discussed.

1.4.1 MODIS

The Moderate Resolution Imaging Spectroradiometer (MODIS) is an instrument onboard NASAs Terra and Aqua satellites, which were launched in May 2002 and December 1999, respectively. They are part of NASA's A-Train, a constellation of satellites that provide global daily coverage of the Earth's surface. The coordinated group of satellites allows for near-simultaneous observations of a wide variety of parameters to aid in understanding the Earth's climate. The A-Train is comprised of sun-synchronous near-polar orbiting satellites. Near-polar orbiting satellites pass nearly above the Earth's poles on each revolution and are synchronized with the sun meaning that each successive orbital pass over the equator occurs at the same local time of the day and at a different longitude. The Terra satellite is on the descending orbit, crossing the equator at 10:30 am local time and the Aqua satellite is on the ascending orbit, crossing the equator at 1:30 p.m. local time. Aqua and Terra fly approximately 700km above the Earth's surface and with MODIS having a scan angle of $\pm 55°$, MODIS views the Earth with an across-track swath of 2330km and 10km along-track. This allows for near global coverage on a daily basis with repeat orbits occurring every 16 days (Figure 1.3).

MODIS is a radiometer that measures the spectral radiance (I_λ) reflected from the Earth-atmosphere system (Equation 1.13) in 36 spectral bands, or groups of wavelengths, from the solar to the thermal infrared (0.41μm -14.235μm). Satellite detectors give direct measurement of the intensity (I_λ) integrated over the instrument channel c (λ_{c1} to λ_{c2}) (Equation 1.29).

$$I_c(\tau;\mu,\phi) = \int_{\lambda_{c1}}^{\lambda_{c2}} I_\lambda(\tau;\mu,\phi)d\lambda \tag{1.29}$$

Of the 36 spectral bands, the aerosol retrieval makes use of 7 bands in the shortwave (Table 1.1) and several others for cloud screening. The MODIS algorithm uses spectral reflectance (R_λ) (Equation 1.17, 1.30) in the seven wavelength bands, which is a function of the measured spectral radiance (I_c), the solar zenith angle (θ_o) and the solar irradiance integrated over the wavelength channel of interest ($F_{o,c}$). Spectral reflectance values are reported at the central wavelength of the band (λ) (Table 1.1).

$$R_\lambda = \frac{\pi I_c}{cos(\theta_o F_{o,c})} \tag{1.30}$$

Processing of R_λ for use in the aerosol retrieval requires several steps. In each MODIS scan (2330km across-track and 10km along-track), there are approximately 1354 pixels with a 1km channel resolution at nadir view. The number of pixels increases for higher resolution channels (250m, 500m). In order to process, the pixels are first averaged into 10 km^2 boxes with approximately 135 boxes per swath. Once averaged, R_λ are corrected for water vapor, ozone, and carbon dioxide using ancillary datasets (MODIS atmospheric profile product (Level 2), NCEP (National Center for Environmental Prediction) 1°x1° 6-hour meteorological analysis, TOVS 1°x1° daily ozone analysis), allowing isolation of the aerosol signal. Following the correction, observations must be identified as cloudy or clear-sky. If identified as clear, the surface type is determined in order to account for differences in radiance reflection at the Earth's surface as well as differences in aerosol type. The boxes are screened for clouds using the MODIS cloud-mask (Level 2, 10 km^2 resolution) product. The cloud-mask product is also used for identification of the surface type. If any pixel within a 10 km^2 box is identified as land, the box is identified as land surface. Otherwise, a box is identified as ocean. Separate retrieval algorithms are used for ocean and land surfaces. A detailed description of pixel selection can be found in Remer et al, 2005 [77].

As mentioned previously, aerosol retrievals require assumptions about the types of aerosol present in the atmosphere. In the ocean algorithm, nine aerosol types are used including four fine modes and five coarse modes, each described by a log-normal size distribution (mean size(r_g), distribution standard deviation (σ)) and the complex index of refraction (n-ik) at several wavelengths (Table 1.2). The aerosol types were identified by analysis of AERONET data [32] [77].

A forward radiative transfer model is used to generate reflectance look-up tables (LUT) for each aerosol type. The reflectance depends on the viewing geometry (solar zenith angle, satellite view zenith angle, azimuth angle), the amount of aerosol, and the surface. Computations are performed for combinations of 9 solar zenith angles (6°, 12°, 24°, 36°, 48°, 54°, 60°, 66°, and 72°), 16 satellite view zenith angles (0°to 72° with increments at 6°) and 16 relative sun/satellite azimuth angles (0° to 180°, increments of 12°) for a total of 2304 angular combinations. Reflectances are calculated for six aerosol optical depths to account for changes in the amount of aerosol with values ranging from a pure molecular (Rayleigh) atmosphere (τ=0) to a highly turbid atmosphere (τ=3). Ocean surface reflection calculations include sun glint reflection off of surface waves [17], reflection by whitecaps [52] and

Lambertion (directionally independent) reflectance from underwater scattering (sediments, chlorophyll, etc). The surface wind speed is assumed to be 6.0 m/s.

The retrieval selects a fine and coarse mode pair and determines which twenty combinations of fine and coarse modes and their relative optical contributions best reproduce the MODIS-observed spectral reflectance. The reflectance from each mode is combined using a weighting parameter η,

$$R_{\lambda}^{LUT}(\tau_{0.55}^{tot}) = \eta R_{\lambda}^{f}(\tau_{0.55}^{tot}) + (1-\eta) R_{\lambda}^{c}(\tau_{0.55}^{tot}) \tag{1.31}$$

where R_{λ} $(\tau_{0.55}^{tot})$ is a weighted average reflectance of an atmosphere with a pure fine mode (f) and an optical thickness at 0.55μm $(\tau_{0.55}^{tot})$ and an atmosphere with a pure coarse mode (c), again with an optical thickness $\tau_{0.55}^{tot}$. The pair of fine and coarse aerosol models is then identified by minimizing a fitting error ϵ,

$$\epsilon = \sqrt{\frac{\sum_{\lambda=1}^{6}\left(\frac{R_{\lambda}^{m}-R_{\lambda}^{LUT}}{R_{\lambda}^{m}-R_{\lambda}^{ray}+0.01}\right)^{2}}{\sum_{\lambda=1}^{6} N_{\lambda}}} \tag{1.32}$$

where N_{λ} is the sum of good pixels at wavelength λ, R_{λ}^{m} is the measured MODIS reflectance at wavelength λ, R_{λ}^{ray} is the reflectance contribution from Rayleigh scattering and R_{λ}^{LUT} is the calculated LUT reflectance from the combination of fine and coarse modes. The value of 0.01 is added to prevent division by zero. The solution requires that an exact match occurs in the 0.86μm channel and then a best fit is found for the remaining wavelengths. The sensitivity of the 0.86μm channel to variability in water leaving radiances is expected to be less than the shorter wavelength channels. At the same time, the channel still exhibits a strong aerosol signal. Therefore, the variability in chlorophyll is expected to have a negligible effect on the optical depth retrieval by emphasizing accuracy in this band. Once the best solution is identified, a variety of parameters are inferred. The primary retrieved products are the total τ at 0.55μm, the fine mode weighting η, and the selected fine and coarse modes. From the primary retrievals, a number of other parameters including the fine and coarse aerosol optical depth $(\tau_{0.55}^{f}, \tau_{0.55}^{c})$ and the angstrom exponent (α, Equation 1.33) are derived.

$$\alpha = \frac{ln[\tau(\lambda_1)/\tau(\lambda_2)]}{ln[\lambda_2/\lambda_1]} \tag{1.33}$$

A different algorithm is used for retrievals over land surfaces, however, LUTs generated for a set of predetermined aerosol models and surface conditions are used, similar to the ocean retrieval. Cluster analysis of AERONET data was used to determine a set of aerosol models [56]. The identified aerosol models included three spherical (moderately absorbing, absorbing and non-absorbing) fine-dominated models, one spheroid coarse dust model and a continental model. Optical properties and size distribution information for the land retrieval aerosol models are shown in Table 1.3. LUTs are then generated at four wavelengths (0.466, 0.553, 0.646 and 2.12μm) and for several values of aerosol loading and viewing geometries. The total calculated reflectance is treated as a linear sum of the reflectance from the atmosphere above a dark surface and surface reflection that is directly transmitted to the TOA. Surface reflectance calculations over land take advantage of the 2.12μm band which is not sensitive to atmospheric aerosol and is effectively a measure of the surface reflection only. Studies have shown that the reflection in the 2.12μm band is strongly correlated with the surface reflection in the visible [47]. Therefore, the 2.12μm band reflection is used to calculate reflection in the three remaining visible channels. The algorithm proceeds with optical model selection in a similar manner to the ocean algorithm.

The aerosol products from the MODIS algorithms have a 10 km^2 resolution and are referred to as Level 2 product. Higher level daily and monthly products are then produced by averaging the Level 2 product onto a $1°$x$1°$ grid. Validation efforts on the Level 3 product reveal a MODIS AOD retrieval error that is higher over land than ocean with a land error of $\pm0.05\pm0.2\tau$ and an ocean error of $\pm0.03\pm0.05\tau$. The difference in error is due to complicated land surface reflectance properties. The Level 3 daily averaged MODIS aerosol products, including aerosol optical depth and angstrom exponent ($\tau_{0.55}$,α), are used for assimilation in this work.

MODIS observations for the year 2007 are used for constraining model predictions in this work, therefore, the spatial and temporal patterns in the observations are examined. Seasonally and yearly averaged aerosol optical depth and angstrom exponent MODIS products for the year 2007 are shown in Figures 1.4 through 7. Aerosol retrievals cannot be conducted over very bright surfaces such as the Sahara desert and the Arabian Peninsula and as a result, there are no observations for constraining aerosol amount and size in these regions. Angstrom exponent retrievals are shown for over ocean only. Errors in angstrom retrievals over land are too large for use in assimilation. The area-weighted globally averaged aerosol optical depth observed by MODIS is 0.161 for the year 2007 with seasonal averages of 0.155 for December/January/February, 0.168 for March/April/May, 0.165 for June/July/August and 0.160 for September/October/November. The area-weighted over-ocean average angstrom exponent observed by MODIS is 0.65 for the year 2007 with seasonal averages of 0.66 for December/January/February, 0.62 for March/April/May, 0.65 for June/July/August and 0.67 for September/October/November.

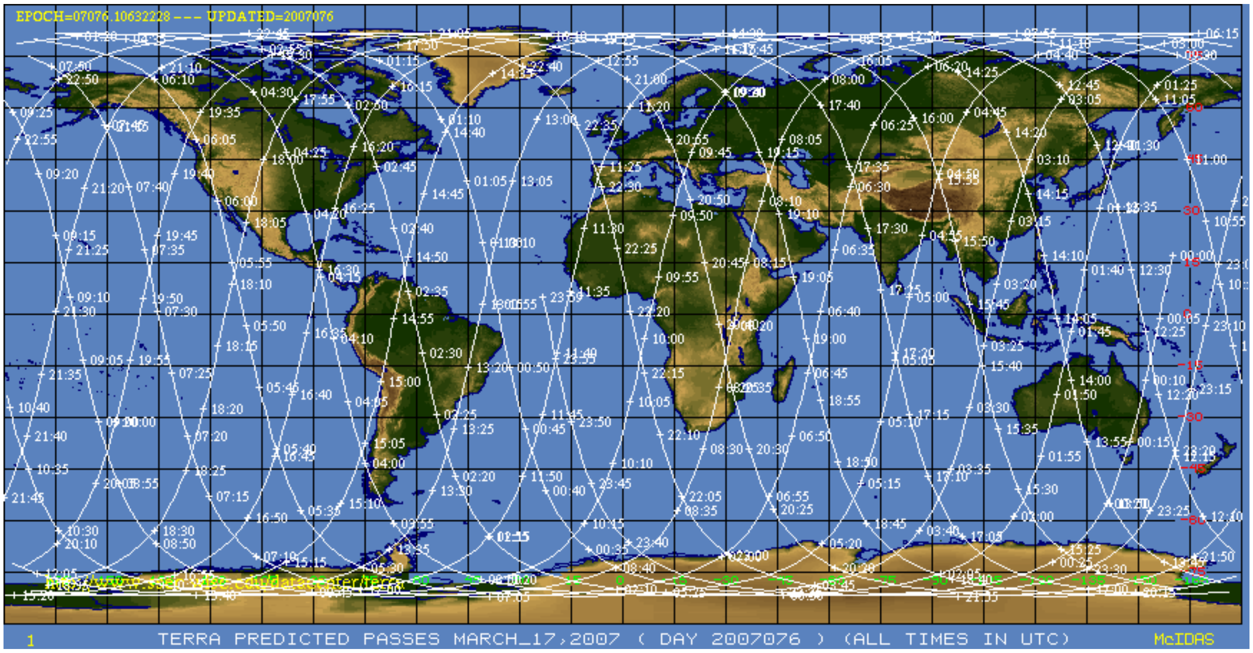

Figure 1.3: Predicted MODIS orbit track for March 17, 2007 (http://modis-atmos.gsfc.nasa.gov)

Band (c)	Bandwidth (c1 to c2)	Central Wavelength (nm)	Resolution (m)
1	620 - 670 nm	646	250
2	841 - 876 nm	855	250
3	459 - 479 nm	466	500
4	545 - 565 nm	553	500
5	1230 - 1250 nm	1243	500
6	1628 - 1652 nm	1632	500
7	2105 - 2155 nm	2119	500

Table 1.1: MODIS wavelength bands used in the aerosol retrieval algorithm. The bands are defined by the upper and lower wavelength, the central wavelength and the measurement resolution.[78]

#	λ: 0.47μm 0.86μm	λ: 1.24μm	λ: 1.64μm	λ: 2.12μm	r_g (μm)	σ (μm)	Model
1	1.45-0.0035i	1.45-0.0035i	1.43-0.01i	1.40-0.005i	0.07	0.40	Water Soluble
2	1.45-0.0035i	1.45-0.0035i	1.43-0.01i	1.40-0.005i	0.06	0.60	Water Soluble
3	1.40-0.0020i	1.40-0.0020i	1.39-0.005i	1.36-0.003i	0.08	0.60	Water Soluble with Humidity
4	1.40-0.0020i	1.40-0.0020i	1.39-0.005i	1.36-0.003i	0.10	0.60	Water Soluble with Humidity
5	1.35-0.001i	1.35-0.001i	1.35-0.001i	1.35-0.001i	0.40	0.60	Wet Sea Salt
6	1.35-0.001i	1.35-0.001i	1.35-0.001i	1.35-0.001i	0.60	0.60	Wet Sea Salt
7	1.35-0.001i	1.35-0.001i	1.35-0.001i	1.35-0.001i	0.80	0.60	Wet Sea Salt
8	1.53-0.003i	1.46-0.000i	1.46-0.001i	1.46-0.000i	0.60	0.60	Dust-Like Type
9	1.53-0.003i	1.46-0.000i	1.46-0.001i	1.46-0.000i	0.50	0.80	Dust-Like Type

Table 1.2: Aerosol Models for the MODIS ocean retrieval algorithm (MODIS L2 ATBD)

Model	Mode	r_v (μm)	σ	Refractive Index (n+ki)
Continental	Soluble	0.176	1.09	1.53-0.005i: 0.47μm 1.53-0.006i: 0.55μm 1.53-0.006i: 0.66μm 1.42-0.01i: 2.12μm
	Dust	17.6	1.09	1.53-0.008i: 0.47μm 1.53-0.008i: 0.55μm 1.53-0.008i: 0.66μm 1.22-0.009i: 2.12μm
	Soot	0.050	0.693	1.75-0.45i: 0.47μm 1.75-0.44i: 0.55μm 1.75-0.43i: 0.66μm 1.81-0.50i: 2.12μm
Moderately Absorbing	Accum	$0.0203\tau+0.145$	$0.1365\tau+0.3738$	1.43-($-0.002\tau+0.008$)i
	Coarse	$0.3364\tau+3.101$	$0.098\tau+0.7292$	1.43-($-0.002\tau+0.008$)i
Non-Absorb/ Industrial	Accum	$0.0434\tau+0.1604$	$0.1529\tau+0.3738$	1.42-($-0.0015\tau+0.007$)i
	Coarse	$0.1411\tau+3.3252$	$0.1638\tau+0.7292$	1.42-($-0.0015\tau+0.007$)i
Absorb/ Smoke	Accum	$0.0096\tau+0.1335$	$0.0794\tau+0.3834$	1.51-0.02i
	Coarse	$0.9489\tau+3.4479$	$0.0409\tau+0.7433$	1.51-0.02i
Spheroid/ Dust	Accum	$0.1416\tau^{-0.0519}$	$0.7561\tau^{0.148}$	$1.48\tau^{-0.021}$-($0.0024\tau^{0.132}$)i: 0.47μm $1.48\tau^{-0.021}$-0.002i: 0.55μm $1.48\tau^{-0.021}$-($0.0018\tau^{0.08}$)i: 0.66μm $1.48\tau^{-0.04}$-($0.0018\tau^{0.3}$)i: 2.12μm
	Coarse	2.2	$0.554\tau^{-0.0519}$	$1.48\tau^{-0.021}$-($0.0024\tau^{0.132}$)i: 0.47μm $1.48\tau^{-0.021}$-($0.0018\tau^{0.08}$)i: 0.66μm $1.48\tau^{-0.04}$-($0.0018\tau^{0.3}$)i: 2.12μm

Table 1.3: Aerosol Models for the MODIS land retrieval algorithm (MODIS L2 ATBD).[78]

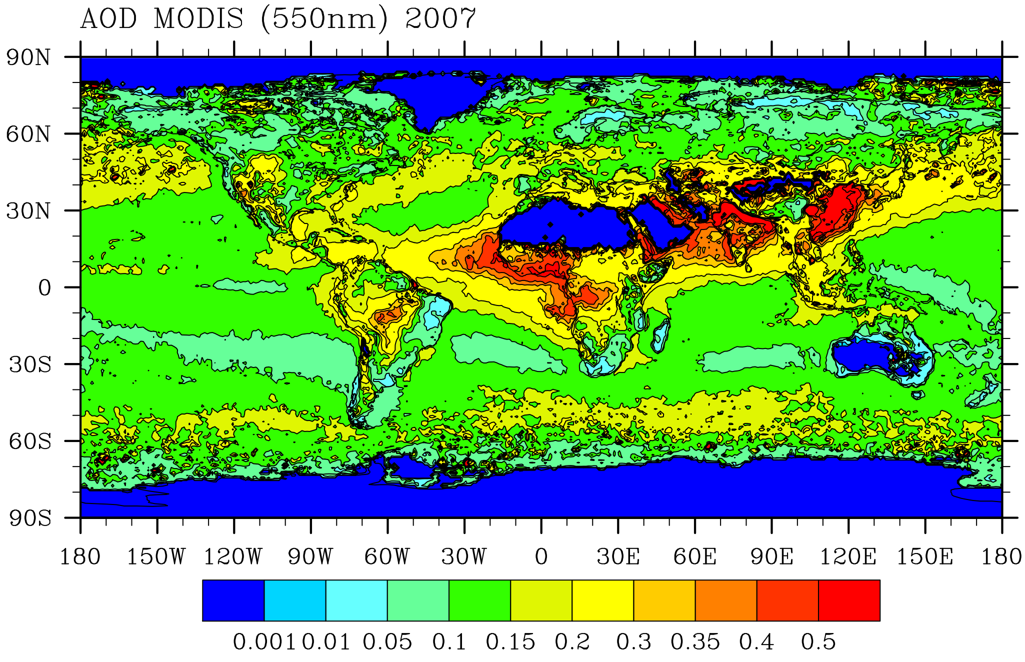

Figure 1.4: Average aerosol optical depth at 550nm observed by MODIS (Terra) for the year 2007. Dark blue regions represent areas where observations are not available.

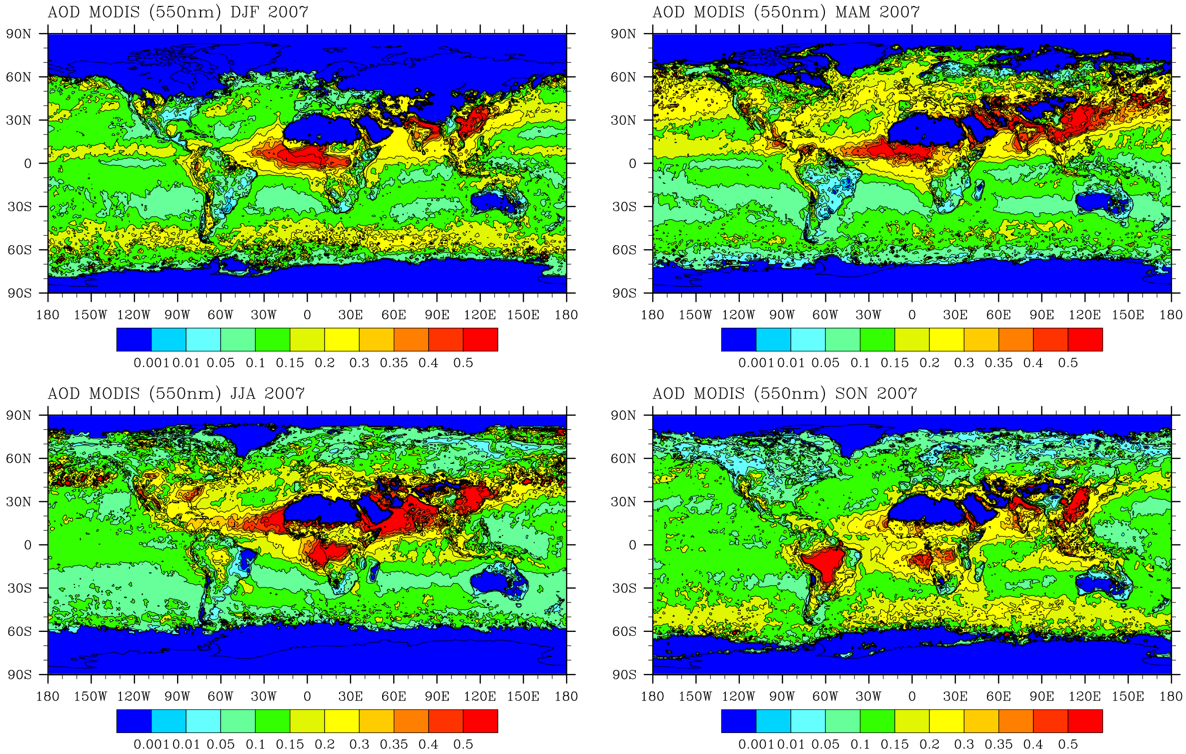

Figure 1.5: Average aerosol optical depth at 550nm observed by MODIS (Terra) for (a) December/January/February (DJF), (b) March/April/May (MAM), (c) June/July/ August (JJA) and (d) September/ October/ November (SON) for the year 2007. Dark blue regions represent areas where observations are not available.

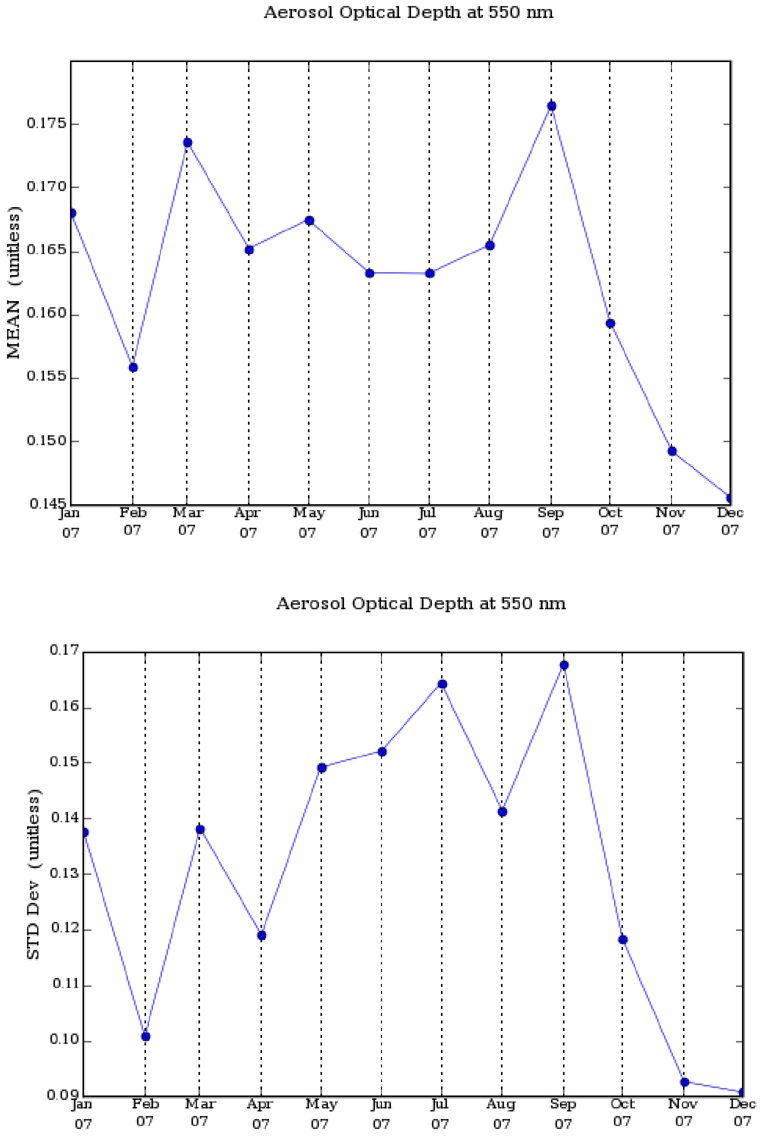

Figure 1.6: Time series of (a)globally averaged MODIS AOD (550nm) and (b)the corresponding standard deviation.

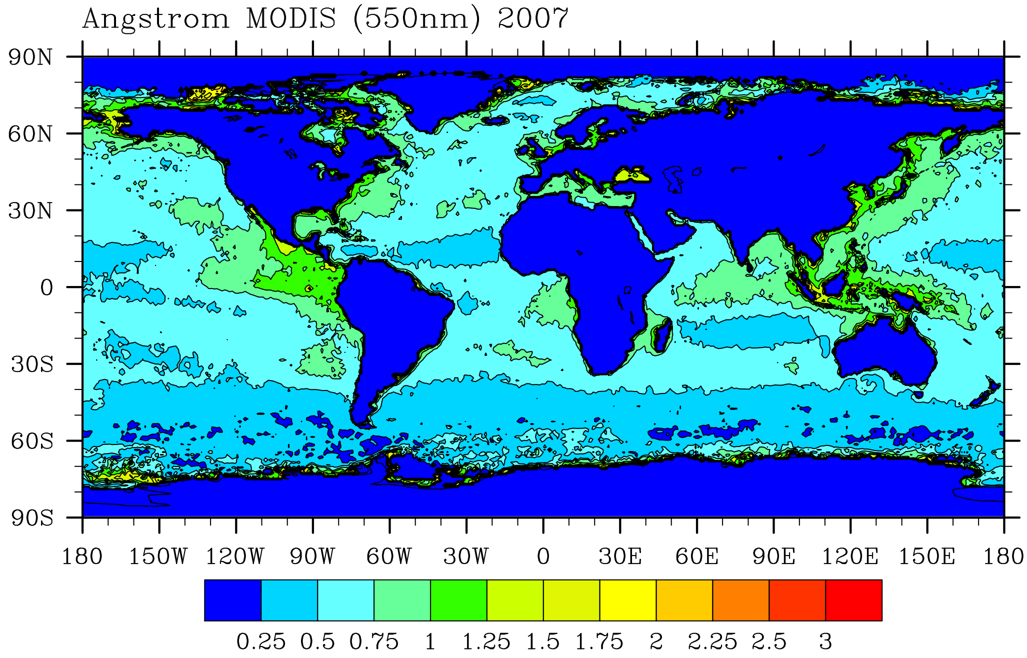

Figure 1.7: Average angstrom exponent (550-865nm) observed by MODIS (Terra, over ocean only) for the year 2007. Dark blue regions represent areas where observations are not available.

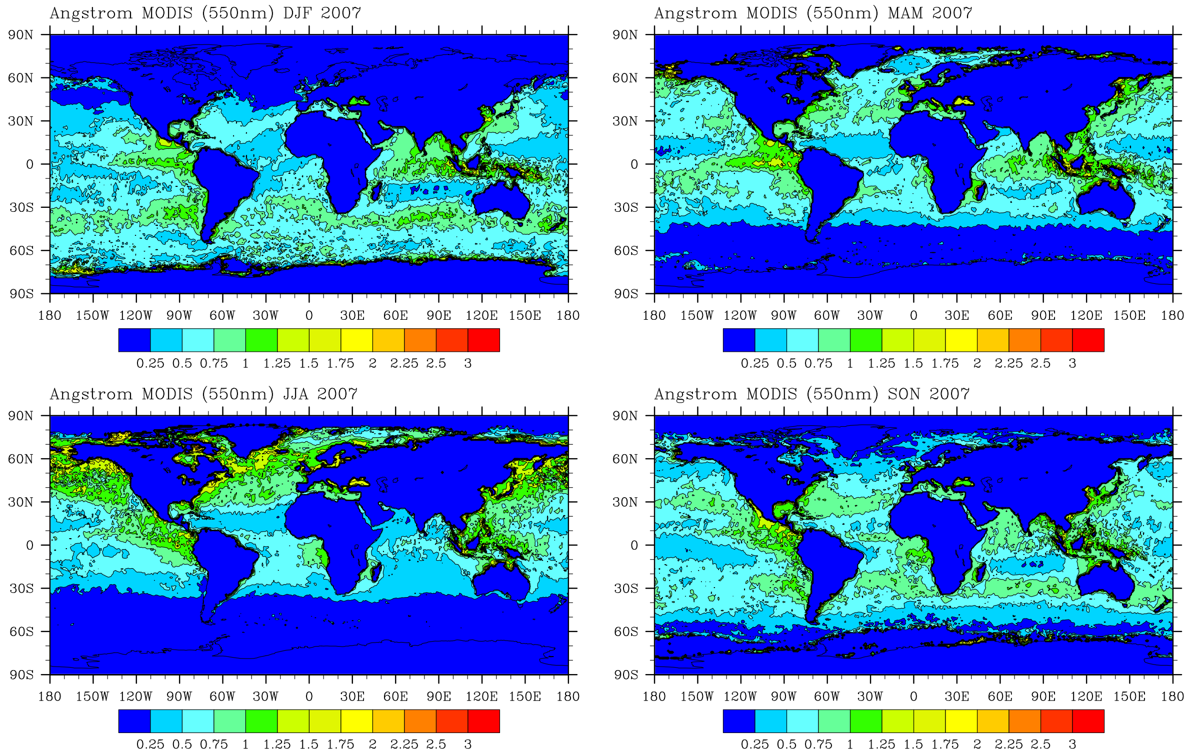

Figure 1.8: Average angstrom exponent (550-865nm) observed by MODIS (Terra, over ocean only) for (a) December/January/February (DJF), (b) March/April/May (MAM), (c) June/July/ August (JJA) and (d) September/ October/ November (SON) for the year 2007. Dark blue regions represent areas where observations are not available.

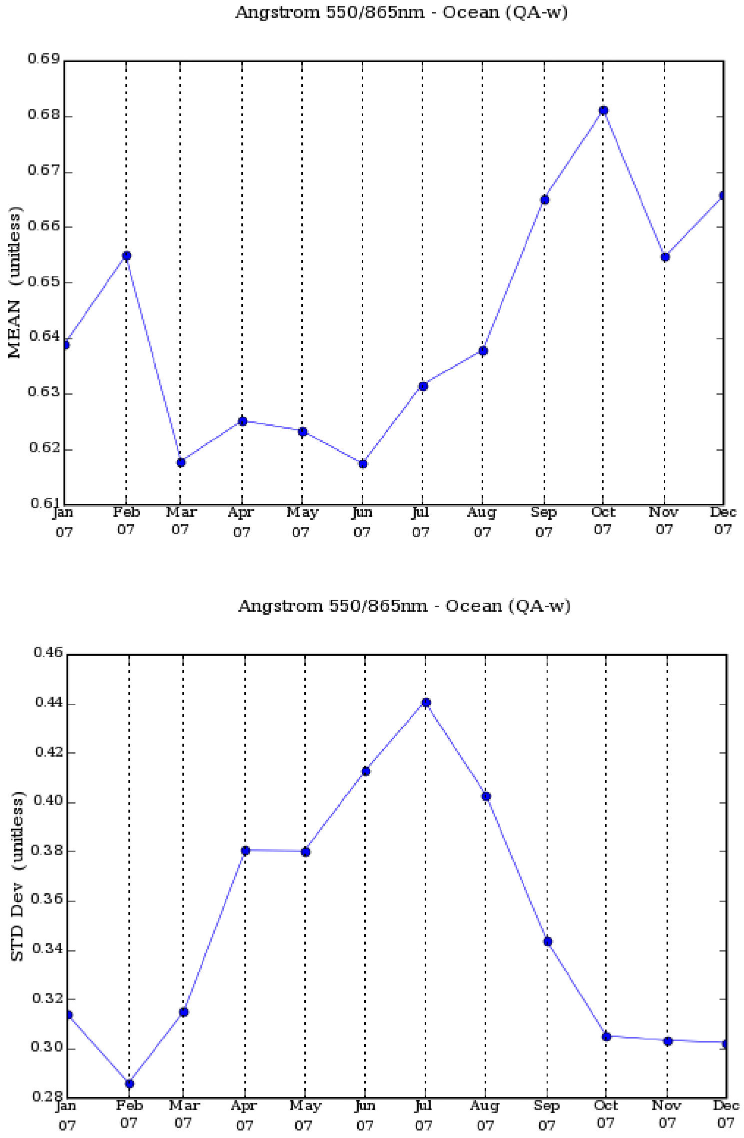

Figure 1.9: Time series of (a)globally averaged MODIS angstrom exponent (550-865nm) and (b)the corresponding standard deviation.

1.4.2 AERONET

The Aerosol Robotic Network (AERONET) is a network of approximately two hundred ground-based sun-photometers, which provide globally distributed and continuous observations of atmospheric aerosol properties (http://aeronet.gsfc.nasa.gov/)[32]. Observations are cloud-screened and include spectral aerosol optical depth (τ) and angstrom exponents (α) as well as inversion products relating to aerosol size such as aerosol optical depth due to fine aerosol, and mean and standard deviation of the size distribution. The location of active AERONET sites for the year 2007 is shown in Figure 1.10.

AERONET instruments measure the extinction of the direct solar beam in eight spectral bands, 340, 380, 440, 500, 670, 870, 940 and 1020nm. Using the spectral extinction, the atmospheric optical depth is determined using the Beer-Lambert Law (Equation 1.6). Attenuation of the beam due to Rayleigh scattering and absorption by ozone and other gaseous pollutants is estimated and removed to isolate the aerosol optical depth. Measurements of aerosol optical depth by AERONET instruments are quite accurate because of the use of the direct solar beam. Possible offsets in solar channel calibration are expected to generate a wavelength independent absolute uncertainty in AERONET aerosol optical depth at the level of ± 0.01 [32]. This is more accurate than MODIS AOD observations, which require information about surface reflectance properties that are not well quantified. As a result of the low uncertainty, AERONET measurements are commonly used for validation of aerosol forecasts and satellite observations. In addition to AOD, AERONET reports angstrom exponents, which are calculated using AERONET AOD values for all available wavelengths (870,670, 500 and 440nm). In this research, the AERONET angstrom exponent observations are used for assimilation, while the AOD and AOD fine contribution is used for model validation.

AERONET observations are compared against MODIS retrievals in Figure 1.11. The comparisons presented are at 500 nm for the AERONET Level 2 cloud-screened measurements and use the 550nm MODIS band. Monthly mean AERONET AODs have been constructed for months where at least ten days of measurements are available at a particular site. These are compared to the monthly-mean AODs from the MODIS Level 3 product (Figure 1.11). Monthly AOD values compare reasonably well between MODIS and AERONET, despite some scatter existing. The optical depths due to fine aerosol measured by AERONET are in general higher than retrieved by MODIS.

Radiance measurements and inversions of the AERONET dataset from 1993 to 2002 were used to classify AERONET sites by aerosol type [69]. More than 143,000 AERONET records were used to generate the optical properties of aerosols at more than 250 sites globally. A cluster analysis was done resulting in six significant clusters. Using the mean values of the optical and microphysical parameters as well as geographic locations, the clusters were identified as desert dust, biomass burning, urban industrial pollution, rural background, polluted marine and dirty pollution. Summaries of the properties for the six identified site categories are shown in Table 1.4. The locations of the sites identified under the six category types are shown in Figure 1.12. Monthly-mean AODs from the MODIS Level 3 product are compared against AERONET data by site category (Figure 1.13). Comparison of aerosol optical depth and other aerosol properties predictions against AERONET by site category is a useful way to examine how well we are doing by aerosol type. The majority of sites are categorized as industrial pollution with AERONET predicting higher optical depths than MODIS. The largest deviations are observed in the rural sites with MODIS measuring higher optical depths than AERONET.

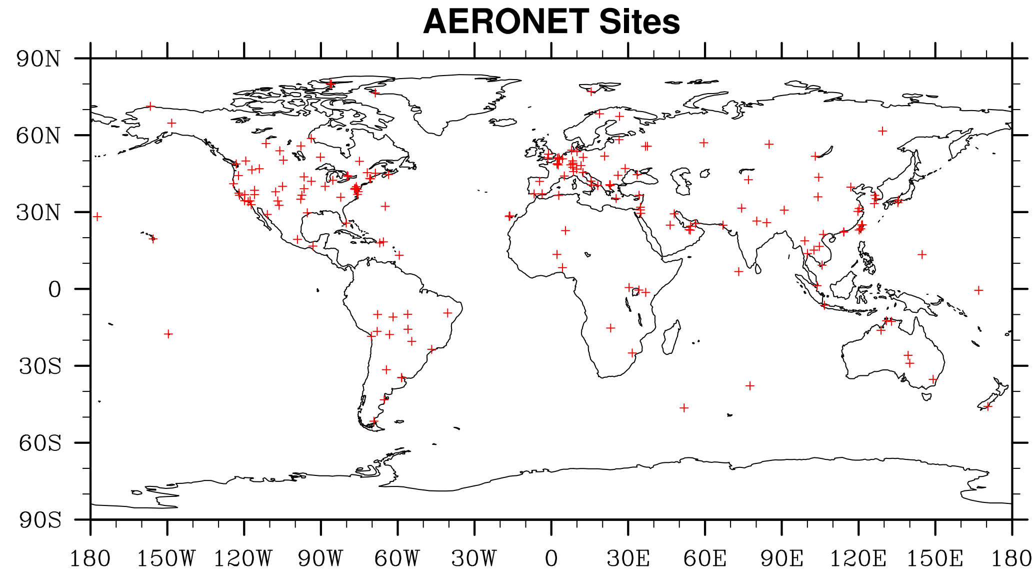

Figure 1.10: AERONET sites with observations for the year 2007.

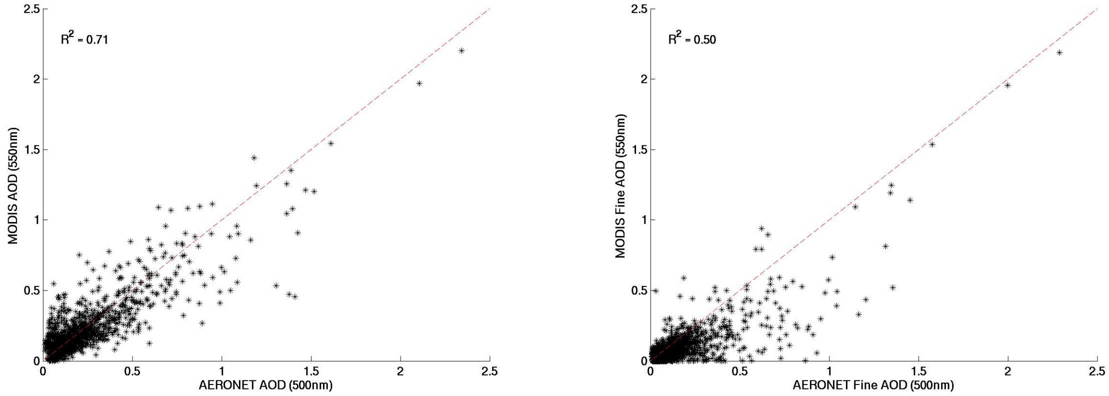

Figure 1.11: Monthly-averaged comparison between AERONET Level two cloud-screened data (500nm) and MODIS Level 3 data (550nm) for aerosol optical depth (left) and fine aerosol optical depth (right).

	Desert Dust	Biomass Burning	Rural	Industrial Pollution	Polluted Marine	Dirty Pollution
Single Scattering Albedo (ω)	0.93	0.80	0.88	0.92	0.93	0.72
Real Refractive Index (n)	1.452	1.520	01.450	1.410	1.394	1.410
Imaginary Refractive Index (k)	0.0036	0.0245	0.0092	0.0063	0.0044	0.0337
Optical Depth (673nm) (τ)	0.327	0.190	0.036	0.191	0.140	0.100
Angstrom Exponent (441/673nm) (α)	0.608	1.391	1.534	1.597	0.755	1.402
Asymmetry Factor (σ)	0.668	0.603	0.580	0.612	0.711	0.594
Fine Fraction by Volume	0.22	0.33	0.38	0.53	0.26	0.49

Table 1.4: Summary of the six identified site categories and their average aerosol properties. Results are derived from a cluster analysis of AERONET data [69]

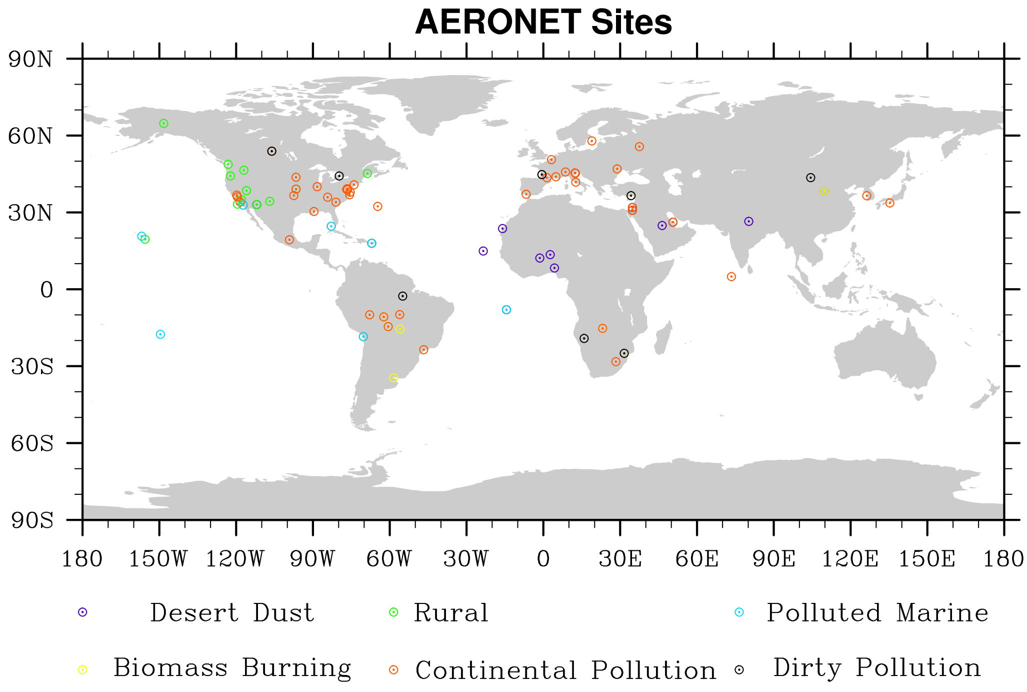

Figure 1.12: AERONET sites classified by six aerosol types, desert dust, biomass burning, rural, industrial pollution, polluted marine and dirty pollution.

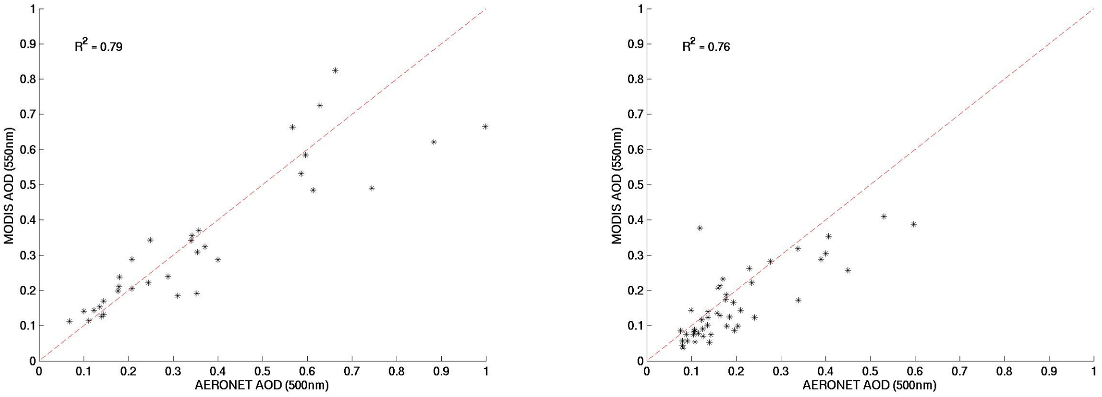

(a) desert dust (b) biomass burning

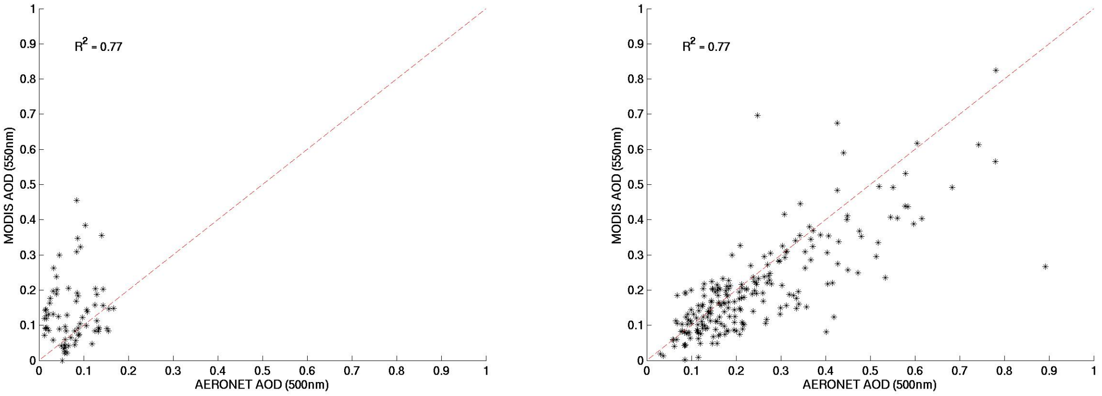

(c) rural (d) industrial pollution

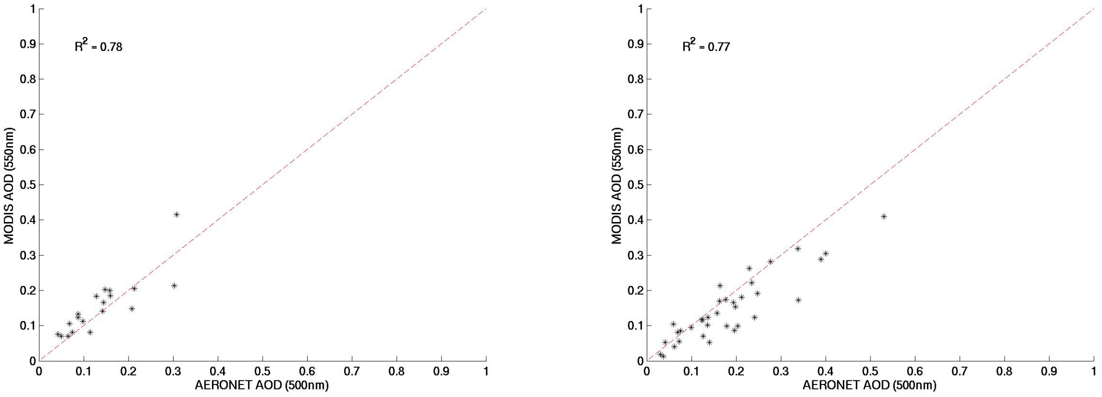

(e) polluted marine (f) dirty pollution

Figure 1.13: Monthly-averaged aerosol optical depth comparison between AERONET Level two cloud-screened data (500nm) and MODIS Level 3 data (550nm) by aerosol site category: a) desert dust b)biomass burning c)rural d)industrial pollution e)polluted marine and f)dirty pollution.

1.4.3 CALIPSO

The Cloud-Aerosol Lidar with Orthogonal Polarization (CALIOP) instrument, onboard the CALIPSO satellite, provides information about the vertical distribution of aerosols and clouds, cloud (ice/water) phase and qualitative classification of aerosol size. CALIOP consists of a two-wavelength polarization sensitive lidar that takes backscatter measurements at 532nm and 1064nm and polarization measurements in the 532nm channel. The active laser provides high vertical resolution and also allows retrieval of aerosol profiles when clouds are present. Backscatter measurements are taken from the surface to 40km with a sampling resolution of 30m in the vertical and 333m in the horizontal. The instrument has been operational since June 2006. CALIPSO is part of NASA's A-Train and flies in formation with the Aqua satellite, crossing the equator at approximately 1:30 p.m. local time.

The signal measured by CALIOP is described by the general form of the lidar equation (Equation 1.34) where P(r) is the measured signal after background subtraction and artifact removal, r is the range from the satellite to the sample volume, E_o is the average laser energy for a single pulse, ξ is the lidar system parameter, β(r) is the volume backscatter coefficient at range r, T(r) is the one-way transmittance from the lidar to the scattering volume at range r, τ is the optical depth, and σ(r') is the volume extinction coefficient at range r. The lidar system parameter ξ is the product of many instrument parameters that govern the sensitivity and efficiency of the instrument including the receiver area and optical efficiency and the detector efficiency. It is separated into two components, the amplifier gain G_A(k) and the calibration constant C(k) (Equation 1.36). Amplifiers are set to one of a number of values that are determined prior to launch and the calibration constant must be determined.

$$P(r,k) = \frac{1}{r^2} E_o(k)\xi(k)\beta(r,k)T^2(r,k) \tag{1.34}$$

$$T^2(r,k) = exp(-2\tau(r)) = exp\left[-2\int_0^r \sigma(r',k)dr^{'}\right] \tag{1.35}$$

$$\xi(k) = G_A(k)C(k) \tag{1.36}$$

CALIOP retrieval algorithms use a range-scaled, energy normalized, gain normalized version of the signal as shown in Equation 1.37. The lidar data consists of normalized profiles for the three LIDAR channels (532nm perpendicular, 532nm parallel, 1064nm) (Equations 1.37-1.41). Calibration coefficients for each channel are determined through separate algorithms. More details on this can be found in the CALIPSO Level 1 ATBD document [34]. The resulting data products, referred to as Level 1 products, are the attenuated backscatter coefficients which are written in a general form in Equation 1.37. The total backscatter in the 532nm channel is the sum of the perpendicular and parallel backscatter coefficients. The two-way transmittance for each wavelength is the product of the transmittance due to molecular species (T_m^2(r)), ozone ($T_{O_3}^2$(r)) and particulates (T_p^2(r))(aerosol or cloud). The backscatter coefficient can also be viewed as the sum of molecular and particulate backscattering.

$$X(z) = \frac{r^2 P(r,k)}{E_o(k)G_A(k)} = C(k)\beta(r,k)T^2(r,k) \tag{1.37}$$

$$X_{532,\perp}(z) = C(k)_{532,\perp}\beta(r,k)_{532,\perp}T^2_{532}(r,k) \tag{1.38}$$

$$X_{532,\parallel}(z) = C(k)_{532,\parallel}\beta(r,k)_{532,\parallel}T^2_{532}(r,k) \tag{1.39}$$

$$X_{1064}(z) = C(k)_{1064}\beta(r,k)_{1064}T^2_{1064}(r,k) \tag{1.40}$$

$$\beta'_{\lambda} = \frac{X_{\lambda}}{C_{\lambda}} = (\beta_m(r,k) + \beta_p(r,k))T^2_m(r)T^2_{O_3}(r)T^2_p(r) \tag{1.41}$$

Processing of the Level 1 lidar data includes the determination of the spatial extent (cloud and aerosol layer boundaries), identification of either aerosol or cloud in the profile and retrieval of the optical properties. Identification of layer boundaries is done using attenuated scattering ratio profiles in the 532nm channel. In a noise-free profile, the slope of R' with respect to altitude is approximately zero (Equation 1.42). The baseline value of R' at which the slope is zero is identified as the threshold. Threshold exceedances are identified as features.

$$R'(r) = \frac{\beta'(r)}{\beta_m(r)T^2_m(r)T^2_{O_3}(r)} = \left(1 + \frac{\beta_p(r)}{\beta_m(r)}\right)T^2_p(r) \tag{1.42}$$

Once atmospheric features are identified within the profile, the cloud-aerosol discrimination (CAD) algorithm is used for classification. Since clouds generally consist of large particles compared to the CALIPSO wavelengths, backscatter and extinction coefficients of clouds are expected to have little spectral variation compared to aerosols. For clouds, the particulate backscatter ratio χ (Equation 1.43) is expected to be approximately one while aerosols are expected to have a ratio less than one. However, use of the ratio for identification requires removal of the molecule and ozone in order to isolate the particulate component. Therefore, additional information is required for feature identification. Discrimination of aerosols and clouds is accomplished by calculating the value of a confidence function with three inputs that are measurable feature attributes. The three inputs are: 1) the mid-feature altitude (Equation 1.44) 2) the feature mean attenuated backscatter at 532nm (Equation 1.45) and 3) the feature integrated attenuated backscatter ratio (Equation 1.46). The confidence function F is given by Equation 1.47 where $P_{feature}$ (Z,χ',($\bar{\beta'}_{532}$)) is the probability distribution function for a given feature type and K is a scaling factor that quantifies the relative frequency of occurrence of the two feature types. Possible values of F range from -1 to 1 with the sign of F determining the feature type. Negative values are aerosols while positive values are clouds.

$$\chi = \frac{\beta_{1064}}{\beta_{532}} \tag{1.43}$$

$$Z_{mid} = \frac{1}{2}(Z_{top} + Z_{base}) \tag{1.44}$$

$$\bar{\beta'}_{532} = \frac{1}{Z_{top} - Z_{base}} \int_{Z_{top}}^{Z_{base}} \beta'_{532}(r)dr \tag{1.45}$$

$$\chi' = \frac{\int_{Z_{top}}^{Z_{base}} \beta'_{1064}(r)dr}{\int_{Z_{top}}^{Z_{base}} \beta'_{532}(r)dr} \tag{1.46}$$

$$F(Z,\chi',\bar{\beta}'_{532}) = \frac{P_{cloud}(Z,\chi',\bar{\beta}'_{532}) - K(z)P_{aerosol}(Z,\chi',\bar{\beta}'_{532})}{P_{cloud}(Z,\chi',\bar{\beta}'_{532}) + K(z)P_{aerosol}(Z,\chi',\bar{\beta}'_{532})} \tag{1.47}$$

Once features are identified, an optical analysis is conducted. The first step is determination of the lidar ratio S_p (Equation 1.48). For aerosols, CALIPSO determines a value for S_p using a model-matching approach. The model includes six aerosol types determined from analysis of AERONET data (polluted continental, biomass burning, desert dust, polluted dust, clean continental, and clean marine). The calculated optical properties ($\bar{\beta}'_{532}$,χ', δ_v=$\beta'_{532,\perp}\beta'_{532,\parallel}$), the location (latitude, longitude) and season are used to identify a most likely aerosol model for each aerosol layer. Using the lidar ratio, profiles of backscatter and extinction coefficients for aerosols and clouds are determined using the linear iterative method [104] [105]. The final products are averaged. For aerosols, the spatial scale of variability is greater than clouds. Additionally, aerosols have a weaker scattering signal. As a result, aerosols require more averaging than clouds to obtain accurate results. Aerosol profile products are averaged to a downgraded 40km in the horizontal and 120m in the vertical. [96]

$$S_p = \frac{\sigma_p}{\beta_p} \tag{1.48}$$

Zonally averaged CALIPSO profiles for the year 2007 are shown in Figure 1.14, including the AOD profile and the fractional distribution of AOD in the vertical is shown in Figure 1.15. Results are shown by season (December-January-February, March-April-May, June-July-August, September-October-November). Although there are some differences across seasons, in general, the aerosol extends up to approximately 300 hPA with some aerosol near the tropopause. In the tropics, the aerosol extends further up into the atmosphere. This is expected since the tropics are associated with deep convection and therefore, vertical transport of aerosol. The aerosol is more concentrated at the surface at high latitudes, although transport of aerosol into the upper troposphere still occurs. The CALIPSO observations show that aerosol is vertically distributed in the atmosphere and not limited to the surface.

Kittaka et. al.(2011) [51] compared column-integrated aerosol optical depth at 0.532μm derived from CALIPSO profiles and MODIS 0.55μm AOD from the period June 2006 through August 2008 using the CALIPSO aerosol layer product (Version 2) and MODIS collection 5 data. Both positive and negative regional biases were observed which varied with season. On a regional-seasonal basis, the difference between the two sensors over oceans with less than 30% cloud cover was within the expected uncertainty of the MODIS over-ocean product, $\pm 0.03 \pm 0.05\tau$. Differences were found to increase as the ocean environment became cloudier. Larger discrepancies were found over land. The brighter land surface relative to oceans increases the noise in the measured signals and with regard to CALIPSO, makes detection of the aerosol layer base height more difficult [51]. Issues with base height lead to an underestimation in AOD [51]. Additionally, bright land surfaces introduce more uncertainty into MODIS as well, resulting in greater differences between the two sensors. Most land areas were found to exhibit larger differences than the expected MODIS error over land ($\pm 0.05 \pm 0.2\tau$).

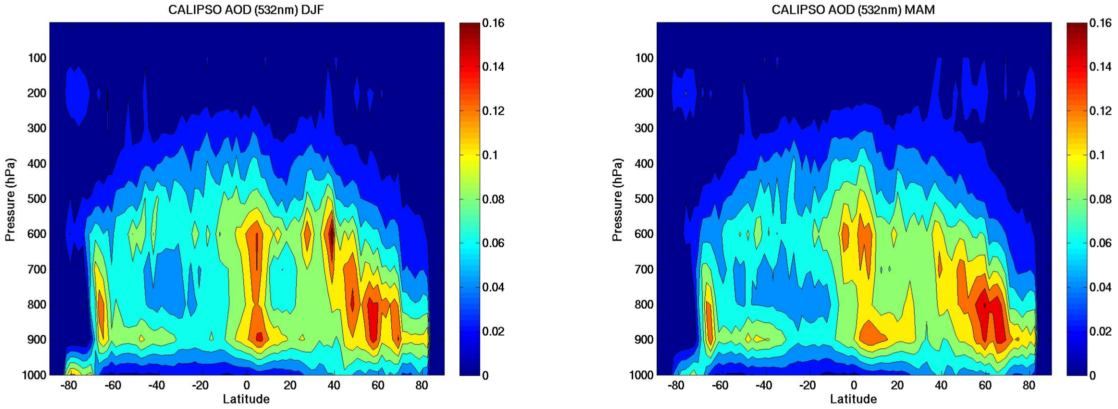

(a) December-January-February

(b) March-April-May

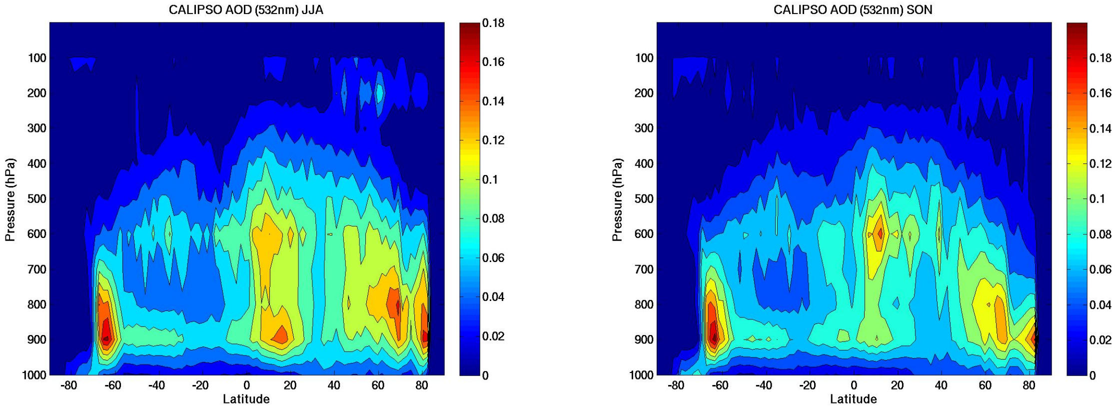

(c) June-July-August

(d) September-October-November

Figure 1.14: Zonally averaged aerosol optical depth profiles observed by CALIPSO for the year 2007 by season a) (December-January-February (DJF) b) March-April-May (MAM) c) June-July-August (JJA) and d) September-October-November (SON)).

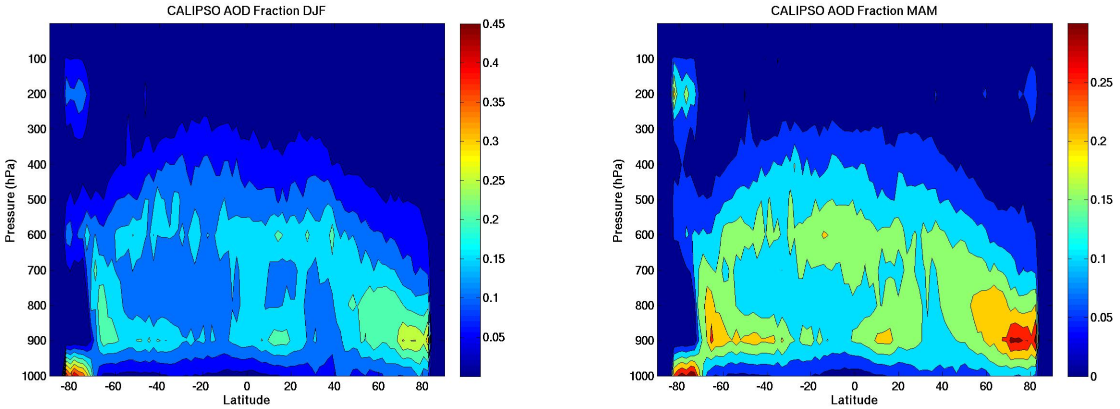

(a) December-January-February (b) March-April-May

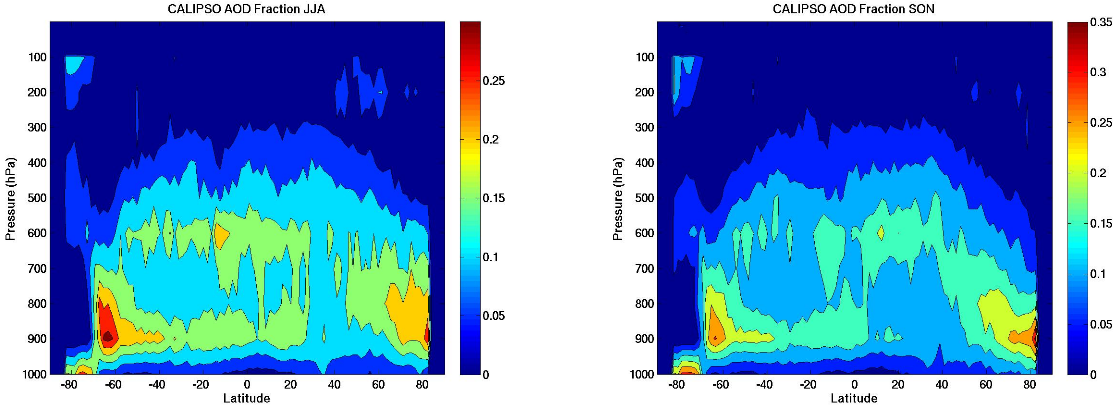

(c) June-July-August (d) September-October-November

Figure 1.15: Zonally averaged AOD fractional profiles (at a given latitude, the fraction of the total column optical depth at a given pressure level) observed by CALIPSO for the year 2007 by season a) (December-January-February (DJF) b) March-April-May (MAM) c) June-July-August (JJA) and d) September-October-November (SON)).

1.5 Aerosol Uncertainty and AEROCOM

The aerosol intercomparison (AEROCOM) project is an international effort, aiming to compare aerosol predictions across atmospheric models and evaluate model performance against observations. As part of AEROCOM, aerosol optical depth predictions have been compared across twenty atmospheric models and against ground-based and space-based remote-sensing observations (AERONET, MODIS+others). Simulations of globally averaged AOD range from 0.11 to 0.14 and are at the lower end of global averages from remote-sensing instruments with a ground-based AERONET average of 0.135 and a space-based MODIS average of 0.15 [49]. While global annual averages are in reasonable agreement (in part due to ad hoc adjustments to model parameterizations), detailed comparisons reveal large differences in regional distributions and significant differences in compositional mixtures with especially large model diversities for contributions by dust and carbonaceous aerosols. Additional in-depth studies have been conducted to determine the major sources of disagreement across models. Textor et al, 2007 [91] investigated the use of unified emissions across several models on global aerosol predictions. It was concluded that harmonization of aerosol sources has only a small impact on the simulated inter-model diversity of the global aerosol burden, and consequently global optical properties are largely controlled by model-specific transport, removal, chemistry and parameterizations of aerosol microphysics.

Investigation of aerosol life cycles across models highlighted some major differences of particular importance for aerosol radiative forcing calculations, including large differences in the mass of aerosol in the radiatively active fine mode, dry aerosol composition, aerosol water content, and vertical aerosol dispersal [91]. These results indicate that aerosol parameterizations are poorly constrained and/or understood [84] . Given the importance of simulating aerosols for understanding global climate change despite our incomplete knowledge of aerosol processes, it is evident that empirical methods are needed to reduce the effects of these uncertainties and enhance the fidelity of the aerosol models. The proposed solution is data assimilation, a technique that uses observations to constrain global scale model predictions. For this work, MODIS, AERONET, and CALIPSO observations are combined with aerosol predictions from NCAR's CAM model.

Chapter 2

Atmospheric Modeling

This chapter introduces the atmospheric model that is used for all simulations in this research. Specifically, the treatment of aerosol is addressed including representation of mass, mixing state, emissions, chemistry and processes important for aerosol such as nucleation, condensation, coagulation, water uptake and deposition. Simulation results are presented for a 2007 control run without the use of an assimilation system. The control simulation is used as the baseline of comparison for all assimilation runs.

2.1 The Community Atmosphere Model (CAM)

The global atmospheric simulations for this work are run using the National Center of Atmospheric Research's (NCAR) Community Atmosphere Model (CAM4) [66]. The simulations are run on a 1.9 by 2.5 degree horizontal grid with 28 vertical levels. CAM is run with a finite volume dynamical core in an offline mode, driven by the National Centers for Environmental Prediction (NCEP) 6-hour meteorological data [42] [50]. Use of reanalysis NCEP winds helps to minimize errors in the model runs.

Aerosols are simulated in CAM using a modal aerosol treatment which predicts both aerosol mass and number concentration [101]. The modal technique represents aerosols as multiple, independent populations of aerosol, called modes. The aerosols within each mode are represented by a separate size distribution function and for this work specifically, a lognormal size distribution function. The lognormal distribution provides a good fit to measured ambient distributions [82]. The lognormal size distribution for aerosol number concentration (N) is shown in Equation 2.1 where $\bar{D_p}$ is the average diameter of the population and σ_g is the standard deviation of the distribution. This work uses a three-mode aerosol treatment with the modes corresponding to nucleation, accumulation and coarse size modes and a prescribed standard deviation for each mode. With the standard deviation fixed, there are two unknowns in the size distribution corresponding to the integral under the curve (N) and the mean size. Therefore, two equations are required per size mode. The necessary equations describe the evolution of the moments of the size distribution (M_k) with time(Equation 2.2). The moments used are the zeroth moment (k=0) and the third moment (k=3). These moments correspond to the number concentration (Equation 2.1) and volume or mass concentration when multiplied by the aerosol density, respectively. The advantage of using a modal scheme is that it predicts aerosol number and mass for multiple modes, and therefore allows the aerosol size distribution to change in response to a variety of atmospheric and microphysical processes. This is an improvement upon bulk aerosol schemes which only predict aerosol mass [19].

$$n(D_p) = \frac{dN}{dD_p} = \frac{N}{(2\pi)^{1/2} D_p \ln \sigma_g} \exp\left(-\frac{({}_p - \ln \bar{D}_p)^2}{2 \ln^2 \sigma_g} \right) \tag{2.1}$$

$$M_k = \int_0^\infty D_p^k n(D_p) dD_p \tag{2.2}$$

There are six types of aerosols represented within CAM: sulfate (SO_4), secondary organic carbon (SOA), primary organic carbon (POM), sea salt (NCL), black carbon (BC), and soil dust (DST). Within each size mode, aerosols are an internal mixture of these aerosol types (Figure 2.1). The nucleation (or Aitken) mode is a mixture of sulfate, secondary organic carbon and sea salt and the accumulation mode is a mixture of sulfate, primary and secondary organic carbon, black carbon, soil dust and sea salt. These two modes comprise fine aerosol while the coarse mode is composed of dust, sea salt and sulfate. Including number concentration, this leads to a total of 15 transported aerosol tracers (Figure 2.1). The properties of the six aerosol types including density and hygroscopicity are shown in Table 2.1. Aerosol optical properties for each mode are parameterized in terms of wet refractive index and wet radius, as described by Ghan and Zaveri (2007) [27]. Refractive indices for water and other aerosol components are taken from the Optical Properties of Aerosols and Clouds (OPAC) database [31].

Anthropogenic emissions, which include primary aerosol and precursor gases such as SO_2, come from the IPCC AR5 emissions data set [55]. The dataset accounts for agricultural, domestic, transportation, waste, shipping, fires, energy and industrial sources. Biogenic emissions come from AEROCOM and MOZART-2 datasets and account for sulfate sources including volcanic SO_2 and sulfate and dimethylsulfide (DMS) surface fluxes. Additionally, isoprene, monoterpenes, toluene, big alkane and big alkene fluxes used to derive secondary organic carbon emissions are included [33]. Average 2007 anthropogenic and biogenic emissions used in CAM for black carbon, organic carbon, and SO_2 and are shown in Figures 2.2 through 2.4, respectively. Emissions of DMS are also shown in Figure 2.5. Ocean sea salt emissions are parameterized as a function of water temperature, wind speed and size interval [63]. Dust emission calculations are a function of wind speed and soil moisture, based on the Dust Entrainment and Deposition Model [61] [62] [103].

CAM includes simple gas-phase chemistry for sulfate aerosol. The main reactions are: 1) DMS oxidation with OH and NO_3 to form SO_2; 2) SO_2 oxidation with OH to form H_2SO_4 (gas); 3) H_2O_2 production; and 4) H_2O_2 loss from photolysis. Reaction rate coefficients come from the MOZART model [21]. Oxidation of SO_2 by H_2O_2 and O_3 in bulk cloud water is based on the MOZART treatment [94]. Irreversible uptake of H_2SO_4 (gas) to cloud droplets is also calculated [82]. A simple treatment is used for secondary organic aerosol (SOA) which assumes fixed mass yields for anthropogenic and biogenic precursor volatile organic compounds (VOCs), then directly emits this mass as primary aerosol particles (Table 2.2). In the gas phase, a single lumped SOA species is simulated in order to dynamically treat condensation and evaporation, with the equilibrium partial pressure for each aerosol mode expressed in terms of Raoult's Law.

Aerosol processes that are represented within CAM include nucleation, condensation, coagulation, water uptake, activation/resuspension, wet deposition and dry deposition. These processes can be categorized into source, transformation and loss processes. Binary $H_2SO_4-H_2O$ homogenous nucleation, a source of new sulfate particles in the nucleation mode, is represented using a parameterization by Vehkamaki et al (2002) [97]. Aerosol growth occurs through condensation and coagulation and can result in growth from the nucleation to the accumulation mode. Condensation is treated dynamically using standard mass transfer expressions [82]. Coagulation occurs in both the Nucleation and Accumulation modes with rates calculated using the fast/approximate algorithms of the Community Multiscale Air Quality (CMAQ) model, version 4.6. Growth by water uptake is based on equilibrium Kohler theory [27] using the relative humidity and the mean hygroscopicity for each mode. In addition to growth processes, aerosols are transferred or become activated from an interstitial phase to a cloud-borne phase using a parameterization that is a function of updraft velocity [1]. Resuspension into the interstitial state occurs during cloud dissipation. Aerosol loss processes, including wet and dry deposition, act to reduce atmospheric aerosols. Aerosol wet removal treats in-cloud scavenging and below cloud scavenging by multiplying a first order loss rate by a solubility factor [75] [9]. Aerosol that is scavenged at one altitude can be resuspended at a lower altitude if precipitation evaporates. Aerosol dry deposition velocities are calculated using aerosol size [107].

Radiation transfer calculations are provided by the radiation code RRTMG, which uses a correlated k-distribution technique [39] [65]. In the shortwave, there are fourteen bands extending over the spectral range of 0.2μm to 12.2μm with sources of extinction including H_2O, O_3, CO_2, O_2, CH_4, N_2, clouds, aerosols, and Rayleigh scattering. The model uses a two-stream $\delta-$Eddington approximation assuming homogeneously mixed layers. Aerosol radiative properties, including optical depth (τ), single-scattering albedo (ω) and asymmetry parameter(σ), are combined before being passed to the radiative transfer solver. If the optical depth of species i in band b is τ_{ib}, the single scattering albedo is ω_{ib}, and the asymmetry parameter is σ_{ib}, then the aerosol optics are combined as shown in Equations 2.3 through 2.5 in order to produce the total aerosol optical depth, single-scattering albedo and asymmetry parameter for band b.

$$\tau_b = \sum_{i=1}^{N} \tau_{ib} \tag{2.3}$$

$$\omega_b = \sum_{i=1}^{N} \tau_{ib}\omega_{ib}/\tau_b \tag{2.4}$$

$$\sigma_b = \sum_{i=1}^{N} \tau_{ib}\omega_{ib}\sigma_{ib}/(\tau_b\omega_b) \tag{2.5}$$

The aerosol optical depth calculated for a given wavelength band is insufficient for this work. In order to compare model predictions against observations, modeled optical depth values at a specific wavelength are needed. Additionally, this work requires calculating the angstrom exponent (α) which is related to the relative amount of fine and coarse aerosol with higher angstrom values indicating a larger fine aerosol contribution. Angstrom exponent calculations require optical depths at specific wavelengths. In order to remedy this problem, equations were developed relating the optical depth at a single wavelength to the average optical depth over a band. The equations were developed using the definition of the Angstrom exponent α (Equation 2.6) where τ_1 and τ_2 are the optical depths at wavelengths λ_1 and λ_2, respectively.

$$\frac{\tau_2}{\tau_1} = \left(\frac{\lambda_1}{\lambda_2}\right)^{\alpha} \tag{2.6}$$

The wavelengths of interest exist in bands with upper and lower wavelength limits such that:

$$\lambda_{L1} \leq \lambda_1 \leq \lambda_{H1} \tag{2.7}$$

$$\lambda_{L2} \leq \lambda_2 \leq \lambda_{H2} \tag{2.8}$$

The optical depth at λ_2 is isolated and then averaged over the band interval giving the following equation:

$$\bar{\tau_2} = \frac{1}{\lambda_{H2} - \lambda_{L2}} \int_{\lambda_{L2}}^{\lambda_{H2}} \tau_1 \left(\frac{\lambda_1}{\lambda_2}\right)^{\alpha} d\lambda_2 \tag{2.9}$$

The equation is then integrated to solve for the band-averaged optical depth $\bar{\tau_2}$.

$$\bar{\tau_2} = \frac{1}{\lambda_{H2} - \lambda_{L2}} \tau_1 \lambda_1^{\alpha} \left[\frac{\lambda_{H2}^{1-\alpha} - \lambda_{L2}^{1-\alpha}}{1-\alpha}\right] \tag{2.10}$$

The same process is repeated to solve for the band-averaged optical depth $\bar{\tau_1}$.

$$\bar{\tau_1} = \frac{1}{\lambda_{H1} - \lambda_{L1}} \tau_2 \lambda_2^{\alpha} \left[\frac{\lambda_{H1}^{1-\alpha} - \lambda_{L1}^{1-\alpha}}{1-\alpha}\right] \tag{2.11}$$

The equations are then rearranged to solve for the optical depths at λ_1 and λ_2.

$$\tau_1 = \bar{\tau_2} \left(\frac{\lambda_{H2} - \lambda_{L2}}{\lambda_1^{\alpha}}\right) \left(\frac{1-\alpha}{\lambda_{H2}^{1-\alpha} - \lambda_{L2}^{1-\alpha}}\right) \tag{2.12}$$

$$\tau_2 = \bar{\tau_1} \left(\frac{\lambda_{H1} - \lambda_{L1}}{\lambda_2^{\alpha}}\right) \left(\frac{1-\alpha}{\lambda_{H1}^{1-\alpha} - \lambda_{L1}^{1-\alpha}}\right) \tag{2.13}$$

Once the equations for optical depth were determined, the angstrom exponent is related to the band-averaged optical depths by first rearranging Equation 2.6 and then plugging in Equations 2.12 and 2.13 to produce Equation 2.15.

$$\alpha = ln\left(\frac{\tau_2}{\tau_1}\right)/ln\left(\frac{\lambda_2}{\lambda_1}\right) \tag{2.14}$$

$$\frac{\bar{\tau_2}}{\bar{\tau_1}} = \left(\frac{\lambda_{H2}^{1-\alpha} - \lambda_{L2}^{1-\alpha}}{\lambda_{H1}^{1-\alpha} - \lambda_{L1}^{1-\alpha}}\right)\left(\frac{\lambda_{H1} - \lambda_{L1}}{\lambda_{H2} - \lambda_{L2}}\right) \tag{2.15}$$

In order to calculate the wavelength specific optical depths and angstrom exponent, the angstrom exponent α must first be determined using Equation 2.15. The angstrom exponent cannot be explicitly solved; instead a bisection method is used since the value of α has upper and lower bounds. The values of τ_1 and τ_2 can then be calculated using Equations 2.12 and 2.13. The code was tested for wavelengths 0.55μm and 0.86μm within bands 8 and 10 (Table 2.3). A comparison between the optical depth at 0.55μm and the optical depth in band 10 are shown in Figure 2.6. The optical depths fall close to the one to one line as expected.

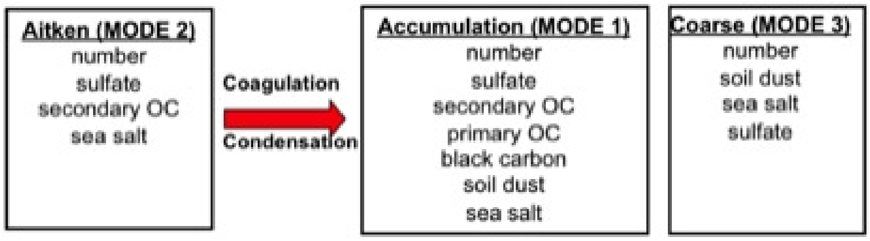

Figure 2.1: CAM aerosol size modes (nucleation or Aitken, accumulation, and coarse) and the 15 tracers used in the modal aerosol treatment. Coagulation and condensational growth are treated in the model to allow growth from the nucleation to the accumulation mode.

	Sulfate (SO4)	Sea Salt (NCL)	Primary Organic Carbon (POM)	Secondary Organic Carbon (SOA)	Black Carbon (BC)	Dust (DST)
Density (kg/m^3)	1770	1900	1000	1000	1700	2600
Hygroscopicity (b)	0.507	1.16	1e-10	0.14	1e-10	0.068

Table 2.1: Density and hygroscopicity for the six aerosol types represented in CAM

Species	Mass Yield	Reference
Big Alkanes	5%	Lim and Ziemann (2005) [57]
Big Alkenes	5%	Assumed
Toluene	15%	Odum et al. 1997 [68]
Isoprene	4%	Kroll et al. 2006 [54]
Monoterpenes	25%	Ng et al. 2007 [67]

Table 2.2: Prescribed secondary organic carbon aerosol percent mass yields from volatile organic compound emissions that are used in CAM.

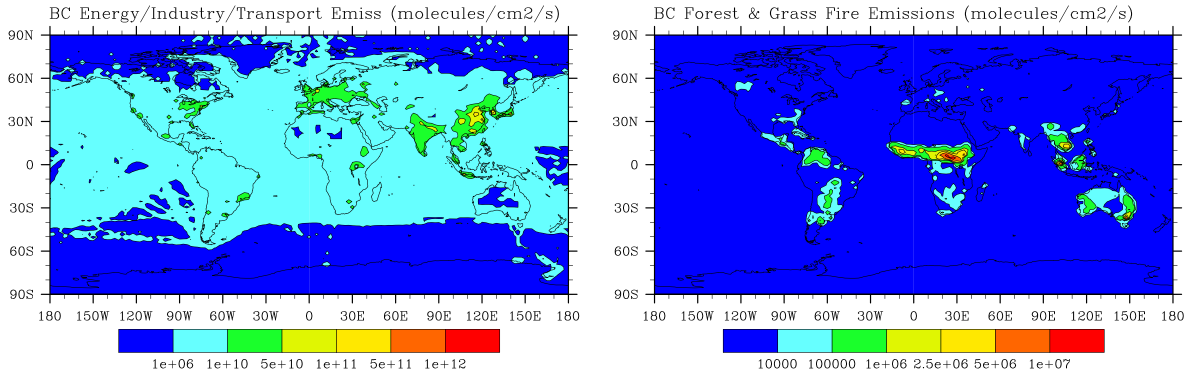

(a) anthropogenic

(b) biogenic

Figure 2.2: Average 2007 black carbon (BC) emissions for a) energy, industrial, domestic and transportation sources including shipping (anthropogenic) and b) forest and grass fires (biogenic).

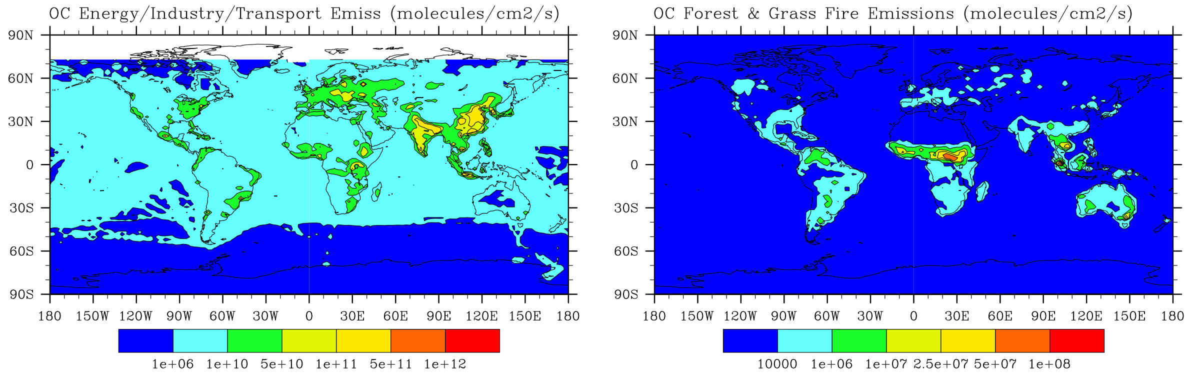

(a) anthropogenic

(b) biogenic

Figure 2.3: Average 2007 organic carbon (OC) emissions for a) energy, industrial, domestic and transportation sources including shipping (anthropogenic) and b) forest and grassfires (biogenic).

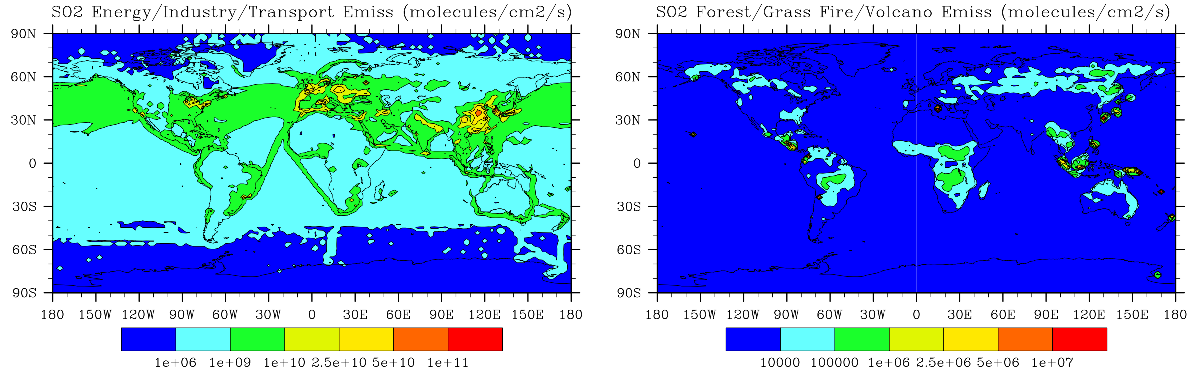

(a) anthropogenic

(b) biogenic

Figure 2.4: Average 2007 sulfur dioxide (SO2) emissions for b) energy, industrial, domestic and transportation sources including shipping and b) forest and grass fires and volcano emissions.

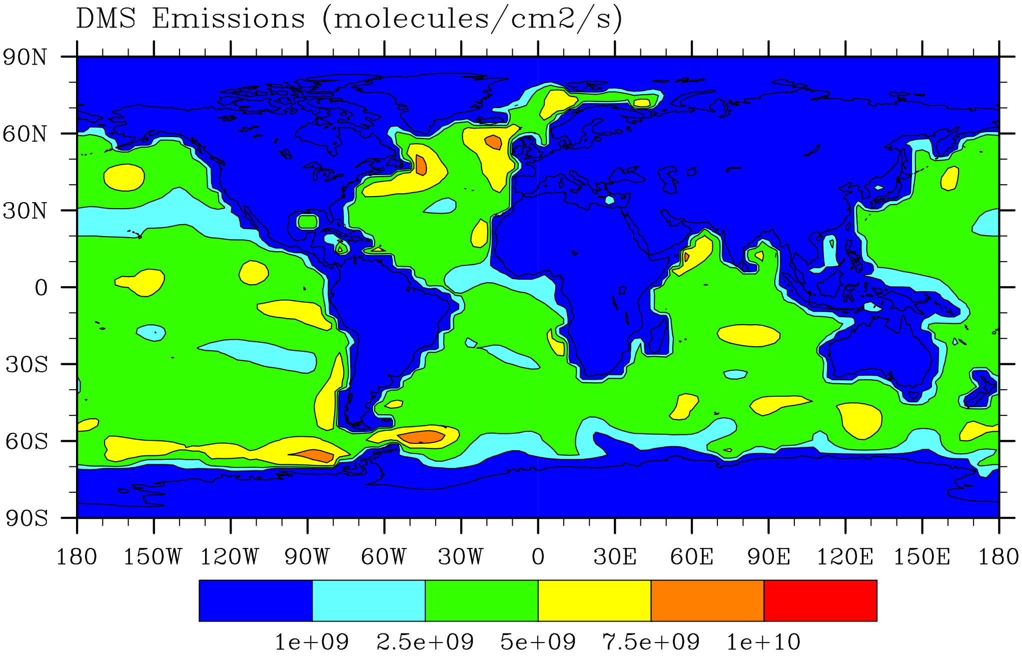

Figure 2.5: Average 2007 DimethylSulfide (DMS) emissions used in CAM.

Band Index	Band Minimum μm	Band Maximum μm
1	3.077	3.846
2	2.500	3.077
3	2.150	2.500
4	1.942	2.150
5	1.626	1.942
6	1.299	1.626
7	1.242	1.299
8	0.778	1.242
9	0.625	0.778
10	0.442	0.625
11	0.345	0.442
12	0.263	0.345
13	0.200	0.263
14	3.846	12.195

Table 2.3: Shortwave bands and their upper and lower wavelength limits used in the radiative transfer code RRTMG within CAM

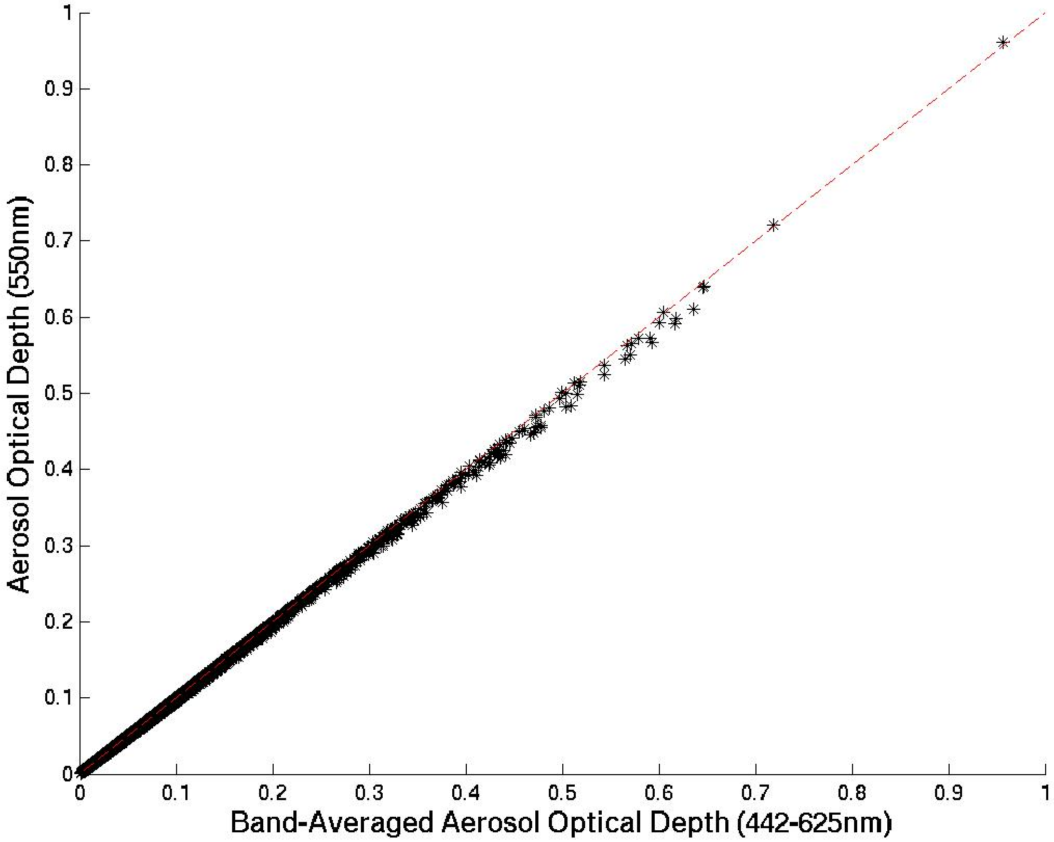

Figure 2.6: Plot of band-averaged optical depth (band 8, 442-625nm) against aerosol optical depth at 550nm calculated using Equations 61-64.

2.2 Control Run

CAM was run for several months (October-December, 2006) in order to generate initial conditions for the control simulation. The full control simulation was run for the year 2007. Of particular interest are the aerosol-related fields, including AOD (0.55μm), angstrom exponent (0.55-0.86μm) and AOD fine fraction (0.55μm). The averages of the three parameters for 2007 are shown in Figures 2.7,2.9 and 2.11, respectively. Seasonal averages for December-January-February (DJF), March-April-May (MAM), June-July-August (JJA) and September-October-November (SON) are shown in Figures 2.8, 2.10 and 2.12. Global averages, both for the year and seasonally, are presented in Table 2.4. There is little variation in the predicted aerosol fields with consistent average values across seasons. The greatest optical depths are observed over parts of Africa, the Arabian Peninsula and Asia with peak optical depths exceeding 0.5. Clear spatial patterns are observed in angstrom exponents with lower angstrom values over the oceans and dusty regions including the Sahara and Arabian Peninsula. This indicates a larger coarse aerosol contribution. The angstrom exponent pattern is reflected in the fine AOD contribution, as expected. Over most land regions, the fine aerosol contribution exceeds ninety percent. Oceans and dusty regions have a larger coarse contribution.

The composition of the predicted aerosol in the control run is examined on a mass basis. Percent of the total aerosol mass is shown for the six aerosol types in Figure 2.13. It should be noted that mass tends to be weighted towards coarse mode aerosol since mass scales with size to the third power. In this simulation, coarse aerosol is composed of sea salt, dust and sulfate. Over ocean regions, sea salt is the dominant aerosol type. Dust has a clear signal over known dusty regions including the Sahara, Arabian Peninsula, Asia and Australia. Both sea salt and dust aerosols are consistent with surface flux maps (Figures 2.14 and 2.15). Over North America, parts of South America, and Europe, sulfate makes up a significant portion of the aerosol mass. This is consistent with high SO_2 emission regions. Primary and secondary organic aerosols have signals over South America and Southern Africa. While black carbon does not make up a large portion of the mass, black carbon levels are higher over the Eastern United States, South America, parts of Africa, Southeast Asia and Europe.

Average aerosol compositions are shown for all aerosol combined (Figure 2.16), fine aerosol and coarse aerosol (Figure 2.17). Global averages are presented as well as averages over land and ocean. The total global aerosol composition is dominated by sea salt and dust, two of the coarse aerosol components, with sea salt being more important over oceans and dust over land. Sulfate is of particular importance for fine aerosol, although all six aerosol types show up in the fine mode. The presence of dust and sea salt in the fine mode indicates that the fine mode has an important biogenic component, different than expected. Fine aerosol makes up 26% of the total mass and coarse aerosol makes up 74%. On a number concentration basis, the fine mode makes up greater than ninety percent of the aerosol.

The results of the control simulation are compared to MODIS in Figures 2.18 and 2.19. Figure 2.18 shows the percent difference in predicted and observed MODIS AOD that is seasonally averaged. The comparison reveals a persistent negative bias in CAM AOD with larger deviations occurring over land. This indicates that CAM is possibly underestimating emissions, overestimating loss rates or incorrectly characterizing the aerosol optics. With respect to the angstrom exponent, negative biases are observed over most ocean regions indicating the model is over-predicting the importance of coarse aerosol. Positive bias bands are seen over mid to high latitude regions indicating the model is over-predicting the importance of fine aerosol in these areas. Model predictions were also compared against AERONET observations by site category (1=desert dust, 2=biomass burning, 3=rural, 4=industrial pollution, 5=polluted marine, 6=dirty pollution) (Figure 2.20). Similar to the MODIS comparison, CAM predicts AOD low relative to AERONET. CAM and AERONET AOD means were compared using a t-test analysis (95% confidence) with the mean of the rural sites found to not be statistically different. All other site categories were statistically different. The model does much better in comparison against AERONET fine AOD fraction (Figure 2.20). Mean AOD fine fraction for biomass burning and rural sites were not statistically different from AERONET observations based on t-test analysis (95% confidence). For all other site categories, CAM predicts higher fine fraction than observed by AERONET. Monthly averaged AOD time series were also compared between control run results and AERONET with select sites shown in Figure 2.21. The time series reaffirm that the model is predicting AOD low relative to AERONET with the best comparison found for rural sites.

The vertical aerosol optical depth profile predicted by CAM is examined in Figure 2.22 with both zonally averaged aerosol optical depth profiles (Figure 2.22a) and fractional optical depth profiles (Figure 2.22b) presented. The zonally averaged optical depth (Figure 2.22a) shows that the peaks in optical depth occur around 20 and 40 degrees North and around 10 and 40 degrees South. These peaks are consistent with the global AOD maps shown in Figures 2.7 and 2.8 and coincide with the dusty Sahara, mid-latitude anthropogenic emission regions of North America, Europe and Asia, biomass burning regions over Africa and South America, and high sea salt emission regions, respectively. In terms of vertical profile, the majority of extinction occurs in approximately the first 2km of the atmosphere (greater than 800 hPa) in the tropics to mid latitudes with the exception occurring around 40 degrees North. This differs from CALIPSO profiles, which show aerosol extending higher into the troposphere at most latitudes. At high latitudes, the total aerosol optical depth predicted by CAM is much smaller than lower latitudes, however, the majority of extinction is occurring in the upper troposphere.

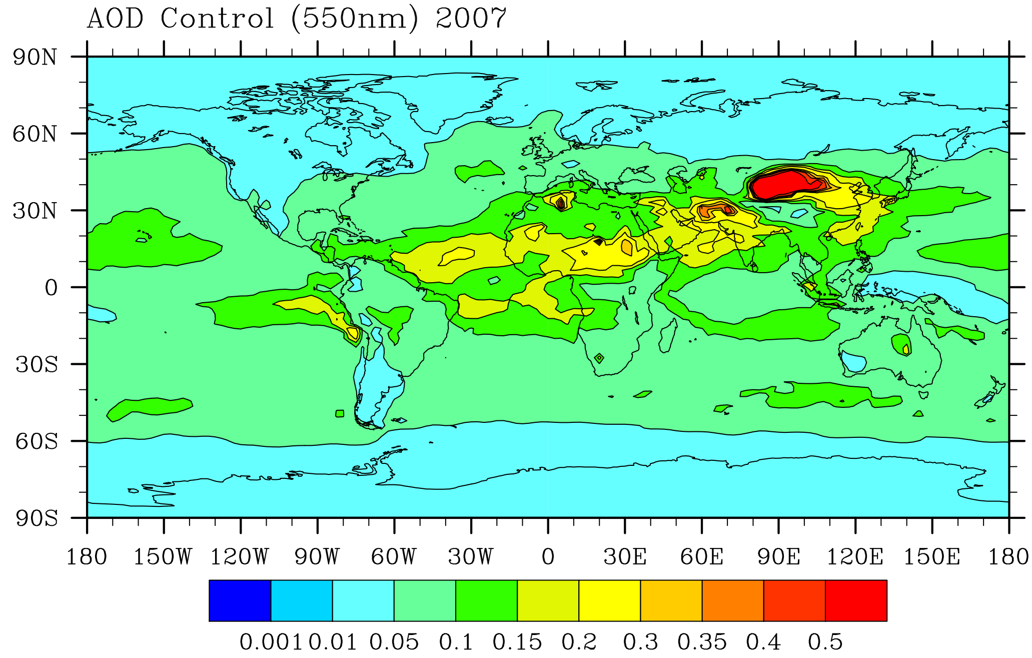

Figure 2.7: Average aerosol optical depth at 550nm for the 2007 CAM control run.

Variable	**Season**	**MODIS**	**CAMControl**
AOD (550nm)	DJF	0.155(±0.01)	0.082(±0.05)
	MAM	0.168(±0.02)	0.088(±0.07)
	JJA	0.165(±0.02)	0.090(±0.09)
	SON	0.16(±0.02)	0.082(±0.07)
	Year	0.161(±0.09)	0.086(±0.06)
Angstrom Exponent (550-865nm) (ocean only)	DJF	0.66(±0.09)	0.66(±0.28)
	MAM	0.62(±0.13)	0.66(±0.35)
	JJA	0.65(±0.19)	0.64(±0.40)
	SON	0.67(±0.11)	0.62(±0.38)
	Year	0.65(±0.30)	0.65(±0.35)
AOD Fine Fraction (550nm) (Land and Ocean)	DJF	0.47(±0.04)	0.73(±0.13)
	MAM	0.43(±0.05)	0.73(±0.16)
	JJA	0.44(±0.06)	0.72(±0.16)
	SON	0.48(±0.05)	0.71(±0.16)
	Year	0.45(±0.16)	0.72(±0.15)

Table 2.4: Global averages of aerosol optical depth (550nm), angstrom exponent (550-865nm) and the fractional contribution of fine aerosol to optical depth. Averages are shown by season (December-January-February (DJF), March-April-May (MAM), June-July-August (JJA) and September-October-November (SON) and for the year 2007 (Year).

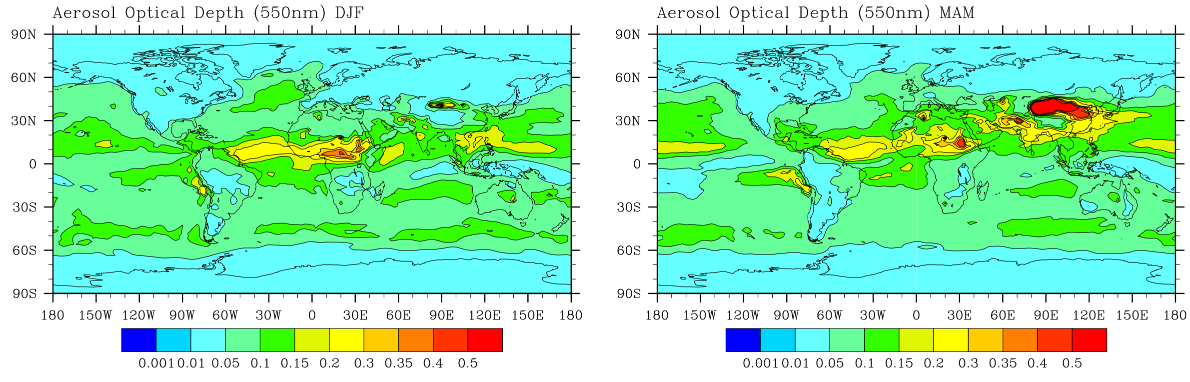

(a) December-January-February (b) March-April-May

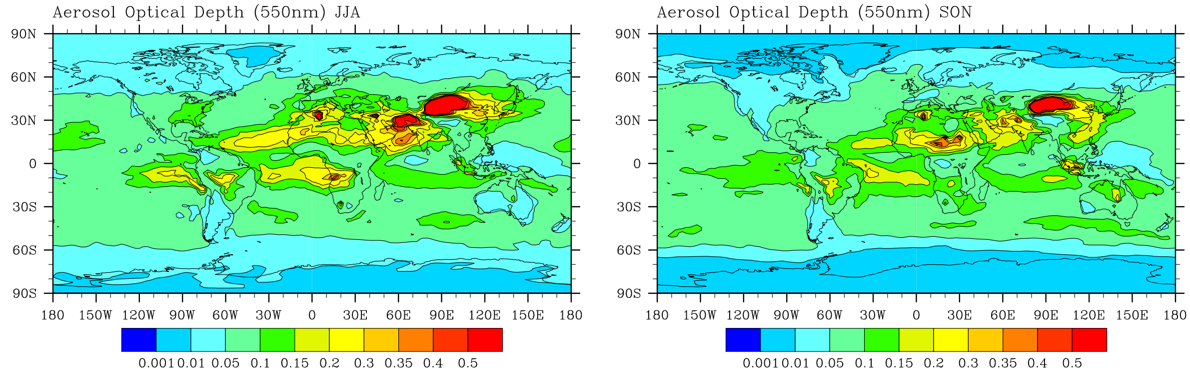

(c) June-July-August (d) September-October-November

Figure 2.8: Seasonally averaged aerosol optical depth at 550nm for the 2007 CAM control run. Optical depth values are averaged for a) December/January/February b) March/April/May c) June/July/August and d) September/October/November.

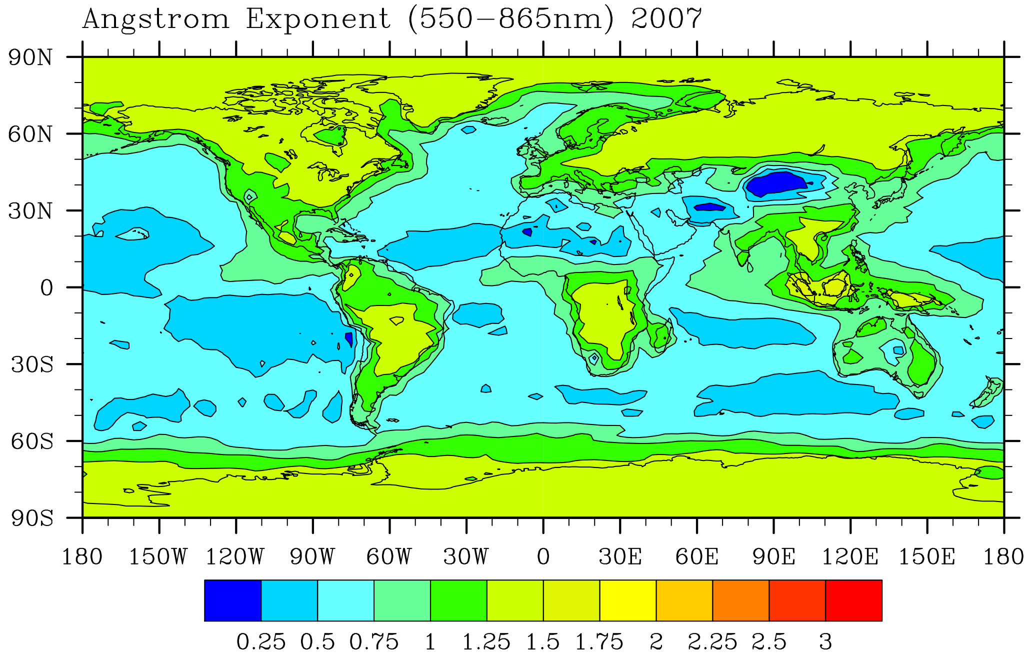

Figure 2.9: Average angstrom exponents (550nm-865nm) for the 2007 CAM control run.

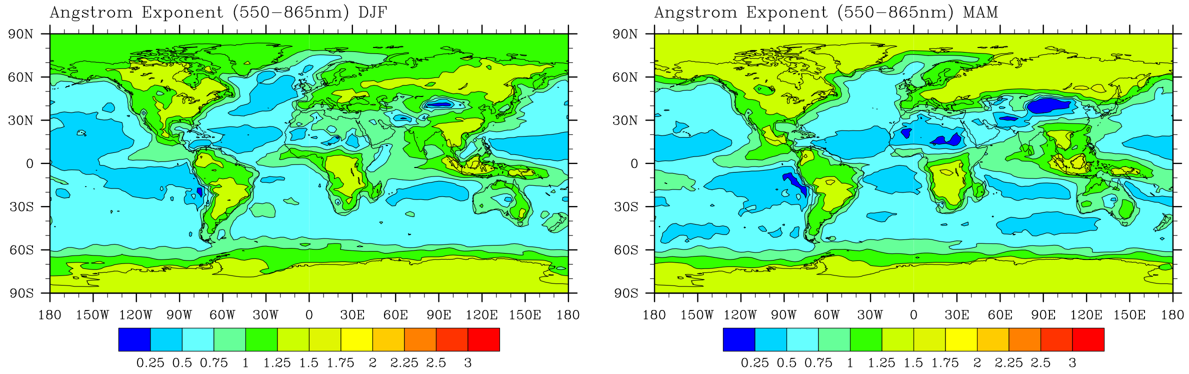

(a) December-January-February

(b) March-April-May

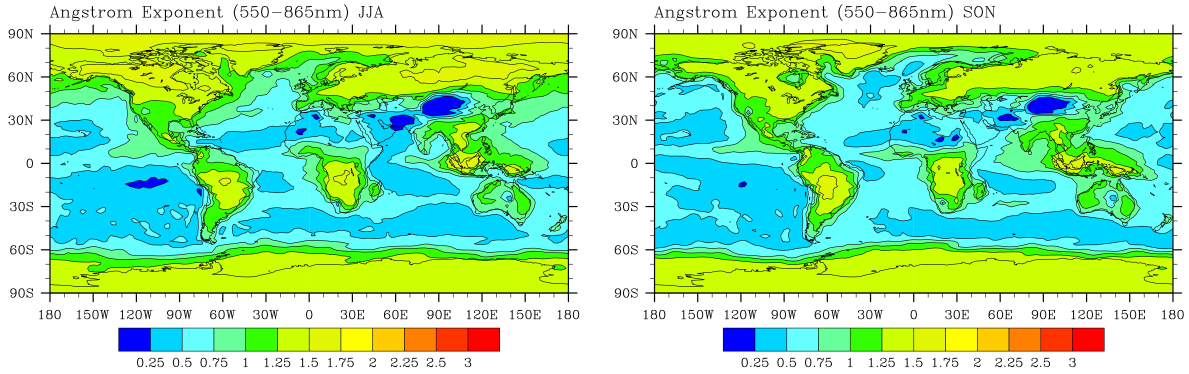

(c) June-July-August

(d) September-October-November

Figure 2.10: Seasonally averaged angstrom exponents (550nm-865nm) for the 2007 CAM control run. Angstrom values are averaged for a) December/January/February b) March/April/May c) June/July/August and d) September/October/November.

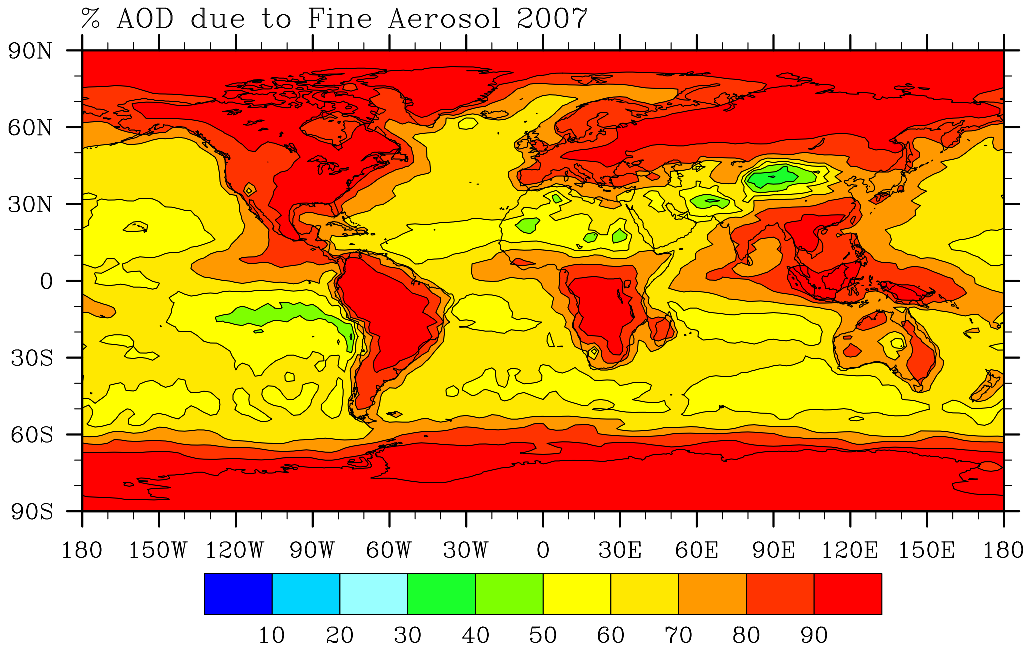

Figure 2.11: Averaged percent of AOD at 550nm due to fine aerosol (Nucleation + Accumulation Modes) for the 2007 CAM control run.

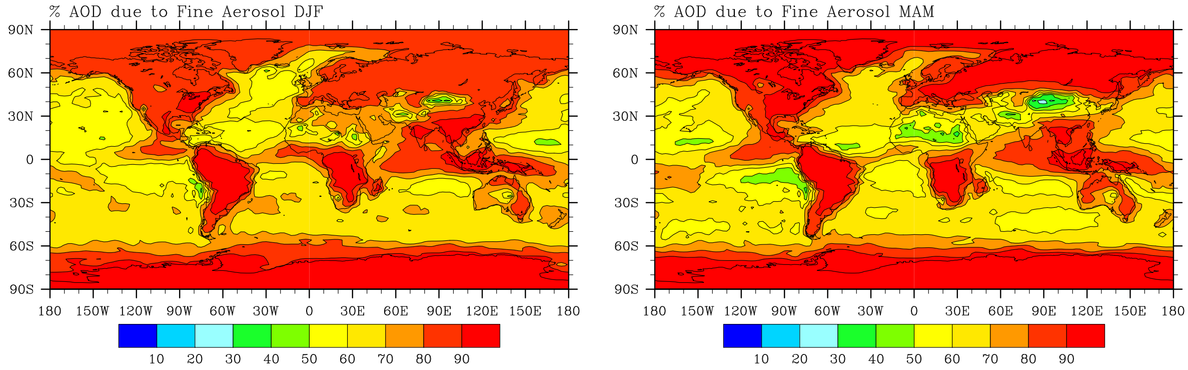

(a) December-January-February (b) March-April-May

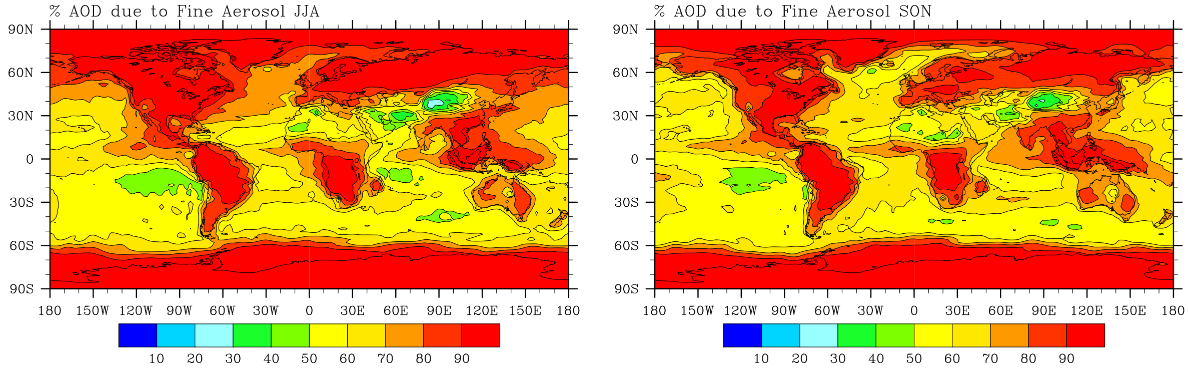

(c) June-July-August (d) September-October-November

Figure 2.12: Seasonally averaged percent of AOD at 550nm due to fine aerosol (Nucleation + Accumulation Modes) for the 2007 CAM control run. Fine AOD percentages are averaged for a) December/January/February b) March/April/May c) June/July/August and d) September/October/November.

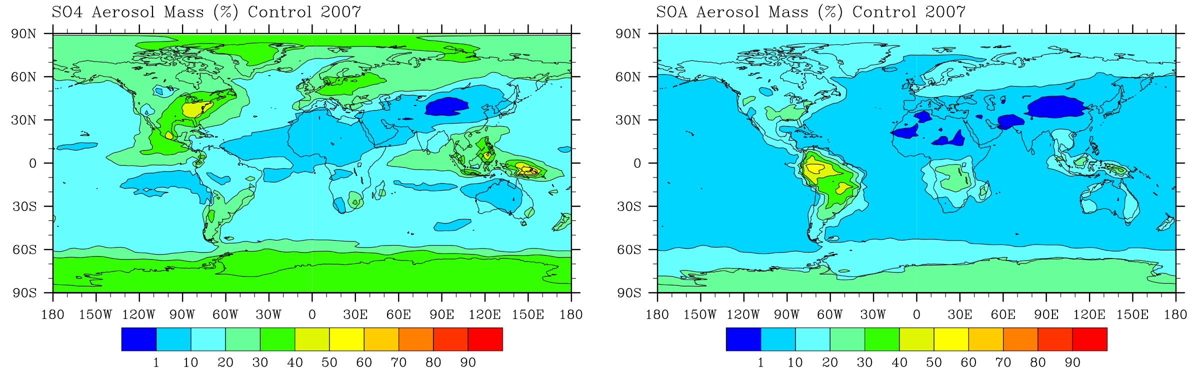

(a) Sulfate (b) Secondary Organic Aerosol

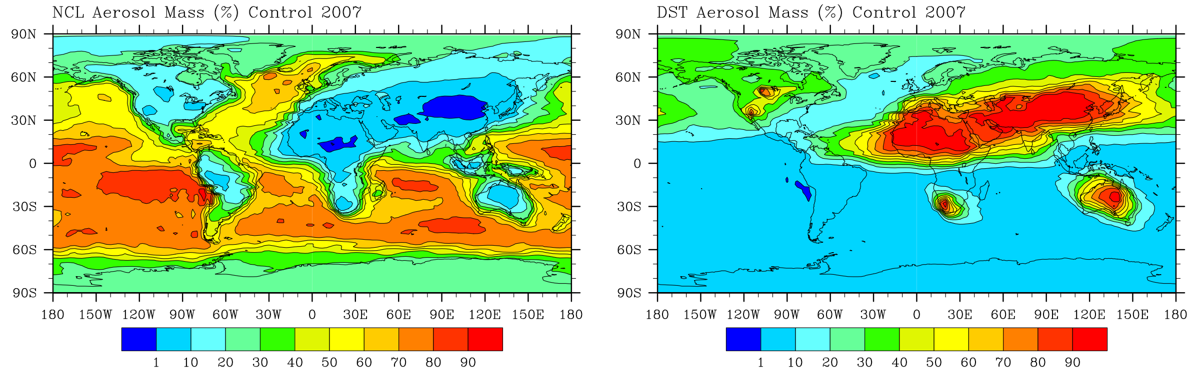

(c) Sea Salt (d) Dust

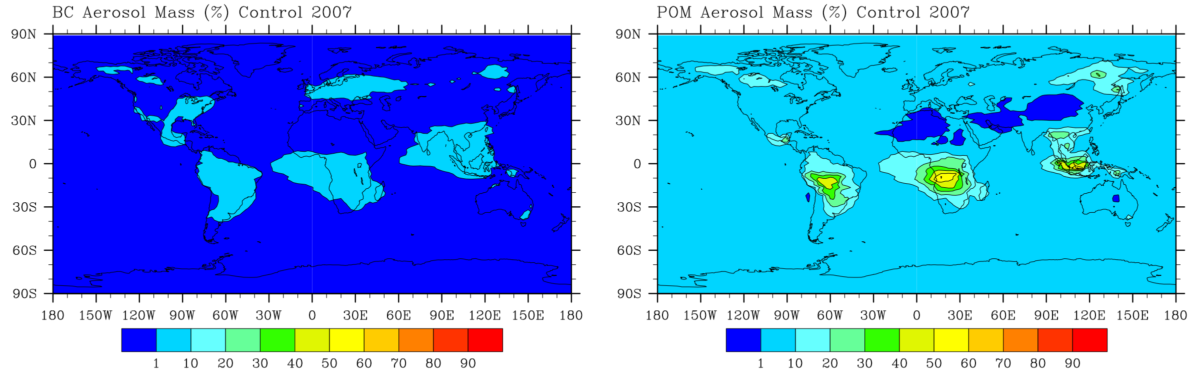

(e) Black Carbon (f) Primary Organic Aerosol

Figure 2.13: Average aerosol mass composition for the 2007 control simulation by percent. Results are shown for a) sulfate (SO4) b) secondary organic aerosol (SOA) c) sea salt (NCL) d) dust (DST) e) black carbon (BC) and f) primary organic aerosol (POM).

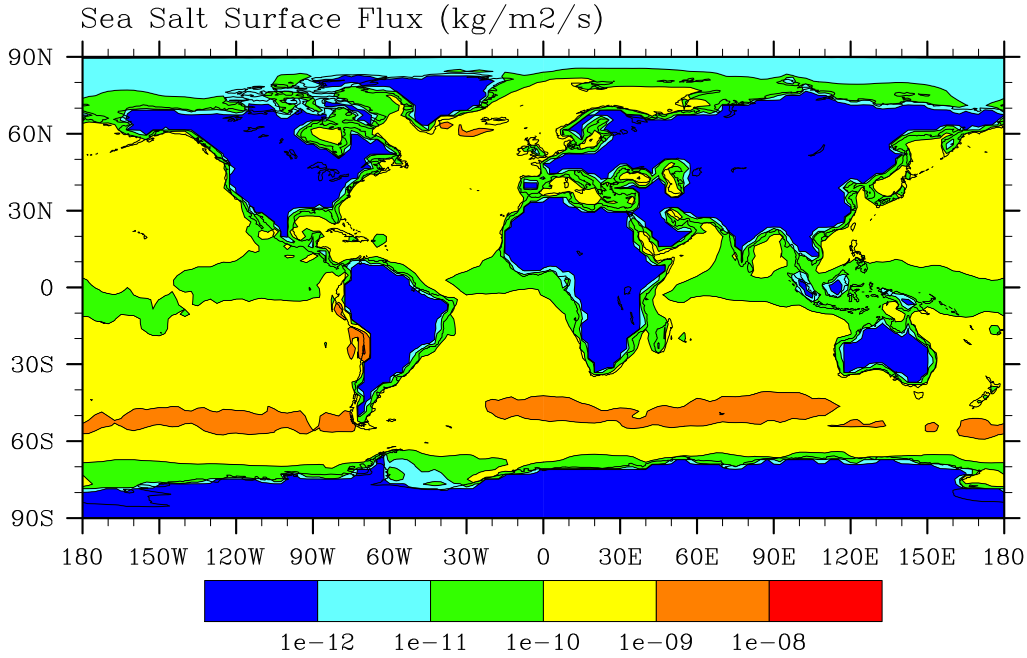

Figure 2.14: Average sea salt surface flux for the 2007 CAM control run.

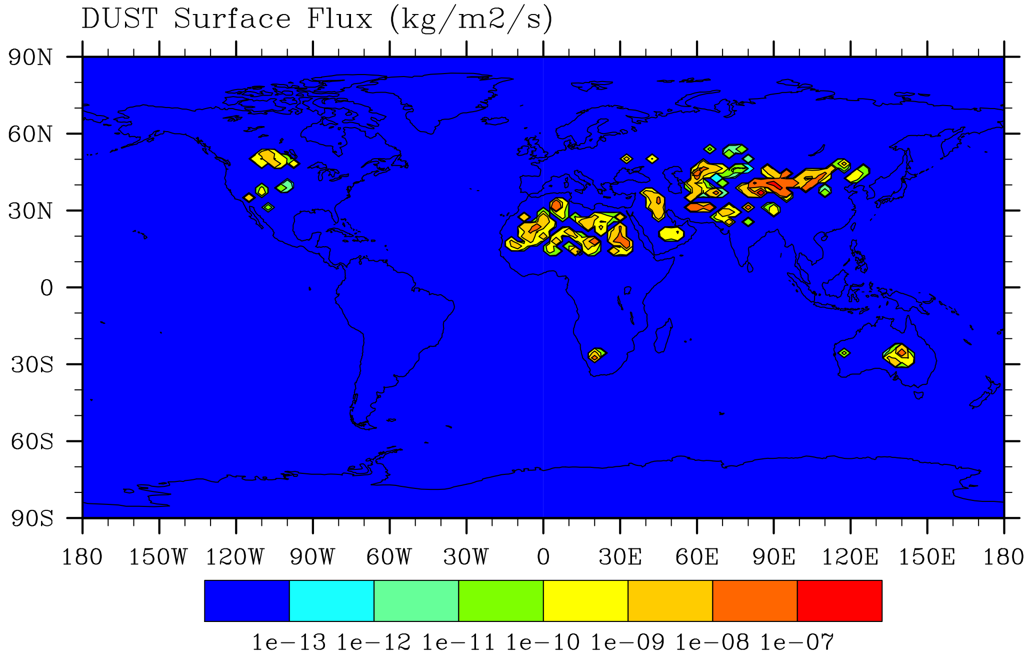

Figure 2.15: Average dust surface flux for the 2007 CAM control run.

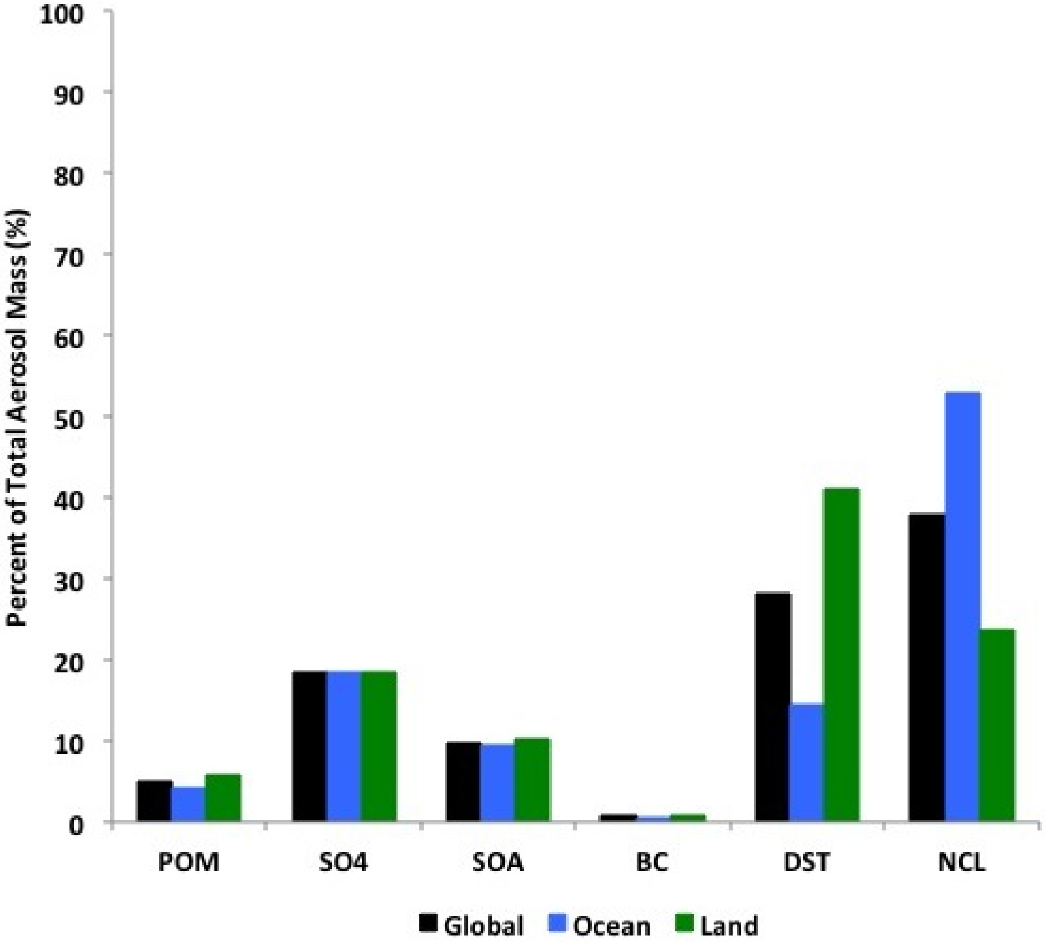

Figure 2.16: Control run average aerosol composition by percent mass for the six aerosol types (primary organic aerosol, sulfate, secondary organic aerosol, black carbon, dust and sea salt). Results are globally averaged (Global), averaged over ocean only (Ocean), and over land only (Land).

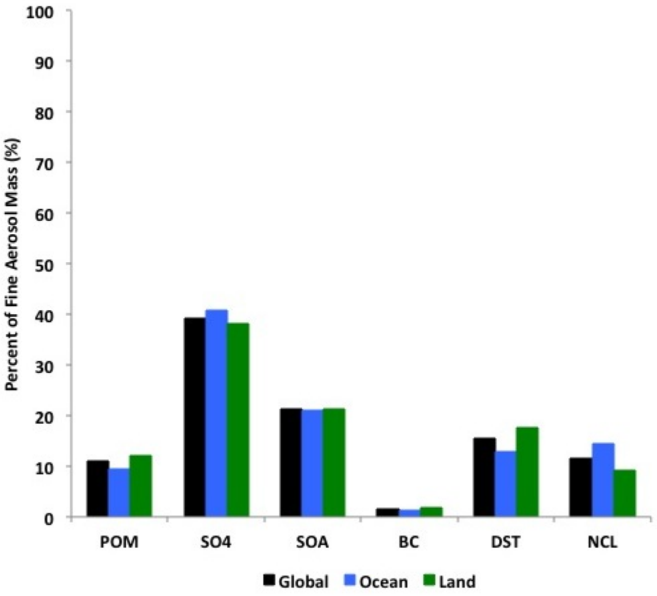

(a) Fine

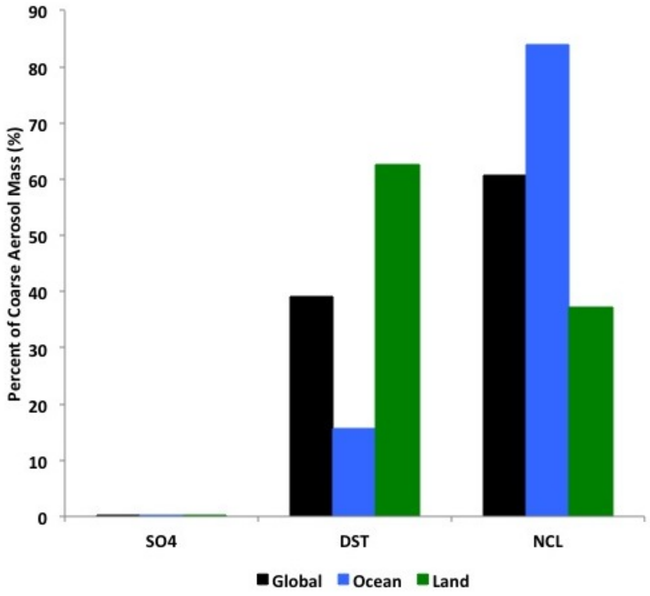

(b) Coarse

Figure 2.17: Control run average aerosol composition by percent mass for the six aerosol types (primary organic aerosol, sulfate, secondary organic aerosol, black carbon, dust and sea salt) for a) fine aerosol and b) coarse aerosol. Results are globally averaged (Global), averaged over ocean only (Ocean), and over land only (Land).

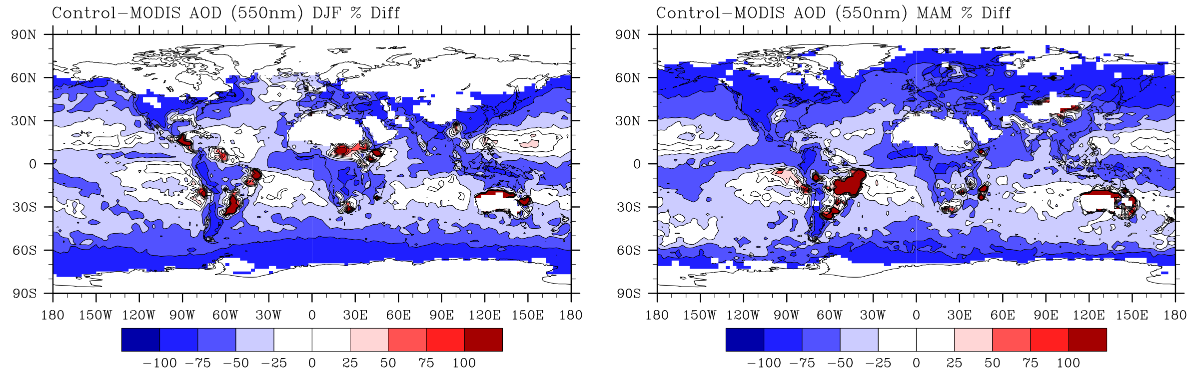

(a) December-January-February

(b) March-April-May

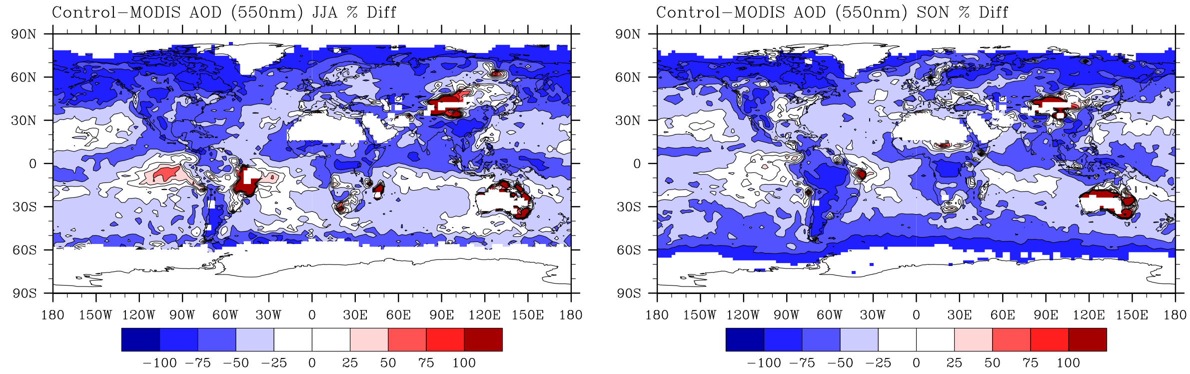

(c) June-July-August

(d) September-October-November

Figure 2.18: Seasonally averaged comparison between Control run and MODIS aerosol optical depth observations. Results are shown as a percent different (control modis) for a) December/January/February (DJF) b) March/April/May (MAM) c) June/July/August (JJA) and d) September/October/November (SON).

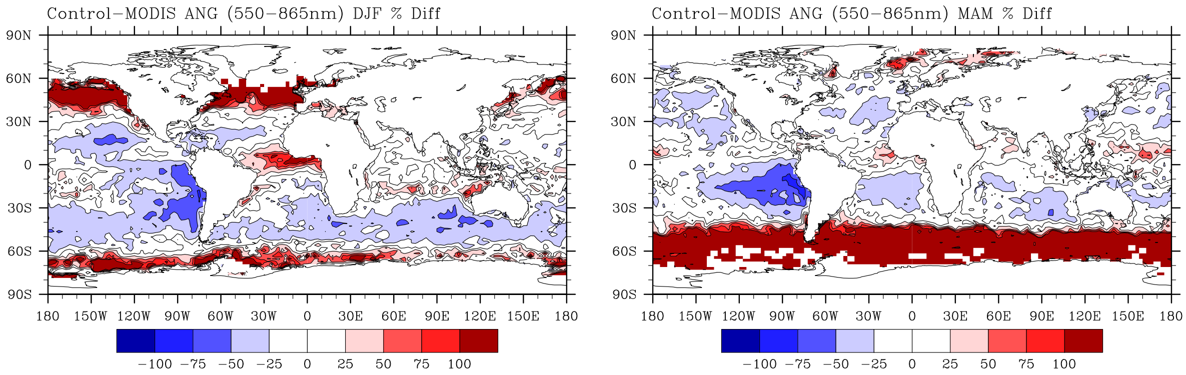

(a) December-January-February (b) March-April-May

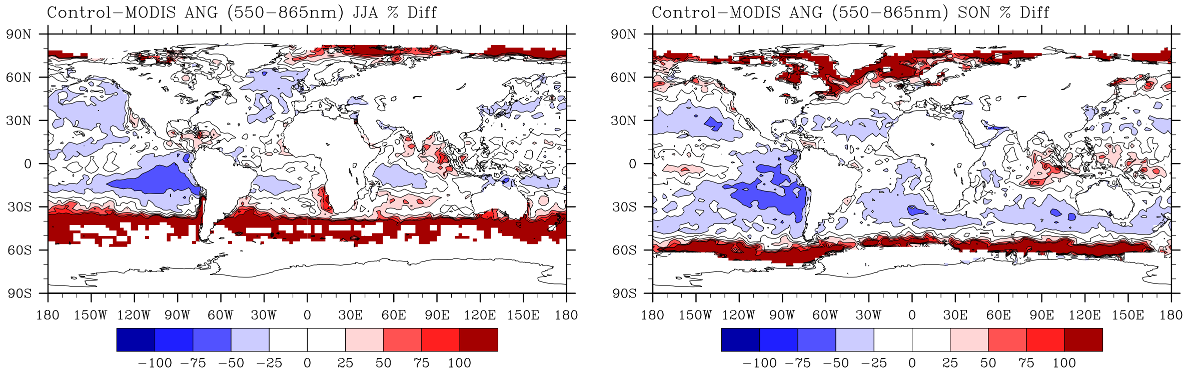

(c) June-July-August (d) September-October-November

Figure 2.19: Seasonally averaged comparison between Control run and MODIS angstrom exponent observations. Results are shown as a percent different (control modis) for a) December/January/February (DJF) b) March/April/May (MAM) c) June/July/August (JJA) and c) September/October/November (SON). Angstrom comparisons are shown for over ocean only.

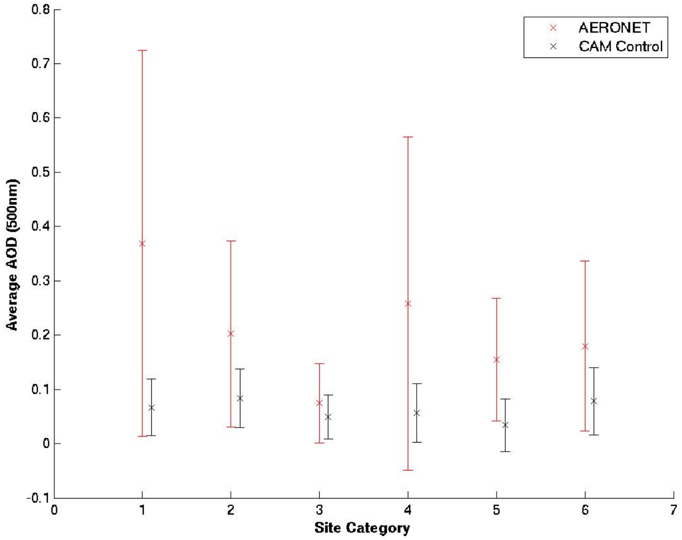

(a) Aerosol Optical Depth

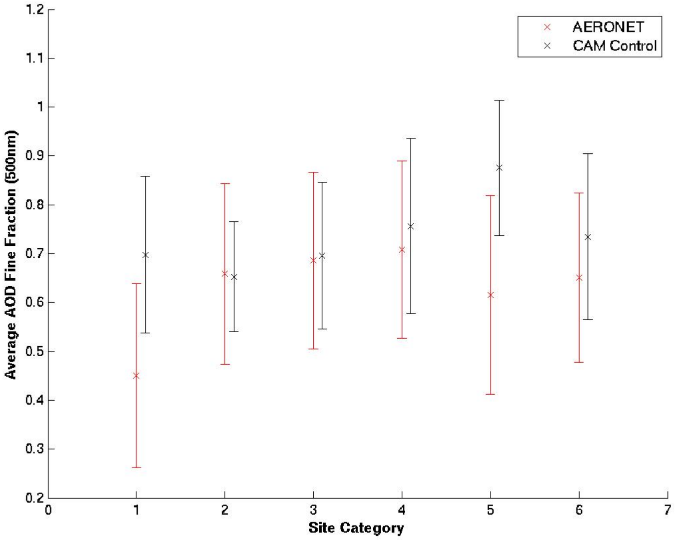

(b) Aerosol Optical Depth Fine Fraction

Figure 2.20: Comparison (mean ± standard deviation) between CAM control and AERONET a) aerosol optical depth and b) the fraction of aerosol optical depth due to fine aerosol. Comparisons are made by site category (1=desert dust, 2=biomass burning, 3=rural, 4=industrial pollution, 5=polluted marine, 6=dirty pollution).

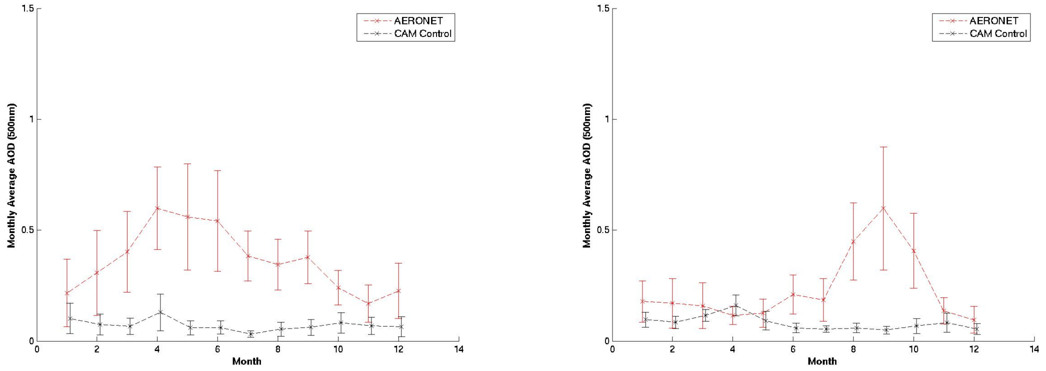

(a) desert dust

(b) biomass burning

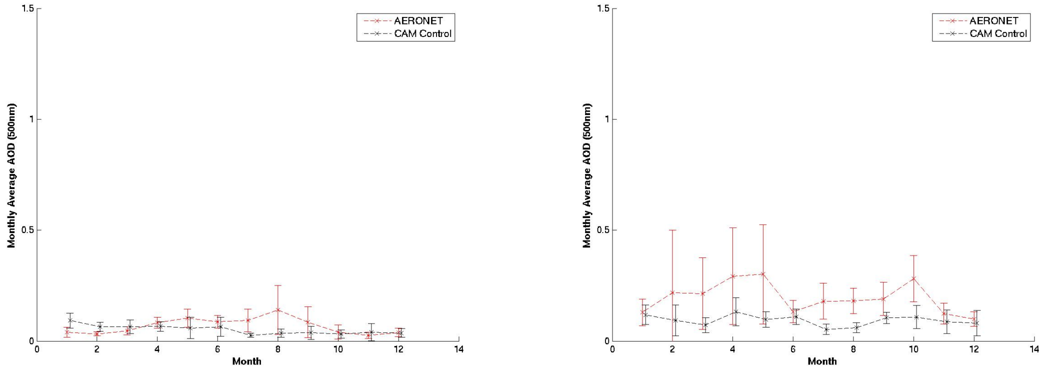

(c) rural

(d) industrial pollution

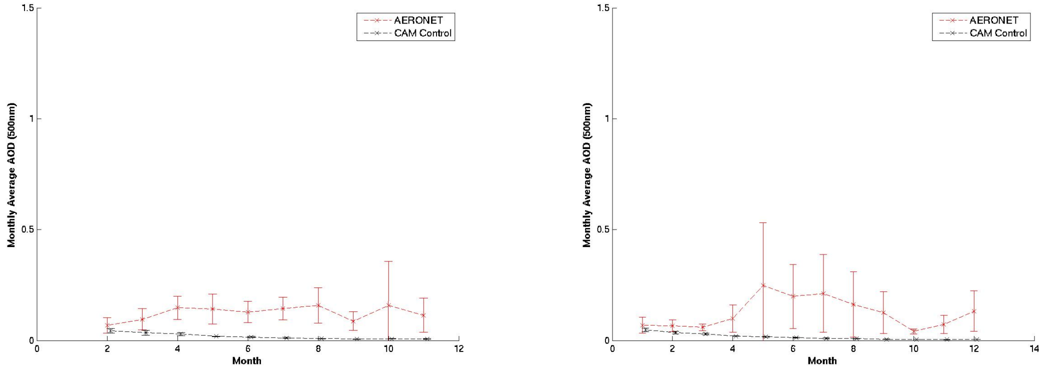

(e) polluted marine

(f) dirty pollution

Figure 2.21: Aerosol optical depth monthly-averaged timeseries comparisons between CAM control run and AERONET. Results are shown for select AERONET sites from each of the six site categories a)desert dust b) biomass burning c) rural, d) industrial pollution e) polluted marine f) dirty pollution).

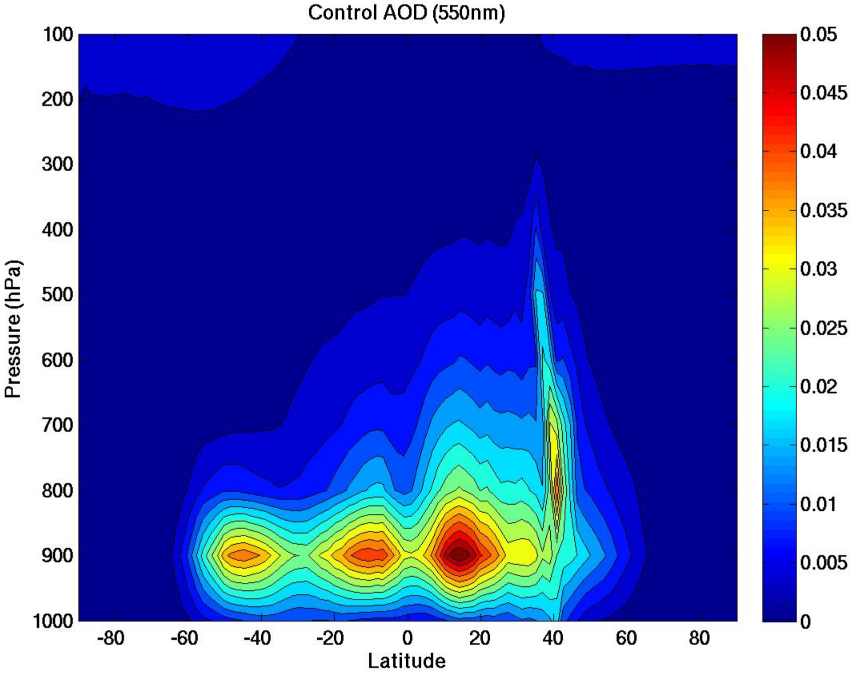

(a)

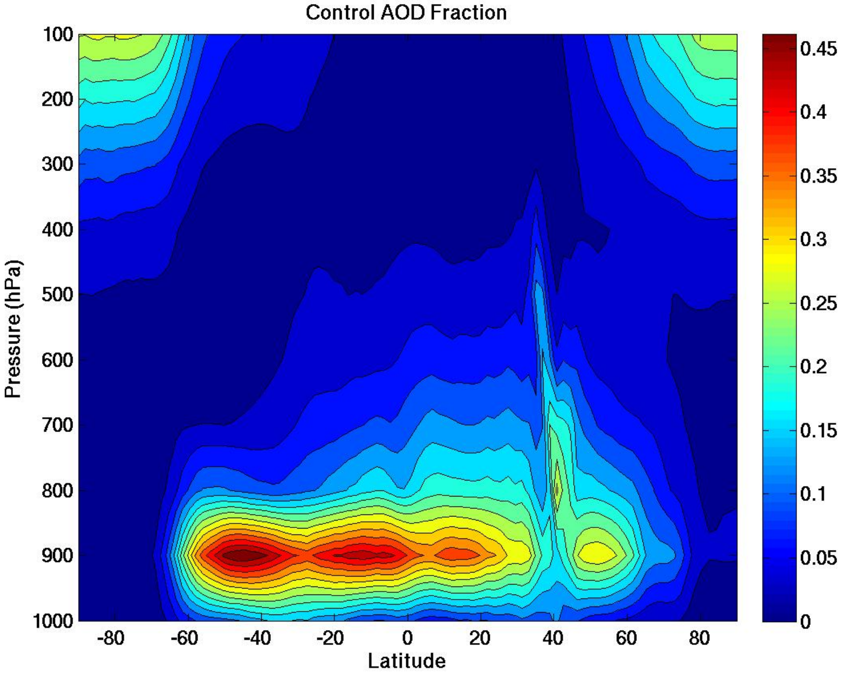

(b)

Figure 2.22: Control zonally averaged a) aerosol optical depth and b) fraction of AOD in the vertical column profile for the year 2007.

Chapter 3

Independent Information Analysis

Prior to developing an aerosol assimilation system, it is important to understand what adjustments can be made to aerosol within the constraints of the observations. The goal of this chapter is twofold: 1) to investigate the various degrees of freedom in predicting global aerosol and their importance for shortwave radiative forcing estimates and 2) to verify that the available observational data can be used to make the identified adjustments in the proposed aerosol assimilation system.

3.1 Aerosol Adjustments and Radiative Forcing

There are many degrees of freedom in predicting global aerosol fields. As discussed previously, CAM uses a lognormal modal scheme for predicting global aerosol fields with 3 modes corresponding to the nucleation, accumulation and coarse aerosol size modes. A lognormal size distribution is fully described by three parameters: 1) mean size 2) spread of the distribution 3) total integral under the curve (ie. number concentration for the zeroth moment of the size distribution). The lognormal scheme used in CAM allows prediction of the mean size and the number concentration; however, the spread of the lognormal distributions is fixed. With respect to the size distribution, this results in two degrees of freedom per aerosol mode with a total of six degrees of freedom. Additional degrees of freedom are associated with the composition of the aerosols. Aerosols within each mode are treated as internally mixed aerosols, having a mixture of aerosol types. The nucleation mode is composed of sulfate, secondary organic carbon and sea salt. The accumulation mode is composed of sulfate, primary and secondary organic carbon, black carbon, soil dust and sea salt and the coarse mode is composed of soil dust, sea salt and sulfate. With a number of degrees of freedom and limited information content in observational datasets, it is necessary to understand what adjustments can be made within the constraints of the observations for use in data assimilation. This problem can first be addressed by understanding the consequences of aerosol adjustments for radiative forcing since the ultimate goal is to look at the affect of the assimilation on aerosol radiative forcing.

The goal of this exercise is to understand how changes in aerosol properties affect outgoing shortwave radiant flux (W/m^2) at the top of the atmosphere and what the changes mean for radiative forcing. If it is assumed that a model has correctly determined the fraction of the total aerosol that is fine and coarse in size, we can investigate how a change in the total aerosol number concentration affects the outgoing flux. This simple experiment is performed using the single scattering approximation [58], which assumes only single scattering events occur. For domains where the optical depth is small (τ<0.1), large portions of scattering events are dominated by single scattering of the direct solar beam. This occurs in optically thin cirrus clouds and aerosol atmospheres [58]. The equation of radiative transfer for the upward radiation intensity (I,[W$m^{-2}sr^{-1}$]) in a plane parallel atmosphere (variations in atmospheric parameters in the vertical only) is given by Equation 3.1 where μ is the cosine of the zenith angle θ, ϕ is the azimuth angle and J is the source function. The first term in the equation represents the attenuation of the radiant intensity by the medium and the second term represents the emission contribution from the medium along the path. Under the single scattering approximation, the upward intensity at the top of the atmosphere (τ=0) for a black surface (I(τ^*;μ,ϕ)=0) is described by Equation 3.2 where $F_\odot$ is the solar irradiance at the top of the atmosphere, P is the phase function, ω is the single scattering albedo, and τ^* is the total atmospheric optical depth.

$$I(\tau;\mu,\phi) = I(\tau^*;\mu,\phi)e^{-(\tau^*-\tau)/\mu)} + \int_{\tau}^{\tau^*} J(\tau';\mu,\phi)e^{-(\tau'-\tau)/\mu}\frac{d\tau'}{\mu}(1 \geq \mu > 1) \tag{3.1}$$

$$I(0;\mu,\phi) = \frac{\mu_o F_\odot}{\pi}\frac{\omega}{4(\mu+\mu_o)}P(\mu,\phi;-\mu_o,\phi_o)\left(1 - exp\left[-\tau * \left(\frac{1}{\mu}+\frac{1}{\mu_o}\right)\right]\right) \tag{3.2}$$

The single scattering approximation calculations were done for sulfate particles with aerosol optical properties (single scattering albedo, extinction coefficient, asymmetry parameter) taken from OPAC database [31]. The total number concentration of the size distribution was varied (N=100,500,1000 [$\#/cm^3$]). In this first experiment, the only property that is changing is the total aerosol optical depth, which scales linearly with aerosol number concentration for optical depth values less than one [58]. Outgoing shortwave fluxes are shown in Figure 3.1, and as expected for a scattering aerosol, an increase in the number concentration results in increased outgoing radiation. Therefore, the change in shortwave radiative forcing is proportional to the change in aerosol concentration. If we examine the relationship between the outgoing flux and the optical depth under the single scattering approximation in Figure 3.2a, an approximately linear relationship is observed for optical depths typically observed in the atmosphere. This relationship indicates that the change in radiative forcing is proportional to the change in optical depth ($\delta F_r \propto \delta\tau$) as well as aerosol concentration. From this experiment, it was determined that an increase in aerosol concentration or optical depth for a scattering aerosol will result in a change in the radiative forcing. For aerosols, which already have a negative radiative forcing [84], this indicates an increased cooling effect. Conversely, a decrease in aerosol concentration will decrease the cooling effect of aerosols.

The same experiment is duplicated assuming the total amount of aerosol is correct and allowing for a change in the fraction of fine aerosol. In this experiment, the aerosol optical depth at 0.55μm is held fixed, but the optical properties change with wavelength. As shown in Figure 3.3a, decreasing the fraction of fine aerosol results in a wavelength shift with an increased outgoing flux at longer wavelengths and decreased flux in the visible part of the spectrum (0.4-0.7μm). Fine aerosols scatter more efficiently in the visible while larger, coarse particles scatter more efficiently in the near infrared, resulting in the observed spectrum shift with changing fine aerosol fraction. By examining the flux with wavelength on a natural log scale (Figure 3.3b), it is shown that the slope of the curve is greater (more negative) when a larger fraction of the aerosol is fine in size. As discussed previously, the outgoing radiant flux is proportional to the optical depth (Figure 3.2a). Therefore, it is expected that the slope of the optical depths with wavelength will exhibit a similar pattern to the slope of the outgoing flux with wavelength. This is examined in Figure 3.2b where the slope of the optical depth, also known as the angstrom exponent (Equation 1.33) is plotted against the slope of the outgoing flux on a natural log scale also called normalized flux. A linear relationship is observed. In this experiment, changing the aerosol size resulted in a shift in wavelength in outgoing flux as well as optical depth.

We have considered both the total amount of aerosol as well as aerosol size with the first two experiments. We also need to consider changes in aerosol composition. This is a more difficult issue to address since aerosols typically exist as a mixture of species and surface reflectance properties affect radiative forcing. However, for this simplified experiment, the size distribution and the optical depth are held fixed. The variation occurs in the refractive indices for each species, which result in changes in optical properties such as the single scattering albedo and phase function. Refractive indices were again taken from OPAC for sulfate, sea salt, black carbon, dust and organic carbon [31]. Results are again calculated using the single scattering approximation above a dark surface and are shown in Figure 3.4. While the shape of the spectral curves are the same across all species, differences are observed in the magnitude between species which are strong scatterers ($\omega \approx 1$) such as sulfate, sea salt and organic carbon and those that have an absorbing component such as dust and black carbon. Larger outgoing fluxes for the strong scatterers are associated with a larger cooling effect. While properly identifying aerosol species is important for understanding radiative forcing, given only spectral radiance measurements, it would be difficult to distinguish one species from another as differences in curve magnitude could also be attributed to the total amount of atmospheric aerosol. Additionally, aerosols typically exist in mixtures, making it even more difficult to determine aerosol composition. Although aerosol species is important, the results indicate that given spectral measurements from an instrument such as MODIS, it is unlikely that adjustments in species can be made in addition to amount and size.

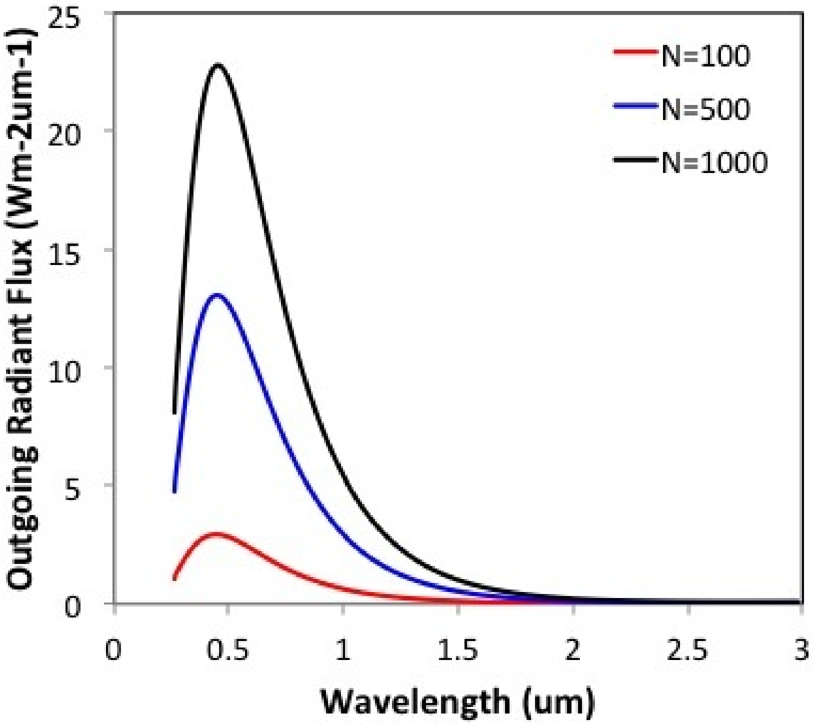

Figure 3.1: Outgoing radiant flux (Wm^{-2}) as a function of wavelength for three cases of sulfate aerosol number concentration (N=100,500,1000 cm^{-3}). Fluxes were calculated using the single scattering approximation above a black surface. Results show that for a scattering aerosol, the outgoing flux increases with increasing number concentration.

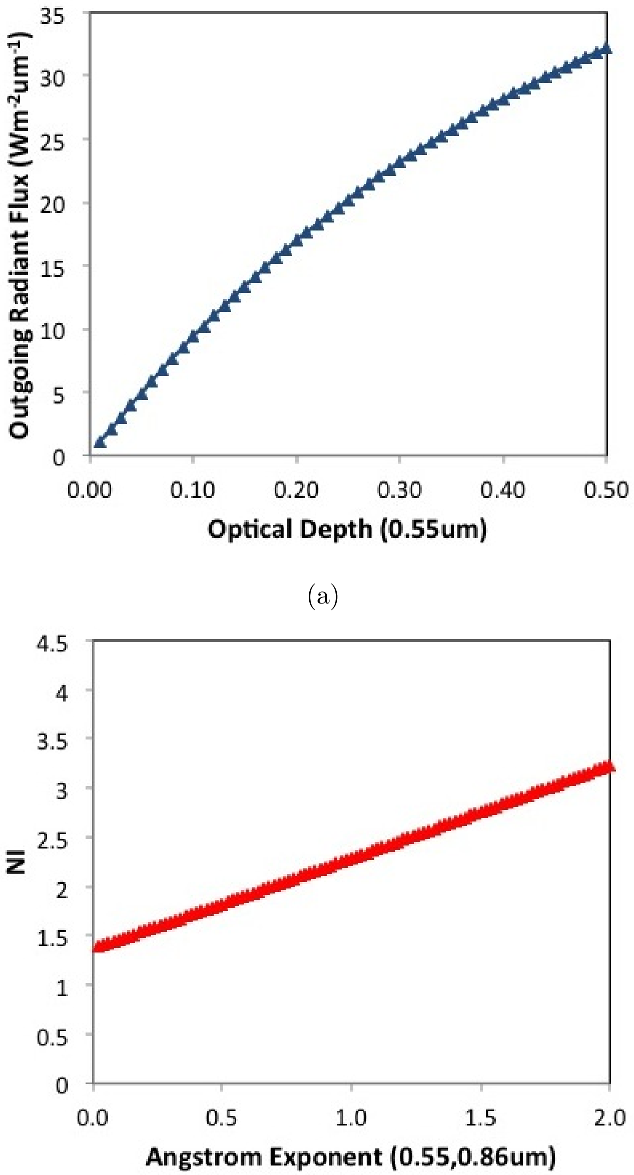

(a)

(b)

Figure 3.2: Results are shown for single scattering approximation calculations with a) outgoing flux plotted against optical depth at 0.55 μm and b) normalized outgoing flux (NI) (slope of outgoing flux with wavelength on a natural log scale) against angstrom exponent values.

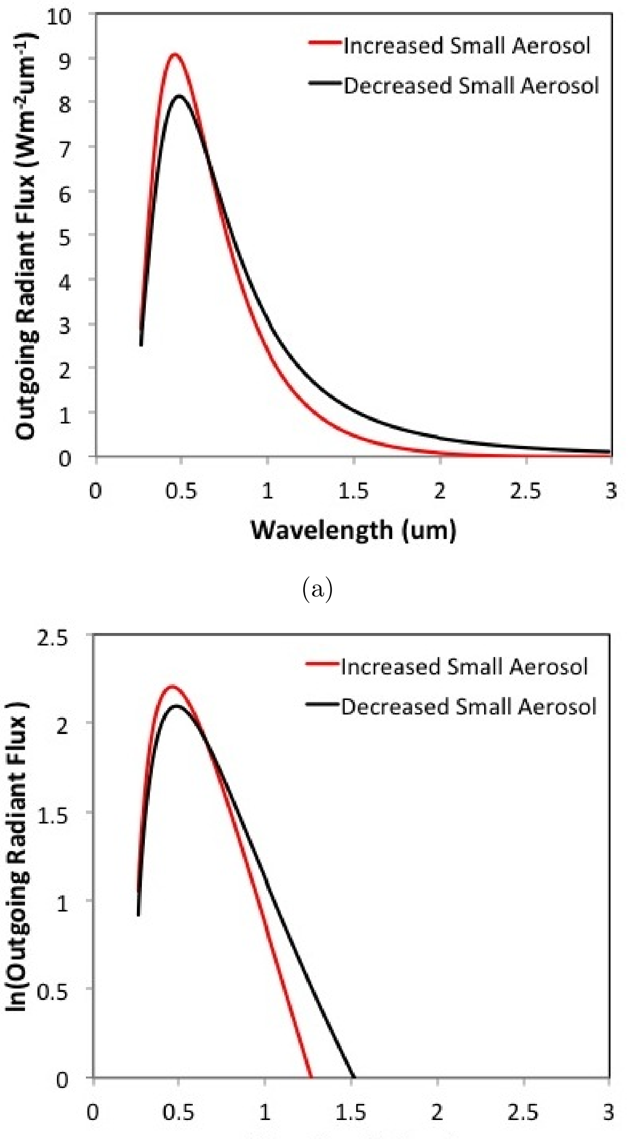

(a)

(b)

Figure 3.3: Outgoing radiant flux (Wm^{-2}) as a function of wavelength (left). These same results are also shown on a natural log scale (right). Fluxes were calculated for sulfate aerosol using the single scattering approximation above a black surface. In the red line case, there is an increase in the fraction of fine aerosols (<1μm). For the black line, there is a decrease in the fraction of fine aerosol and a corresponding increase in coarse aerosol (>1μm).

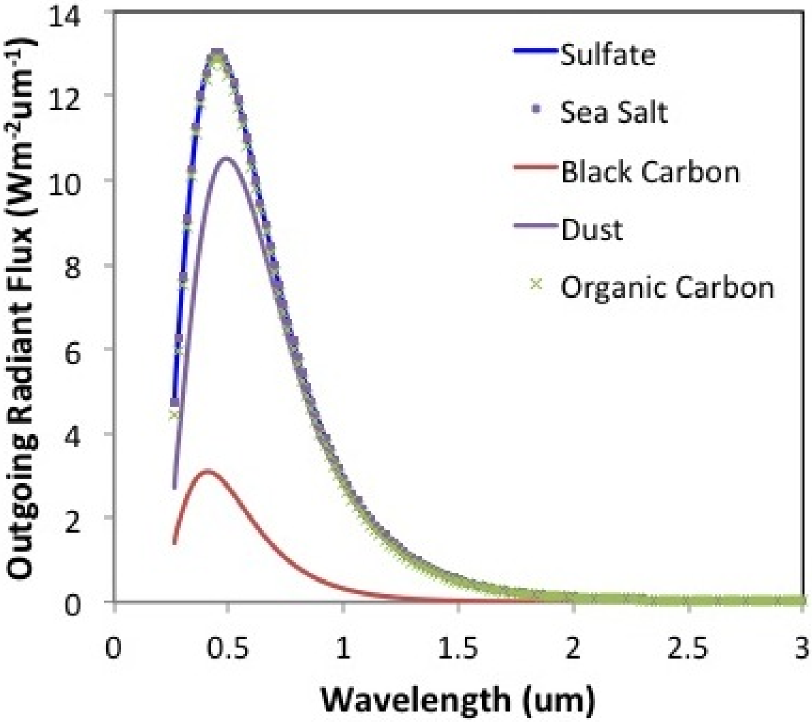

Figure 3.4: Outgoing radiant flux (Wm^{-2}) as a function of wavelength for five different aerosol types (sulfate, sea salt, black carbon, dust and organic carbon). Fluxes were calculated using the single scattering approximation above a black surface.

3.2 MODIS Independent Information Analysis

The previous three experiments demonstrated the effect of adjustments in aerosol on radiative forcing and indicate that the focus of the assimilation should be in adjusting aerosol amount and the fraction of aerosol that is fine in size. In order to use these adjustments in data assimilation, it is first necessary to confirm that there are two independent pieces of information contained in the observational dataset, MODIS spectral radiances. The number of adjustments that can be made to aerosols is dependent on the number of independent pieces of information in the observations. Therefore, we need at least two pieces of information for our proposed assimilation. A principle component analysis (PCA) was conducted to determine the degrees of freedom in simulated MODIS spectral radiances. PCA is a statistical analysis that uses an orthogonal transformation to convert a number of possibly correlated variables into a smaller number of uncorrelated (mutually independent) variables called principle components. The transformation is defined such that the first principle component accounts for as much of the variability in the data as possible.

In PCA, i simulated radiance measurements at j wavelengths are stored in the matrix $\mathbf{R_{ij}}$. The matrix $\mathbf{R}$ is standardized such that for each wavelength j, the average of all simulated values is zero and the standard deviation is one. The covariance matrix $\mathbf{A} = \mathbf{RR^T}$ is diagonalized according to Equation 3.3 such that the row vectors of the matrix $\mathbf{V}$ from an ortho-normal set of $\mathbf{k}$ eigenvectors and that the eigenvalues on the diagonal of the matrix $\mathbf{D}$ are sorted in descending order. The eigenvectors are referred to as the Principal Components (PC) of the measurements with the maximum number of PCs equal to the total number of variables j. Each simulated value can be decomposed into a weighted sum of principal components (Equation 3.4) where $\mathbf{\hat{R}_{ij}}$ are the elements of the reconstructed measurement matrix with an error ϵ. In this analysis, there are seven variables that are being examined for correlation and these correspond to simulated radiances (I) measured by the satellite at seven wavelength bands in the visible and infrared (0.47, 0.55, 0.64, 0.86, 1.24, 1.63 and 2.12μm). Radiances measured at these bands are used in MODIS AOD retrievals [37].

$$A = V^T DV \tag{3.3}$$

$$R_{i,j} = \hat{R}_{ij} + \epsilon = \sum_{k}^{k_{max}} W_{ik} V_{kj} + \epsilon \tag{3.4}$$

Outgoing radiances (I) were simulated using a one-dimensional radiative transfer code, MODTRAN, which allows insertion of aerosols into the model atmosphere by specification of aerosol optical properties [11] [12]. Aerosol optical properties were calculated using refractive indices from the OPAC database and Mie scattering theory. Results of the Mie calculations over a range of wavelengths and mean radius of the size distribution are shown in Figures 3.5, 3.6, and 3.7. Results are shown for the five aerosol types (dust, sulfate, soot, organic carbon and sea salt) and include the three optical properties: 1) normalized extinction coefficient ($k_{ext}/k_{ext,0.55}$) 2) single scatter albedo (ω) and 3) the asymmetry parameter (σ). In Figure 3.5, normalized extinction coefficients as a function of wavelength for several aerosol sizes are shown for sulfate aerosol only. Similar relationships were found for all species, therefore, results for only one species are presented. The results show that as the size of the aerosol increases, extinction becomes more uniform across wavelength. In Figure 3.6, single scattering albedo as a function of mean size and wavelength are presented. Sulfate and sea salt have approximately the same refractive indices and therefore, the same results are found for both of these species (Figure 3.6a). Extinction due to all of the species examined, except for black carbon, is mostly due to scattering (values close to 1). Wavelength and size dependence for organic carbon, dust and soot single scattering albedos exist while sulfate and sea salt show almost no variation. Asymmetry parameters as a function of size and wavelength are shown in Figure 3.7. All species have an increase in asymmetry parameter with size, indicating increased forward scattering as the size of the aerosol increases.

By varying the aerosol composition and lognormal size distribution (mean radius) through changes in optical properties inserted into MODTRAN, a dataset with hundreds of cases (i) of radiances at the 7 wavelengths (j) were generated for use in the PCA analysis. Three sets of PCA analyses were conducted: 1) PCA analyses were conducted for the five aerosol types separately. The five aerosols correspond to aerosols from the OPAC database and are consistent with the aerosols simulated in the global atmospheric model for this research [31] [66]. This analysis identifies the information content in the radiances when we consider size distribution only; 2) one PCA analysis was conducted by combining all the aerosol cases used in the first five analyses. This analysis identifies the information content in the radiances when we consider both size distribution and composition for cases where aerosol type is not mixed; 3) Each case used is a combination of three size distribution functions corresponding to the nucleation, accumulation and coarse mode used in CAM. For each case used in the PCA, the composition of the three size distributions were randomly selected from each of the five aerosol types and the mean radius of the distribution within the constrains of the selected size mode were also randomly generated. This analysis identifies the information content in the radiances when we consider size and composition for mixed aerosols. The identified principle components for each analysis were examined.

In the PCA analysis, outgoing radiances (I) were normalized to remove the effect of number concentration. At the relatively small concentrations characteristic of atmospheric aerosols, the outgoing radiance scales with number concentration and hence optical depth as demonstrated previously [14]. Normalizing by the radiance at a reference wavelength removes this signal and facilitates identification of additional underlying structures in the data. The radiances were normalized (NI) to look like an angstrom exponent (Equation 1.33). Since it is known that optical depth is proportional to outgoing radiances via the single scattering approximation, it is expected that outgoing radiances will exhibit a similar behavior with large NI values for small aerosol and smaller NI values for larger aerosol. Since we are interested in making adjustments to aerosol size, this is a useful way to normalize the data. Normalized radiances are calculated using Equation 3.5. The number of variables j is reduced to six since one of the bands of interest is being used for normalization (0.86μm). An example of NI data that was used in the PCA analysis for a dust aerosol is shown in

Figure 3.8. The NI values are larger for small aerosols as expected.

$$NI = \frac{ln[I(\lambda_1)/I(0.86\mu m)]}{ln[0.86\mu m/\lambda_1]} \tag{3.5}$$

After removing for the effect of number concentration, the first principal component (PC) identified in all PCA analyses explained approximately 95% of the variance in the data. In PCA analysis, a useful way of understanding the meaning of a principle component is to examine correlations with the original data. For the first PC, a very strong correlation ($R^2 \geq 0.98$) was found with the average NI. The relationship between the first PC and the average NI for three types of PCA analyses are shown in Figure 3.9. This indicates that besides the number concentration, the spectral shape of the radiances explains the majority of the variance. While the remaining variance may be explained by species differences, the remaining principal components explained very little variance (<5%) in the data and could not easily be used in the assimilation. The independent piece of information analysis revealed there are at least two pieces of information contained in the spectral radiances, one associated with the number concentration and the other with the average of the angstrom-like exponent, or shape of the spectral radiance curves, verifying that two adjustments can be made to aerosol properties. As shown previously, the optical depth scales with the magnitude of the outgoing radiance and the angstrom exponent scales with the normalized radiances. The optical depth and the angstrom exponent will be the two independent pieces of information used in the aerosol assimilation.

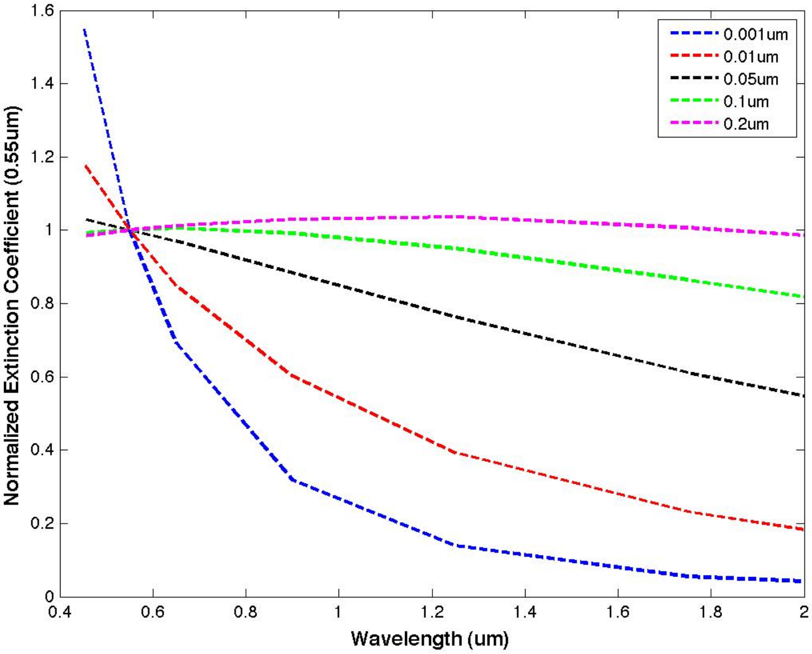

Figure 3.5: Normalized extinction coefficients ($k_{ext}/k_{ext,0.55}$) as a function of wavelength for a sulfate aerosol. Extinction coefficients are calculated using Mie scattering theory and normalized by the extinction coefficient at 0.55 μm. Extinction coefficients are shown for a range of aerosol sizes. Results were very similar across aerosol species. The extinction coefficient becomes more uniform across wavelength as the size of the aerosol increases.

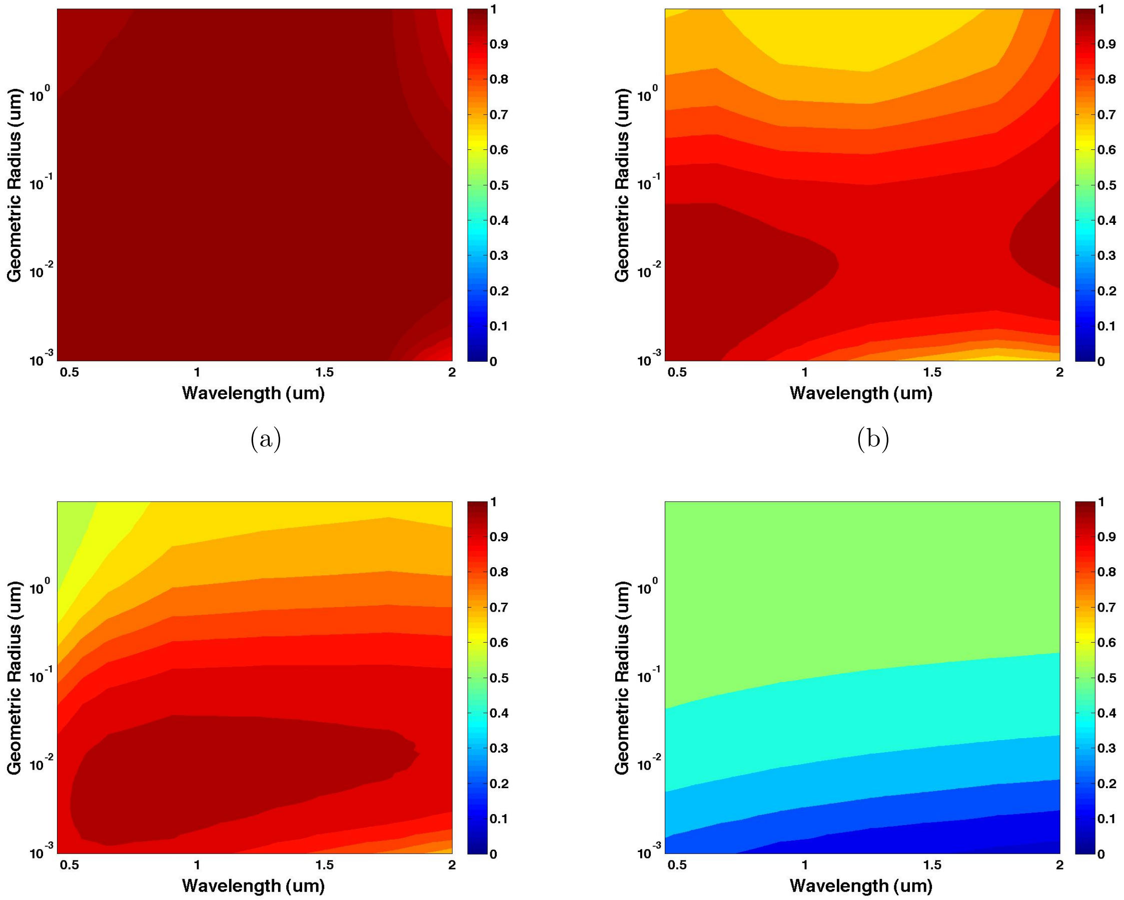

(a)

(b)

(c)

(d)

Figure 3.6: Single scattering albedo (ω) calculating as a function of wavelength and mean radius of the size distribution for a) sulfate and sea salt b) organic carbon c) dust and d) black carbon. A value of 1 means a complete scattering aerosol and a value of 0 means a completely absorbing aerosol. Black carbon has a much stronger absorbing component than the other species.

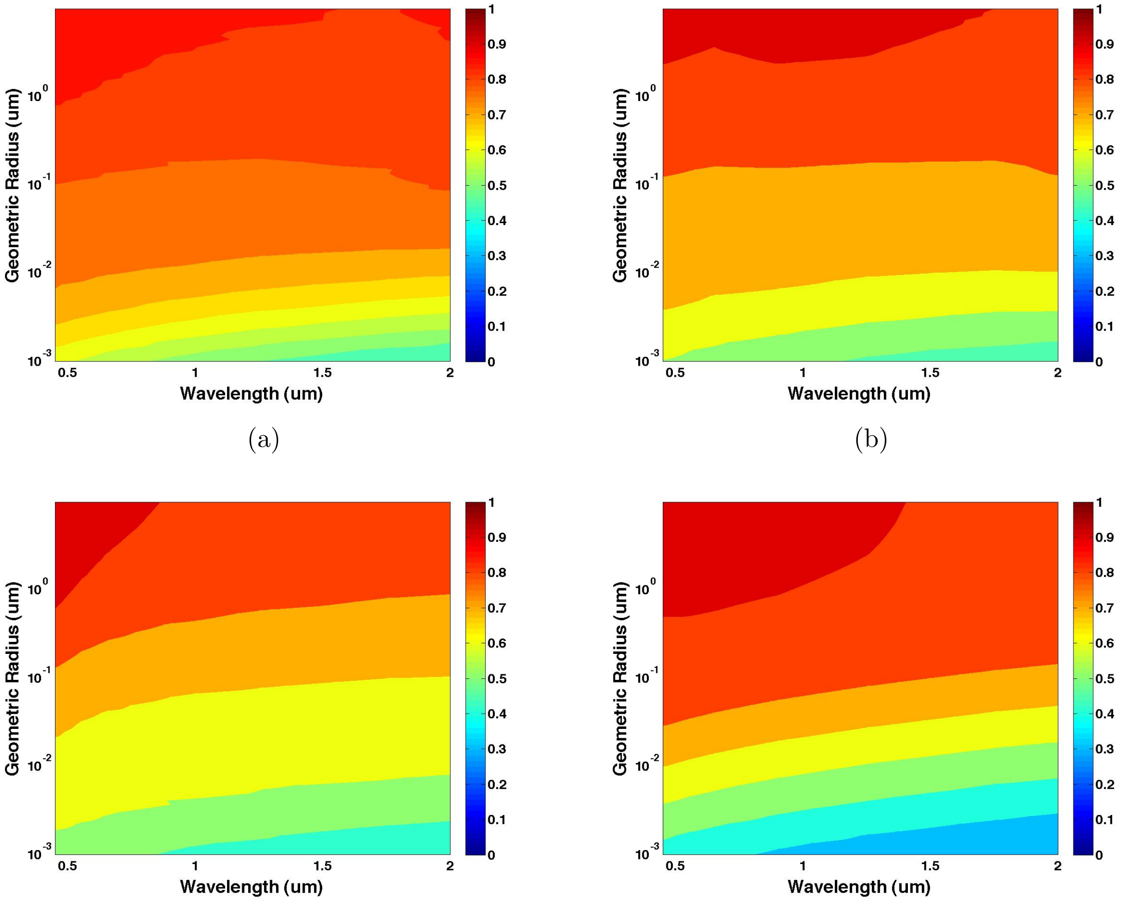

(a) (b)

(c) (d)

Figure 3.7: Asymmetry parameter (σ) calculated as a function of wavelength and mean radius of the size distribution for a) sulfate and sea salt b) organic carbon c) dust and d) black carbon. A value of 1 means a complete scattering aerosol and a value of 0 means a completely absorbing aerosol. Black carbon has a much stronger absorbing component than the other species.

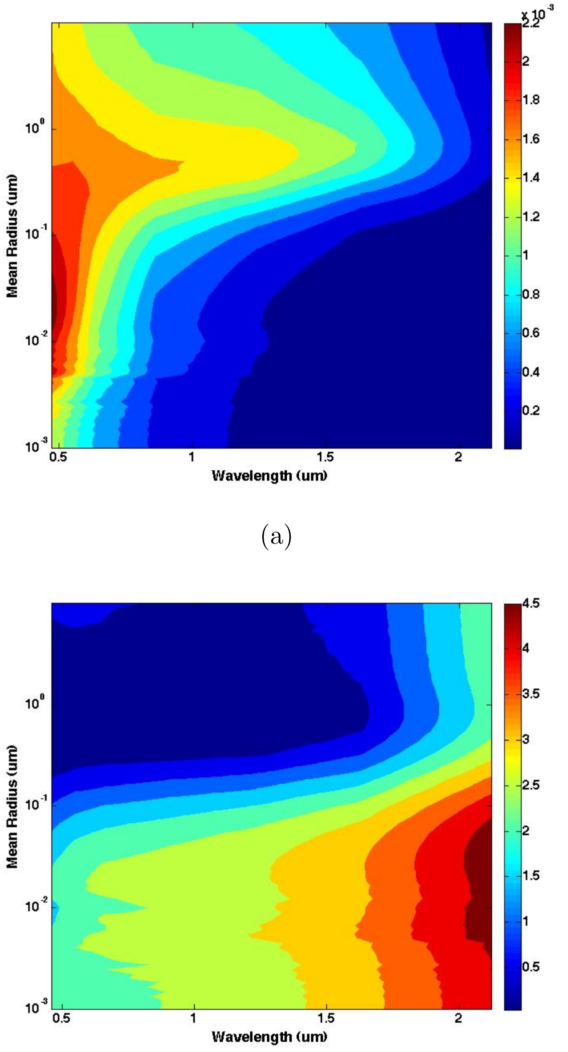

(a)

(b)

Figure 3.8: Data used in the PCA analysis for a dust aerosol with a) spectral radiances (W$m^{-2}\mu m^{-1} sr^{-1}$) as a function of wavelength and mean radius and b) NI values derived from the data in a. Figure b) represents the slope in the radiance with wavelength for a specified mean radius, relative to the middle 0.86μm band. A larger value indicates a greater change in radiance, as expected for small aerosols.

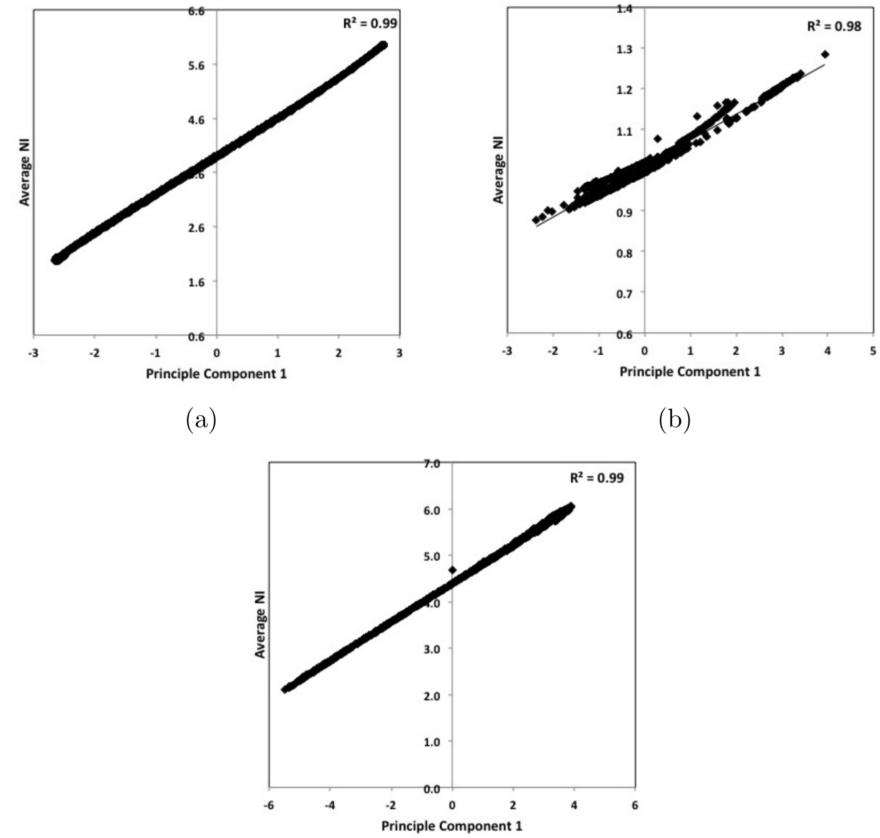

(a) (b)

(c)

Figure 3.9: Plots of averaged normalized radiances (NI) against the first identified principal component for a) sulfate PCA only b) sulfate, sea salt, organic carbon, black carbon and dust unmixed aerosol PCA and c) mixed aerosol size distribution PCA. Strong correlations were found for all PCA analyses indicating the first principal component is related to the spectral shape of the radiances.

Chapter 4

Data Assimilation

This chapter includes an introductory discussion of data assimilation as well as the current state of aerosol assimilation research. The assimilation systems developed for this work are presented including an assimilation which adjusts the total amount and the relative amount of fine and coarse aerosols (AOD/ANG) as well as an assimilation which uses vertical profile observations (VERT). The novel features of the new assimilation system are discussed. Assimilation results are presented for the year 2007 and compared to the control simulation.

4.1 Introduction to Data Assimilation

It has been shown that modeled predictions can be improved by using observational data to constrain model forecasts, for example the Numerical Weather Prediction (NWP) and the National Centers for Environmental Prediction meteorological forecasts [41] [86]. The statistical combination of observations and prior information about the physical state of a system (background or predicted value) to determine the best estimate of the state has been termed data assimilation. For atmospheric applications, Talagrand (1997) [87] defined data assimilation as the process through which all available information is used to estimate the state of the atmosphere with the available information including observations and the physical laws that govern the atmosphere (ie. numerical models). Statistical data assimilation techniques use a least squares approach, which is used to determine the combination of the predicted and observed states that produce a minimum mean squared error in the adjusted state value or analysis value. Statistical information about the errors in both the predicted and observational states is required to determine the optimal combination.

The least squares approach, the basis for data assimilation, is demonstrated under a simplified case in which the background (x_b) and observational information (x_o) are scalar values of the same variable at the same location [41]. Each piece of information has an associated error ϵ defined as the deviation from the true value x_t (Equation 4.1 and Equation 4.2).

$$x_b = x_t + \epsilon_b \tag{4.1}$$

$$x_o = x_t + \epsilon_o \tag{4.2}$$

Several assumptions are made including unbiased background and observational information (ie. the expected values of the errors are zero, E(ϵ_b)=E(ϵ_o)=0), the errors are uncorrelated (E($\epsilon_b\epsilon_o$)=0), and the variances are known (E(ϵ_b^2)=σ_b^2,E(ϵ_o^2)=σ_o^2). Additionally, it is assumed that the two pieces of information can be linearly combined, using weights a_b and a_o, such that the analysis estimate x_a is closest to the truth (ie. minimizes ϵ_a) (Equation 4.3). The analysis estimate is also assumed to be unbiased (E(x_a)=E(ϵ_t)), implying that the sum of the weights a_b and a_o is equal to one (Equation 4.4).

$$x_a = a_b x_b + a_o x_o \tag{4.3}$$

$$a_b + a_o = 1 \tag{4.4}$$

The best estimate of the state x is achieved when the chosen weights minimize the mean squared error σ_a^2 (Equation 4.5). This occurs where the derivative of the variance with respect to the weights is equal to zero ($\frac{d\sigma_a^2}{da_b}$=0). Using the defined assumptions and Equation 4.5, the weights that minimize ϵ_a are determined (Equations 4.6 and 4.7).

$$\sigma_a^2 = E[(a_b(x_b - x_t) + a_o(x_o - x_t))^2] \tag{4.5}$$

$$a_b = \frac{\sigma_o^2}{\sigma_b^2 + \sigma_o^2} \tag{4.6}$$

$$a_o = \frac{\sigma_b^2}{\sigma_b^2 + \sigma_o^2} \tag{4.7}$$

Plugging the optimal weights back into Equation 4.3 results in the basic form of the equation for data assimilation. The analysis value x_a is expressed in Equation 4.8 where W is the optimal weight and d, the difference between x_o and x_b, is termed the innovation.

$$x_a = x_b + \frac{\sigma_b^2}{\sigma_b^2 + \sigma_o^2}(x_o - x_b) = x_b + Wd \tag{4.8}$$

The least squares approach reveals that the optimal analysis state is obtained by adding to the first guess or background value (x_b) the difference between the observed and background state, weighted by an optimal weight. The optimal weight is the background error variance divided by the total error variance, indicating that the larger the background error, the larger the correction to the first guess.

The previous discussion illustrates the basic concept of data assimilation. In larger scale systems such as atmospheric models, practical implementation must be considered. Two types of data assimilation techniques exist, variational and sequential [41]. In variational methods, the best estimate of the atmospheric state is determined by minimizing a cost function where the cost function is defined as the distance between the model-predicted and observed states weighted by the inverse of the error variance [41]. The cost function is used to seek the initial condition leading to a forecast that best matches the observations within an assimilation window. The minimization of the cost function requires the gradient of the cost function, which involves the use of tangent linear and adjoint models. It should be noted that the minimization of the error variance previously discussed and the minimization of the cost function in the variational approach are equivalent [41]. Commonly used variational schemes are three-dimensional and four-dimensional variational schemes (3-D Var, 4-D Var) and require an iterative approach for finding the cost function minimum. Sequential schemes produce estimates of the system state sequentially by propagating information only forward in time as opposed to the variational approach, which includes information at previous timesteps [41]. Common sequential schemes are the Kalman Filter and its derivatives including the Ensemble Kalman Filter (EnKF).

The focus of this work will be on sequential data assimilation due to its relative ease of implementation compared to variational schemes. In particular, this work will use the Ensemble Kalman Filter (EnKF). Studies comparing the EnKF to variational approaches in atmospheric applications have shown similarities in performance. Whitaker et al. 2008 [100] and Szunyogh et al. 2008 [85] compared the EnKF to the 3-D Var scheme used by NCEP and found that the EnKF performed better. In Canada, Houtekamer and Mitchell , 2006 [36] showed that the EnKF performs just as well as the 4D-Var scheme. Hunt et al. showed that the EnKF is accurate and very fast [38]. Additional advantages of the EnKF will be discussed.

In the sequential approach, each assimilation cycle involves two steps: 1) a forecast phase to update the prior state ($\mathbf{x_b}$) and its error variance by integrating a numerical model (M) forward in time and 2) an analysis phase to combine observations and prior state information to produce an analysis state ($\mathbf{x_a}$) and a corresponding error variance (σ_a^2). The forecast phase of the assimilation updates the prior or background state $\mathbf{x_b}$ from time t_i to t_{i+1} (Equation 4.9). The state variable of interest at a given time is contained in the vector $\mathbf{x}$ with length n where n is equal to the total number of grid points times the number of state variables being adjusted. In CAM, each two-dimensional state variable has a length of 13824 (144 by 96 horizontal grid) and each three-dimensional variable has a length of 387072 (144 by 96 horizontal and 28 vertical levels). The observational data is contained in the vector $\mathbf{y}$ of length p. In general, the modeled state variables of interest cannot be directly observed. Instead, measurements of quantities influenced by the variables of interest are available, as is the case with aerosol optical depth measurements and the mass of aerosol in the atmosphere. Additionally, measurements are often made at locations that differ from the modeled grid points, resulting in a need for spatial interpolation. Due to these differences, a forward observational operator ($\mathbf{H}$) is needed to transform state data to observational space (Equation 4.10).

$$x_b(t_{i+1}) = M[x_a(t_i)] \tag{4.9}$$

$$y = H(x) \tag{4.10}$$

The EnKF, the chosen approach for this work, is a derivative of the Kalman filter, therefore, the Kalman filter will first be discussed. The basic equation for the Kalman filter is the same format as the simple scalar example. The analysis is the background plus the innovation weighted by an optimal weight. The difference is the background and observations are vectors and the weights are given by a matrix of dimension (nxp). Errors are expressed in covariance matrices obtained by multiplying a vector error by its transpose ($\bar{\epsilon}\epsilon^T$) where the diagonal elements are the variances of the vector error components. The background error covariance $\mathbf{B}$ is a matrix of size nxn and the observational error covariance $\mathbf{R}$ is a matrix of size pxp. Additionally, the innovation $\mathbf{d}$ must now take into account differences in state and observational space using the observational operator $\mathbf{H}$. The optimal weight, also known as the Kalman gain matrix, is shown in Equation 4.11 and can be interpreted similarly as the scalar problem where the larger the background error, the larger adjustment is made to the first guess. In matrix form, the analysis vector is obtained from Equations 4.11 and 4.12. [41]

$$\mathbf{W} = \mathbf{B}\mathbf{H}^{\mathbf{T}}(\mathbf{R} + \mathbf{H}\mathbf{B}\mathbf{H}^{\mathbf{T}})^{-1} \tag{4.11}$$

$$\mathbf{x_a} = \mathbf{x_b} + \mathbf{W}[\mathbf{y_o} - \mathbf{H}(\mathbf{x_b})] \tag{4.12}$$

In Kalman filtering, forecasting the error covariance through the analysis cycle is a difficult task for a model that changes nonlinearly in time. The Ensemble Kalman filter is an alternative approach to the traditional Kalman filter where the underlying principle is to perform an ensemble of forecasts and analysis cycles with the ensemble members treated as a random draw from the probability distribution of the model's state [22] [23] [13]. Assuming the distribution is Gaussian, the error statistics are generated using a finite sample of model states (K) as an alternative to explicitly handling a large error covariance matrix. The ensemble generated error statistics are shown in Equation 4.13 where an overbar indicates the ensemble average [41]. The ability to characterize errors of predicted fields using the ensemble members is a major advantage of the EnKF. In atmospheric applications of the EnKF, sixty to eighty ensemble members are recommended in the literature [7]. A total of sixty ensemble members is used in this work. All simulations make use of the Ensemble Kalman Filter from the Data Assimilation Research Testbed (DART) [4] [5].

$$\mathbf{R^f} \approx \frac{1}{K-1}\sum_{k=1}^{K}(x_b^f - \bar{x^f})(x_b^f - \bar{x^f})^T \tag{4.13}$$

The success of an EnKF is dependent on the ensemble being statistically representative of the distribution of model states. However, computational costs limit the ensemble number. Undersampling of the model space can result in issues such as long-range spurious correlations. Spurious correlations are correlations in the background error covariance between state components that are not physically related and often at a significant distance from each other. In reality, it is expected that the true correlation will decrease at a distance from the observation. [72] Covariance localization [35] [29] [99] is an approach used to correct for undersampling issues by cutting off long-range correlations at a specified distance. A correlation function ρ is defined that is similar in shape to a Gaussian function. For this work, a fifth order piecewise rational function defined by Gaspari and Cohn (1999) is used where z is the distance between a grid point and the observation location and c is a defined cutoff value (Equation 4.14) [26]. In the covariance localization approach, an adjusted Kalman Gain Matrix ($\mathbf{W}'$) is used which takes into account the specified function (Equation 4.15) (Houtekamer and Mitchell, 2001).

$$\rho = \begin{cases} -\frac{1}{4}(\frac{|z|}{c})^5 + \frac{1}{2}(\frac{|z|}{c})^4 + \frac{5}{8}(\frac{|z|}{c})^3 - \frac{5}{3}(\frac{|z|}{c})^2 + 1, & 0 \leq |z| \leq c \\ \frac{1}{12}(\frac{|z|}{c})^5 - \frac{1}{2}(\frac{|z|}{c})^4 + \frac{5}{8}(\frac{|z|}{c})^3 + \frac{5}{3}(\frac{|z|}{c})^2, & c \leq |z| \leq 2c \\ 0, & 2c \leq |z| \end{cases} \tag{4.14}$$

$$\mathbf{W}' = [\rho] \circ \mathbf{BH^T}](\mathbf{R} + [\rho \circ \mathbf{HBH^T}])^{-1} \tag{4.15}$$

Data assimilation has been applied to aerosol forecasts with varying degrees of complexity. Collins et al. 2001 conducted a regional scale assimilation over the Indian Ocean as part of the Indian Ocean Experiment (INDOEX) using Advanced Very High Resolution Radiometer (AVHRR) AOD retrievals to adjust aerosol mass mixing ratios [16]. The assimilation improved the models ability to capture daily variations in modeled AOD. Yu et al, 2003 conducted a global scale assimilation of monthly AOD in a chemical transport model using higher resolution satellite data from MODIS [106]. Improvements were shown in the correlations between model-forecasted AOD and ground-based AERONET data. More recently, Weaver et al, 2007, demonstrated the concept of directly assimilating MODIS radiances in a chemical transport model to adjust aerosol mass mixing ratios, although the observational operator H was highly simplified in this study [98]. While these studies have demonstrated the ability to reduce uncertainty in aerosol forecasts, additional measures can be taken.

The previously mentioned studies simulated aerosol mass only with a fixed aerosol size distribution (bulk aerosol treatment) and used the assimilation to make adjustments in aerosol mass mixing ratios. Data assimilation with adjustments to aerosol mass and size distribution parameters is expected to further reduce uncertainties in aerosol forecasts and radiative forcing estimates. This can be accomplished by employing an aerosol scheme that predicts both mass and size distribution in time (ie. modal scheme) and using additional observational data. Additionally, studies have suggested that modeled aerosols tend to become trapped near the surface [73]. The use of vertical observations in data assimilation could improve the vertical distribution of aerosol, which is tightly coupled to atmospheric lifetime and horizontal transport [8].

Two types of assimilations are conducted for this work. The first assimilation makes adjustments in the mass and number concentration of aerosol in the atmosphere and the amount of fine versus coarse aerosol. This assimilation is expected to be an improvement upon the previously mentioned studies, which adjusted aerosol mass only. The second assimilation will be similar to the first with the addition of vertical adjustments using vertical extinction observations. The novel features of the assimilations presented in this research are 1) the joint adjustment of the total mass and number concentration and the allocation between fine and coarse aerosol particles; 2) the use of vertical extinction observations to adjust aerosol vertical profiles and 3) an assessment of the implications of aerosol assimilation on radiative forcing estimates.

4.2 Amount and Size Aerosol Assimilation

Through the independent information analysis presented in Chapter 3, it was confirmed that there are two independent pieces of information observed by MODIS radiometers, related to the amount of atmospheric aerosol and the relative contribution of fine and coarse aerosol. These pieces of information scale with the two retrieved quantities, aerosol optical depth and the angstrom exponent, respectively. This indicates that changes to AOD and angstrom exponents can be used to scale changes in the amount of aerosol and relative size contribution. This finding is the main driver for the approach used in the aerosol amount and size (AOD/ANG) assimilation.

The state vector $\mathbf{x}$ used in this assimilation is composed of model-predicted AOD and angstrom exponent (α) values. The use of AOD and angstrom exponents in the state vector allows for a direct comparison with observational data and, therefore, no observational operator $\mathbf{H}$ is required. The observational data contained in vector $\mathbf{y}$ is composed of MODIS level 3 daily-averaged AOD retrievals and a combination of daily-averaged angstrom exponent Level 3 retrievals from MODIS and retrievals from AERONET. As discussed previously, MODIS angstrom retrievals over land are very uncertain and therefore, unsuitable for use in data assimilation. AERONET retrievals are used to provide some constraint on aerosol size over land. Daily average observations are used in the assimilation with a daily mid-day analysis cycle conducted. Studies have shown that measured aerosol from polar-orbiting satellites are able to represent the daily average impact of aerosol on climate, independent of the measurement time with small diurnal variations in AOD and angstrom exponent about the mean [45]. The lack of sensitivity of the measurements to time of day was attributed to relatively long aerosol lifetimes (several days), which reduce the difference between morning and afternoon observations and the close relationship between aerosol loading and the frequency of synoptic scale meteorological processes which are largely independent of diurnal cycles [45]. As a result, daily-averaged observations are representative, independent of the time the assimilation adjustment is made [45]. Sixty versions of CAM (ie. ensembles) are run in parallel and stopped mid-day for comparison with observations. For each analysis cycle, the EnKF filter is applied to produce an analysis or posterior state vector $\mathbf{x_a}$ composed of adjusted AOD and angstrom values. Consistent with the independent information analysis findings, the adjustments to the model-predicted AOD and angstrom values are then used to adjust the model-predicted mass and number concentration fields using a set of equations derived for this work. The adjusted model parameters are then used to reinitialize the ensembles.

The scaling equations are derived by using two pieces of information: 1) the total optical depth ($\tau(\lambda)^t$) is the sum of the optical depth due to fine ($\tau(\lambda)^f$) and coarse aerosol ($\tau(\lambda)^c$) (Equation 4.16) and 2) the definition of the angstrom exponent (Equation 4.17). Since the approach is to adjust the relative contribution of fine and coarse aerosol and not the mean radius of the size distributions, the number concentration scales exactly as the mass concentration. In addition, the presented aerosol assimilation does not change the composition of the internally mixed aerosol within each size mode since this information cannot be extracted from MODIS observations, as demonstrated in the previous chapter. In the end, the presented assimilation includes two scaling equations, one to adjust the nucleation and accumulation size modes with a fine scaling equation and one to adjust the coarse mode with a coarse scaling equation.

$$\tau(\lambda)^t = \tau(\lambda)^f + \tau(\lambda)^c \tag{4.16}$$

$$\tau(\lambda_2) = \tau(\lambda_1)\left(\frac{\lambda_1}{\lambda_2}\right)^{\alpha} \tag{4.17}$$

Equation 4.16 is rewritten as a function of two wavelengths using the definition of the angstrom exponent (Equation 4.18). It should be noted that the wavelength dependence of the optical depth for fine aerosol is different than coarse; therefore, each has an associated angstrom exponent (α_f, α_c). The total angstrom exponent (α_t) describes the wavelength dependence of the optical depth for all aerosols combined.

$$\tau(\lambda_1)^t\left(\frac{\lambda_1}{\lambda_2}\right)^{\alpha_t} = \tau(\lambda_1)^f\left(\frac{\lambda_1}{\lambda_2}\right)^{\alpha_f} + \tau(\lambda_1)^c\left(\frac{\lambda_1}{\lambda_2}\right)^{\alpha_c} \tag{4.18}$$

The total optical depth can also be expressed as a fractional contribution from fine and coarse aerosol as shown in Equation 4.19 where $\phi_f$is defined as the fraction of the total optical depth due to fine aerosol.

$$\tau(\lambda_1)^t = \frac{\tau(\lambda_1)^f}{\tau(_1)^t}\tau(\lambda_1)^t + \frac{\tau(\lambda_1)^c}{\tau(\lambda_1)^t}\tau(\lambda_1)^t = \phi_f\tau(\lambda_1)^t + (1-\phi_f)\tau(\lambda_1)^t \tag{4.19}$$

Using Equation 4.19, Equation 4.18 is then rewritten as a function of ϕ_f(Equation 4.20).

$$\tau(\lambda_1)^t\left(\frac{\lambda_1}{\lambda_2}\right)^{\alpha_t} = \phi_f\tau(\lambda_1)^t\left(\frac{\lambda_1}{\lambda_2}\right)^{\alpha_f} + (1-\phi_f)\tau(\lambda_1)^t\left(\frac{\lambda_1}{\lambda_2}\right)^{\alpha_c} \tag{4.20}$$

The fraction of the AOD due to fine aerosol (ϕ_f) is then solved (Equation 4.21).

$$\phi_f = \frac{\left(\frac{\lambda_1}{\lambda_2}\right)^{\alpha_t} - \left(\frac{\lambda_1}{\lambda_2}\right)^{\alpha_c}}{\left(\frac{\lambda_1}{\lambda_2}\right)^{\alpha_f} - \left(\frac{\lambda_1}{\lambda_2}\right)^{\alpha_c}} \tag{4.21}$$

This equation expresses the dependence of the fine aerosol contribution on the angstrom exponent. Since the assimilation does not adjust the mean size or composition of the aerosol, the fine and coarse angstrom exponents will not change through the analysis phase. Therefore, the one variable changing is the total angstrom exponent (α_t). As a result, the prior (background) and posterior (adjusted) fine aerosol contributions can be expressed using the prior and posterior total angstrom exponents where ϕ_f is the prior fine aerosol contribution and ϕ'_f is the posterior contribution (Equation 4.22 and 4.23).

$$\phi_f = \frac{\left(\frac{\lambda_1}{\lambda_2}\right)^{\alpha_{t,PRIOR}} - \left(\frac{\lambda_1}{\lambda_2}\right)^{\alpha_c}}{\left(\frac{\lambda_1}{\lambda_2}\right)^{\alpha_f} - \left(\frac{\lambda_1}{\lambda_2}\right)^{\alpha_c}} \tag{4.22}$$

$$\phi'_f = \frac{\left(\frac{\lambda_1}{\lambda_2}\right)^{\alpha_{t,POST}} - \left(\frac{\lambda_1}{\lambda_2}\right)^{\alpha_c}}{\left(\frac{\lambda_1}{\lambda_2}\right)^{\alpha_f} - \left(\frac{\lambda_1}{\lambda_2}\right)^{\alpha_c}} \tag{4.23}$$

The next step is to consider the relationship between optical depth and the amount of aerosol in the atmosphere. The optical depth can be written as an extinction cross section ($\sigma(\lambda)^t$, units = area per mass or area per number) times the aerosol mass or number (M^t, units = mass per area or number per area) as shown in Equation 4.24. The same equation can be written for the fine and coarse aerosol optical depths (Equations 4.25 and 4.26).

$$\tau(\lambda)^t = \sigma(\lambda)^t M^t \tag{4.24}$$

$$\tau(\lambda)^f = \sigma(\lambda)^f M^f = \phi_f \tau(\lambda)^t \tag{4.25}$$

$$\tau(\lambda)^c = \sigma(\lambda)^c M^c = (1-\phi_f)\tau(\lambda)^t \tag{4.26}$$

The total aerosol (mass or number) can be expressed as the sum of the amount of fine and coarse aerosol using Equations 4.24 through 4.26 (Equation 4.27).

$$M_t = \frac{\tau(\lambda)^t}{\sigma(\lambda)^t} = \frac{\phi_f \tau(\lambda)^t}{\sigma(\lambda)^f} + \frac{(1-\phi_f)\tau(\lambda)^t}{\sigma(\lambda)^c} = \frac{\phi_f \tau(\lambda)^t \sigma(\lambda)^c + (1-\phi_c)\tau(\lambda)^t \sigma(\lambda)^f}{\sigma(\lambda)^f \sigma(\lambda)^c} \tag{4.27}$$

By taking the ratio of the posterior and prior aerosol amount (Equation 4.28), the posterior can be rewritten as the prior amount times a scaling factor (F^t) (Equation 4.29).

$$\frac{M_{t,POST}}{M_{t,PRIOR}} = \frac{\tau(\lambda)^{t,POST}}{\tau(\lambda)^{t,PRIOR}} \frac{\phi'_f \sigma(\lambda)^c + (1-\phi'_f)\sigma(\lambda)^f}{\phi_f \sigma(\lambda)^c + (1-\phi_f)\sigma(\lambda)^f} \tag{4.28}$$

$$M_{t,POST} = \frac{\tau(\lambda)^{t,POST}}{\tau(\lambda)^{t,PRIOR}} \frac{\phi'_f \sigma(\lambda)^c + (1-\phi'_f)\sigma(\lambda)^f}{\phi_f \sigma(\lambda)^c + (1-\phi_f)\sigma(\lambda)^f} M_{t,PRIOR} = F^t M_{t,PRIOR} \tag{4.29}$$

The same approach is used to express the fine and coarse posterior amounts as a scaling factor times the prior where the scaling factors are a function of optical depth and fine aerosol contribution (Equations 4.30 through 4.35).

$$M^f = \frac{\phi_f \tau(\lambda)^t}{\sigma(\lambda)^f} \tag{4.30}$$

$$\frac{M_{f,POST}}{M_{f,PRIOR}} = \frac{\phi'_f}{\phi_f}\frac{\tau(\lambda)^{t,POST}}{\tau(\lambda)^{t,PRIOR}} \tag{4.31}$$

$$M_{f,POST} = \frac{\phi'_f}{\phi_f}\frac{\tau(\lambda)^{t,POST}}{\tau(\lambda)^{t,PRIOR}}M_{f,PRIOR} = F^f M_{f,PRIOR} \tag{4.32}$$

$$M^c = \frac{(1-\phi_f)\tau(\lambda)^t}{\sigma(\lambda)^c} \tag{4.33}$$

$$\frac{M_{c,POST}}{M_{c,PRIOR}} = \frac{(1-\phi'_f)}{(1-\phi_f)}\frac{\tau(\lambda)^{t,POST}}{\tau(\lambda)^{t,PRIOR}} \tag{4.34}$$

$$M_{c,POST} = \frac{(1-\phi'_f)}{(1-\phi_f)}\frac{\tau(\lambda)^{t,POST}}{\tau(\lambda)^{t,PRIOR}}M_{c,PRIOR} = F^c M_{c,PRIOR} \tag{4.35}$$

Since the total aerosol is the sum of the fine and the coarse, the total amount is expressed using the fine and coarse scalings (Equation 4.36).

$$M_{t,POST} = F^f M_{f,PRIOR} + F^c M_{c,PRIOR} \tag{4.36}$$

In the end, there are two equations for scaling the amount of atmospheric aerosol, a fine aerosol equation (Equation 4.32) and a coarse aerosol equation (Equation 4.35). The fine equation is used to scale the nucleation and accumulation size modes and the coarse equation is used to scale the coarse aerosol size mode. In the assimilation, each ensemble member is scaled using the ensemble specific prior and posterior values.

Observational errors for MODIS Level 3 daily-averaged AOD retrievals are defined using error parameterizations discussed in Section 1.4.1. MODIS Angstrom exponent uncertainties are defined as the standard deviation across the grid box for the Level 3 MODIS retrievals. AERONET angstrom uncertainties ($\epsilon_{Ang,AER}$) are defined using the uncertainties in AERONET AOD retrievals (Equation 4.37).

$$\epsilon_{Ang,AER} = max\left(\alpha_{AER} \pm \left(ln\left(\frac{\tau(440nm) \pm \epsilon_{AOD,AERONET}(440nm)}{\tau(870nm) \pm \epsilon_{AOD,AERONET}(870nm)}\right)\right)/ln\left(\frac{870}{440}\right)\right) \tag{4.37}$$

The ensemble initial conditions were generated by adding random Gaussian noise to the initial fields [83]. Additionally, since CAM is driven by NCEP meteorology, Gaussian perturbations were applied to model temperature fields to maintain ensemble spread. The temperature perturbation was carefully selected by running the ensembles at various perturbation values. The selection criterion was the highest perturbation within the uncertainty of the NCEP temperature fields that produced a normally distributed spread in the aerosol fields. At perturbations above this criterion, high levels of atmospheric instability resulted in increased aerosol deposition and a skewed distribution. The selected perturbation was 0.1 percent. Additionally, a ten percent inflation of the ensemble posterior values was applied during the analysis phase to maintain ensemble spread. The selected cutoff distance for the covariance localization is 500 km. The 60-ensemble assimilation was run for the year 2007, the same time period as the control run.

4.2.1 Analysis Phase Adjustment

The first step in examining the assimilation results is to look at the adjustments made in the analysis phase for the amount and size assimilation (AOD/ANG). This is done to determine whether the EnKF is behaving as expected, as well as an important way of understanding the assimilation run results. From the initial comparison of the CAM control simulation and MODIS observations (Figures 2.18), a clear negative bias was seen in AOD predictions. Based on this comparison, the expectation of the EnKF is to increase AOD. This is confirmed in the seasonally averaged adjustments made to CAM AOD in the analysis phase where the adjustments are mostly positive (Figure 4.1). The average ratio of the posterior (adjusted) to prior AOD for the full year run is 1.016 ± 0.0326, indicating an average increase in AOD on the order of a percent. With respect to the angstrom exponent, comparison with MODIS revealed some negative and some positive bias regions. The expectation is that the EnKF increases the angstrom values in negative bias regions and decreases in positive bias regions. With respect to the angstrom exponent, increases are observed in regions where the model predicted low (Figure 4.2). A good example is the clear positive signal off the west coast of South America. Additionally, a decrease is observed in the Southern Hemisphere around 60°S, a region associated with sea salt aerosol in which the model was predicting high angstrom values relative to MODIS. The average ratio of the posterior to prior angstrom exponent for the full year run is 0.988 ± 0.027, indicating an average decrease in angstrom on the order of a percent. This translates to a posterior to prior ratio of AOD fine fraction of 0.992 ± 0.0171, using Equation 4.21. However, the scaling on the aerosol number and mass concentration depends on a combination of the AOD and fine fraction adjustments. Seasonally average fine and coarse scale factors (F^f, F^c) are shown in Figures 4.4 and 4.5. Values greater than one indicate an increase in aerosol while values less than one indicate a decrease.

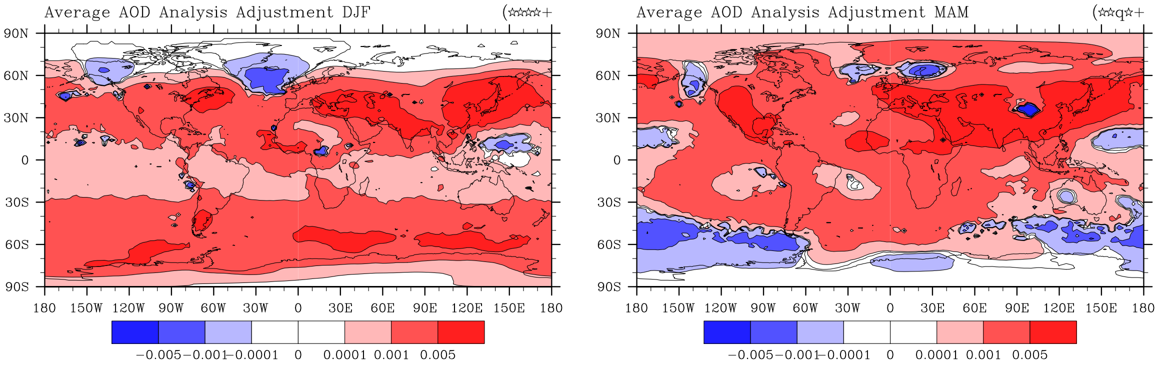

(a) December-January-February (b) March-April-May

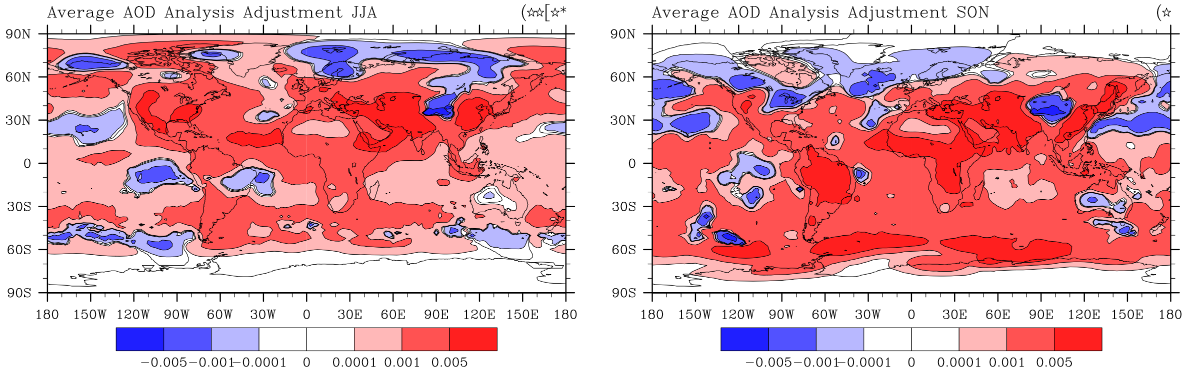

(c) June-July-August (d) September-October-November

Figure 4.1: Seasonally averaged adjustments (Posterior minus Prior) to AOD during the analysis phase in which the EnKF is applied. Positive regions indicate an increase in AOD and negative regions indicate a decrease.

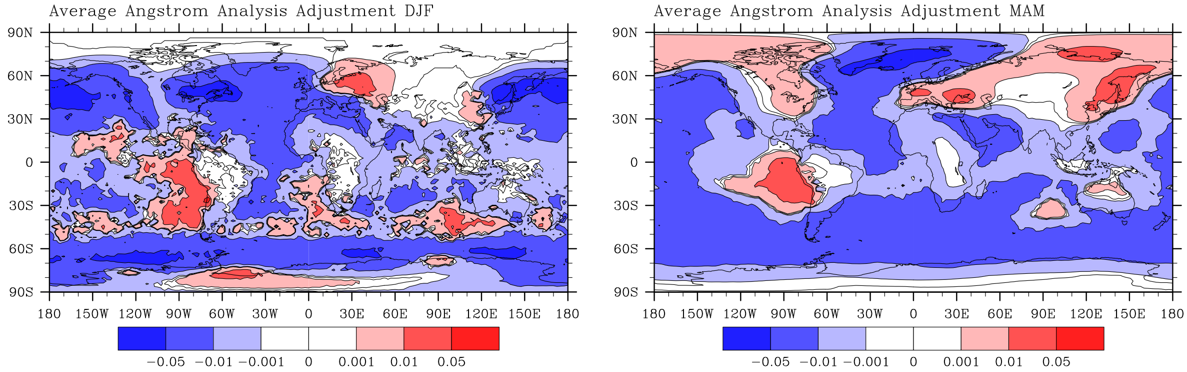

(a) December-January-February (b) March-April-May

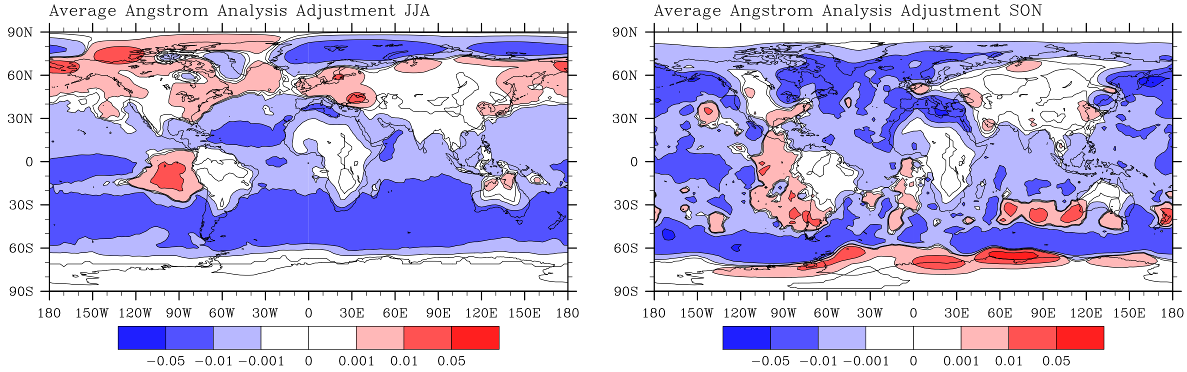

(c) June-July-August (d) September-October-November

Figure 4.2: Seasonally averaged adjustments (Posterior minus Prior) to angstrom exponents during the analysis phase in which the EnKF is applied. Positive regions indicate an increase in angstrom exponent and negative regions indicate a decrease.

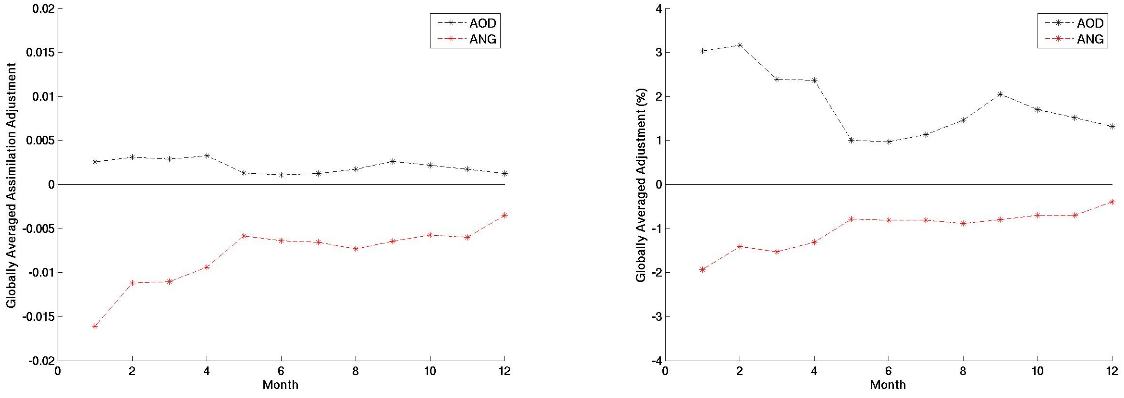

(a) (b)

Figure 4.3: Timeseries of globally averaged EnKF a) absolute and b) percent adjustments in AOD and angstrom exponent.

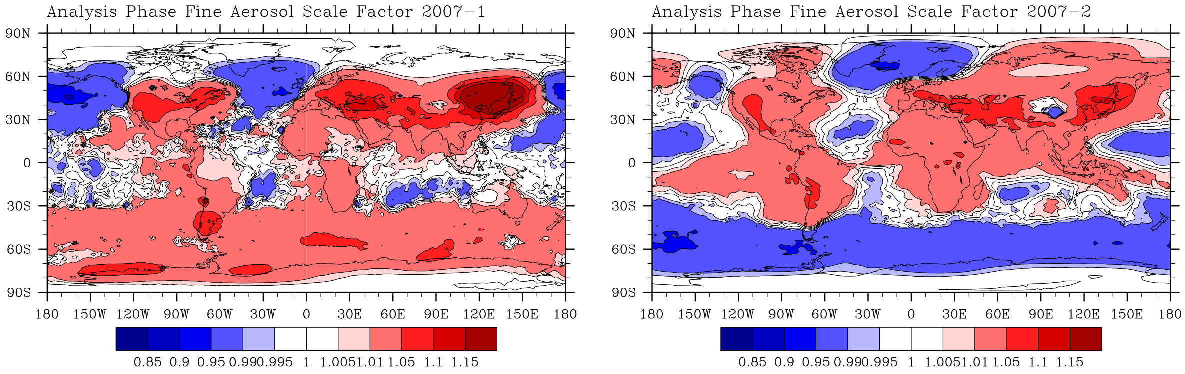

(a) December-January-February (b) March-April-May

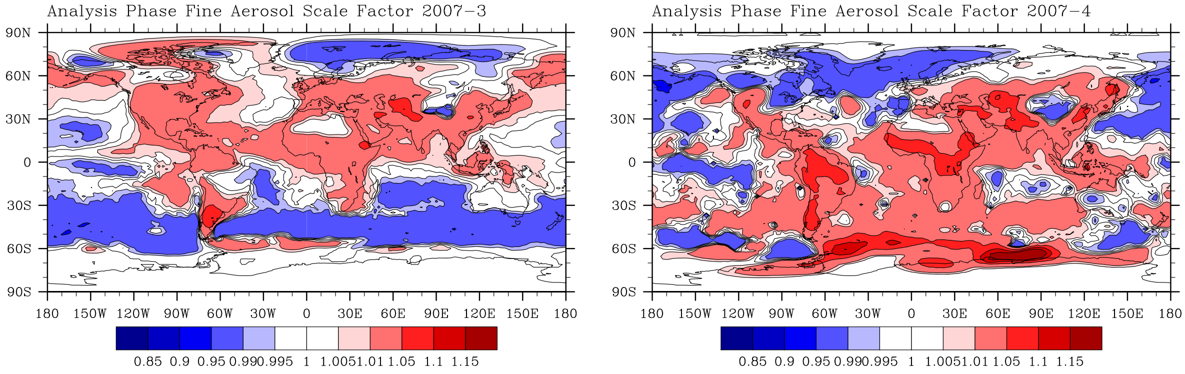

(c) June-July-August (d) September-October-November

Figure 4.4: Seasonally averaged fine aerosol scale factor (F^f). Red areas indicate an increase in fine aerosol while blue areas indicate a decrease.

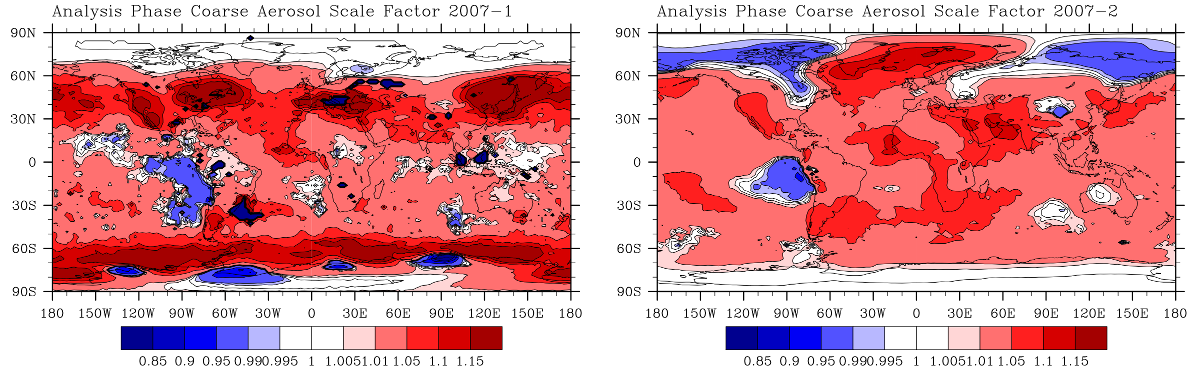

(a) December-January-February (b) March-April-May

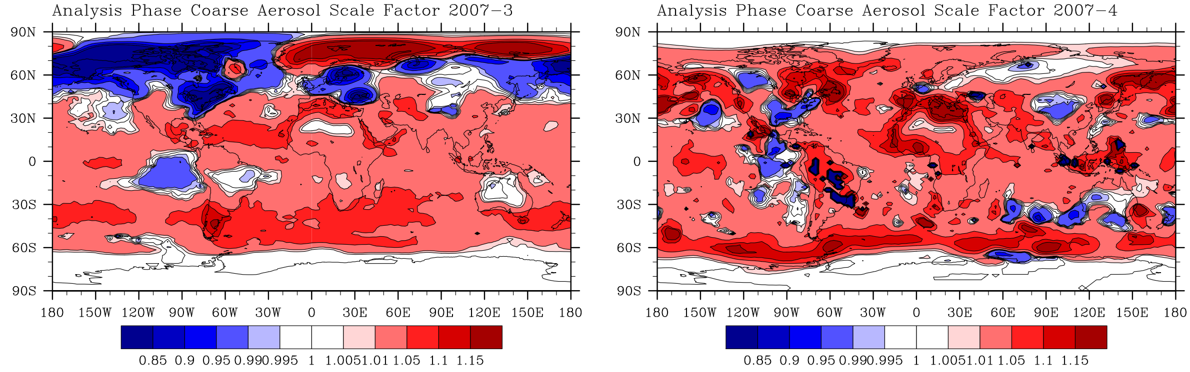

(c) June-July-August (d) September-October-November

Figure 4.5: Seasonally averaged coarse aerosol scale factor (F^c). Red areas indicate an increase in fine aerosol while blue areas indicate a decrease.

4.2.2 Model + Assimilation Results

The overall model results are a combination of the adjustments made in the analysis phase and the model's evolution of the adjusted aerosol. Average AOD for the full 2007 run as well as seasonal averages are shown in Figures 4.6 and 4.7. A comparison with the control run simulation indicates higher AOD values in almost all locations with exceptions occurring in the tropics, especially over the Sahara (Figure 4.8). A clear seasonality is observed in the assimilation results with the lowest optical depths occurring in the winter months and highest in the spring through summer. Additionally, differences are seen between the northern and southern hemispheres. Due to higher emission rates of anthropogenic aerosols in the northern hemisphere (Figures 2.2 through 2.4), higher AOD values are expected. This is unlike the control simulation, which showed little variation in aerosol related fields throughout the year and little difference between AOD in the northern and southern hemispheres. The average ensemble-generated uncertainties in predicted AOD for the full model run are presented in Figure 4.9, including both absolute and percent uncertainty. The ensemble spread reveals larger uncertainties in high latitude regions on the order of $0.01(\sim 20\%)$ compared to the mid-latitude regions with uncertainties ranging from 0.001 to $0.01(<10\%)$. The globally averaged AOD uncertainty for the assimilation is 8.7%. Using t-test analysis (95% confidence), the average AOD predicted by the control and the AOD/ANG assimilation were found to be statistically different.

A time series of globally averaged AOD values for MODIS, the CAM control run and the CAM assimilation run are shown in Figure 4.10. Similar to Figure 4.8, the time series shows that the assimilation run AOD is higher than that of the control run. Additionally, the assimilation predictions are closer to the MODIS observations with the AOD distributions overlapping. This shows an improvement over the control run. A comparison with seasonally averaged MODIS observations (Figure 4.11) shows that many of the negative bias regions have decreased. Some positive biases have developed over higher latitude regions and parts of South America and Australia. This may be due to the use of one lengthscale (500km) to determine the spatial influence of observations on state variables. Aerosols with a short lifetime will have a shorter correlation lengthscale whereas long-lived aerosols will have a larger correlation lengthscale. Additionally, as the latitude increases, the size of the grid cell decreases. At a fixed lengthscale, observations can influence state variables several grid cells away at high latitudes. The use of variable lengthscales is an active area of data assimilation research (discussions with J.L. Anderson). However, on average, the optical depth predicted by CAM with the AOD and angstrom assimilation compares better to MODIS than the CAM control simulation. Comparison with AERONET sites show that the average AOD has increased, although still low relative to the observations (Figure 4.12). The mean AOD for rural sites was found to be statistically the same via t-test. The AOD time series for select sites show that predictions from CAM with assimilation are in general closer to AERONET observations than the control run (Figure 4.13).

The average angstrom exponents for the full 2007 run as well as seasonal averages are shown in Figure 4.13 and 4.14. Similar to the AOD fields, angstrom exponents show seasonal variation. Hemispheric differences are observed through most of the year with the smallest differences occurring in the winter months. The lowest angstrom exponents occur during the springtime in the southern hemisphere. A comparison to the CAM control run shows higher angstrom exponents in the tropics to mid latitudes region with larger differences over the dusty areas (Sahara/Arabian peninsula/Asia) (Figure 4.15). The assimilation predicts lower angstrom exponents at the higher latitudes than the control run. The average ensemble-generated uncertainties in predicted angstrom exponent for the full model run are presented in Figure 4.17, including both absolute and percent uncertainty. Similar to AOD, the largest uncertainties by percent occur at high latitudes with maximum uncertainties of 35%. The lowest uncertainties occur mostly over land with values as low as 1%. The globally averaged angstrom uncertainty for the assimilation is 6.6% with the average angstrom exponent found to be statistically different from the control run (t-test, 95% confidence). A time series of over ocean averaged angstrom values for MODIS, the CAM control run and the CAM assimilation run are shown in Figure 4.16. The average angstrom values are lower than the control run in the springtime, but increasingly exceed the control run in other months. This is a counterintuitive result given that the EnKF is acting to decrease angstrom exponents over much of the ocean regions. However, an investigation of the fine and coarse scaling factors shows that both fine and coarse aerosol increase over oceans (Figures 4.4 and 4.5). The hypothesis is that while a decrease in angstrom exponent increases atmospheric coarse aerosol more than fine aerosol, coarse aerosol has a short lifetime relative to accumulation mode fine aerosol and may be depositing quickly out of the atmosphere. On the other hand, accumulation mode aerosols are longer lived. Their persistence in the atmosphere combined with daily EnKF adjustments may have resulted in a buildup of fine aerosol, resulting in a gradual increase of angstrom exponent over time. Additionally, the average analysis phase adjustment (decrease) in angstrom exponent decreases over time (Figure 4.3). This will be investigated further in the aerosol lifetime analysis. A comparison with seasonally averaged MODIS observations (Figure 4.18) show that many of the negative bias regions have decreased, however, the positive biases, although less, still exist. Additionally, new positive bias regions have developed in the tropics. This shows that the model is able to maintain increases in angstrom exponent, but not decreases. Again, removal processes and atmospheric lifetime may be the cause of these results. The results in the AOD fine fraction show similar patterns to the angstrom exponent (Figures 4.20 through 4.22). A comparison of the assimilation run and AERONET AOD fine fraction show improvements in polluted marine and dirty pollution sites (Figure 4.12). A table summarizing the averaged results for AOD, angstrom exponent and AOD fine fraction for the MODIS observations, control run and AOD and angstrom assimilation run are shown in Table 4.1.

The composition of the predicted aerosol in the assimilation run is examined on a mass basis. Percent of the total aerosol mass is shown for the six aerosol types in Figure 4.23. As mentioned previously, mass tends to be weighted towards coarse aerosol. Sea salt and dust still make up a large portion of the aerosol mass, however, comparing the assimilation run to the control run (Figure 4.24) larger differences are seen in these two aerosol types. The contribution of dust has a large decrease in the assimilation run. These decreases are compensated by increases in sea salt, sulfate and secondary and primary organic aerosol. The regions of dust decrease have an increase in fine aerosol composition (Figure 4.8), explaining the increase in importance of sulfate and organics. Large decreases are seen in sulfate and secondary organics in the southern hemisphere high latitudes. This region had increases in coarse aerosol contribution (Figure 4.8), explaining the decrease in these fine aerosol components. The decrease in sulfate and organics is compensated by sea salt increases. A comparison of dust surface fluxes between the assimilation and control run show a decrease in dust emissions, explaining the decrease in coarse aerosol over know dusty regions and the decrease of importance of dust aerosol (Figure 4.25). This may have been caused by unforeseen issues with perturbing model temperature fields and should be considered in future assimilation efforts.

Average aerosol compositions are shown for all aerosol combined (Figure 4.26), fine aerosol and coarse aerosol (Figure 4.27). Global averages are presented as well as averages over land and ocean. The total global aerosol composition is mostly sea salt, dust and sulfate, with sea salt being more important over oceans and dust over land. The sulfate contribution is the same over land and ocean. However, compared to the control run, dust makes up a smaller percent of the aerosol mass. This is expected given the decrease in dust emissions. Sulfate is of particular importance for fine aerosol, although all six aerosol types show up in the fine mode. Again, a biogenic component is present in the fine aerosol.

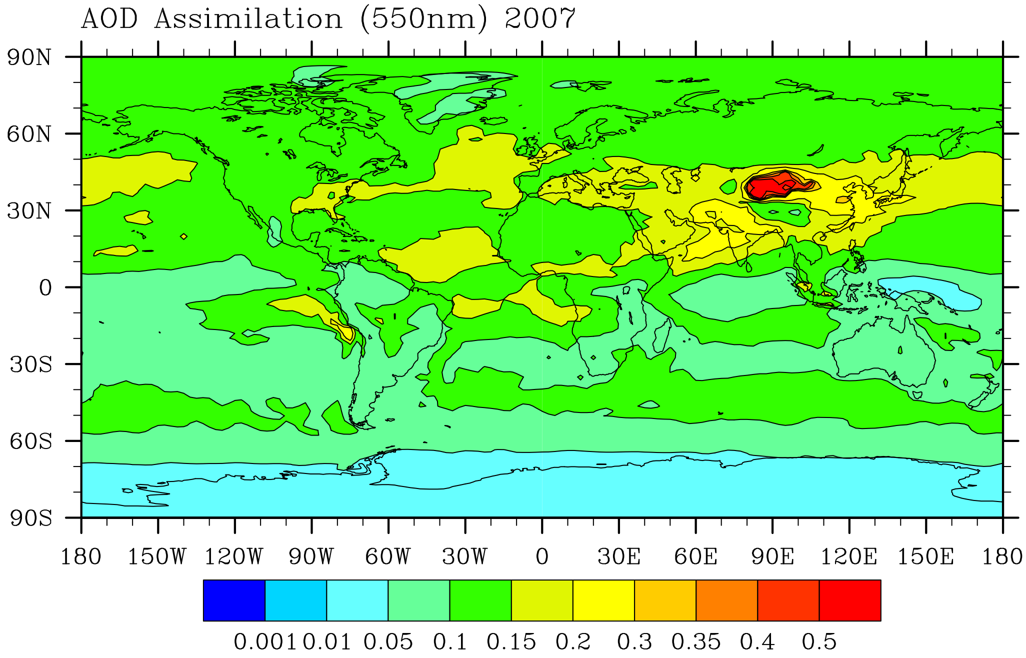

Figure 4.6: Average aerosol optical depth at 550nm for the 2007 CAM with AOD and angstrom assimilation run.

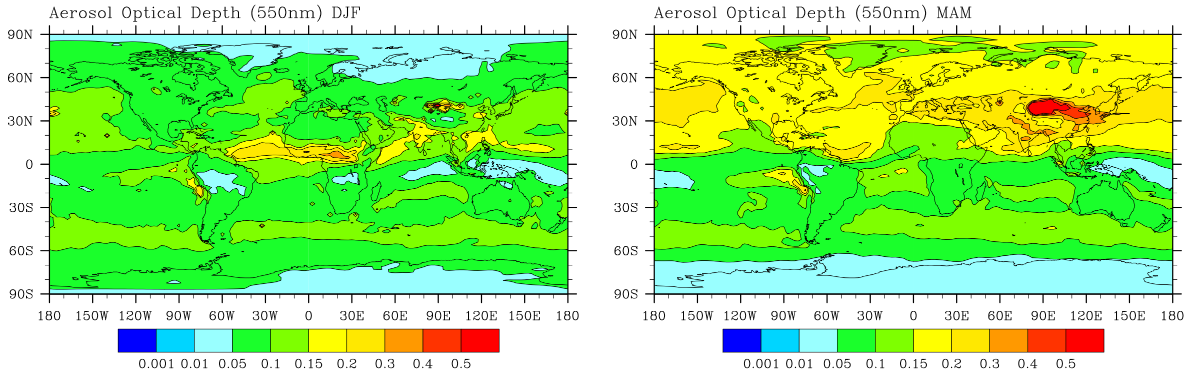

(a) December-January-February

(b) March-April-May

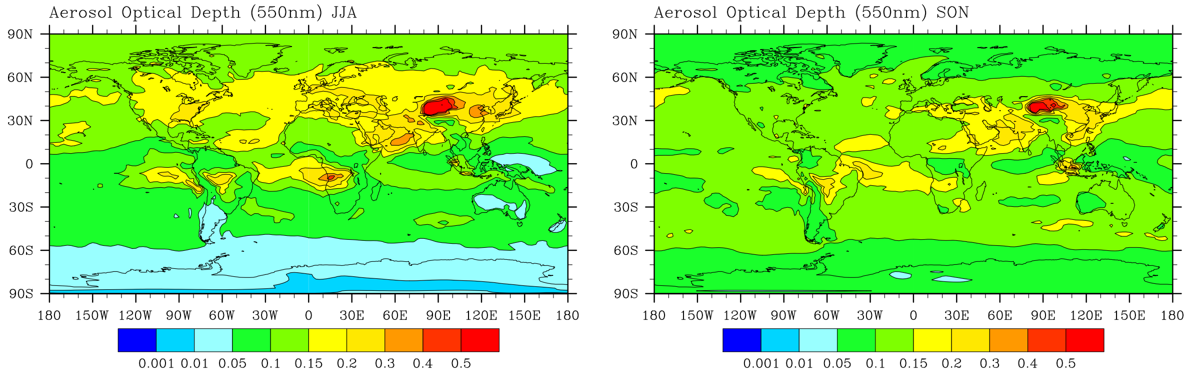

(c) June-July-August

(d) September-October-November

Figure 4.7: Seasonally averaged aerosol optical depth at 550nm for the 2007 CAM with AOD and angstrom assimilation run. AOD values are averaged for a) December/January/February b) March/April/May c) June/July/August and d) September/October/November.

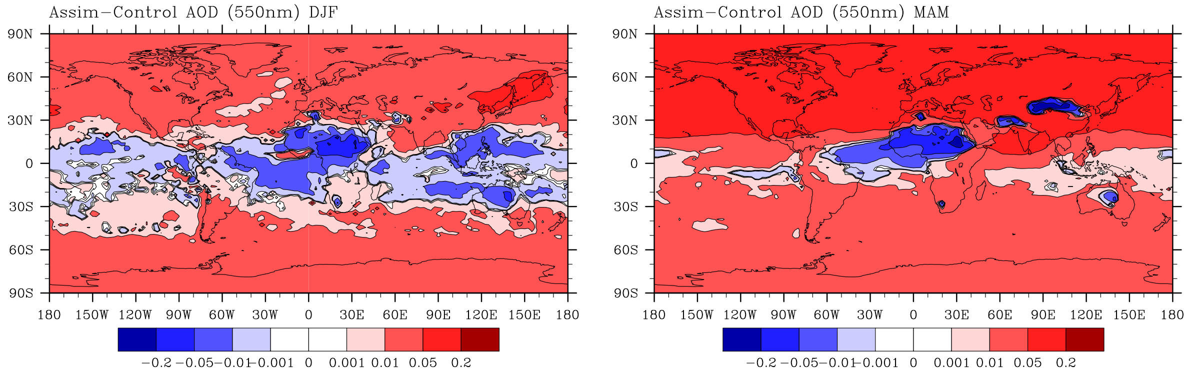

(a) December-January-February (b) March-April-May

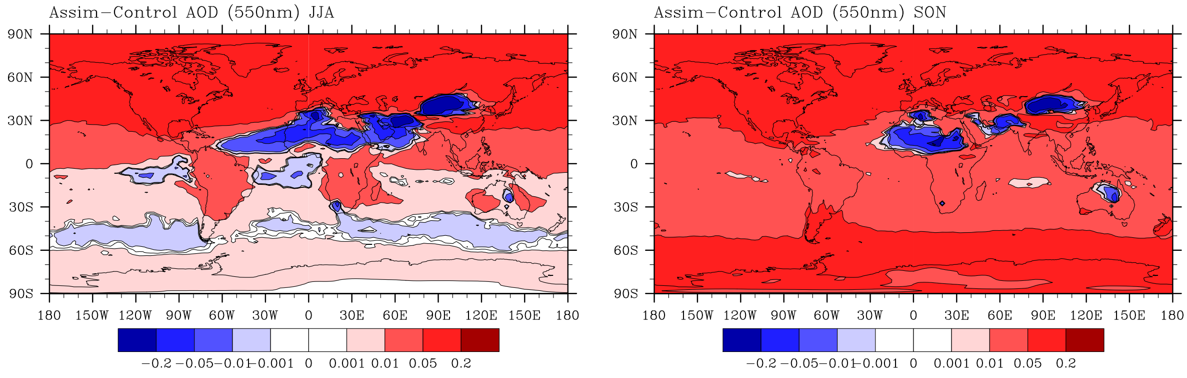

(c) June-July-August (d) September-October-November

Figure 4.8: Seasonally averaged differences in aerosol optical depth at 550nm between the CAM with AOD and angstrom assimilation run and the CAM control run. AOD differences are averaged for a) December/January/February b) March/April/May c) June/July/August and d) September/October/November.

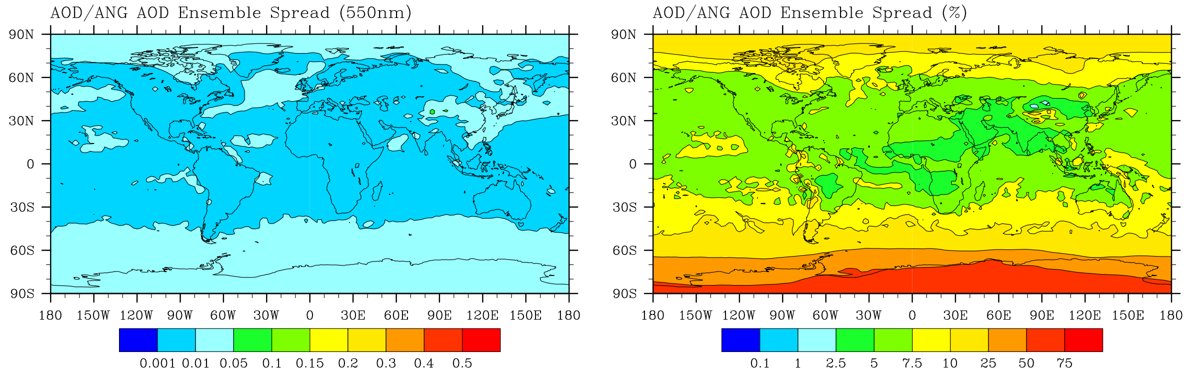

(a) Absolute (b) Percent

Figure 4.9: Average uncertainty in aerosol optical depth at 550nm (absolute and percent) for the 2007 CAM with AOD and angstrom assimilation run.

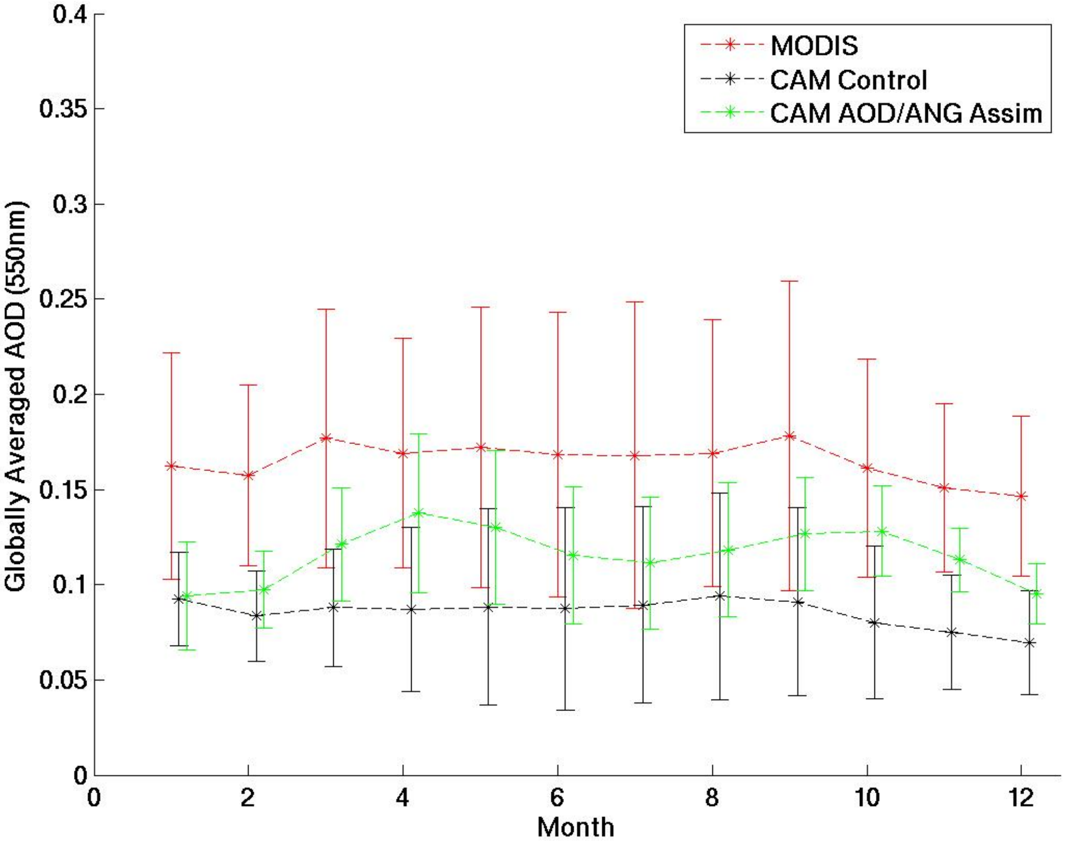

Figure 4.10: Globally averaged aerosol optical depth timeseries for MODIS (red), the CAM control run (black), and the CAM AOD/Angstrom assimilation run (green).

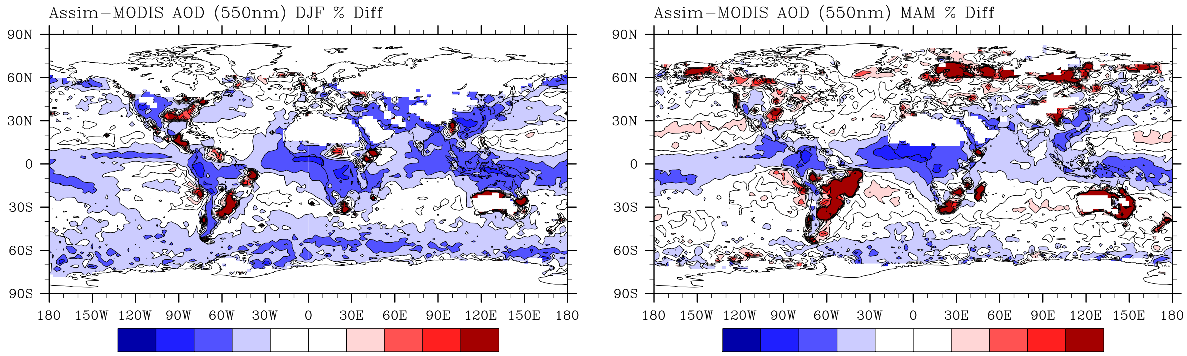

(a) December-January-February (b) March-April-May

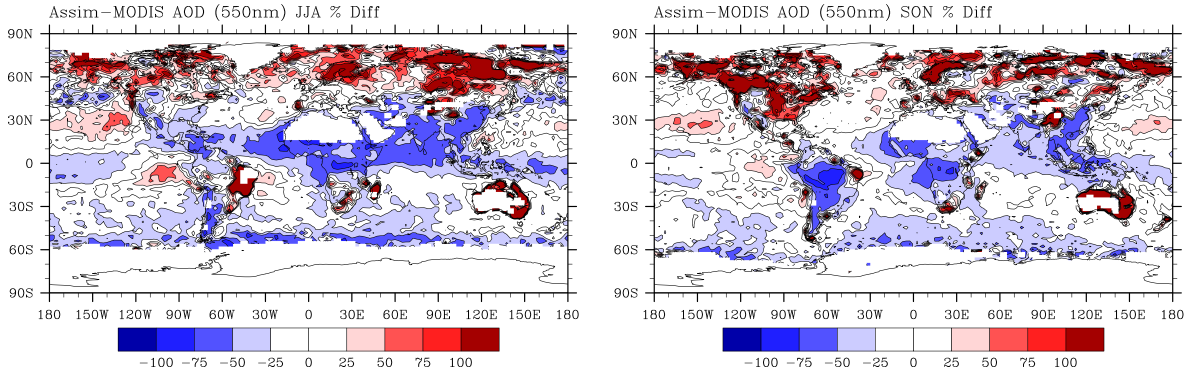

(c) June-July-August (d) September-October-November

Figure 4.11: Seasonally averaged comparison between the CAM AOD and angstrom assimilation run and MODIS aerosol optical depth observations. Results are shown as a percent different (cammodis) for a) December/January/February b) March/April/May c) June/July/August and d) September/October/November.

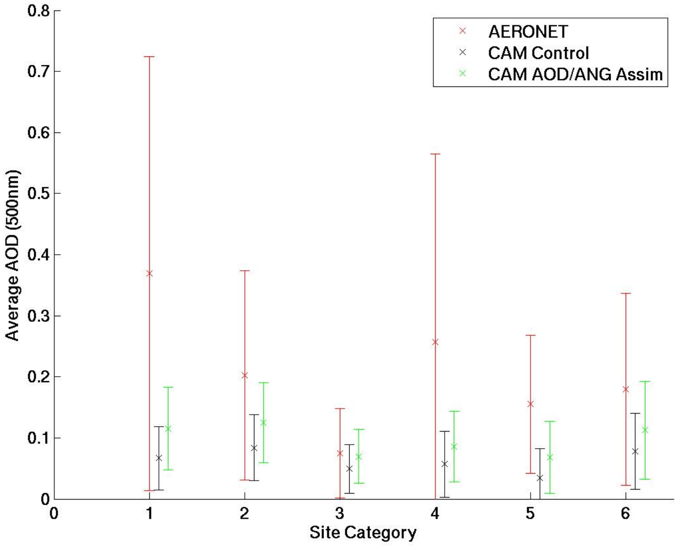

(a) Aerosol Optical Depth

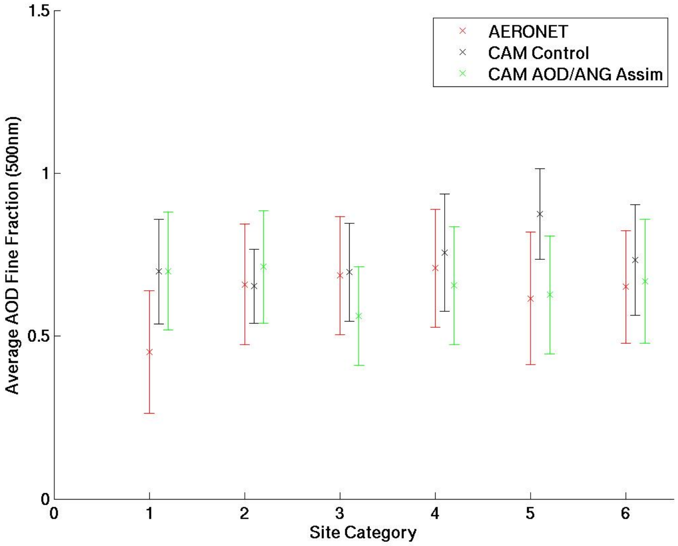

(b) Aerosol Optical Depth Fine Fraction

Figure 4.12: Comparison (mean ± standard deviation) between CAM with AOD and angstrom assimilation, CAM control and AERONET aerosol optical depth (a) and the fraction of aerosol optical depth due to fine aerosol (b). Comparisons are made by site category (1=desert dust, 2=biomass burning, 3=rural, 4=industrial pollution, 5=polluted marine, 6=dirty pollution).

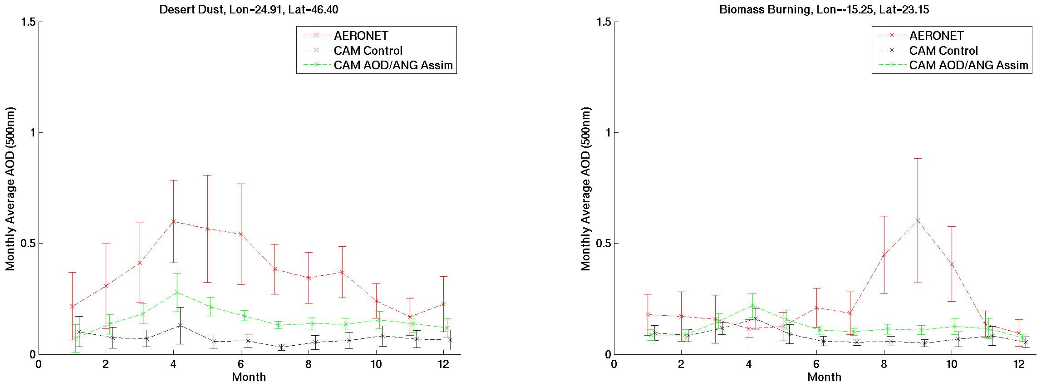

(a) desert dust (b) biomass burning

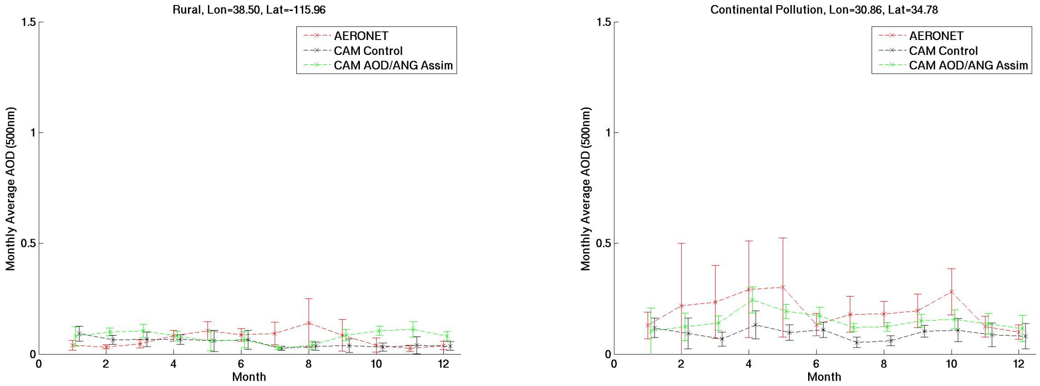

(c) rural (d) industrial pollution

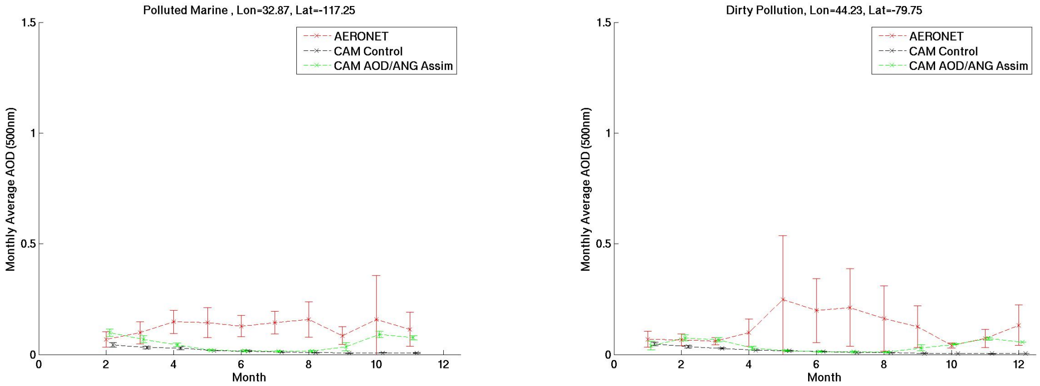

(e) polluted marine (f) dirty pollution

Figure 4.13: Aerosol optical depth monthly-averaged timeseries comparisons between the CAM Control, CAM AOD and angstrom assimilation and AERONET. Results are shown for select AERONET sites from each of the six site categories a)desert dust b) biomass burning c) rural, d) industrial pollution e) polluted marine f) dirty pollution.

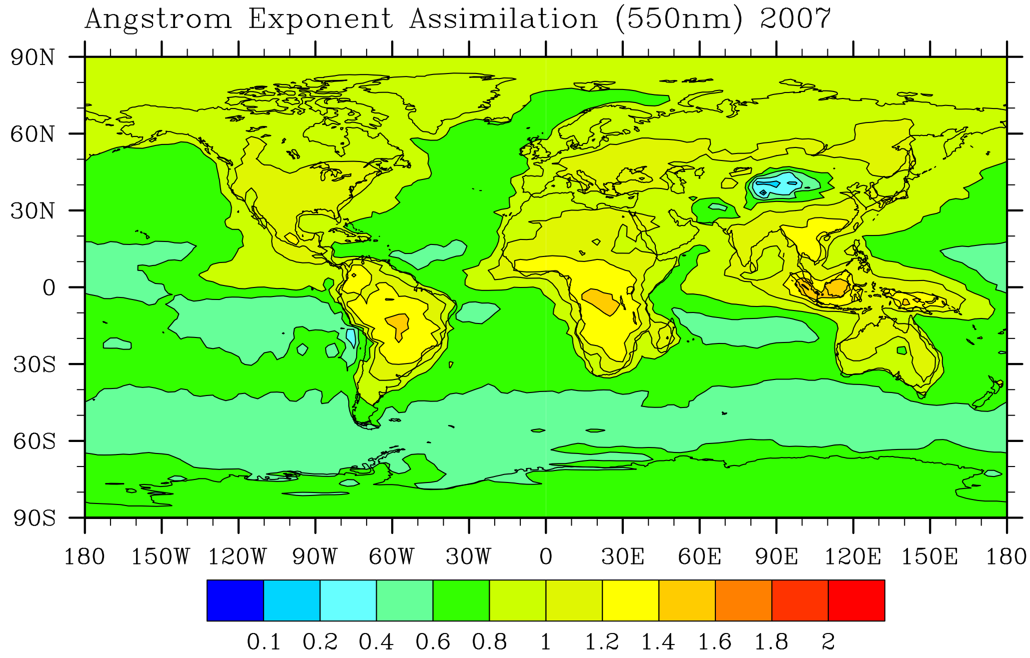

Figure 4.14: Average angstrom exponent (550-865nm) for the 2007 CAM with AOD and angstrom assimilation run.

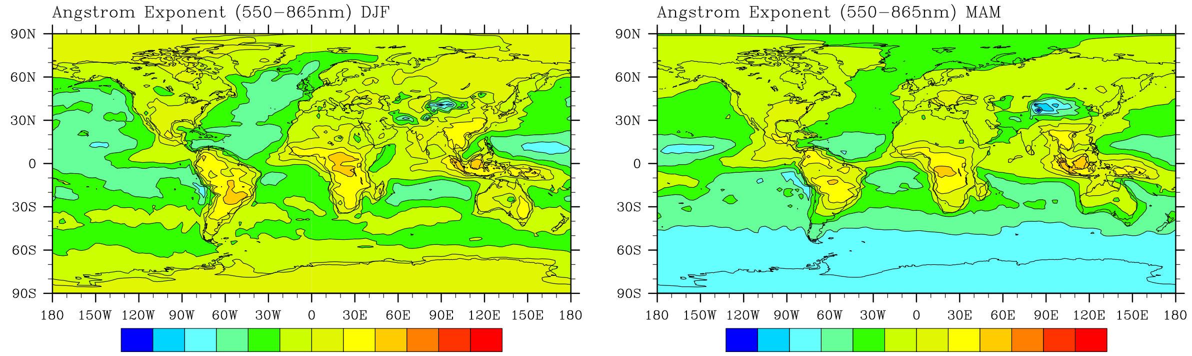

(a) December-January-February (b) March-April-May

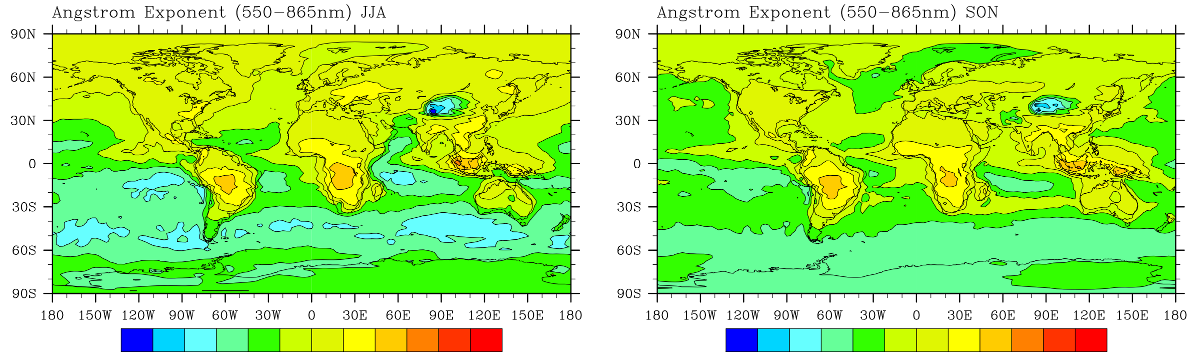

(c) June-July-August (d) September-October-November

Figure 4.15: Seasonally averaged angstrom exponent (550-865nm) for the 2007 CAM with AOD and angstrom assimilation run. Angstrom values are averaged for a) December/January/February b) March/April/May c) June/July/August and d) September/October/November.

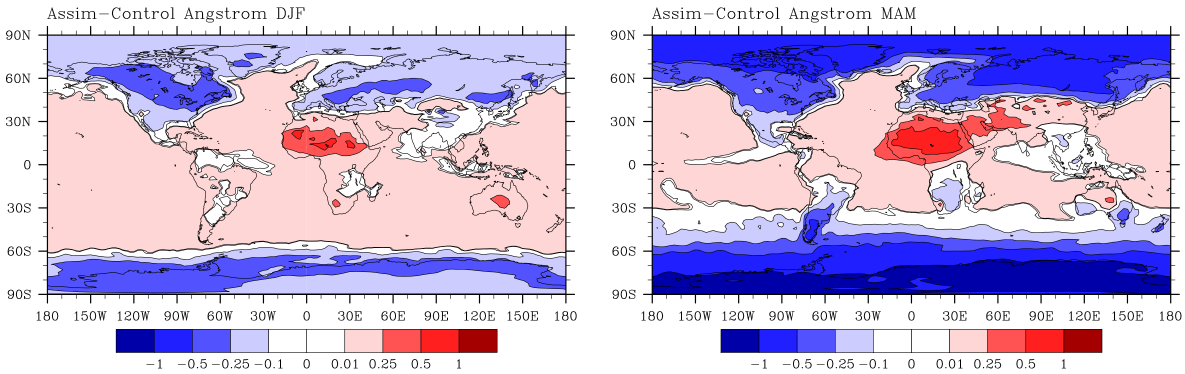

(a) December-January-February (b) March-April-May

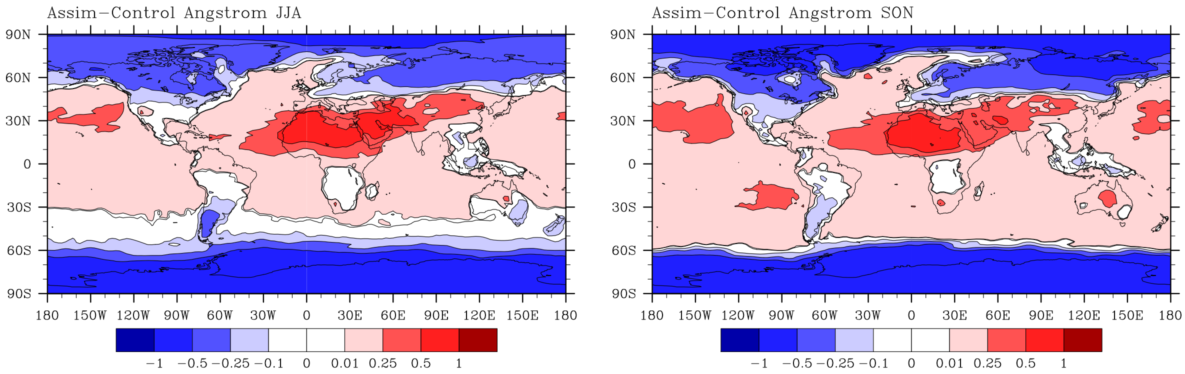

(c) June-July-August (d) September-October-November

Figure 4.16: Seasonally averaged differences in angstrom exponent (550-865nm) between the CAM with AOD and angstrom assimilation run and the CAM control run. Angstrom differences are averaged for a) December/January/February b) March/April/May c) June/July/August and d) September/October/November.

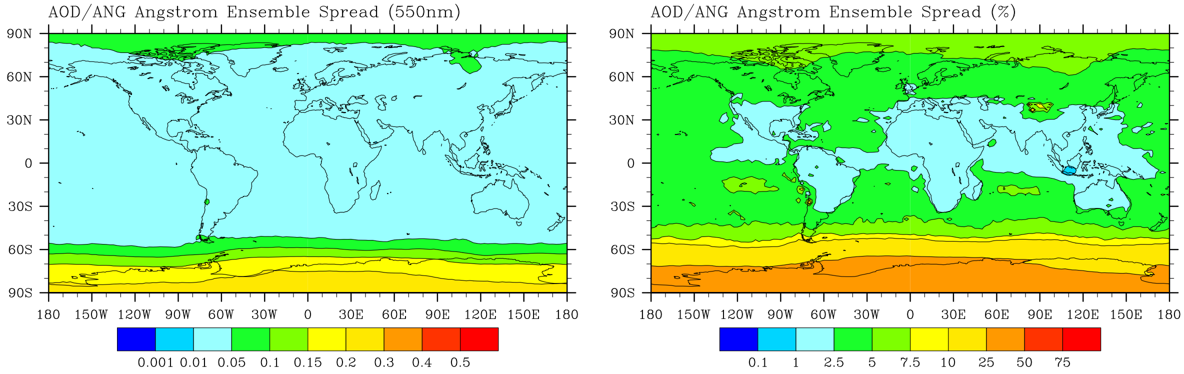

(a) Absolute (b) Percent

Figure 4.17: Average uncertainty in angstrom exponent (absolute and percent) for the 2007 CAM with AOD and angstrom assimilation run.

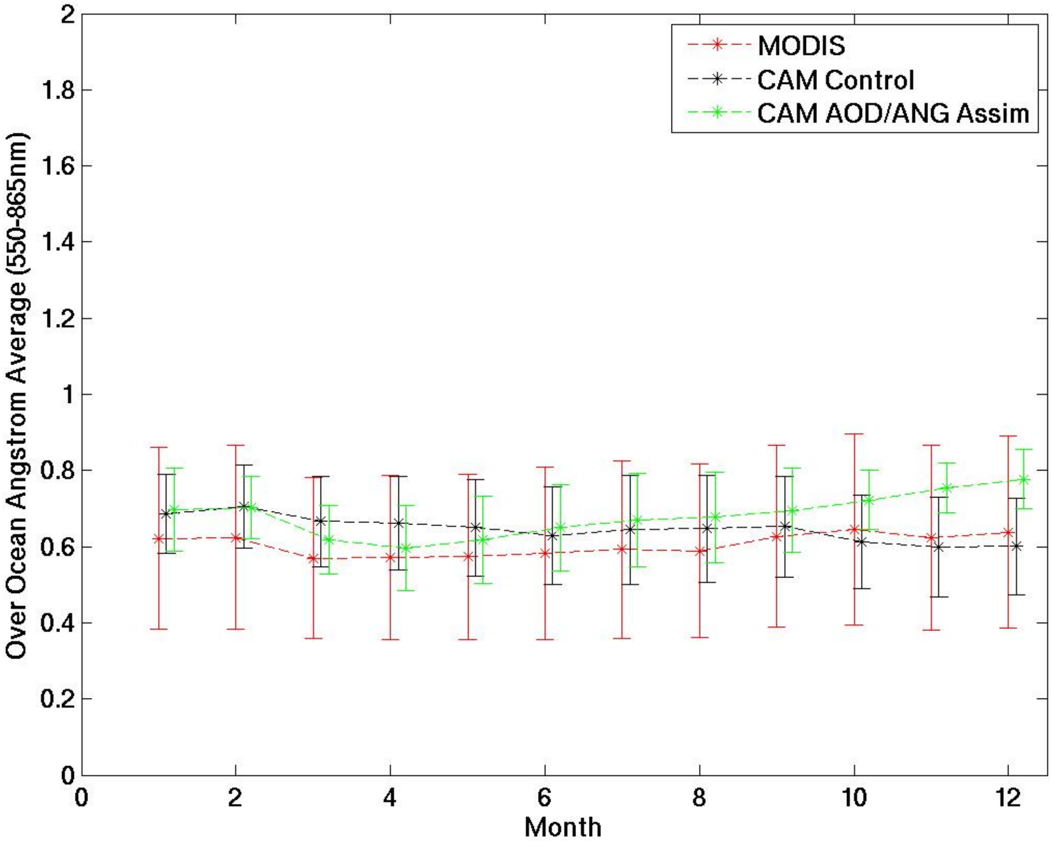

Figure 4.18: Over ocean averaged angstrom exponent timeseries for MODIS (red), the CAM control run (black), and the CAM AOD/Angstrom assimilation run (green).

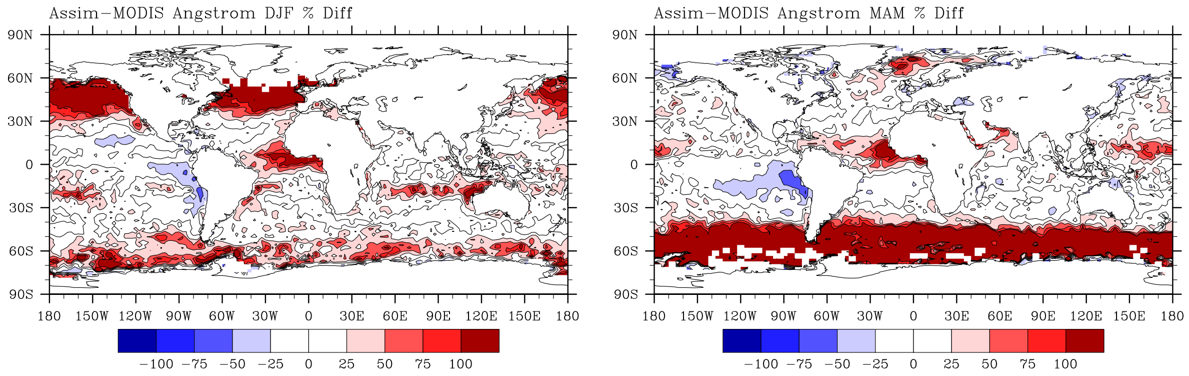

(a) December-January-February (b) March-April-May

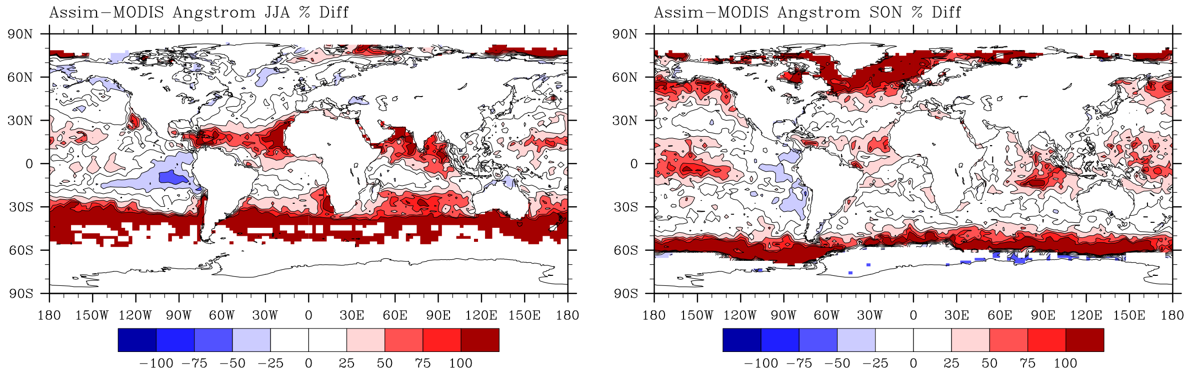

(c) June-July-August (d) September-October-November

Figure 4.19: Seasonally averaged comparison between the CAM AOD and angstrom assimilation run and MODIS angstrom exponent observations. Results are shown as a percent different (cammodis) for a) December/January/February b) March/April/May c) June/July/August and d) September/October/November.

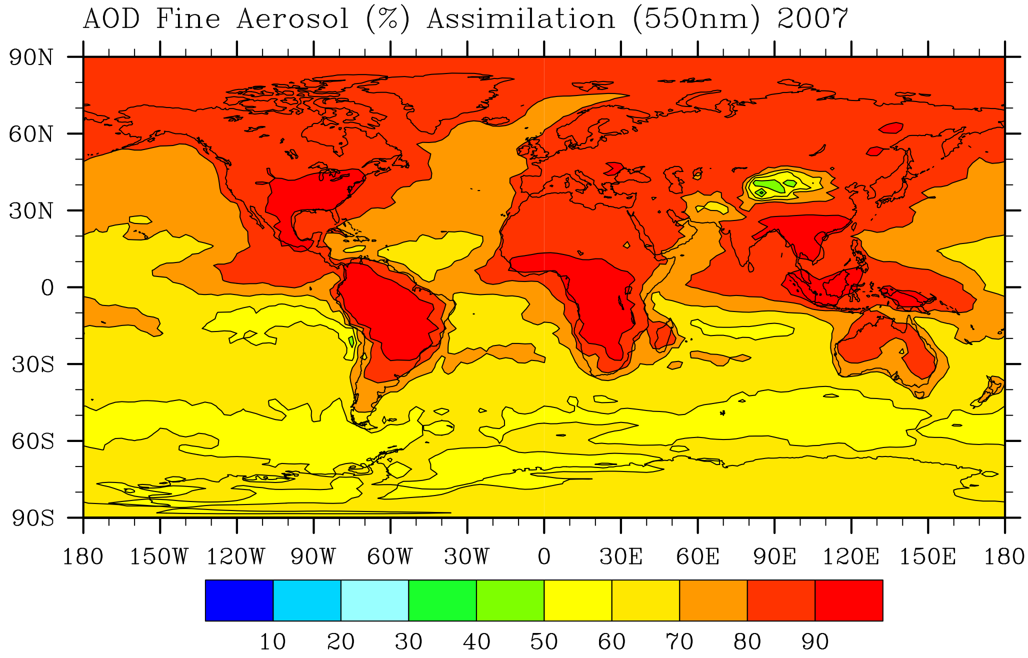

Figure 4.20: Average aerosol optical depth fine fraction at 550nm for the 2007 CAM with AOD and angstrom assimilation run.

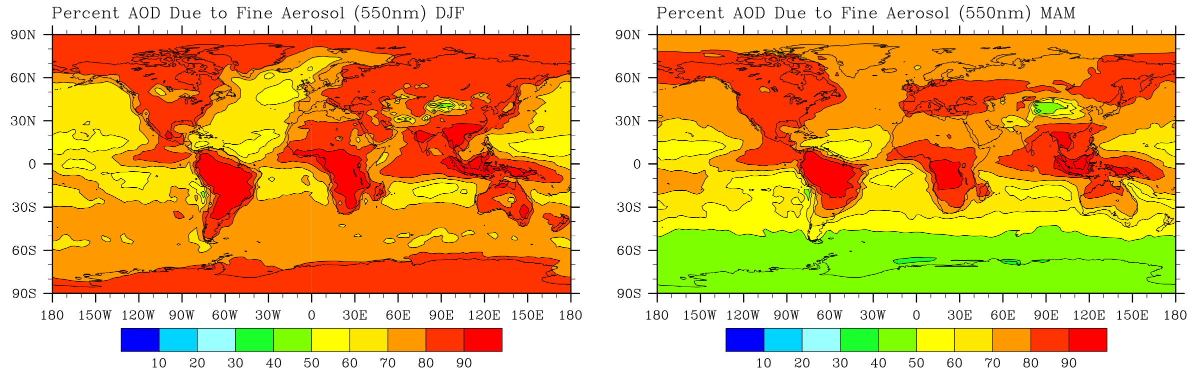

(a) December-January-February (b) March-April-May

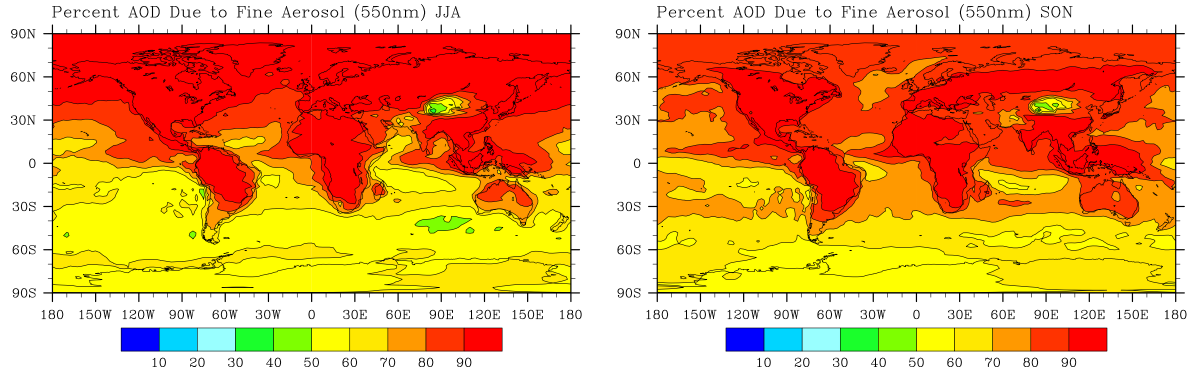

(c) June-July-August (d) September-October-November

Figure 4.21: Seasonally averaged aerosol optical depth fine fraction at 550nm for the 2007 CAM with AOD and angstrom assimilation run. AOD fine contribution values are averaged for December/January/February (upper left), March/April/May (upper right), June/July/August (lower left), and September/October/November (lower right).

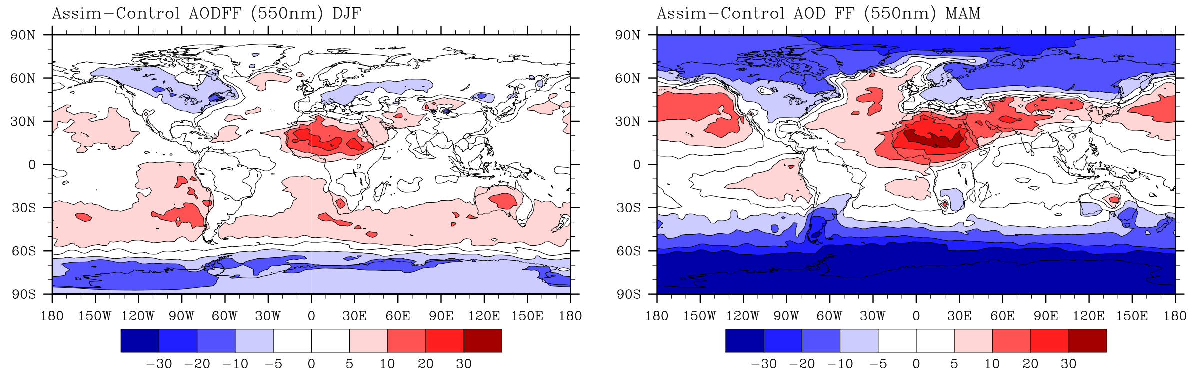

(a) December-January-February

(b) March-April-May

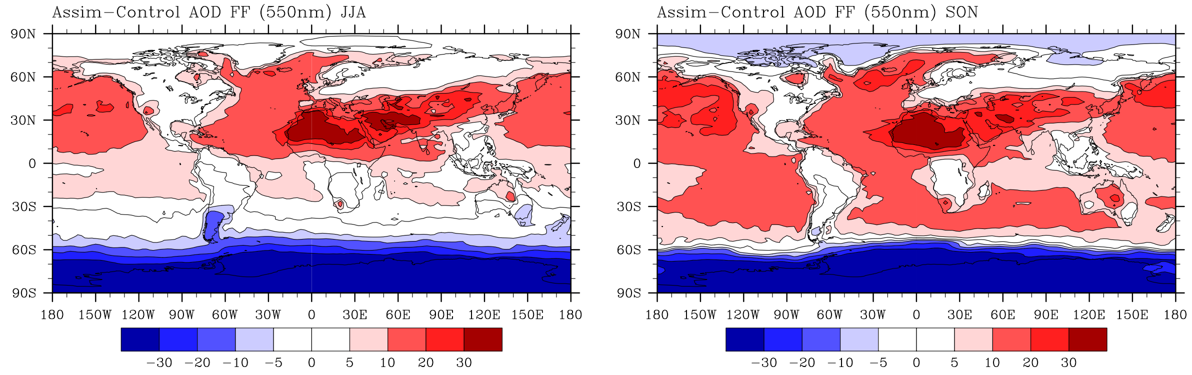

(c) June-July-August

(d) September-October-November

Figure 4.22: Seasonally averaged differences in aerosol optical depth fine contribution at 550nm between the CAM with AOD and angstrom assimilation run and the CAM control run. AOD fine contribution differences are averaged for a) December/January/February b) March/April/May c) June/July/August and d) September/October/November.

Variable	**Season**	**MODIS**	**CAM Control**	**CAM AOD/ANG**
AOD (550nm)	DJF	0.155(±0.01)	0.082(±0.05)	0.092(±0.04)
	MAM	0.168(±0.02)	0.088(±0.07)	0.132(±0.07)
	JJA	0.165(±0.02)	0.090(±0.09)	0.115(±0.07)
	SON	0.16(±0.02)	0.082(±0.07)	0.123(±0.04)
	Year	0.161(±0.09)	0.086(±0.06)	0.115(±0.05)
Angstrom Exponent (550-865nm) (ocean only)	DJF	0.66(±0.09)	0.66(±0.28)	0.72 (±0.18)
	MAM	0.62(±0.13)	0.66(±0.35)	0.60 (±0.21)
	JJA	0.65(±0.19)	0.64(±0.40)	0.67 (±0.25)
	SON	0.67(±0.11)	0.62(±0.38)	0.72 (±0.14)
	Year	0.65(±0.30)	0.65(±0.35)	0.68 (±0.15)
AOD Fine Fraction (550nm) (Land and Ocean)	DJF	0.47(±0.04)	0.73(±0.13)	0.75 (±0.09)
	MAM	0.43(±0.05)	0.73(±0.16)	0.69 (±0.15)
	JJA	0.44(±0.06)	0.72(±0.16)	0.74 (±0.17)
	SON	0.48(±0.05)	0.71(±0.16)	0.75 (±0.13)
	Year	0.45(±0.16)	0.72(±0.15)	0.75 (±0.12)

Table 4.1: Global averages of aerosol optical depth (550nm), angstrom exponent (550-865nm) and the fractional contribution of fine aerosol to optical depth. Averages are shown by season (December-January-February (DJF), March-April-May (MAM), June-July-August (JJA) and September-October-November (SON)) and for the year 2007 (Year).

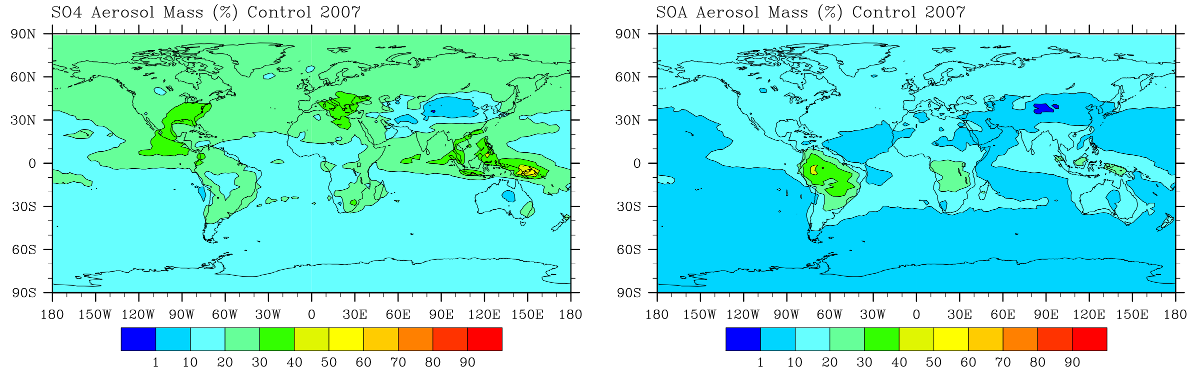

(a) Sulfate (b) Secondary Organic Aerosol

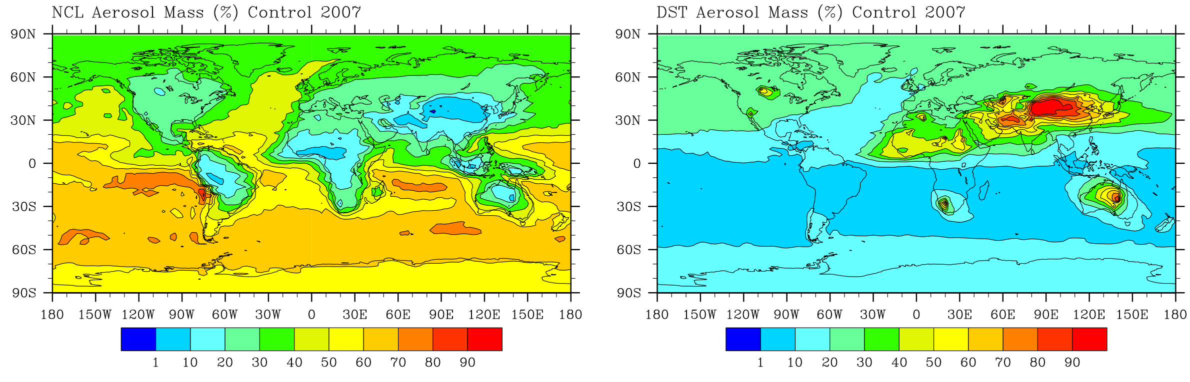

(c) Sea Salt (d) Dust

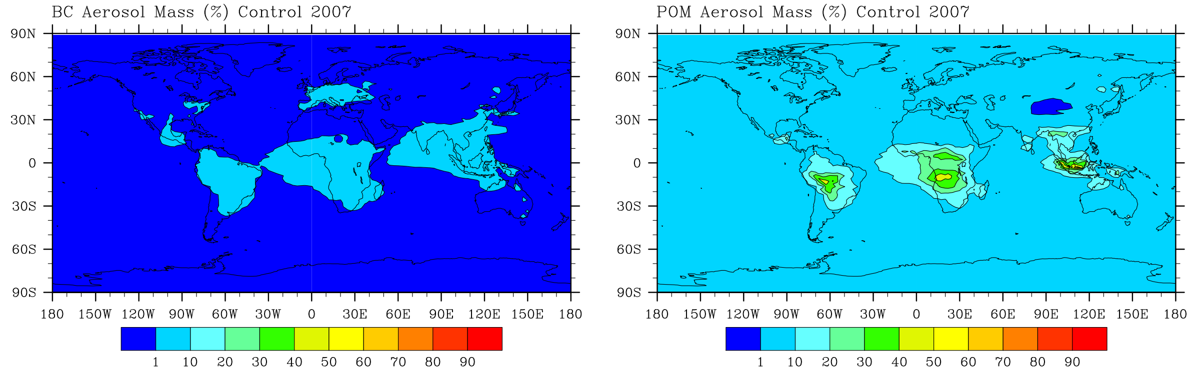

(e) Black Carbon (f) Primary Organic Aerosol

Figure 4.23: Average aerosol mass composition for the 2007 AOD and angstrom assimilation run by percent. Results are shown for a) sulfate (SO4) b) secondary organic aerosol (SOA) c) sea salt (NCL) d) dust (DST) e) black carbon (BC) and f) primary organic aerosol (POM).

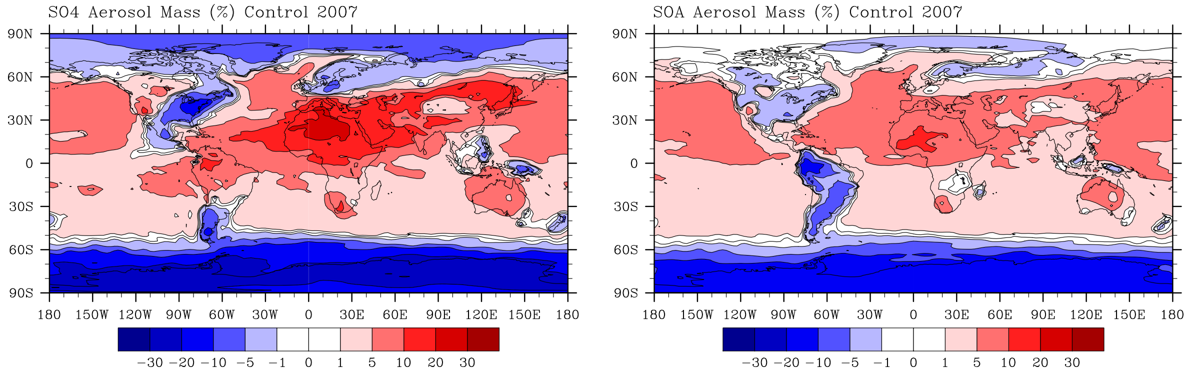

(a) Sulfate (b) Secondary Organic Aerosol

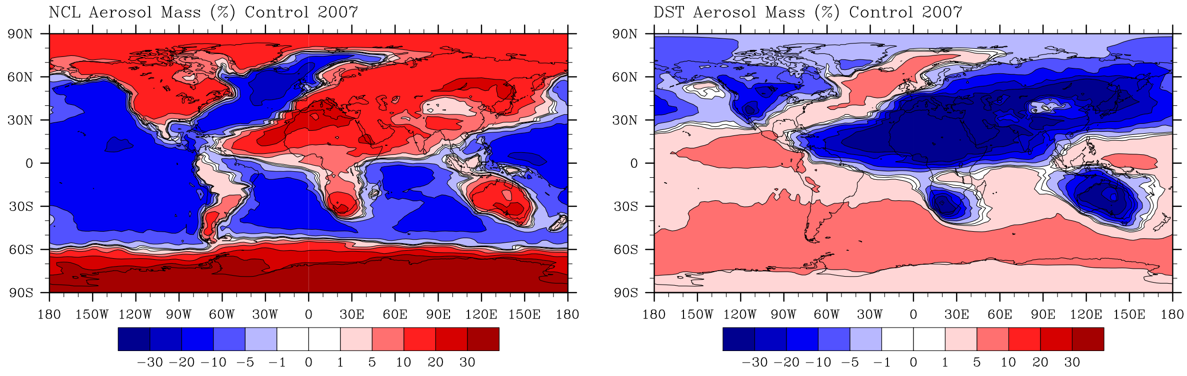

(c) Sea Salt (d) Dust

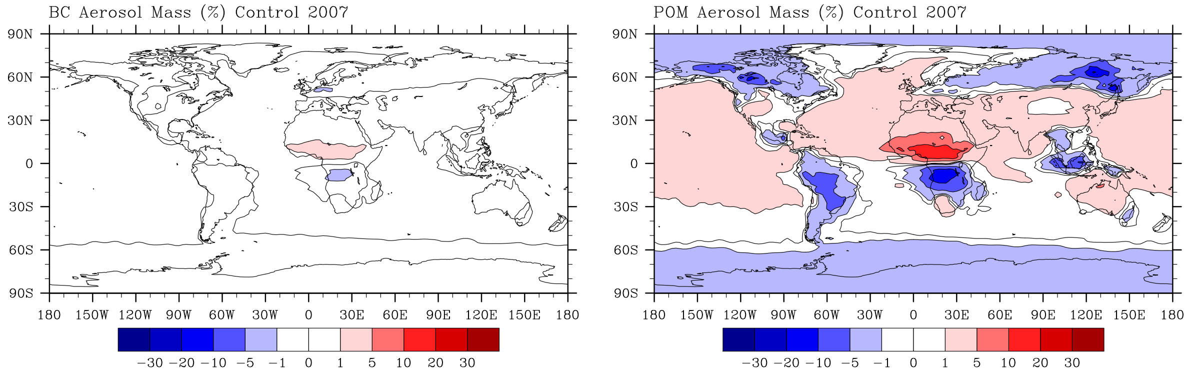

(e) Black Carbon (f) Primary Organic Aerosol

Figure 4.24: Average aerosol mass composition difference (% difference) between the AOD and angstrom assimilation run and the CAM control run. Results are shown for a) sulfate (SO4) b) secondary organic aerosol (SOA) c) sea salt (NCL) d) dust (DST) e) black carbon (BC) and f) primary organic aerosol (POM).

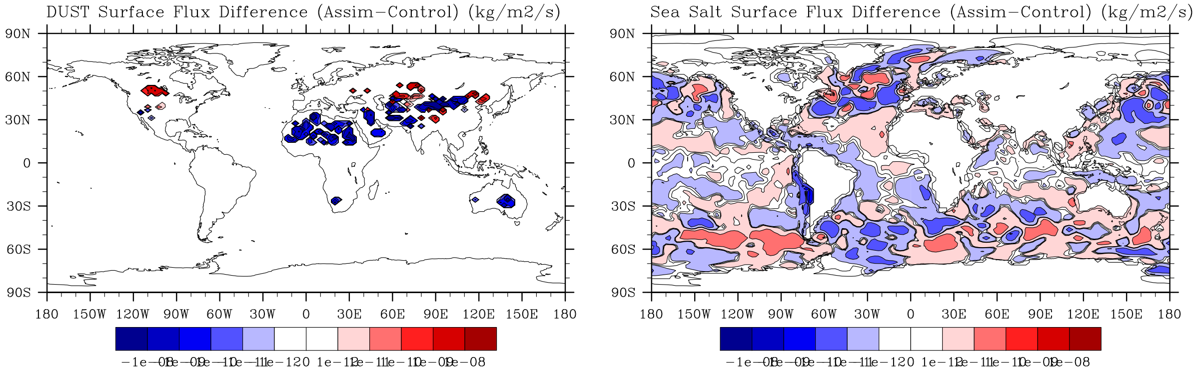

(a) dust

(b) sea salt

Figure 4.25: Difference in surface flux of a) dust and b) sea salt between the AOD and angstrom assimilation run and the control run. Red areas indicate an increase while blue values indicate a decrease.

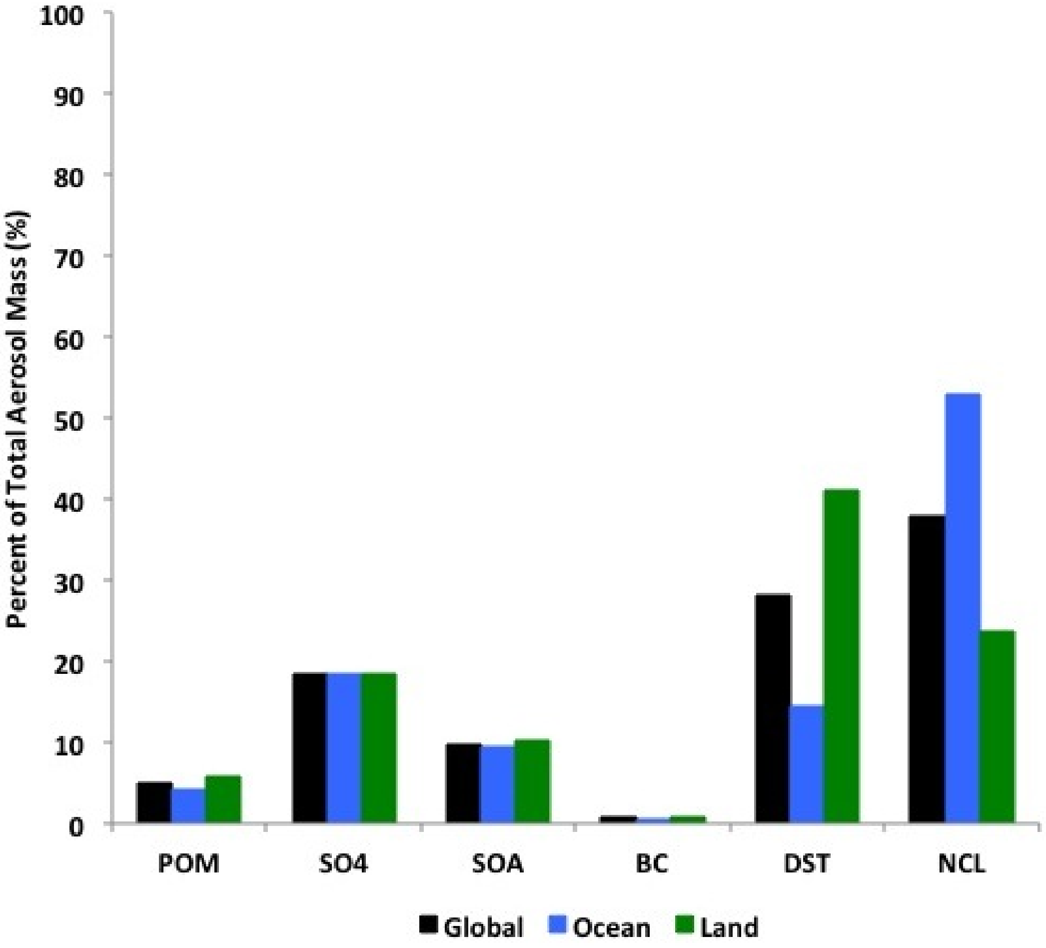

Figure 4.26: AOD/Angstrom assimilation run average aerosol composition by percent mass for the six aerosol types (primary organic aerosol, sulfate, secondary organic aerosol, black carbon, dust and sea salt). Results are globally averaged (Global), averaged over ocean only (Ocean), and over land only (Land).

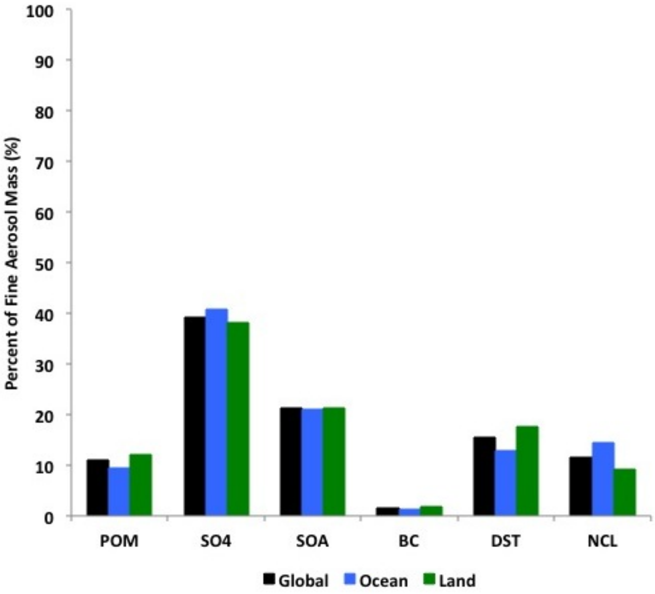

(a) Fine

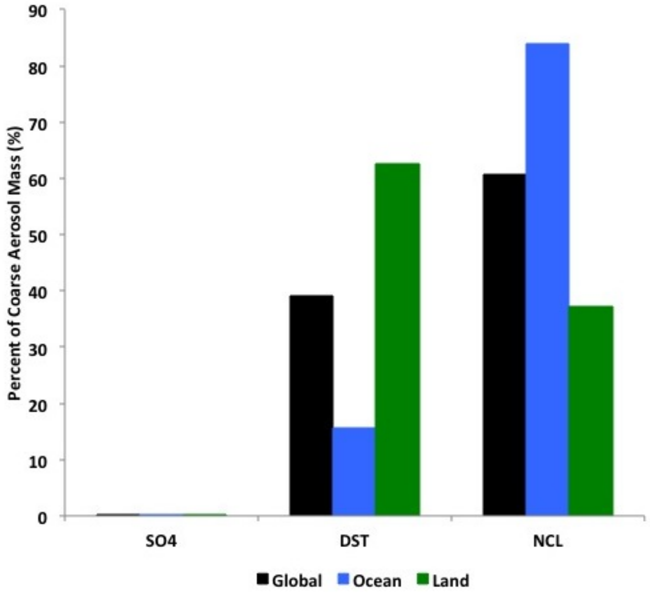

(b) Coarse

Figure 4.27: AOD/Angstrom assimilation run average aerosol composition by percent mass for the six aerosol types (primary organic aerosol, sulfate, secondary organic aerosol, black carbon, dust and sea salt) for a) fine aerosol and b) coarse aerosol. Results are globally averaged (Global), averaged over ocean only (Ocean), and over land only (Land).

4.3 Amount, Size and Vertical Aerosol Assimilation

The second assimilation conducted is similar to the previous in that AOD and angstrom observations are used to scale the amount and relative contribution of fine and coarse aerosol. However, in this assimilation, the vertical distribution of aerosol is considered with the use of vertical extinction observations from CALIPSO. Due to disagreements in AOD observations between MODIS and CALIPSO [51], the chosen approach for the vertical assimilation is to make use of the relative distribution of extinction in the vertical instead of the absolute values (ie. fraction of optical depth in a given layer f_τ). In addition to avoiding a competing effect between the two instruments, this provides a more consistent approach between the two assimilations with the only difference being the vertical redistribution of aerosol.

Prior to formulating the vertical assimilation, the relationship between the vertical AOD profile and the various size modes is examined. This is done to determine if some or all of the modes can be scaled using the vertical observations. Sample profiles of the relative AOD and amount of aerosol predicted by CAM are presented in Figure 4.28. The sampled profiles indicate that the relative AOD profile and the coarse aerosol profile are strongly correlated. This initial finding is confirmed in global maps of correlation coefficients between the AOD vertical profile (fraction of AOD in each layer) and the size-mode specific aerosol profiles (Figure 4.29). In Figure 4.29a, correlation coefficients between the AOD profile and the nucleation mode are presented. Little correlation is found between the two and therefore, the AOD profile should not be used for scaling the nucleation mode. The accumulation mode, on the other hand, shows strong correlations over land regions, but not globally (Figure 4.29b). Use of the AOD profile for scaling would have to be limited to regions that are dominated by fine aerosol. The coarse aerosol profile is strongly correlated with the AOD profile globally, indicating the relative AOD in the vertical is a good proxy for coarse aerosol relative profiles (Figure 4.29c).

Zonally averaged vertical profiles of accumulation and coarse mode aerosol presented in Figure 4.30 reveal that the coarse aerosol is limited to the surface, similar in pattern to the zonally averaged AOD (Figure 2.22), while the accumulation mode is vertically distributed. Additionally, the previous simulations showed a persistent positive angstrom exponent bias in certain regions even in the presence of the EnKF (Figure 4.19). Since a high angstrom exponent value relative to the observation indicates that the fraction of fine aerosol is over-predicted, it is hypothesized that the lifetime of the coarse aerosol may be the contributing factor. Due to the strongly correlated profiles and possible issues with aerosol lifetime, the coarse aerosol will be adjusted using the vertical AOD profile. This approach assumes that the model-predicted vertical profile for fine mode aerosols is correct and the CALIPSO-observed vertical profile is representative of the coarse aerosol profile. It is hypothesized that the lifetime of the coarse aerosol will increase and the angstrom exponent will decrease in regions with high model-predicted values relative to the observations.

CALIPSO extinction profiles were processed prior to the assimilation and averaged onto the same grid as CAM. The observations were screened by QC indices and uncertainties as recommended in the literature [34]. The grid-averaged extinctions were then converted into optical depths (AOD=k_{ext}dz). The fraction of AOD in each layer (f_τ) was then calculated (Equation 4.38). In this assimilation, the total amount of fine and coarse aerosol is adjusted using the fine and coarse scaling equations that were previously discussed (Equation 4.32 and 4.35). However, the coarse aerosol number and mass fields are redistributed vertically using the relative distribution of AOD from CALIPSO. Prior to applying the scaling for the coarse aerosol fields, the column-integrated mass (or number) is calculated for each grid box where CALIPSO observations are available (M(lat,lon), Equation 4.39). The coarse scaling is then applied to the column-integrated coarse mass (or number) M(lat,lon) and then distributed vertically using the fraction of AOD in a given layer as shown in Equation 4.40. For columns where vertical information is not available, the adjustments are made in the same manner as the amount and size assimilation. The remaining details of the vertical assimilation are the same as the previous assimilation, with 60 ensembles run for the year 2007.

$$f_\tau(lat, lon, vert) = \frac{\tau(lat, lon, vert)}{\sum_{vert=1}^{28} \tau(lat, lon, vert)} \tag{4.38}$$

$$M(lat, lon) = \sum_{vert=1}^{28} M(lat, lon, vert) \tag{4.39}$$

$$M^{c,POST}(lat, lon, vert) = f_\tau(lat, lon, vert) F^c M^{c,PRIOR}(lat, lon) \tag{4.40}$$

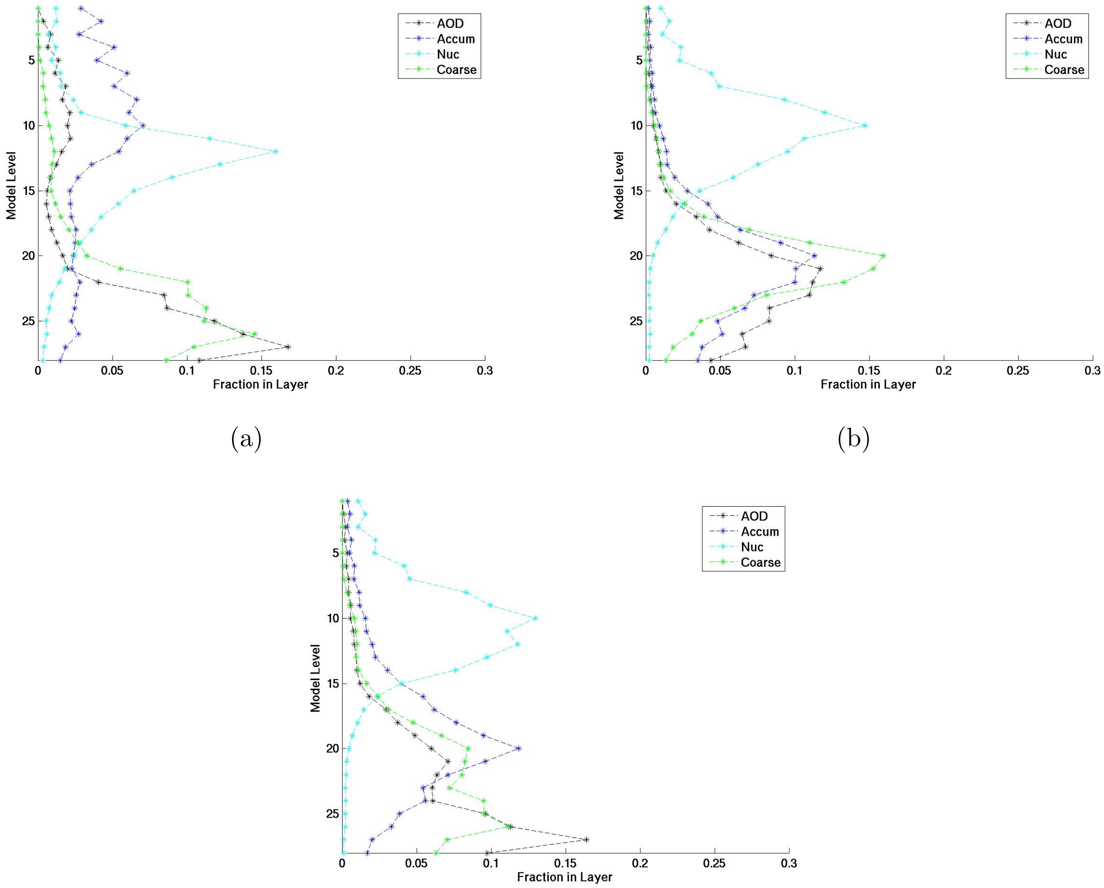

(a)

(b)

(c)

Figure 4.28: Vertical profiles of AOD, accumulation mode aerosol number, nucleation (Nuc) mode aerosol number and coarse aerosol number predicted by CAM. Results are shown as the fraction of the column integrated amount present in each layer. Model level 1 is in the upper atmosphere while model level 28 is closest to the surface.

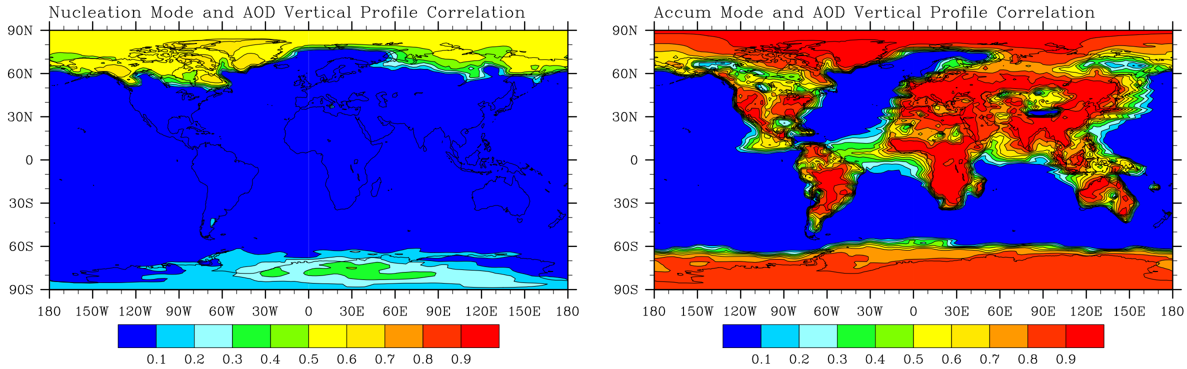

(a) Nucleation (Fine) (b) Accumulation (Fine)

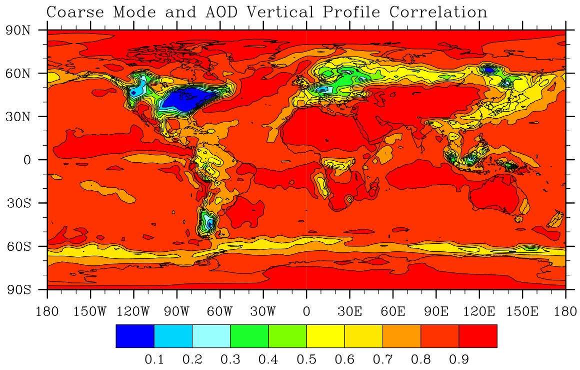

(c) Coarse

Figure 4.29: Correlation coefficients between the AOD vertical profile and the aerosol number profile for the a) nucleation b) accumulation and c) coarse modes from the CAM control run for 2007.

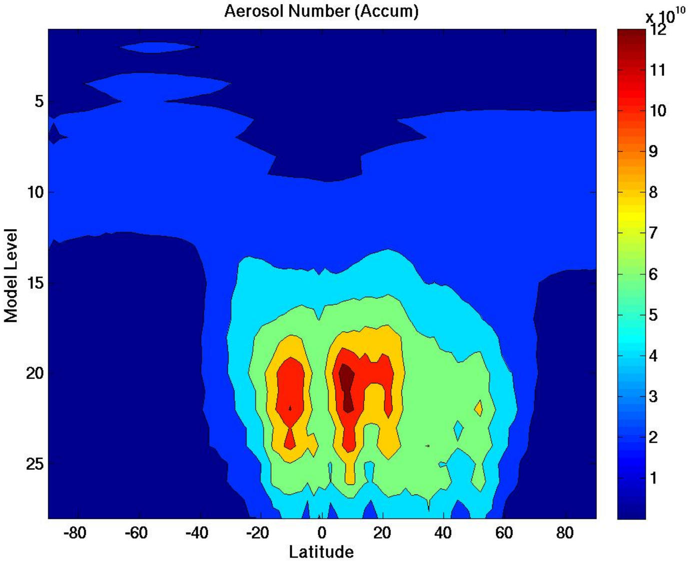

(a)

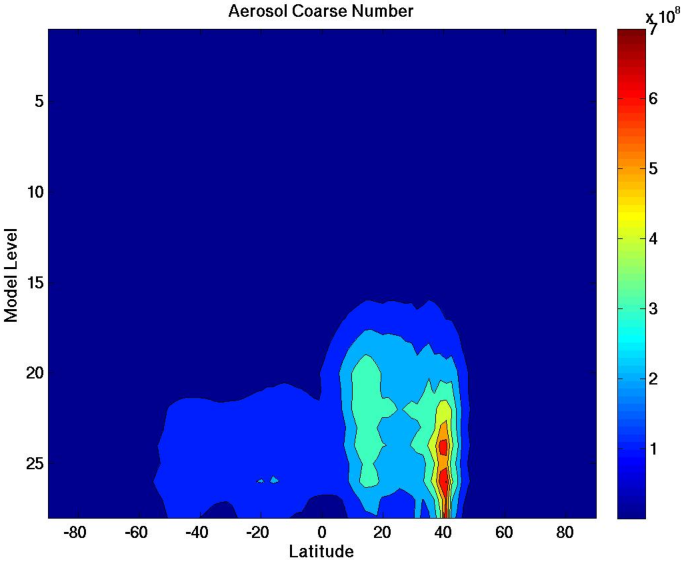

(b)

Figure 4.30: Zonally averaged profiles of a) accumulation mode aerosol number and b) coarse mode aerosol number (right) from the CAM control run for the year 2007.

4.3.1 Analysis Phase Adjustment

The analysis phase adjustments for the amount, size and vertical assimilation (VERT) are presented in Figures 4.31 through 4.35. Again, the clear negative bias in CAM AOD predictions would indicate that the EnKF should increase the AOD in most locations. This is in fact what is found (Figure 4.31), similar to the previous assimilation. Additionally, the EnKF acts to decrease the angstrom exponent in most locations (Figure 4.32). Exceptions include off the coast of South America and parts of Europe and North America, although the increases vary with season. It should be noted that the adjustments to AOD and angstrom exponent are larger in this assimilation, on the order of 3 percent, compared to approximately 1 percent from the AOD/ANG assimilation(Figure 4.33). The larger adjustments are attributed to an increase in the ensemble spread caused by the vertical profile changes. Additionally, the adjustments do not decrease with time as was seen with the angstrom adjustments in the amount and size assimilation, indicating the ensemble spread is being maintained (Figure 4.33).

Seasonally averaged fine and coarse scaling factors are presented in Figures 4.34 and 4.35, respectively. The spatial patterns of both the fine and coarse scalings are similar to the AOD/ANG assimilation with increases in fine aerosol over most land regions and decreases over ocean regions. The coarse scaling factor is positive in most locations with exceptions occuring where the angstrom exponent was increased. The coarse factors appear to be greater than the fine factor, indicating a shift towards coarse aerosol in this assimilation.

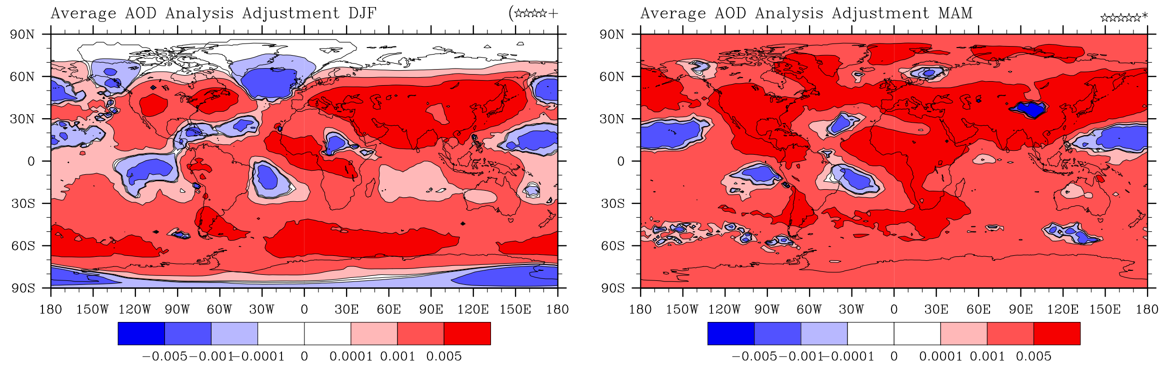

(a) December-January-February (b) March-April-May

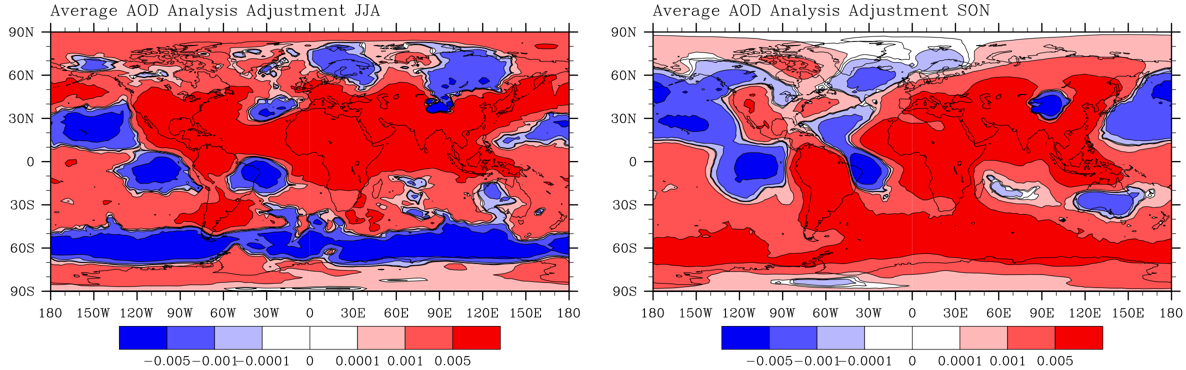

(c) June-July-August (d) September-October-November

Figure 4.31: Seasonally averaged adjustments (Posterior minus Prior) to AOD during the analysis phase in which the EnKF is applied for the assimilation with vertical adjustment. Positive regions indicate an increase in AOD and negative regions indicate a decrease.

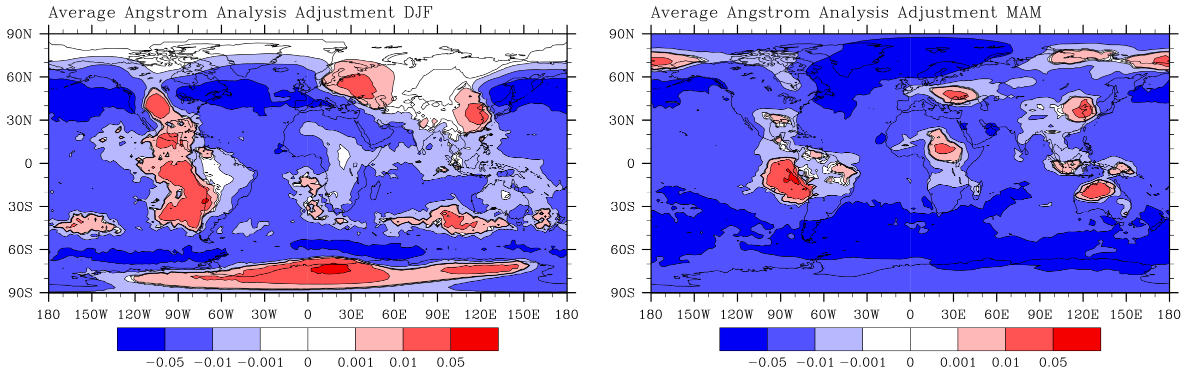

(a) December-January-February

(b) March-April-May

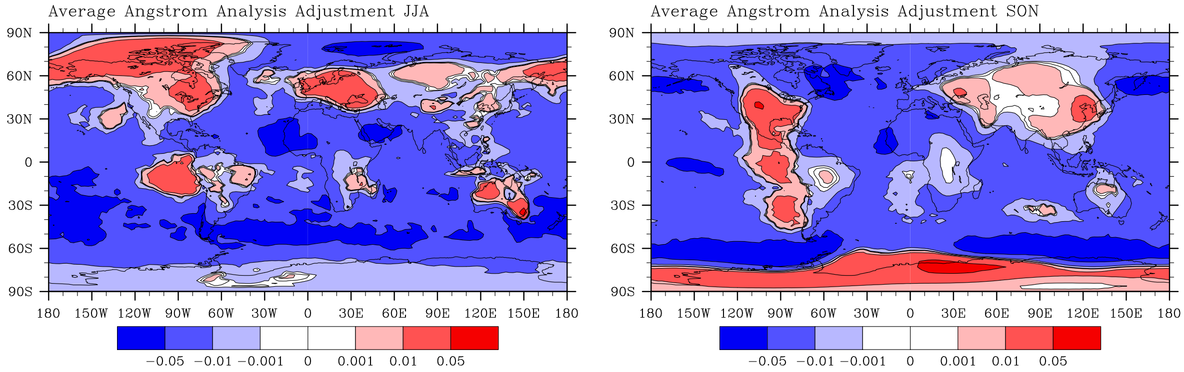

(c) June-July-August

(d) September-October-November

Figure 4.32: Seasonally averaged adjustments (Posterior minus Prior) to angstrom exponents during the analysis phase in which the EnKF is applied for the assimilation with vertical adjustment. Positive regions indicate an increase in angstrom exponent and negative regions indicate a decrease.

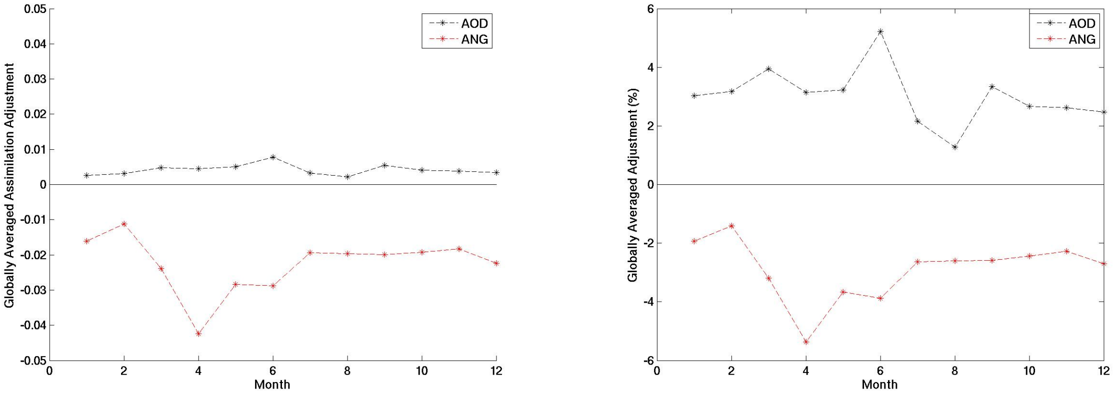

(a) (b)

Figure 4.33: Timeseries of globally averaged EnKF a) absolute and b) percent adjustments in AOD and angstrom exponent for the assimilation with vertical adjustment.

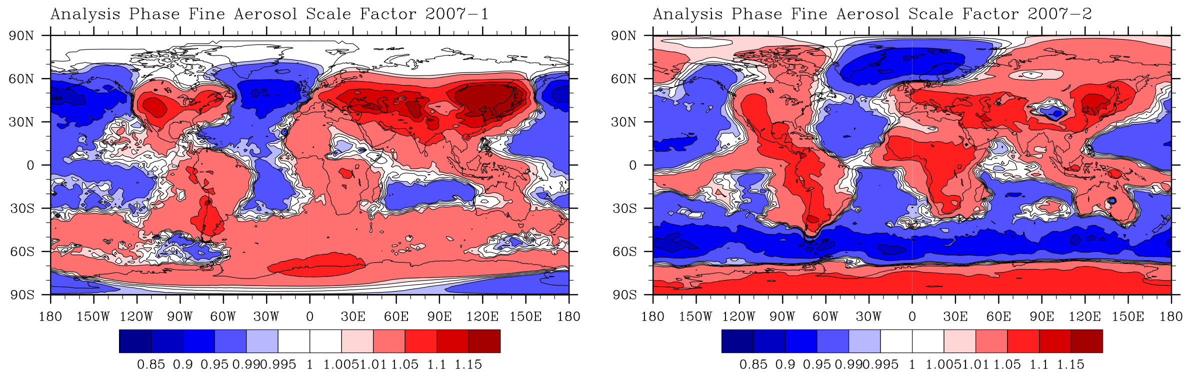

(a) December-January-February (b) March-April-May

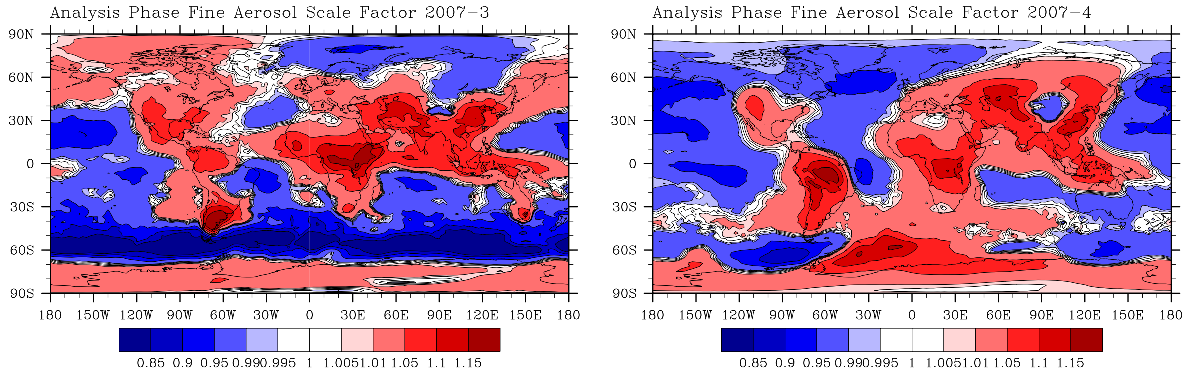

(c) June-July-August (d) September-October-November

Figure 4.34: Seasonally averaged fine aerosol scale factor (F^f) for the assimilation with vertical adjustment. Red areas indicate an increase in fine aerosol while blue areas indicate a decrease.

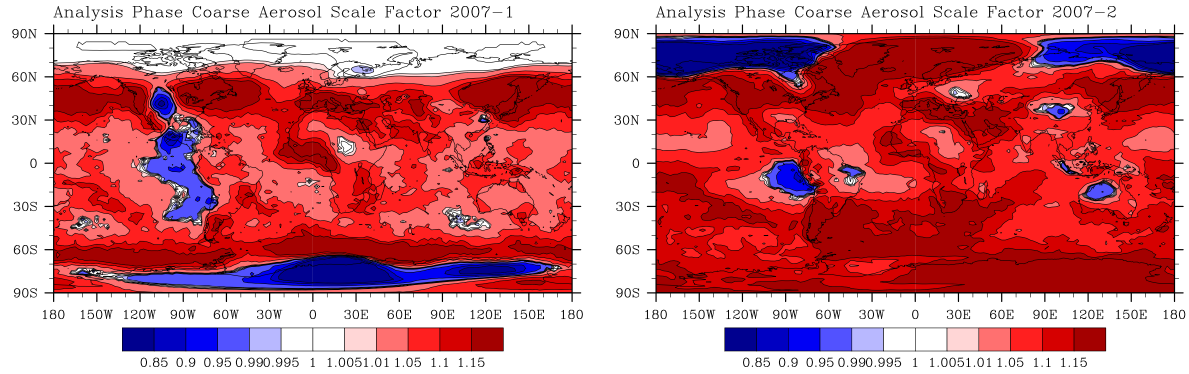

(a) December-January-February

(b) March-April-May

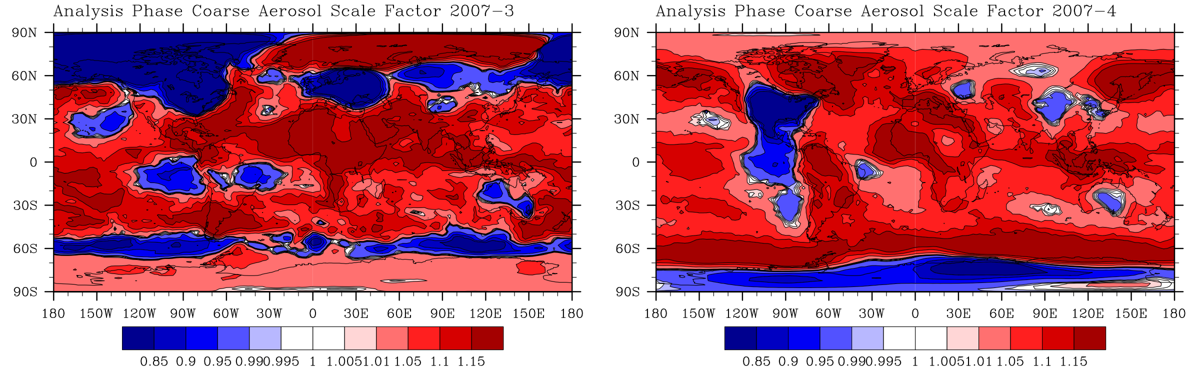

(c) June-July-August

(d) September-October-November

Figure 4.35: Seasonally averaged coarse aerosol scale factor (F^c) for the assimilation with vertical adjustment. Red areas indicate an increase in fine aerosol while blue areas indicate a decrease.

4.3.2 Model+Assimilation Results

The overall model results are a combination of the adjustments made in the analysis phase and the model's evolution of the adjusted aerosol. The average AOD for the year 2007 as well as seasonal averages are shown in Figures 4.36 and 4.37, respectively. The greatest optical depths are observed in the northern hemisphere with peak optical depths in Asia exceeding 0.5. A seasonality is observed in the optical depth, similar to the previous assimilation, with the lowest values occuring in the winter and the greatest in the spring through summer. A comparison to the control simulation (Figure 4.38) shows greater optical depths in almost all locations with exceptions over the dusty Sahara and parts of Asia. This is similar to the previous assimilation, although the differences in the decreased optical depth regions are not as great. This is confirmed in the comparison between the vertical assimilation and the AOD/ANG assimilation with higher values in the tropics and over known dusty regions (Figure 4.39). A larger hemispheric difference is also observed in the springtime. The average ensemble-generated uncertainties in predicted AOD for the full assimilation run are presented in Figure 4.40, including both absolute and percent uncertainty. The ensemble spread reveals larger uncertainties in high latitude regions compared to the mid-latitude regions with uncertainties similar in pattern to the AOD/ANG assimilation. The globally averaged AOD uncertainty for the assimilation is 13%.The ensemble spread is greater than found in the AOD/ANG assimilation. The average AOD predicted by the VERT assimilation was found to be statistically different from both the control and AOD/ANG assimilation average AOD (t-test, 95% confidence).

A timeseries of globally averaged AOD values for MODIS, the CAM control run, the CAM AOD/ANG assimilation run , and the CAM VERT assimilation is shown in Figure 4.41. Similar to Figures 4.38 and 4.39, the time series shows that the AOD predicted by the assimilation with vertical adjustments is higher than the previous two runs. Additionally, the averages almost intersect the MODIS observations. The increased ensemble spread results in an assimilation that was sensitive to the observations, resulting in much higher simulated optical depths. A comparison with seasonally averaged MODIS observations show that many of the negative bias regions have decreased, especially in the tropics (Figure 4.42). Some positive bias regions developed in the northern hemisphere and over Australia. On average, the assimilation compares better to MODIS than the control and AOD/ANG simulations. This is expected given the sensitivity observed. Averaged optical depths are compared to AERONET data in addition to the previous simulations by site category in Figure 4.43. The average AOD increased for industrial pollution, polluted marine and dirty pollution sites and very slightly for rural sites. Little change was observed in the average AOD for the dust and biomass burning sites, however, the spread increased, showing more variation in the predictions. Again, rural sites were found to not be statistically different via t-test analysis (95% confidence). The AOD timeseries for select sites by category (Figure 4.44) show that the assimilation results are in better agreement in general with the AERONET observations with overlapping distributions. However, differences are still found.

The average angstrom exponents for the full 2007 run as well as seasonal averages are shown in Figures 4.45 and 4.46. Similar to the AOD fields and to the previous assimilation work, the angstrom exponent exhibits seasonal variation with the greatest hemispheric difference occurring in the summertime. In general, larger angstrom exponents are observed over land than over oceans. A comparison of seasonally averaged angstrom exponents to the control run reveals lower angstrom values in the high latitudes and over North America, Europe and Asia. This indicates a larger coarse component predicted by the assimilation. Higher angstrom values are found over oceans and known dusty regions such as the Sahara and Arabian peninsula, indicating a larger fine component in the assimilation. In comparison to the AOD/ANG assimilation, lower angstrom values are predicted over the dusty Sahara, indicating a larger coarse component. This result along with the higher AOD values observed in this region suggests that the vertical adjustment is helping maintain coarse aerosol. Additionally, a decrease is observed in summertime angstrom values centered around the 60°S latitude line. The comparison of previous runs with MODIS reveal a persistent positive bias in this region with respect to angstrom exponent. Again, this suggests that coarse aerosol is being maintained in the atmosphere, however, this regional bias is persistent throughout the year and the same decrease in not observed. The average ensemble-generated uncertainties in predicted angstrom exponents for the full assimilation run are presented in Figure 4.49, including both absolute and percent uncertainty. Uncertainties are the largest in the high latitude Southern Hemisphere. The globally averaged angstrom uncertainty for the assimilation is 5%. The average angstrom exponent predicted by the VERT assimilation was found to be statistically different from the control and AOD/ANG assimilation average (t-test, 95% confidence).

A time series of over ocean averaged angstrom values for MODIS and the three simulations are shown in Figure 4.50. The vertical assimilation has higher average angstrom exponent values relative to MODIS in almost all months, except for July. However, the distributions overlap. With respect to the AOD/ANG assimilation, the VERT assimilation predicts higher average angstrom exponents in the spring and lower values from June through December. Given the only difference between the two assimilations is the vertical adjustment, these results suggest that the vertical redistribution affects the coarse aerosol lifetime. A comparison with seasonally averaged MODIS observations (Figure 4.51) reveals that many of the negative bias regions have decreased. The positive bias regions are still present. However, they have decreased, especially in the tropics.

The average percent of AOD due to fine aerosol for the full 2007 run and by season are presented in Figures 4.52 and 4.53. In line with the angstrom exponent results, seasonally differences are observed with a higher fine contribution in the northern hemisphere, consistent with emission fields. Relative to the control simulation, a smaller fine contribution is observed over high latitudes and parts of North America, Europe and Asia with seasonal variations (Figure 4.54). Relative to the AOD/ANG assimilation, the fine contribution is less over the dusty Sahara for all seasons and in the Southern hemisphere ocean, except for springtime. Higher fine contributions are observed in general in the springtime. Differences in fine contribution between the two assimilation runs are on the order of a percent, however, as much as 30 percent differences are observed over Africa and around 60°S. A comparison of the average AOD fine contribution from all simulations and AERONET by site category is presented in Figure 4.43. Relative to the control and the AOD/ANG assimilation, the VERT assimilation predicts lower average fine contributions for all site categories. Since the only difference between the assimilations is the vertical distribution, the lower fine contributions indicate an increase in coarse aerosol lifetime. Relative to AERONET, the VERT assimilation predicts higher average fine contribution for dust sites and lower fine contributions for biomass burning, rural, industrial pollution, polluted marine and dirty pollution sites. The spread of the distributions increased for the VERT assimilation showing increased variability in the fine contributions predicted. The greatest improvement if found for the desert dust sites. This is consistent with expectations given that dust sites are dominated by coarse aerosol. A table summarizing the globally averaged results for the year 2007 and by season for the AOD, angstrom exponent (over ocean) and AOD fine contribution (land and ocean) for MODIS, the control run, the AOD/ANG assimilation and the VERT assimilation are shown in Table 4.2.

The composition of the predicted aerosol in the VERT assimilation run is examined on a mass basis in Figure 4.56. Results are shown as the percent of the total mass for each of the six aerosol types. Similar to the previous simulations, sea salt and dust make up a large portion of the mass. Sea salt contributions are greatest in the Southern hemisphere oceans with contributions reaching as much as 70 percent. Dust contributions are greatest over the dusty Sahara, Arabian peninsula, the Gobi desert and Australia. Dust makes up a larger portion of the mass in the Northern hemisphere with peak contributions around 90 percent in Asia. Again, sulfate contributions are important in the Northern hemisphere, consistent with emission fields, with a contribution of approximately 20 percent. Secondary organic aerosol is also more prevalent in the Northern hemisphere with average contributions around 10 percent. However, peak secondary organic aerosol contributions are found over South America and parts of Africa. Black carbon contributions are on the order of a percent with higher contributions observed over the Eastern United States, Europe, parts of Asia, Africa and South America, consistent with urban pollution emissions and biomass burning. Primary organics are found mostly over South America and Africa. The predicted aerosol composition from the VERT assimilation is compared to the control run in Figure 4.57. The greatest differences are seen with sea salt and dust aerosol. The contribution of sea salt decreases on a percent basis over oceans while dust contributions decrease over land and increase over ocean. Sulfate and secondary organic aerosol increases in the Northern hemisphere on the order of 5 percent. Both increase and decreases in primary organic aerosol on the order of 1 percent are observed. Little change is found with black carbon contributions. Relative to the AOD/ANG assimilation, the greatest differences are again found with sea salt and dust. Sea salt decreases in the Northern hemisphere and increase in the Southern hemisphere mid to high latitudes. Dust, on the other hand, increases in the Northern hemisphere and decreases in the Southern with the greatest increases occuring over the Arabian peninsula, in the Atlantic ocean off of Africa. These differences are consistent with previous results which showed decreases in fine contribution in these areas. The importance of sulfate increases in most locations on the order of a percent with the exception being decreases in dusty regions and high Southern hemisphere latitudes. Secondary organics also increase in most locations with decreases found over parts of Africa and South America. Surface flux emissions of sea salt and dust for the VERT and AOD/ANG assimilation runs were examined and little difference was found. Also, coarse sulfate emissions are the same between the two runs. This indicates that differences in aerosol composition for the coarse species are likely due to changes in aerosol lifetime.

Globally averaged compositions for total aerosol, fine aerosol, and coarse aerosol are presented in Figure 4.60. Similar to the maps of aerosol composition, dust and sea salt make up the majority of the mass with a larger dust contribution over land and a larger sea salt contribution over ocean. Sulfate is the next important component, making up approximately 20 percent of the mass. All aerosol types show up in the fine mode, indicating the presence of a biogenic component, with sulfate and secondary organics being most important. The coarse mode is dominated by dust and sea salt.

The zonally averaged vertical distribution of AOD predicted by the VERT assimilation is presented in Figure 4.61. The optical depth is in fact more distributed in the vertical, although peaks are still observed near the surface. A comparison of the zonally averaged profile against the control simulation shows an increase in optical depth in the upper atmosphere and a corresponding decrease in the lower atmosphere (Figure 4.62). Given the increase in aerosol in the upper atmosphere, it is expected that aerosol lifetime will increase.

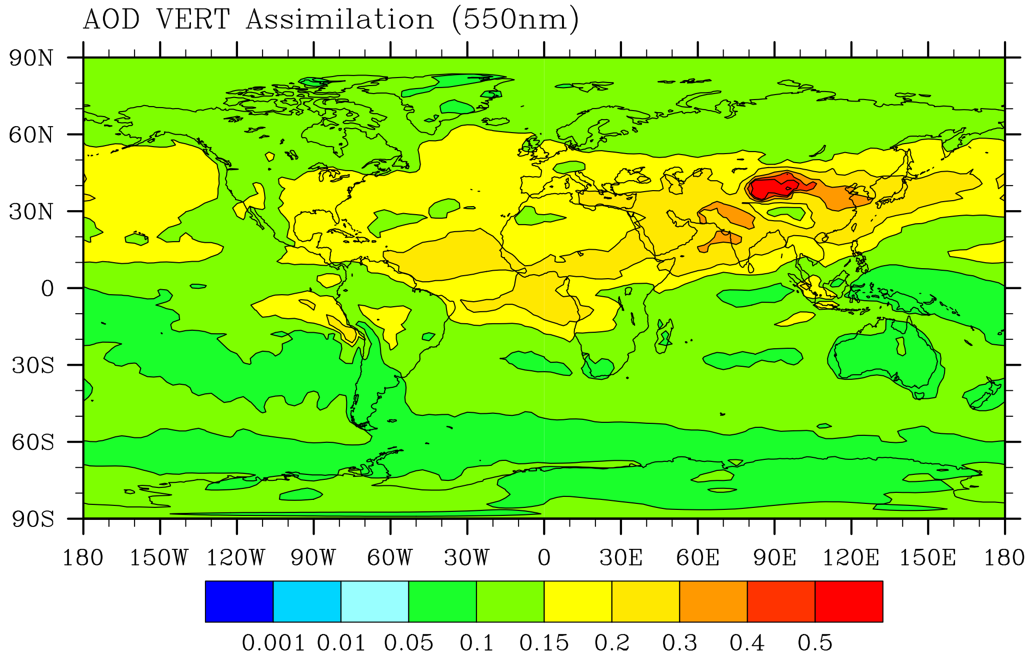

Figure 4.36: Average aerosol optical depth at 550nm for the 2007 CAM with AOD and angstrom with vertical adjustments assimilation (VERT).

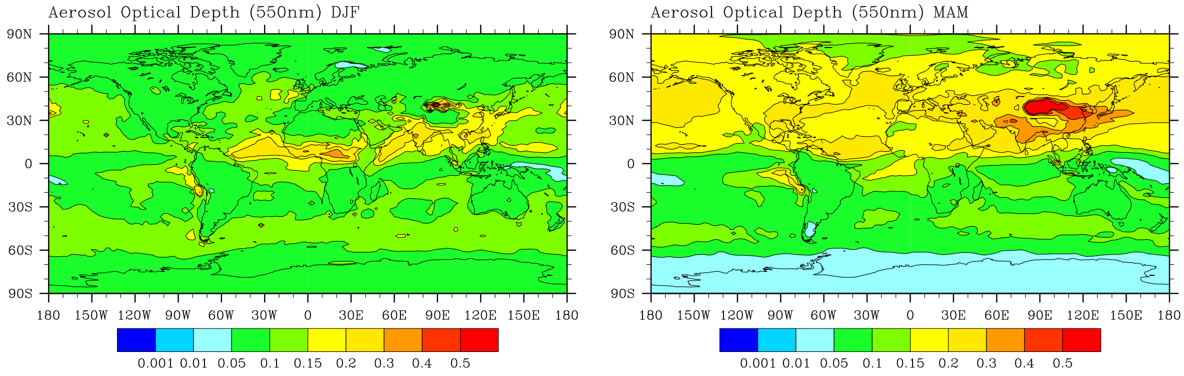

(a) December-January-February (b) March-April-May

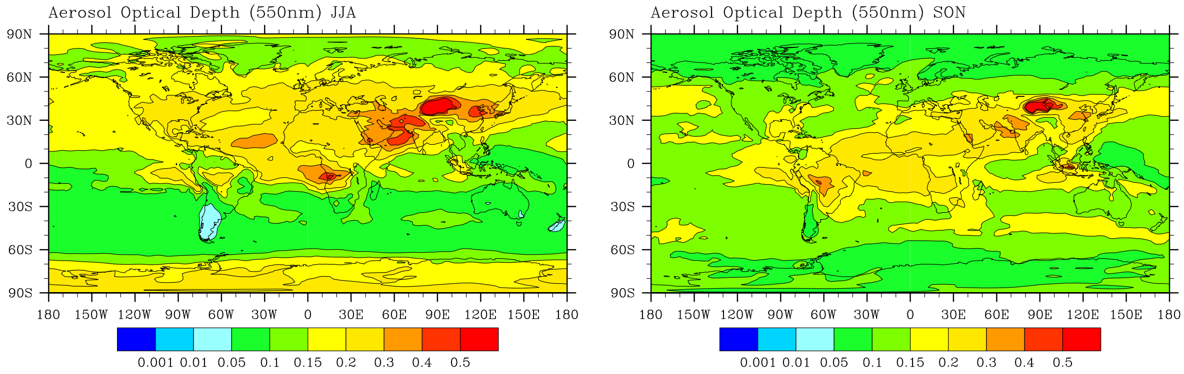

(c) June-July-August (d) September-October-November

Figure 4.37: Seasonally averaged aerosol optical depth at 550nm for the 2007 CAM with AOD and angstrom with vertical adjustments assimilation (VERT). AOD values are averaged for a) December/January/February b) March/April/May c) June/July/August and d) September/October/November.

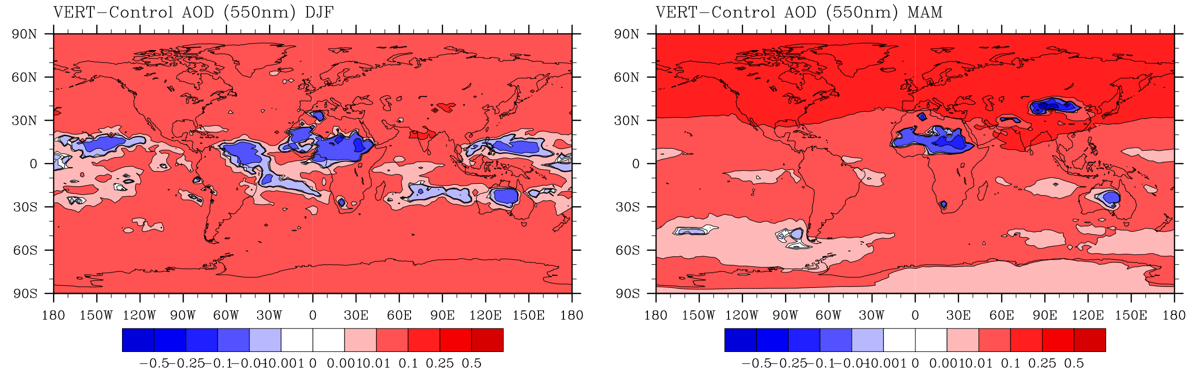

(a) December-January-February (b) March-April-May

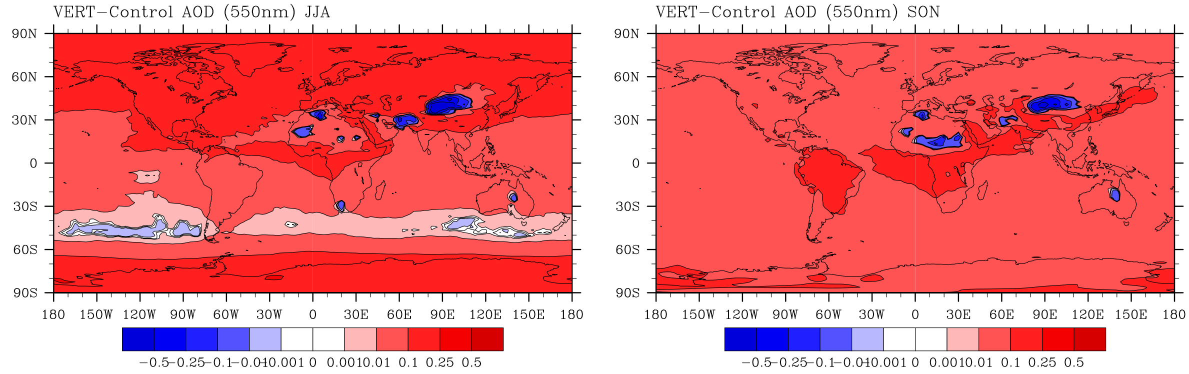

(c) June-July-August (d) September-October-November

Figure 4.38: Seasonally averaged differences in aerosol optical depth at 550nm between the CAM with AOD and angstrom with vertical adjustments assimilation (VERT) and the CAM control run. AOD differences are averaged for a) December/January/February b) March/April/May c) June/July/August and d) September/October/November.

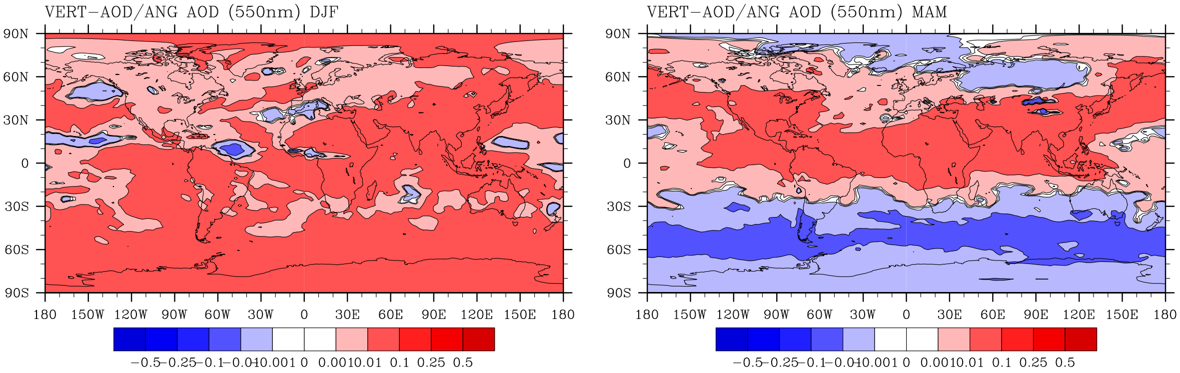

(a) December-January-February (b) March-April-May

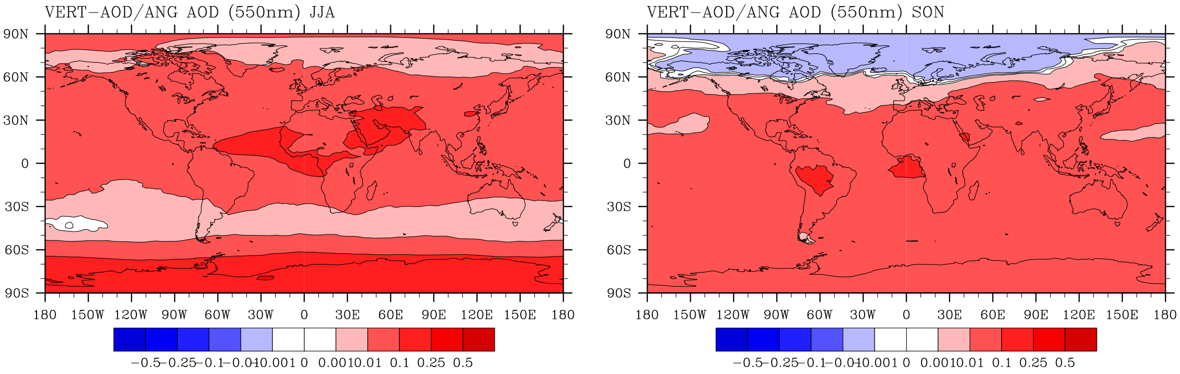

(c) June-July-August (d) September-October-November

Figure 4.39: Seasonally averaged differences in aerosol optical depth at 550nm between the CAM with AOD and angstrom with vertical adjustments assimilation (VERT) and the CAM with AOD and angstrom assimilation (AOD/ANG). AOD differences are averaged for a) December/January/February b) March/April/May c) June/July/August and d) September/October/November.

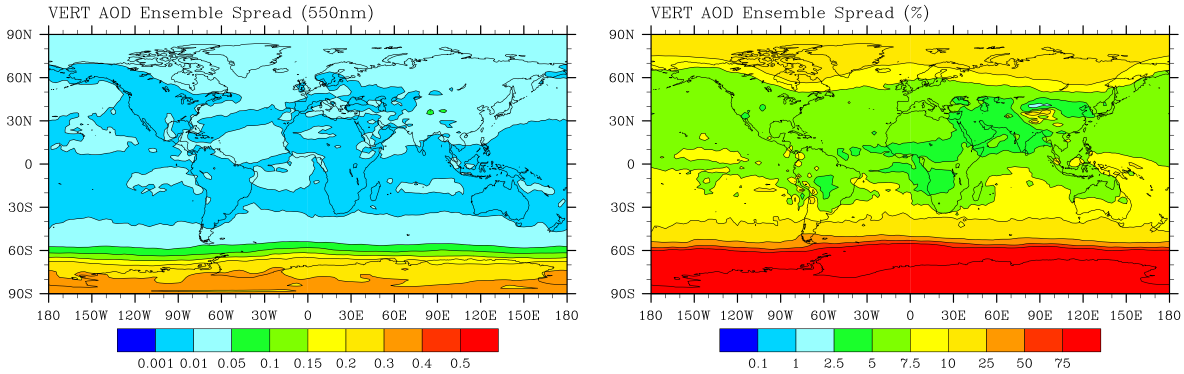

(a) Absolute (b) Percent

Figure 4.40: Average uncertainty in aerosol optical depth at 550nm (absolute and percent) for the 2007 CAM AOD and angstrom with vertical adjustment assimilation run.

Variable	**Season**	**MODIS**	**CAM Control**	**CAM AOD/ANG**	**CAM VERT**
AOD (550nm)	DJF	0.155(±0.01)	0.082(±0.05)	0.092(±0.04)	0.107(±0.04)
	MAM	0.168(±0.02)	0.088(±0.07)	0.132(±0.07)	0.14(±0.08)
	JJA	0.165(±0.02)	0.090(±0.09)	0.115(±0.07)	0.158(±0.08)
	SON	0.16(±0.02)	0.082(±0.07)	0.123(±0.04)	0.154(±0.06)
	Year	0.161(±0.09)	0.086(±0.06)	0.115(±0.05)	0.140(±0.05)
Angstrom Exponent (550-865nm) (ocean only)	DJF	0.66(±0.09)	0.66(±0.28)	0.72 (±0.18)	0.71 (±0.16)
	MAM	0.62(±0.13)	0.66(±0.35)	0.60 (±0.21)	0.65 (±0.21)
	JJA	0.65(±0.19)	0.64(±0.40)	0.67 (±0.25)	0.61 (±0.24)
	SON	0.67(±0.11)	0.62(±0.38)	0.72 (±0.14)	0.69 (±0.13)
	Year	0.65(±0.30)	0.65(±0.35)	0.68 (±0.15)	0.66 (±0.15)
AOD Fine Fraction (550nm) (Land and Ocean)	DJF	0.47(±0.04)	0.73(±0.13)	0.75 (±0.09)	0.75 (±0.09)
	MAM	0.43(±0.05)	0.73(±0.16)	0.69 (±0.15)	0.72 (±0.14)
	JJA	0.44(±0.06)	0.72(±0.16)	0.74 (±0.17)	0.74 (±0.18)
	SON	0.48(±0.05)	0.71(±0.16)	0.75 (±0.13)	0.78 (±0.11)
	Year	0.45(±0.16)	0.72(±0.15)	0.75 (±0.12)	0.75 (±0.11)

Table 4.2: Global averages of aerosol optical depth (550nm), angstrom exponent (550-865nm) and the fractional contribution of fine aerosol to optical depth. Averages are shown by season (December-January-February (DJF), March-April-May (MAM), June-July-August (JJA) and September-October-November (SON)) and for the year 2007 (Year).

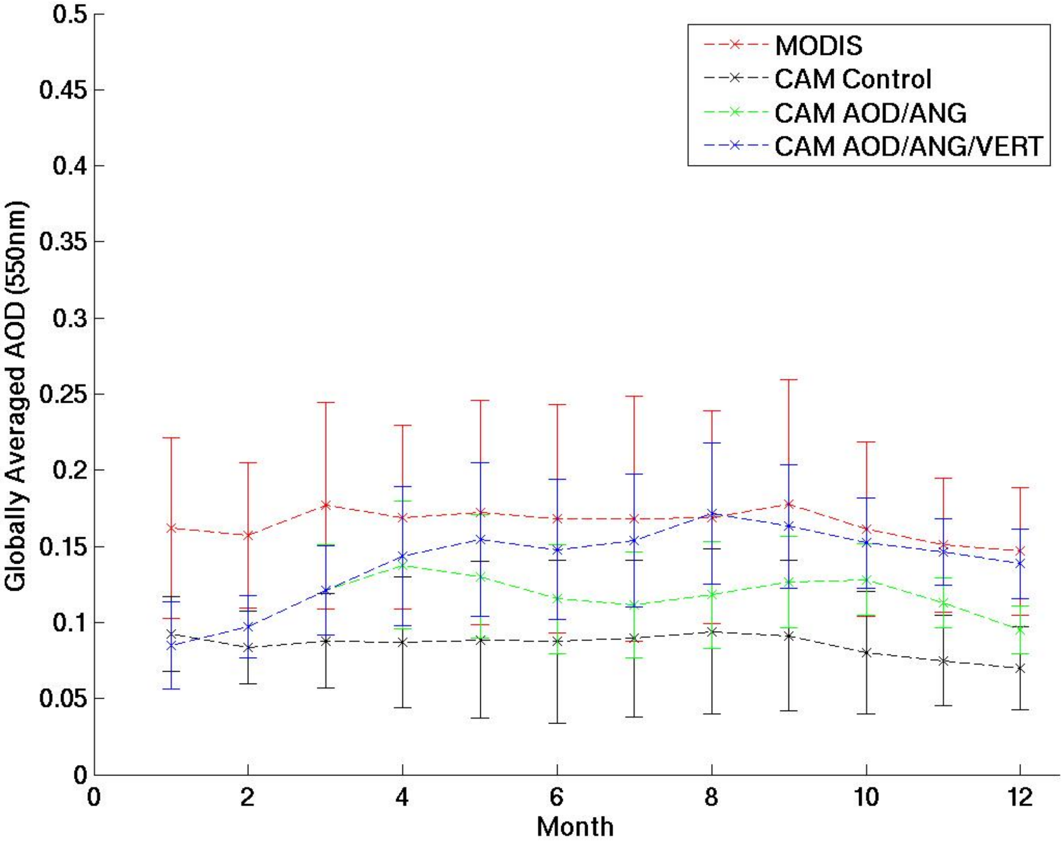

Figure 4.41: Globally averaged aerosol optical depth timeseries for MODIS (red), the CAM control run (black), the CAM AOD and angstrom assimilation (AOD/ANG) (green) and the CAM AOD and angstrom with vertical adjustments assimilation (VERT) (blue).

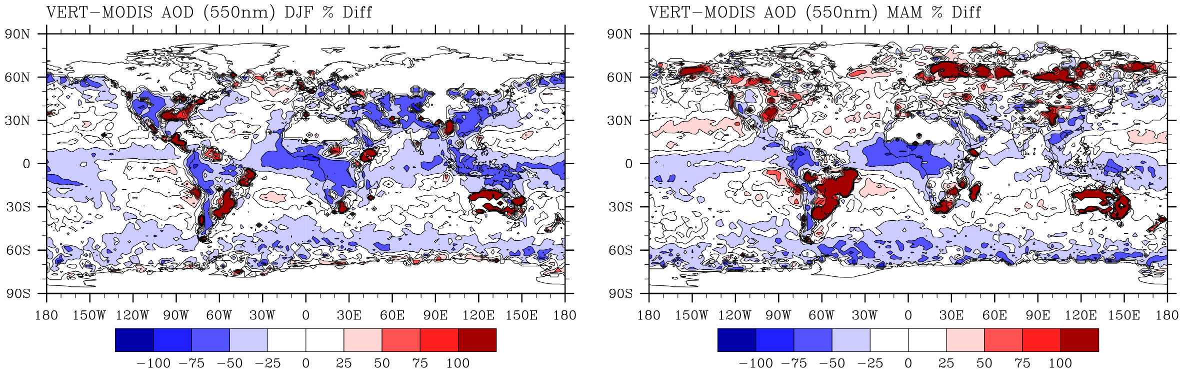

(a) December-January-February (b) March-April-May

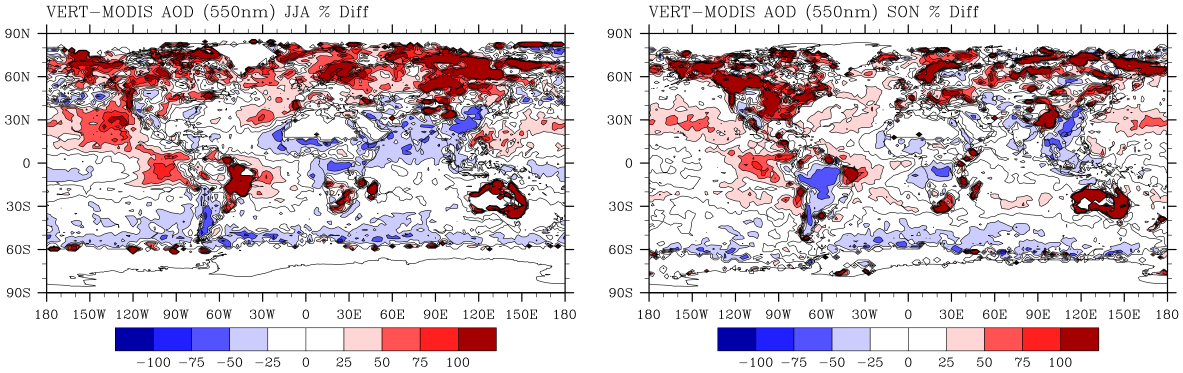

(c) June-July-August (d) September-October-November

Figure 4.42: Seasonally averaged comparison between the CAM AOD and angstrom with vertical adjustment assimilation (VERT) and MODIS aerosol optical depth observations. Results are shown as a percent different (cammodis) for a) December/January/February b) March/April/May c) June/July/August and d) September/October/November.

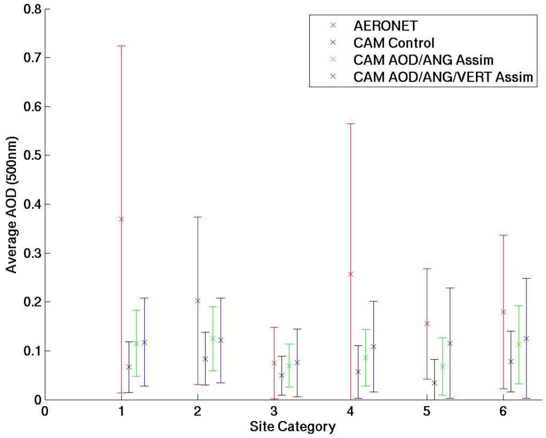

(a) Aerosol Optical Depth

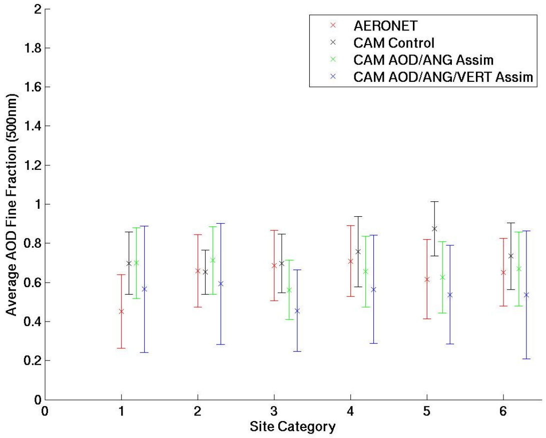

(b) Aerosol Optical Depth Fine Fraction

Figure 4.43: Comparison (mean ± standard deviation) between CAM with AOD and angstrom with vertical adjustment assimilation (VERT), CAM with AOD and angstrom assimilation (AOD/ANG), CAM control and AERONET a) aerosol optical depth and b) the fraction of aerosol optical depth due to fine aerosol. Comparisons are made by site category (1=desert dust, 2=biomass burning, 3=rural, 4=industrial pollution, 5=polluted marine, 6=dirty pollution).

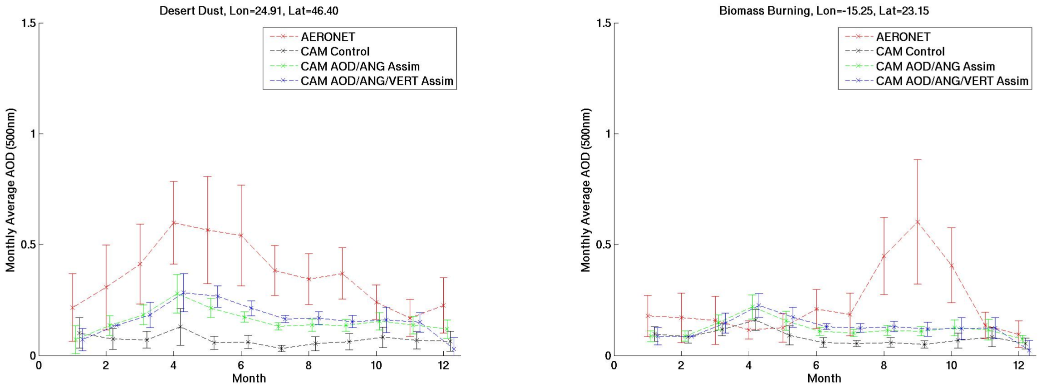

(a) desert dust (b) biomass burning

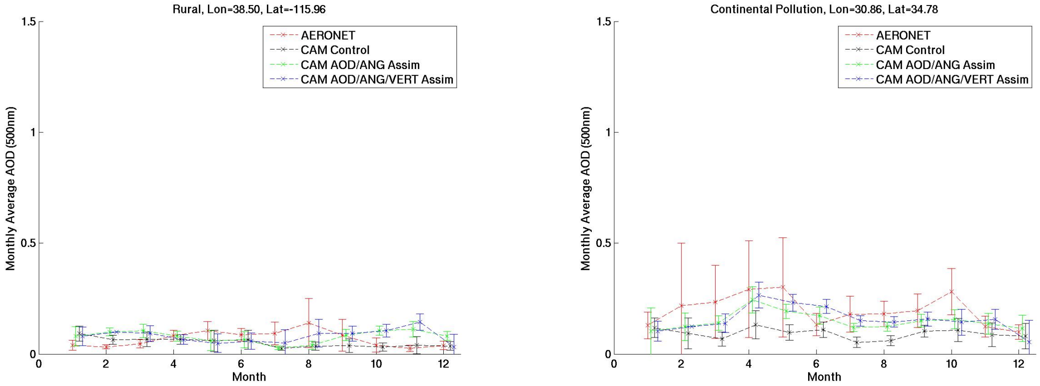

(c) rural (d) industrial pollution

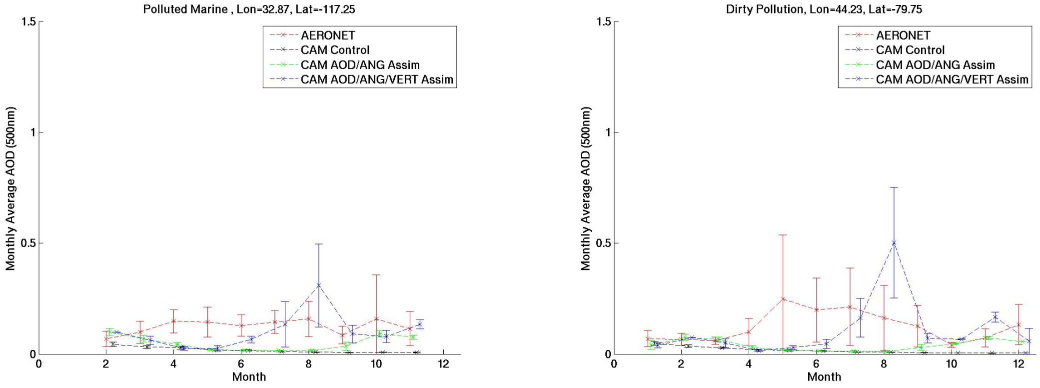

(e) polluted marine (f) dirty pollution

Figure 4.44: Aerosol optical depth monthly-averaged timeseries comparisons between CAM control run, CAM with AOD and angstrom assimilation (AOD/ANG), CAM with AOD and angstrom and vertical adjustment assimilation (VERT) and AERONET. Results are shown for select AERONET sites from each of the six site categories a)desert dust b) biomass burning c) rural, d) industrial pollution e) polluted marine f) dirty pollution.

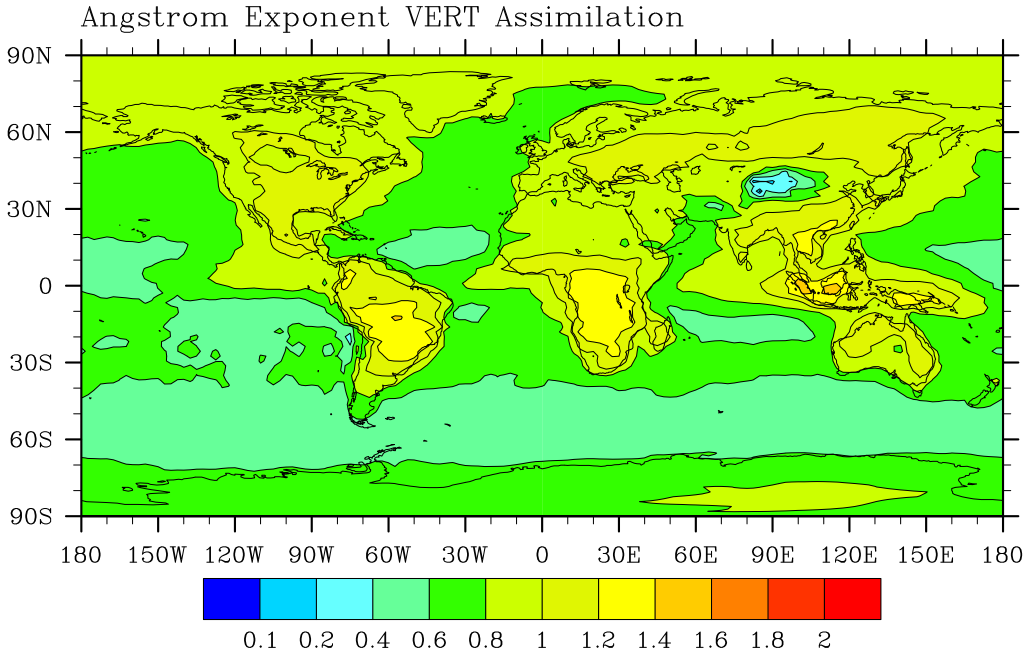

Figure 4.45: Average angstrom exponent (550-865nm) for the 2007 CAM with AOD and angstrom and vertical adjustment assimilation (VERT).

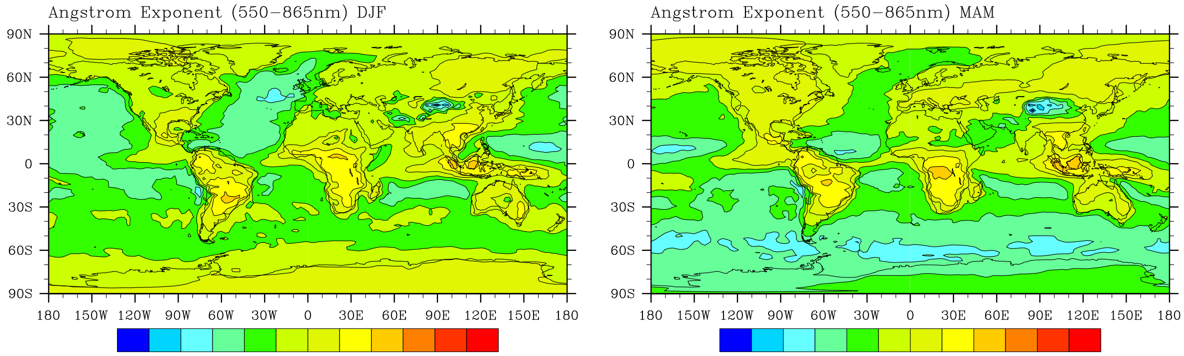

(a) December-January-February (b) March-April-May

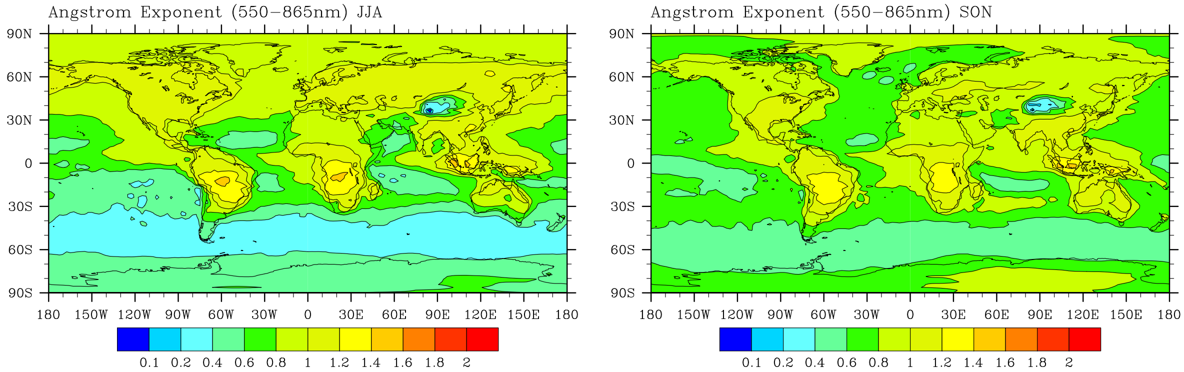

(c) June-July-August (d) September-October-November

Figure 4.46: Seasonally averaged angstrom exponent (550-865nm) for the 2007 CAM with AOD and angstrom with vertical adjustment assimilation (VERT). Angstrom values are averaged for a) December/January/February b) March/April/May c) June/July/August and d) September/October/November.

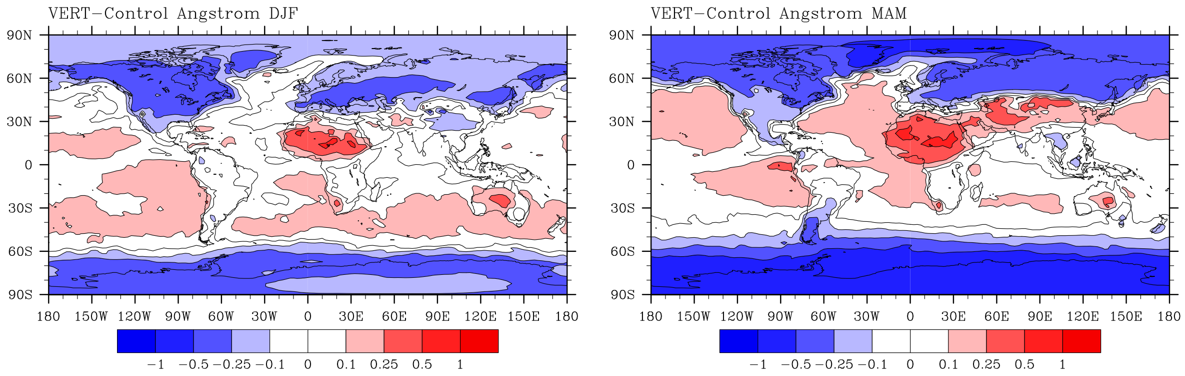

(a) December-January-February (b) March-April-May

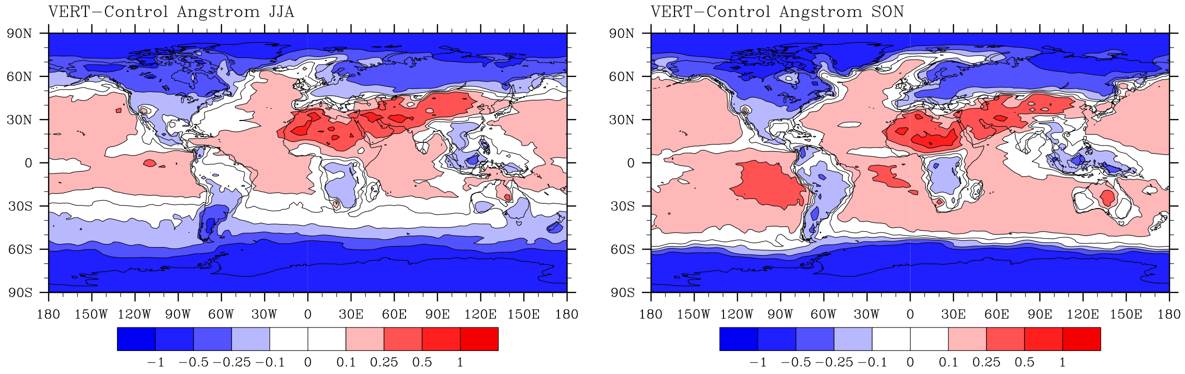

(c) June-July-August (d) September-October-November

Figure 4.47: Seasonally averaged differences in angstrom exponent (550-865nm) between the CAM with AOD and angstrom and vertical adjustment assimilation (VERT) and the CAM control run. Angstrom differences are averaged for a) December/January/February b) March/April/May c) June/July/August and d) September/October/November.

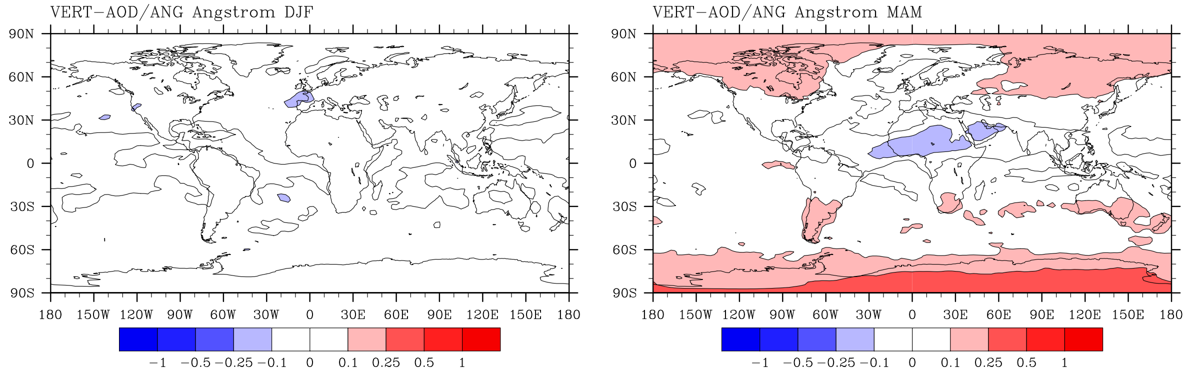

(a) December-January-February

(b) March-April-May

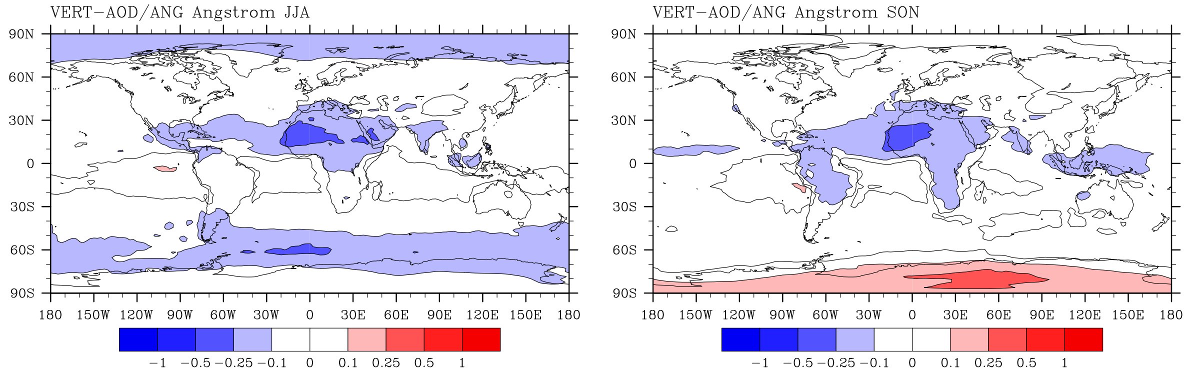

(c) June-July-August

(d) September-October-November

Figure 4.48: Seasonally averaged differences in angstrom exponent (550-865nm) between the CAM with AOD and angstrom with vertical adjustment assimilation (VERT) and the CAM with AOD and angstrom assimilation (AOD/ANG). Angstrom differences are averaged for a) December/January/February b) March/April/May c) June/July/August and d) September/October/November.

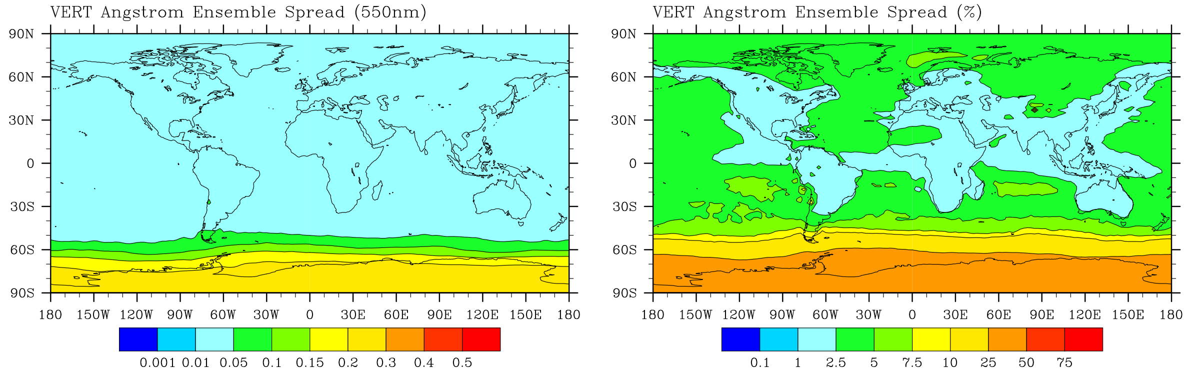

(a) Absolute (b) Percent

Figure 4.49: Average uncertainty in angstrom exponent (absolute and percent) for the 2007 CAM AOD and angstrom with vertical adjustment assimilation run.

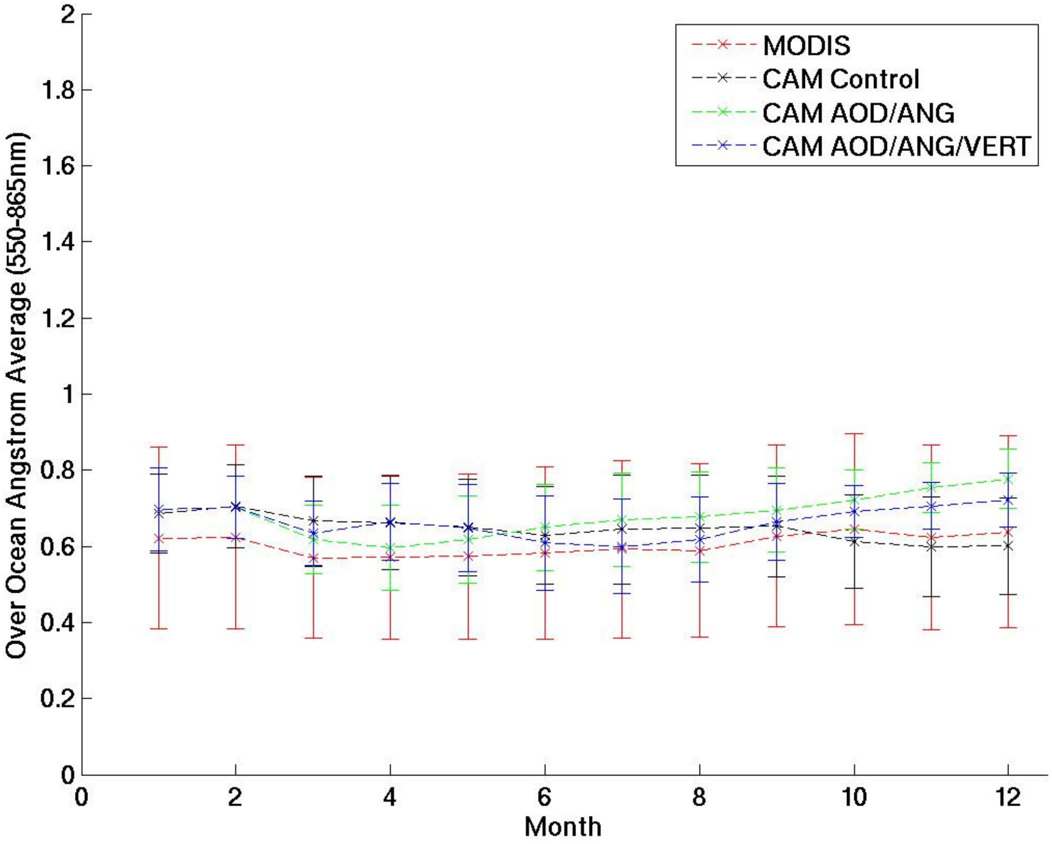

Figure 4.50: Over ocean averaged angstrom exponent timeseries for MODIS (red), the CAM control run (black), the CAM AOD and angstrom assimilation (AOD/ANG) (green) and the CAM AOD and angstrom with vertical adjustments assimilation (VERT) (blue).

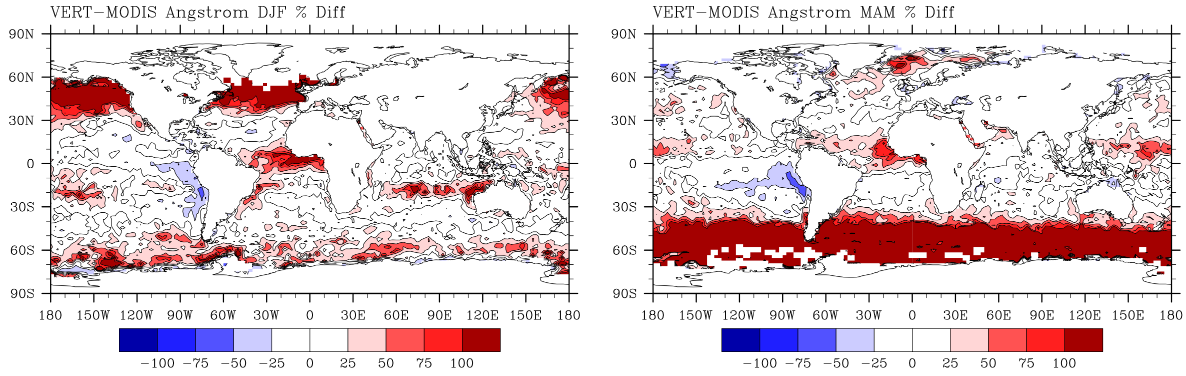

(a) December-January-February (b) March-April-May

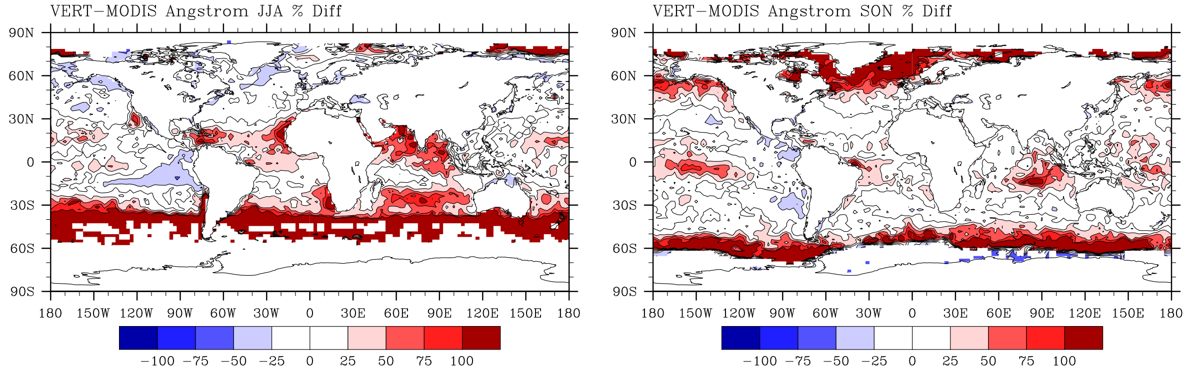

(c) June-July-August (d) September-October-November

Figure 4.51: Seasonally averaged comparison between the CAM AOD and angstrom with vertical adjustment assimilation (VERT) and MODIS angstrom exponent observations. Results are shown as a percent different (cammodis) for a) December/January/February b) March/April/May c) June/July/August and d) September/October/November.

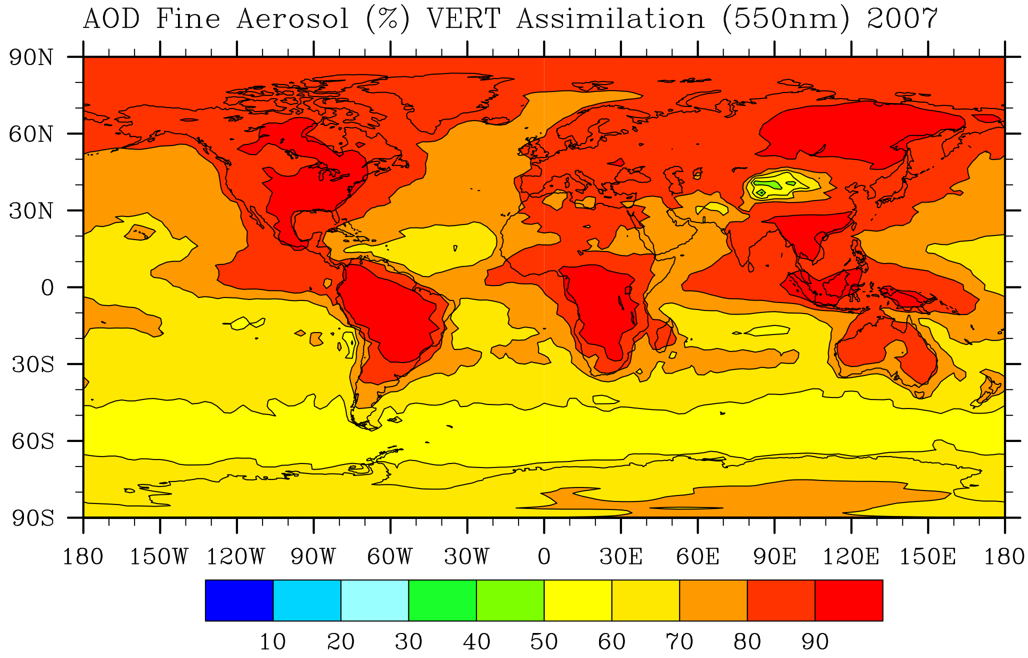

Figure 4.52: Average aerosol optical depth fine contribution at 550nm for the 2007 CAM with AOD and angstrom assimilation run.

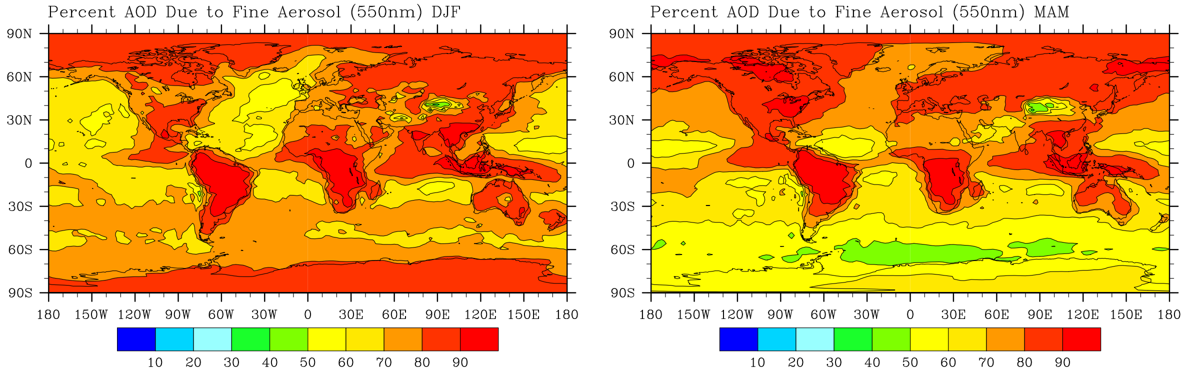

(a) December-January-February (b) March-April-May

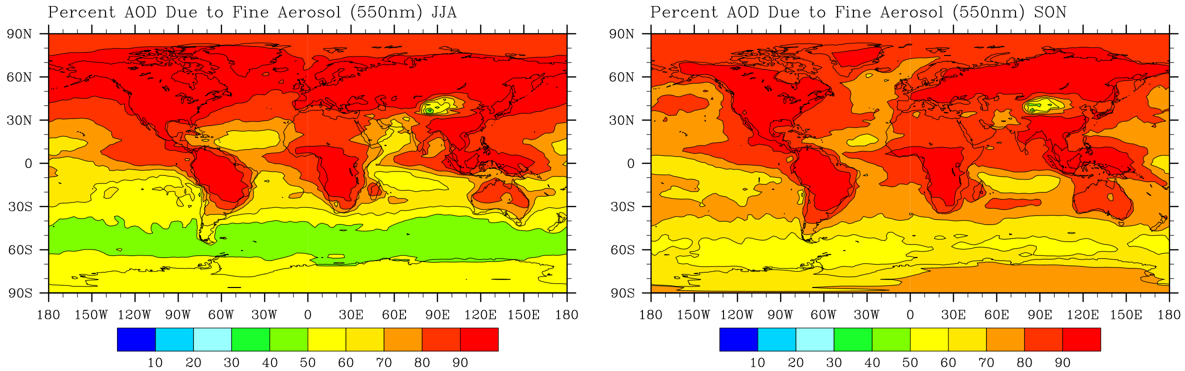

(c) June-July-August (d) September-October-November

Figure 4.53: Seasonally averaged aerosol optical depth fine contribution at 550nm for the 2007 CAM with AOD and angstrom and vertical adjustment assimilation (VERT). AOD fine contribution values are averaged for December/January/February (upper left), March/April/May (upper right), June/July/August (lower left), and September/October/November (lower right).

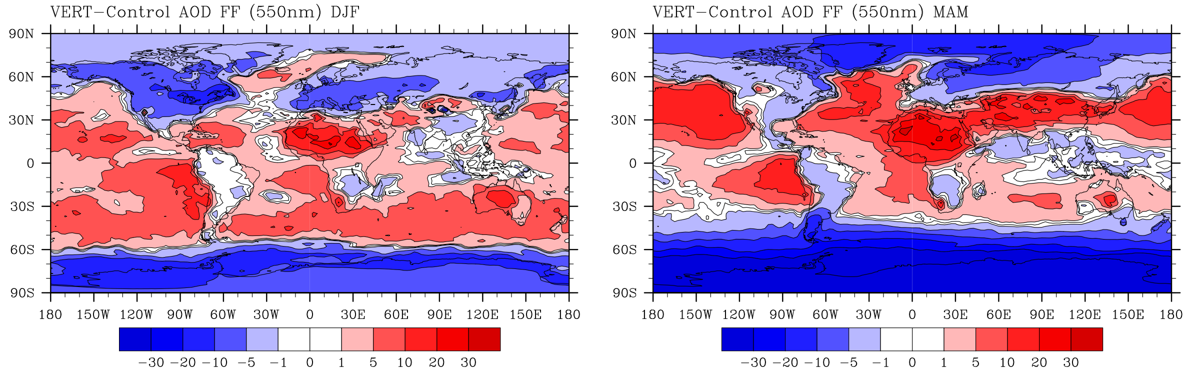

(a) December-January-February

(b) March-April-May

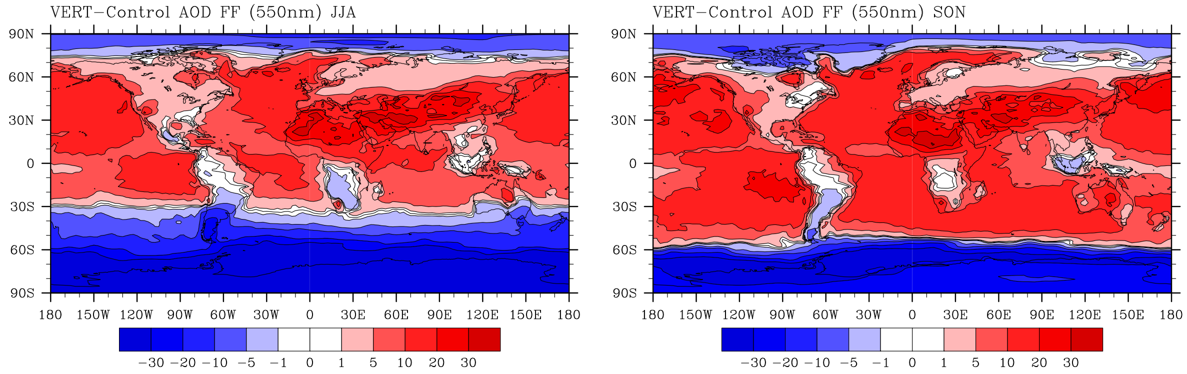

(c) June-July-August

(d) September-October-November

Figure 4.54: Seasonally averaged differences in aerosol optical depth fine contribution at 550nm between the CAM with AOD and angstrom with vertical adjustment assimilation (VERT) and the CAM control run. AOD fine contribution differences are averaged for a) December/January/February b) March/April/May c) June/July/August and d) September/October/November.

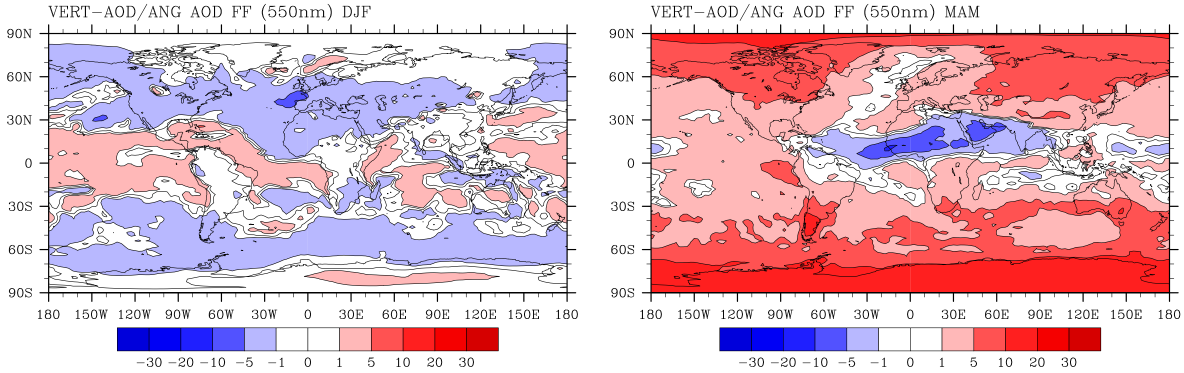

(a) December-January-February

(b) March-April-May

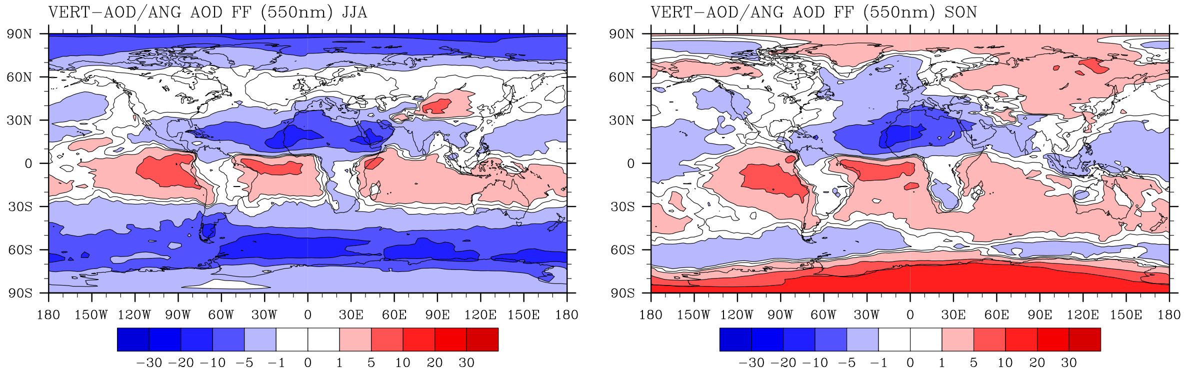

(c) June-July-August

(d) September-October-November

Figure 4.55: Seasonally averaged differences in aerosol optical depth fine contribution at 550nm between the CAM with AOD and angstrom with vertical adjustment assimilation (VERT) and the CAM with AOD and angstrom assimilation (AOD/ANG). AOD fine contribution differences are averaged for a) December/January/February b) March/April/May c) June/July/August and d) September/October/November.

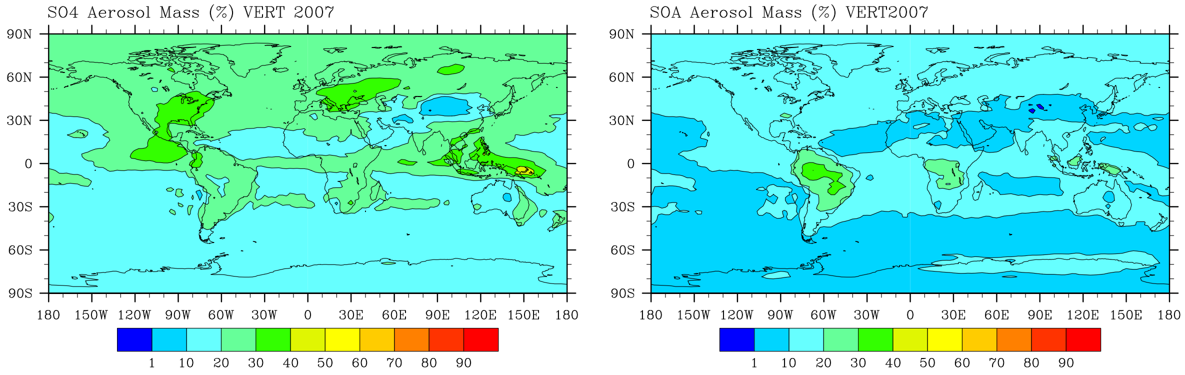

(a) Sulfate (b) Secondary Organic Aerosol

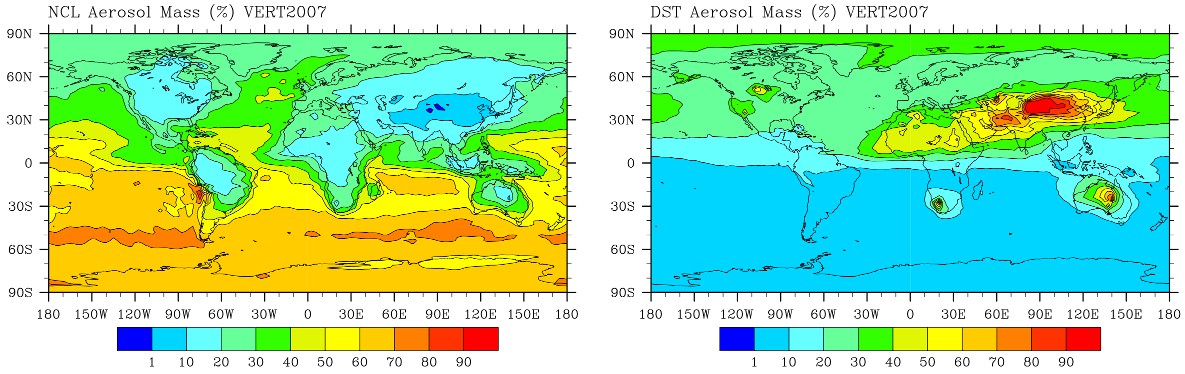

(c) Sea Salt (d) Dust

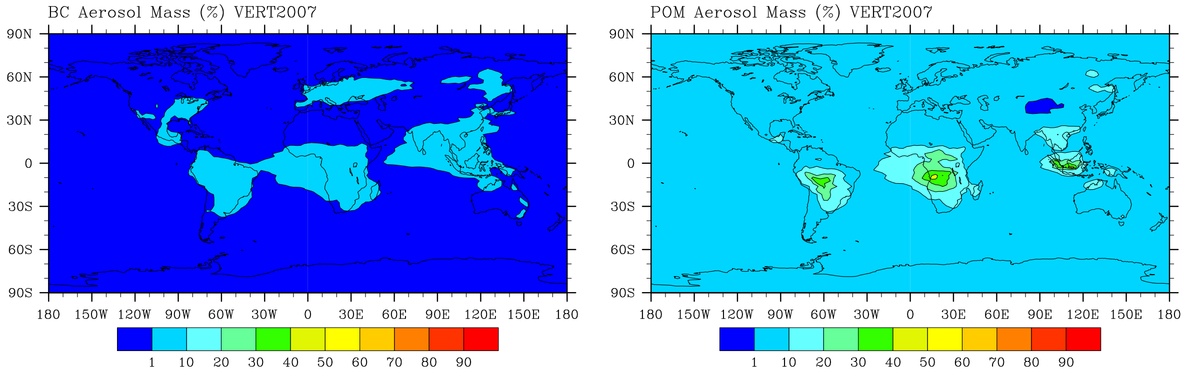

(e) Black Carbon (f) Primary Organic Aerosol

Figure 4.56: Average aerosol mass composition for the 2007 AOD and angstrom with vertical adjustment assimilation run (VERT) by percent. Results are shown for a) sulfate (SO4) b) secondary organic aerosol (SOA) c) sea salt (NCL) d) dust (DST) e) black carbon (BC) and f) primary organic aerosol (POM).

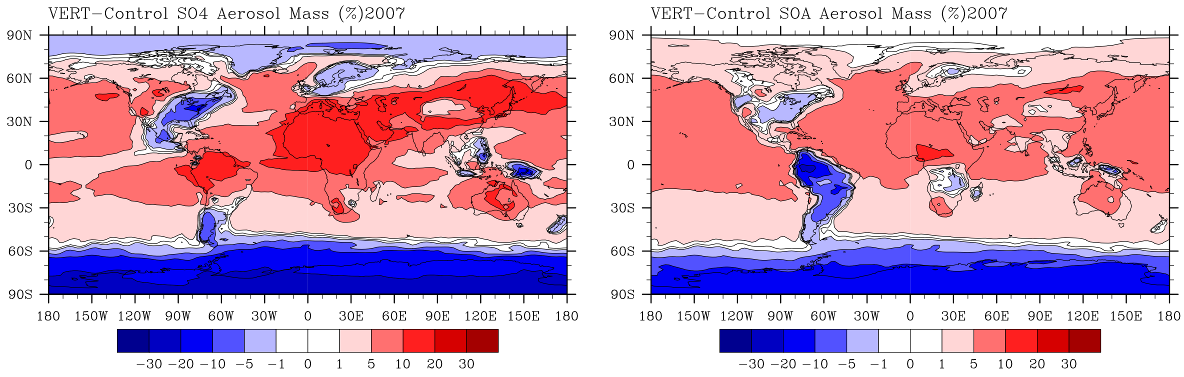

(a) Sulfate (b) Secondary Organic Aerosol

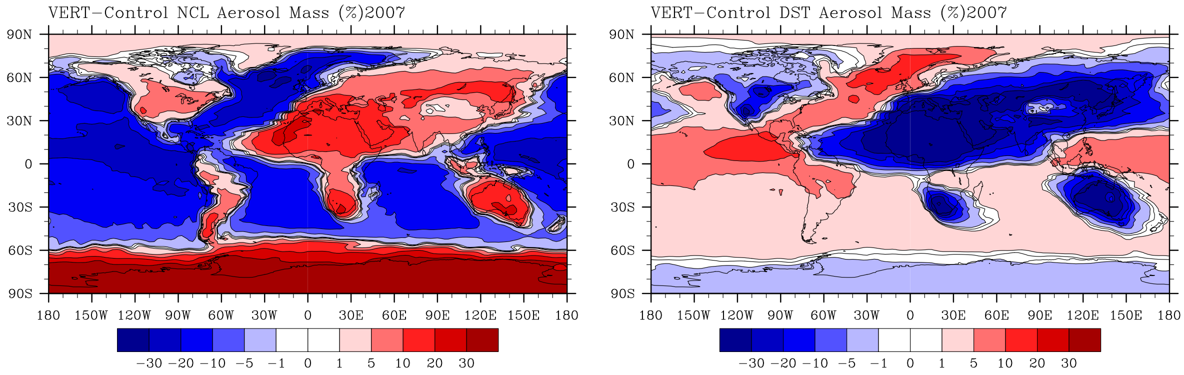

(c) Sea Salt (d) Dust

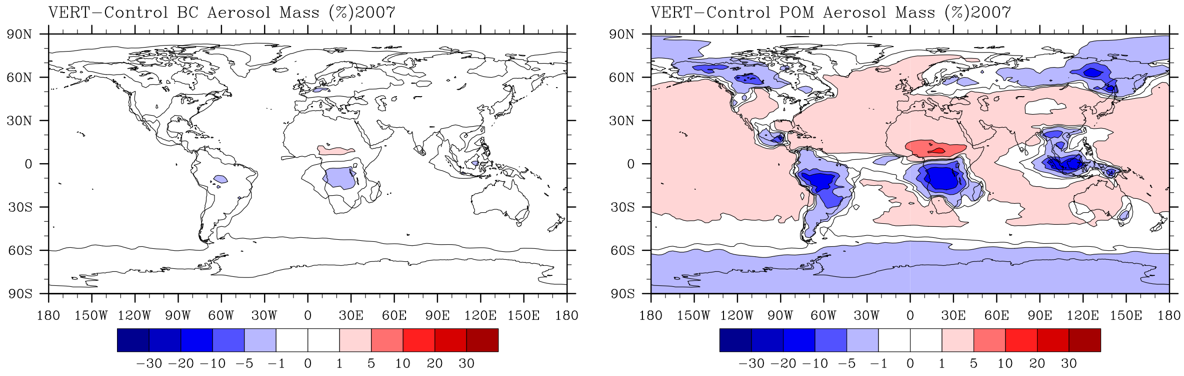

(e) Black Carbon (f) Primary Organic Aerosol

Figure 4.57: Average aerosol mass composition difference (% difference) between the AOD and angstrom with vertical adjustment assimilation run (VERT) and the CAM control run. Results are shown for a) sulfate (SO4) b) secondary organic aerosol (SOA) c) sea salt (NCL) d) dust (DST) e) black carbon (BC) and f) primary organic aerosol (POM).

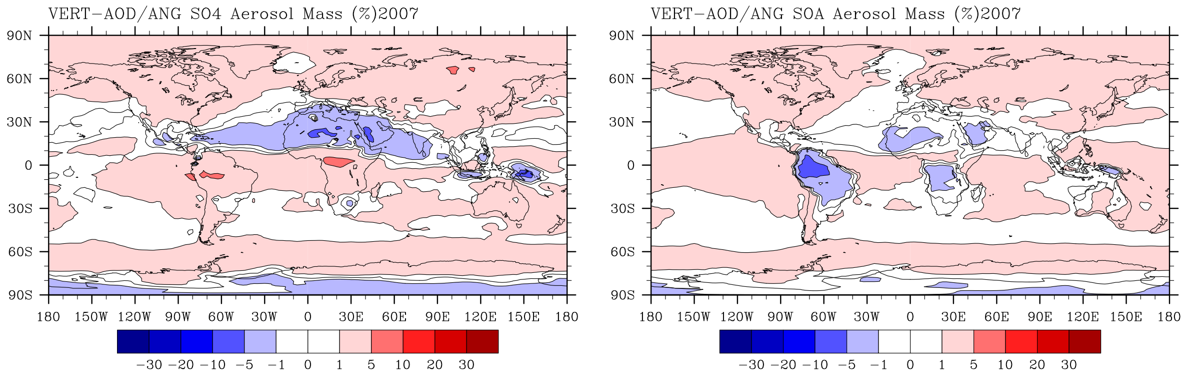

(a) Sulfate (b) Secondary Organic Aerosol

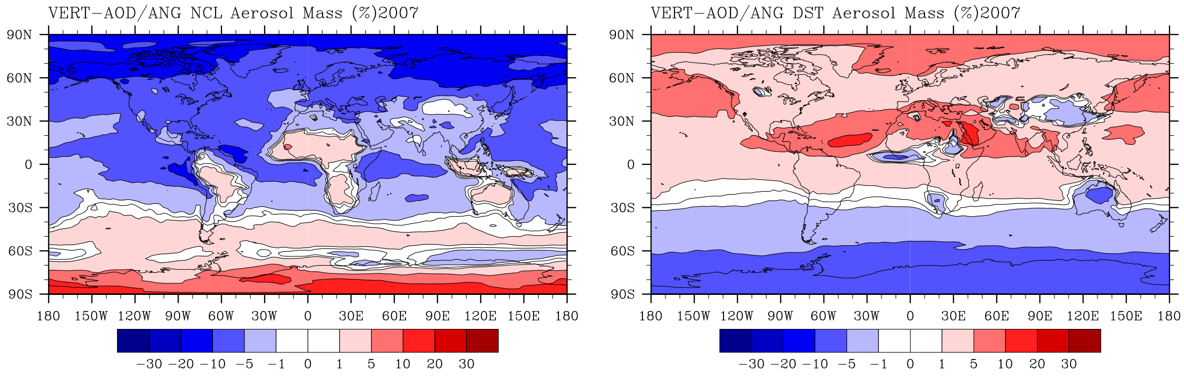

(c) Sea Salt (d) Dust

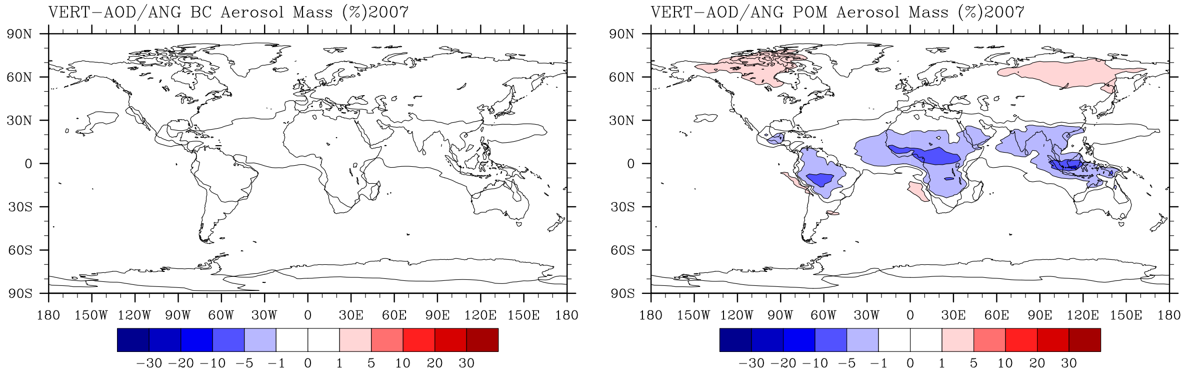

(e) Black Carbon (f) Primary Organic Aerosol

Figure 4.58: Average aerosol mass composition difference (% difference) between the AOD and angstrom with vertical adjustment assimilation run (VERT) and the AOD and angstrom assimilation (AOD/ANG). Results are shown for a) sulfate (SO4) b) secondary organic aerosol (SOA) c) sea salt (NCL) d) dust (DST) e) black carbon (BC) and f) primary organic aerosol (POM).

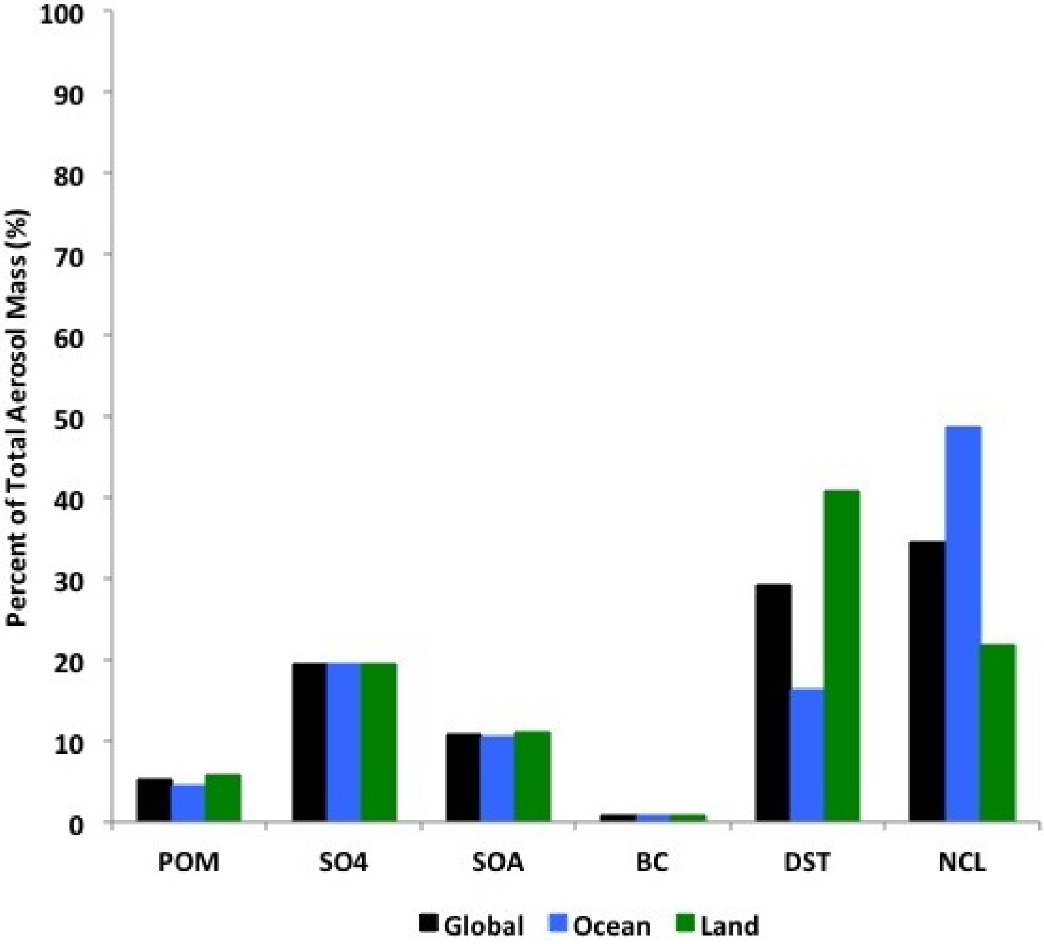

Figure 4.59: AOD and angstrom with vertical adjustment assimilation run (VERT) average aerosol composition by percent mass for the six aerosol types (primary organic aerosol, sulfate, secondary organic aerosol, black carbon, dust and sea salt). Results are globally averaged (Global), averaged over ocean only (Ocean), and over land only (Land).

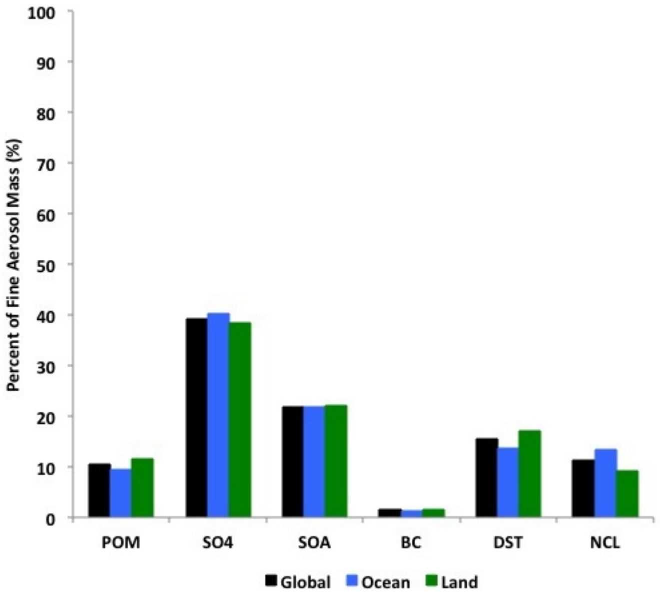

(a) Fine

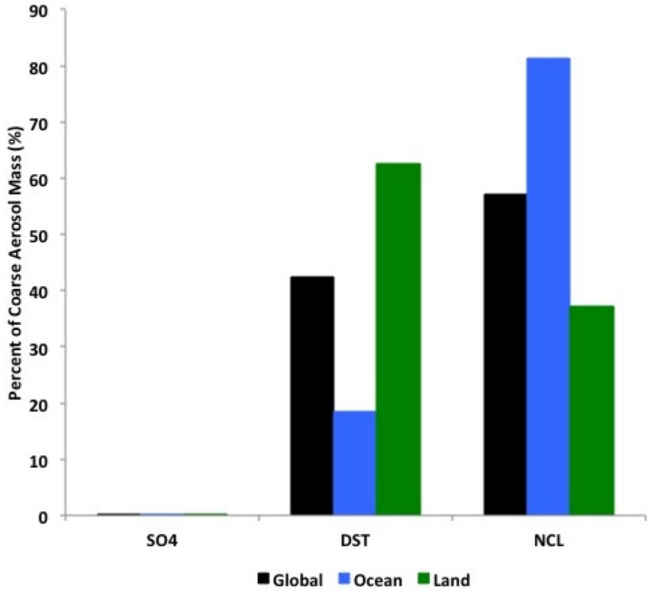

(b) Coarse

Figure 4.60: AOD and angstrom with vertical adjustment assimilation run (VERT) average aerosol composition by percent mass for the six aerosol types (primary organic aerosol, sulfate, secondary organic aerosol, black carbon, dust and sea salt) for a) fine aerosol and b) coarse aerosol. Results are globally averaged (Global), averaged over ocean only (Ocean), and over land only (Land).

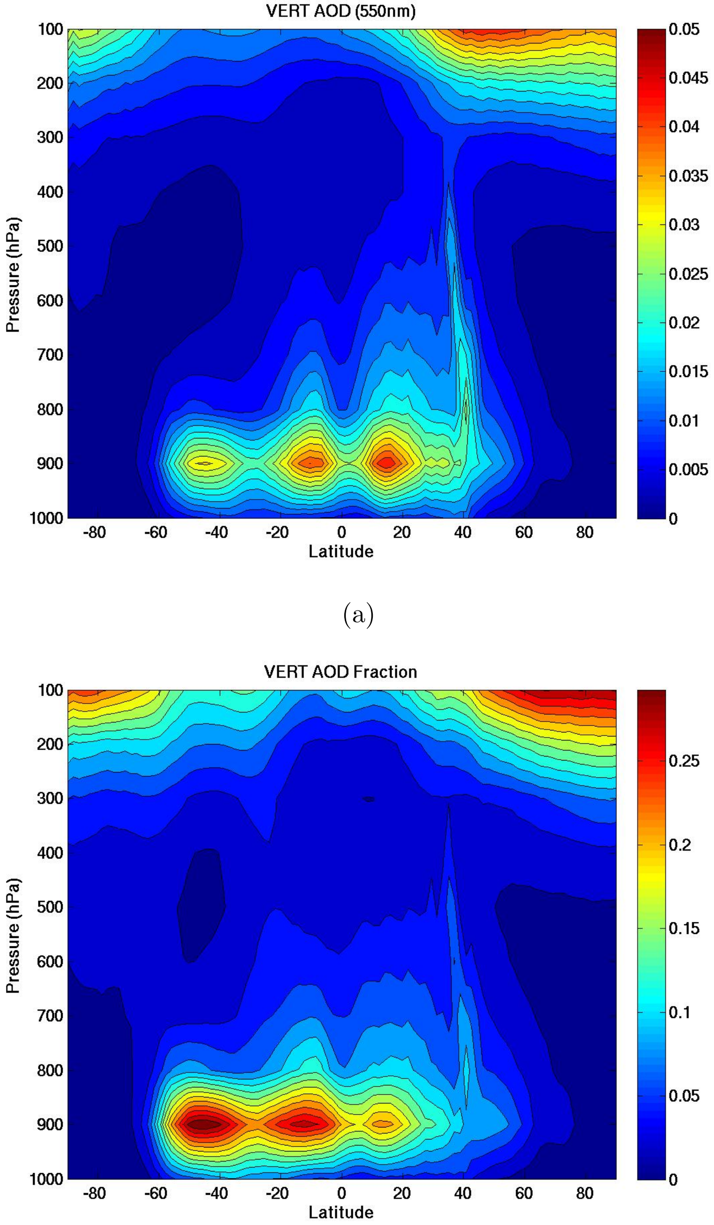

(a)

(b)

Figure 4.61: CAM with AOD and angstrom and vertical adjustment assimilation (VERT) zonally averaged a) aerosol optical depth and b) fraction of AOD in the vertical column profile for the year 2007.

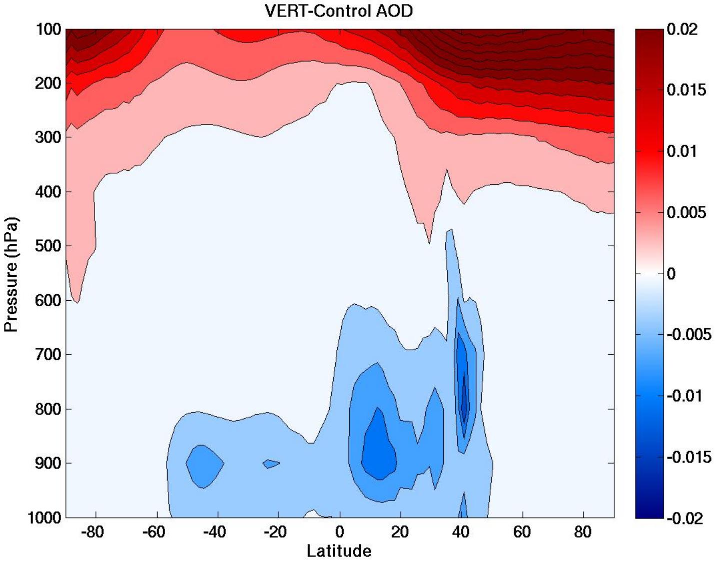

(a)

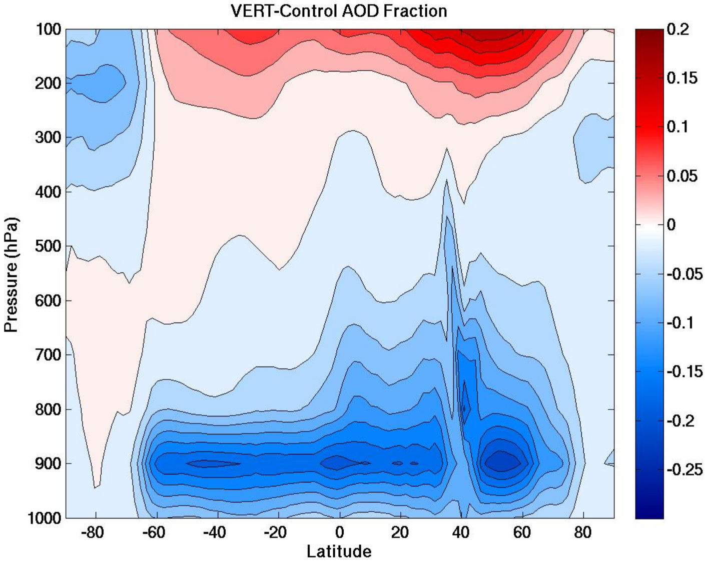

(b)

Figure 4.62: Zonally averaged difference in vertical profile between the CAM with AOD and angstrom and vertical adjustment assimilation (VERT) and the control run for a) aerosol optical depth and b) fraction of AOD in the vertical column profile for the year 2007.

Chapter 5

Anthropogenic Aerosol Analysis

The goal of this chapter is to investigate the anthropogenic contribution to AOD using predicted aerosol fields for the control, AOD/ANG assimilation, and VERT assimilation. As discussed previously, only the anthropogenic aerosol contribution can be considered an external cause of climate change, therefore, it is necessary to separate anthropogenic and natural aerosol contributions to scattering and absorption of shortwave radiation in the atmosphere. The results of this investigation are used in estimating the anthropogenic aerosol direct radiative forcing.

The identification of anthropogenic aerosol contribution to AOD is generally dependent on the distinction between the anthropogenic associated fine aerosol and the natural associated coarse. The simulations conducted in this work predict an average fine AOD contribution of 72.3±15% for the control run, 74.8±11.9% for the AOD/ANG assimilation run, and 75±11% for the VERT assimilation. This can be further broken down into over ocean and over land contributions. The control run predictions are 80.6±13.1% over land and 66.0±9.6% over ocean while the AOD and angstrom assimilation prediction is 82.0±9.9% over land and 69.3±8.1% over ocean and the VERT assimilation is 82.6±9.5% over land and 69.4±8.7% over ocean. Under the assumption that all fine aerosol is anthropogenic in origin, this would result on a global basis in 72.3% (80.6% over land and 66.0% over ocean), 74.8% (82.0% over land and 69.3% over ocean), and 75% (82.6% over land and 69.4% over ocean) of the AOD coming from anthropogenic aerosol for the control, AOD/ANG, and VERT assimilation run, respectively. However, previous analysis of aerosol composition in the fine mode indicates a natural component made up of dust and sea salt. Therefore, this assumption is not valid and the fine AOD percent only provides an upper bounds on the anthropogenic contribution.

As discussed previously, the fine aerosol has six components: black carbon, primary and secondary organic aerosol, sulfate, dust, and sea salt. Of these six components, primary organic aerosol, black carbon, dust and sea salt are primary aerosols meaning they are directly emitted into the atmosphere. As a result, examination of emissions can reveal whether the aerosols are primarily anthropogenic or natural in origin. For primary organic aerosol, natural emission sources include forest and grass fires while anthropogenic emissions include transportation, shipping, waste treatment, domestic, energy and industrial sources. On a mass basis, analysis of POM emissions reveal that greater than 99% is from anthropogenic sources. Black carbon was similar to POM with greater than 99% coming from anthropogenic sources. Therefore, both POM and black carbon are assumed to be all anthropogenic. Sea salt and dust emissions are parameterized and therefore, emission fields cannot be directly examined. However, all sea salt is assumed natural in origin [43]. All dust will be assumed natural as well, although approximately 10% of dust can be from anthropogenic sources [90]. Sulfate aerosol has both an anthropogenic and natural component with natural sulfate aerosol formed from DMS emissions occurring over the ocean. Since sulfate is formed secondarily in the atmosphere through gas to particle conversion processes, a simple examination of emissions cannot be conducted to determine the origin. However, natural sulfate comes from ocean emissions and will therefore, be tied together with sea salt aerosol into a natural marine aerosol. The remaining sulfate is anthropogenic. Similar to sulfate, secondary organic aerosol is formed from both anthropogenic and natural precursors. However, on a global average, SOA makes up only 4.11% of the aerosol mass and is limited to the fine aerosol mode. As a result, SOA is assumed anthropogenic. These assumptions are used to estimate the anthropogenic component of the optical depth.

The optical depth at 550nm (τ^t) is represented as a sum of optical depths from anthropogenic aerosol, dust aerosol, and background marine, which includes sea salt and sulfate aerosol from ocean emissions (Equation 5.1)[43]. The fine aerosol contribution to optical depth is represented in Equation 5.2 where ϕ^{anth}, ϕ^{dust}, and ϕ^{mar} represent the anthropogenic, dust and marine fine contributions to optical depth, respectively.

$$\tau^t = \tau^{anth} + \tau^{dust} + \tau^{mar} \tag{5.1}$$

$$\tau^f = \phi\tau^t = \phi^{anth}\tau^{anth} + \phi^{dust}\tau^{dust} + \phi^{mar}\tau^{mar} \tag{5.2}$$

In this analysis, the fine aerosol contribution to optical depth for each aerosol type is assumed constant [43]. Based on AERONET and MODIS analysis, it is assumed that the background marine optical depth τ^{mar} is 0.06±0.01 [46] [43]. The fine fraction for anthropogenic, dust and marine aerosol are determined by examining model results over specific regions dominated by these aerosol types. For anthropogenic aerosol, the eastern United States from 70° to 90° W and 40° to 50°N is used. The average fine aerosol contribution in this region for the year 2007 is 89.4±2.1%. For dust aerosol, the Sahara desert region is used from 15°W to 15°E and 15° to 30°N with an average fine contribution of 60.1±1.5%. For marine aerosol, 20° to 30°S and 50° to 120°E is used [43] with an average fine contribution of 61.4±8.6%. Using Equations 5.1 and 5.2, the optical depth due to dust is isolated and then plugged back into Equation 5.1 to produce Equation 5.3. With the estimated fine contributions and background marine optical depth, the anthropogenic optical depth can be solved. It should be noted that the background marine optical depth is used for optical depth calculations; however, stronger winds can results in sea salt concentrations that are higher than the background value. In Equation 5.3, extra coarse sea salt aerosol is attributed to dust, resulting in a negative anthropogenic optical depth. In this case, the anthropogenic optical depth is set to zero.

$$\tau^{anth} = \left[\phi\tau^{t} - \phi^{dust}\tau^{t} - \phi^{mar}\tau^{mar} + \phi^{dust}\tau^{mar}\right] / (\phi^{anth} - \phi^{dust}) \tag{5.3}$$

A map of the percent anthropogenic contribution to optical depth averaged for the year 2007 for the control run is shown in Figure 5.1a. The results show mostly anthropogenic contributions over land, except for over the dust regions, and a large natural component over oceans. On average, the anthropogenic contribution is 38.8%. The same calculation is conducted for the AOD/ANG assimilation run with results shown in Figure 5.1b. Clear spatial differences are seen between the control and assimilation run that are consistent with previous results, with higher anthropogenic contributions in the northern hemisphere. On average, the anthropogenic contribution in the assimilation run is 47.6%, higher than the control. The results of the anthropogenic AOD calculation for the VERT assimilation are shown in Figure 5.1c. The results are similar to the AOD/ANG assimilation with the exception of a lower anthropogenic contribution over the dusty Sahara and Arabian peninsulas and a higher anthropogenic contribution over the Southern hemisphere high latitudes. The globally averaged anthropogenic contribution to AOD for the VERT assimilation is 49.5%, higher than the previous simulations. These results can be compared to previously published anthropogenic AOD percentages, which range from 41 to 72% [84].

An uncertainty analysis is conducted, taking into account the errors in the fine aerosol contributions as well as the uncertainty in the background marine optical depth. The analysis uses error propagation techniques that are shown in Equations 5.4 through 5.8. The uncertainty analysis was applied to results for both the control and the two assimilation runs. The average uncertainty in the calculation of the anthropogenic optical depth for the simulations is approximately 30%. It should also be noted that the analysis did not take into account the percent of dust that may be anthropogenic in origin. This omission may result in an underestimation of the anthropogenic component where dust is present. Additionally, the assumption that SOA is 100% anthropogenic likely results in a overestimation of the anthropogenic component in regions such as South America where SOA makes up a larger percent of the aerosol mass.

$$\epsilon\left(\phi^{anth} - \phi^{dust}\right) = \epsilon(\phi^{anth}) + \epsilon(\phi^{dust}) \tag{5.4}$$

$$\epsilon\left(\phi^{dust}\tau^{t}\right) = \epsilon(\phi^{dust})\|\tau^{t}\|(5.5)$$

$$\epsilon(\phi^{mar}\tau^{mar}) = (\phi^{mar}\tau^{mar})\sqrt{\left(\frac{\epsilon(\phi^{mar})}{\phi^{mar}}\right)^2 + \left(\frac{\epsilon(\tau^{mar})}{\tau^{mar}}\right)^2} \tag{5.6}$$

$$\epsilon(\phi^{dust}\tau^{mar}) = (\phi^{dust}\tau^{mar})\sqrt{\left(\frac{\epsilon(\phi^{dust})}{\phi^{dust}}\right)^2 + \left(\frac{\epsilon(\tau^{mar})}{\tau^{mar}}\right)^2} \tag{5.7}$$

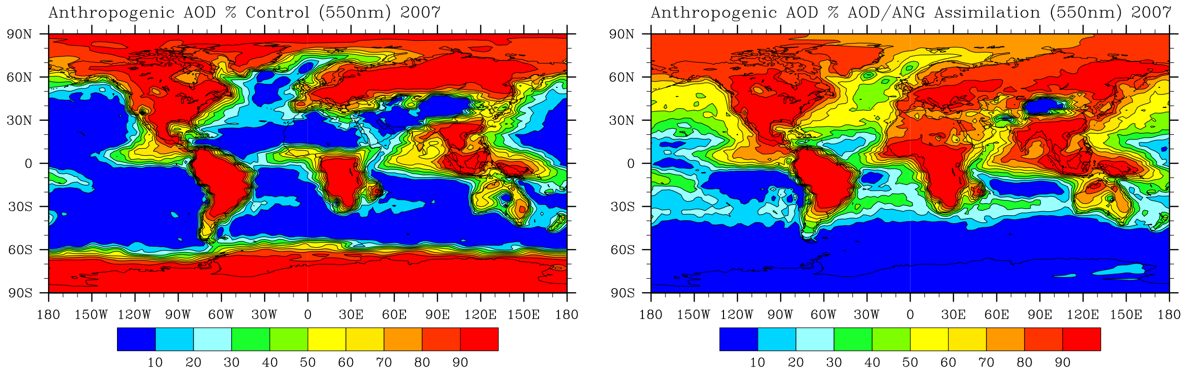

(a) Control)

(b) AOD/ANG

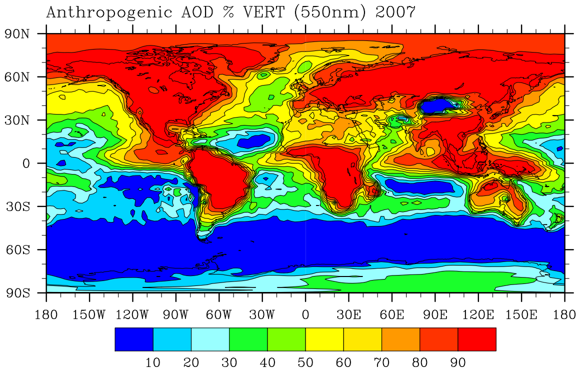

(c) VERT

Figure 5.1: Average estimated anthropogenic optical depth contribution (τ^{anth}) (%) for the 2007 a) control run b) AOD/ANG assimilation and c)VERT assimilation.

$$\epsilon\left(\tau^{anth}\right) = \tau^{anth}\sqrt{\left(\frac{\epsilon\left(\phi^{dust}\tau^{t}\right) + \epsilon\left(\phi^{mar}\tau^{mar}\right) + \epsilon\left(\phi^{dust}\tau^{mar}\right)}{\phi\tau^{t} - \phi^{dust}\tau^{t} - \phi^{mar}\tau^{mar} + \phi^{dust}\tau^{mar}}\right)^{2} + \left(\frac{\epsilon(\phi^{anth} - \phi^{dust})}{\phi^{anth} - \phi^{dust}}\right)^{2}} \tag{5.8}$$

Chapter 6

Aerosol Lifetime Analysis

The goal of this chapter is to investigate the predicted aerosol lifetime, an important factor in aerosol radiative forcing, for the control and the AOD/ANG and VERT assimilation runs. Additionally, the loss processes, which control aerosol lifetime, are examined. The VERT assimilation results are of special interest since adjustments to the vertical profile are expected to affect lifetime.

As previously discussed, loss processes control the lifetime of an aerosol in the atmosphere. Important loss processes, including wet and dry deposition, are dependent on factors including aerosol size, composition and vertical location in the atmosphere. For the aerosols modeled in this work, important loss processes include wet deposition (both in and below cloud scavenging), dry deposition (gravitational settling and turbulent transport to the surface), and activation of an aerosol to form a cloud droplet. Additionally, within the fine mode, coagulation, condensation, and evaporation processes can result in size mode changes between the nucleation and accumulation modes. Globally averaged loss processes were examined by aerosol type and size for each simulation conducted. The percent of the globally averaged aerosol loss rate due to the various loss processes for each of the three size modes is shown in Figures 6.1 through 6.3 . In the nucleation mode, loss of aerosol to the accumulation mode via condensational growth is particularly important (Figure 6.1). Decrease in the number concentration in the nucleation mode is dominated by coagulation. Number concentration is more sensitive to coagulation than mass since any amount of coagulation reduces number, but doesnt necessarily result in a loss of mass until the aerosol grows into the accumulation mode. Slight differences are observed between the control and the assimilation runs with coagulation and condensation becoming more important for sulfate in the assimilations, condensational growth decreasing for secondary organics and coagulation increasing for number concentration. For all species in the accumulation mode, activation to cloud droplets is an important loss process (Figure 6.2). The percent of activation increases from the control to the assimilation runs. The same trend is seen in the coarse mode with activation becoming more important in the assimilation run (Figure 6.3). With respect to the VERT assimilation, the breakdown of loss processes is almost the same as the AOD/ANG assimilation, indicating that changes to the vertical structure did not affect the types of loss processes controlling removal.

In order to understand changes in atmospheric lifetime, changes in the absolute loss rates must also be examined. The absolute values of the total loss rates from the assimilation runs are compared to the control run in Table 6.1. The loss rates increased in both assimilation runs for most species and size modes. Exceptions include nucleation mode sulfate and all dust aerosol. With respect to the two assimilation runs, the loss rates are slightly higher in the VERT assimilation with exceptions including nucleation mode sulfate, secondary organics and number concentration and accumulation mode sea salt. If the loss rate changes proportionally to the mass of aerosol in the atmosphere, then the lifetime should not change. The average mass by size and aerosol type for all simulations are examined in Table 6.2. In general, the mass increased relative to the control simulation with the increase being greater than the increase in the loss rate. This indicates that the aerosol lifetime should increase. Exceptions include coarse mode dust which had a decrease in both mass and loss rate. Between the two assimilations, the mass is higher in the VERT assimilation for the accumulation and coarse modes, but not the nucleation mode. Since the only difference between the two assimilations is the vertical redistribution of the coarse aerosol, it is expected that a difference in the coarse mode will be found. An examination of coarse mode dust shows an increase in mass of approximately 20 percent and an increase in the loss rate of only 2 percent. As a result, the lifetime of coarse dust should increase as expected. Likewise, coarse sea salt mass increases by 7 percent and the loss rate increases by 2 percent, again indicating an increase in lifetime.

The calculated average lifetimes for each species by size are shown in Tables 6.3 for the control, AOD/ANG assimilation and VERT assimilation runs. Additionally, reported AEROCOM lifetimes are included. For the control simulation, the order of species from shortest to longest lifetime is sea salt, dust, black carbon, SOA, POM and sulfate. Relative to AEROCOM, the lifetimes of black carbon, dust and primary organics are shorter while the lifetimes of sulfate and sea salt are longer. The greatest difference is found with sulfate aerosol, with the control simulation predicting a lifetime almost double the AEROCOM value. From the control to the AOD/ANG assimilation, the lifetime increases for all species except number concentration which is controlled by the nucleation mode. Also, coarse mode dust decreases in lifetime. It should be noted that this is consistent with the findings that, in the AOD/ANG assimilation, the angstrom exponent kept increasing despite decreases to the angstrom value by the EnKF (ie. increases in coarse aerosol). The coarse aerosol is not being maintained in the atmosphere while the fine aerosol has increased in lifetime. Compared to AEROCOM, the predicted lifetimes in the AOD/ANG assimilation run are closer to the AEROCOM values for most species, except sulfate which is more than double the AEROCOM value. This may explain the positive bias regions in AOD in the northern hemisphere where sulfate was found to be an important aerosol type. In the VERT assimilation, the lifetime of all species increased from the AOD/ANG assimilation, except for number concentration. Increases in lifetime for coarse mode dust and sea salt were expected given the use of the vertical redistribution. In the VERT assimilation, the lifetimes of sulfate and secondary organics are the longest. This explains the increase in importance of these two species in the Northern hemisphere as well as the positive bias in AOD values observed. Relative to AEROCOM, the lifetimes from the VERT assimilation are closest to the reported values for black carbon, dust and primary organics.

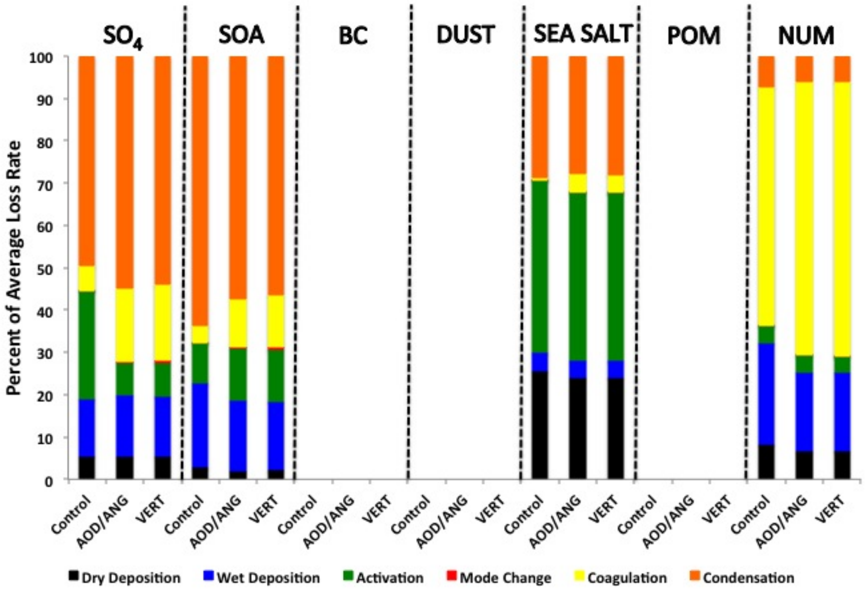

Figure 6.1: Percent of the globally averaged aerosol loss rate due to dry deposition, wet deposition, activation to cloud droplets, mode change by coagulation and mode change by condensational growth for the nucleation size modes. Results are shown for the control simulation (Control), the AOD and angstrom assimilation (AOD/ANG) and the AOD and angstrom with vertical adjustment assimilation (VERT) as well as by aerosol type (sulfate (SO4), secondary organic aerosol (SOA), black carbon (BC), dust (DUST), sea salt (SEA SALT), primary organic matter (POM) and number concentration (NUM)).

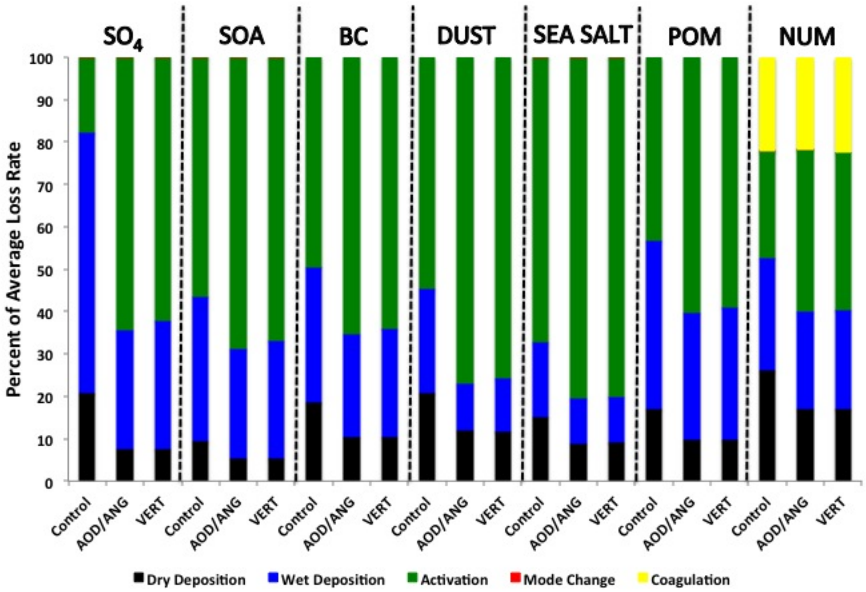

Figure 6.2: Percent of the globally averaged aerosol loss rate due to dry deposition, wet deposition, activation to cloud droplets, mode change by coagulation and mode change by condensational growth for the accumulation size modes. Results are shown for the control simulation (Control), the AOD and angstrom assimilation (AOD/ANG) and the AOD and angstrom with vertical adjustment assimilation (VERT) as well as by aerosol type (sulfate (SO4), secondary organic aerosol (SOA), black carbon (BC), dust (DUST), sea salt (SEA SALT), primary organic matter (POM) and number concentration (NUM)).

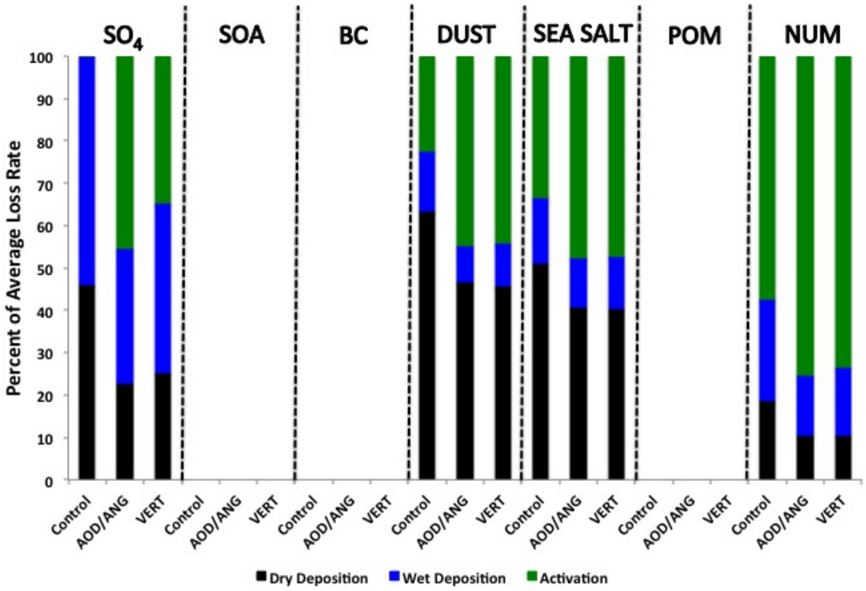

Figure 6.3: Percent of the globally averaged aerosol loss rate due to dry deposition, wet deposition, and activation to cloud droplets for the coarse size modes. Results are shown for the control simulation (Control), the AOD and angstrom assimilation (AOD/ANG) and the AOD and angstrom with vertical adjustment assimilation (VERT) as well as by aerosol type (sulfate (SO4), secondary organic aerosol (SOA), black carbon (BC), dust (DUST), sea salt (SEA SALT), primary organic matter (POM) and number concentration (NUM)).

		LossRate (kg/m^2/s or #/m^2/s)			**%Difference (Assim – Control)**		
	Simulation	**Nuc**	**Accum**	**Coarse**	**Nuc**	**Accum**	**Coarse**
SO$_4$	Control	8.28e-13	4.51e-12	1.21e-13	–	–	–
	AOD/ANG	7.21e-13	9.83e-12	1.84e-13	-12.9	117.8	51.4
	VERT	7.01e-13	9.99e-12	2.57e-13	-15.3	121.5	112.2
SOA	Control	1.83e-13	4.29e-12	–	–	–	–
	AOD/ANG	2.08e-13	5.93e-12	–	14.2	38.3	–
	VERT	2.01e-13	6.22e-12	–	10.0	45.12	–
BC	Control	–	4.76e-13	–	–	–	–
	AOD/ANG	–	6.93e-13	–	–	45.5	–
	VERT	–	7.22e-13	–	–	51.6	–
DUST	Control	–	6.47e-12	1.96e-10	–	–	–
	AOD/ANG	–	4.94e-12	1.28e-10	–	-23.7	-34.3
	VERT	–	5.04e-12	1.31e-10	–	-22.1	-33.3
NCL	Control	4.77e-14	7.77e-12	2.29e-10	–	–	–
	AOD/ANG	5.16e-14	1.21e-11	2.85e-10	8.2	56.0	24.9
	VERT	5.16e-14	1.19e-11	2.91e-10	8.1	53.8	27.2
POM	Control	–	3.09e-12	–	–	–	–
	AOD/ANG	–	4.42e-12	–	–	43.2	–
	VERT	–	4.63-12	–	–	49.7	–
NUM	Control	8.53e6	3.62e6	1.19e4	–	–	–
	AOD/ANG	1.05e7	4.56e6	1.70e4	22.6	26.0	42.4
	VERT	1.01e7	4.65e6	1.83e4	18.5	28.4	53.9

Table 6.1: Loss rates by aerosol species and size for control, AOD and angstrom assimilation (AOD/ANG) and for the vertical assimilation (VERT). Absolute values are shown as well as percent difference from the control run.

		Burden (**kg/m^2 or #/m^2**)			**%Difference** (**Assim – Control**)		
	Simulation	**Nuc**	**Accum**	**Coarse**	**Nuc**	**Accum**	**Coarse**
SO_4	Control	2.29e-7	3.31e-6	3.42e-8	–	–	–
	AOD/ANG	2.33e-7	7.71e-6	7.04e-8	1.8	133.2	105.6
	VERT	2.13e-07	1.00e-5	7.60e-8	-7.0	202.1	122.2
SOA	Control	4.86e-8	1.61e-6	–	–	–	–
	AOD/ANG	5.57e-8	4.22e-6	–	14.6	162.9	–
	VERT	5.16e-8	5.67e-6	–	6.17	252.2	–
BC	Control	–	1.68e-7	–	–	–	–
	AOD/ANG	–	3.14e-7	–	–	86.6	–
	VERT	–	3.96e-7	–	–	136.3	–
DUST	Control	–	2.58e-6	2.14e-5	–	–	–
	AOD/ANG	–	3.11e-6	9.20e-6	–	20.7	-57.0
	VERT	–	4.05e-6	1.14e-5	–	57.0	-46.7
NCL	Control	1.56e-9	1.24e-6	8.40e-6	–	–	–
	AOD/ANG	1.54e-9	2.33e-6	1.43e-5	-1.5	88.0	69.8
	VERT	1.51e-9	2.92e-6	1.53e-5	-3.2	135.5	82.1
POM	Control	–	1.28e-6	–	–	–	–
	AOD/ANG	–	2.20e-6	–	–	72.5	–
	VERT	–	2.76e-6	–	–	115.6	–
NUM	Control	4.63e12	9.89e11	1.87e9	–	–	–
	AOD/ANG	3.94e12	1.35e12	2.73e9	-14.9	36.6	45.5
	VERT	3.61e12	1.44e12	2.93e9	-22.0	45.6	56.7

Table 6.2: Average mass (or number) by aerosol species and size for control, AOD and angstrom assimilation (AOD/ANG) and for the vertical assimilation (VERT). Absolute values are shown as well as percent difference from the control run.

Lifetime (days)	**Simulation**	**Nuc**	**Accum**	**Coarse**	**Total**	**AEROCOM**
SO_4	Control	3.19	8.48	3.26	8.09	4.12
	AOD/ANG	3.72	9.08	4.43	8.88	
	VERT	3.50	10.2	3.42	10.2	
SOA	Control	3.07	4.33	–	4.30	–
	AOD/ANG	3.08	8.24	–	8.17	
	VERT	2.96	10.1	–	10.1	
BC	Control	–	4.09	–	4.09	7.12
	AOD/ANG	–	5.25	–	5.25	
	VERT	–	6.37	–	6.37	
DUST	Control	–	4.60	1.27	1.63	4.14
	AOD/ANG	–	7.28	0.83	2.45	
	VERT	–	9.30	1.00	3.18	
NCL	Control	0.38	1.85	0.43	0.61	0.48
	AOD/ANG	0.34	2.23	0.58	0.81	
	VERT	0.34	2.82	0.61	0.96	
POM	Control	–	4.79	–	4.79	6.54
	AOD/ANG	–	5.77	–	5.77	
	VERT	–	6.92	–	6.92	
NUM	Control	6.28	3.15	1.79	5.73	–
	AOD/ANG	4.36	3.42	1.82	4.12	
	VERT	4.13	3.59	1.82	3.97	

Table 6.3: Average lifetime (days) for the control (Control), AOD and angstrom assimilation (AOD/ANG) and the assimilation with vertical (VERT) for the six modeled species (sulfate, secondary organic aerosol, black carbon, dust, sea salt, and primary organics). Additionally, lifetime is calculated based on number concentration. Results are shown by size mode. Results are compared against average lifetime values reported by AEROCOM [92].

Chapter 7

Aerosol Shortwave Radiative Forcing

The goal of this chapter is to understand the impact of the predicted aerosol fields from the control, AOD/ANG assimilation, and VERT assimilation on the Earth's climate. As discussed previously, radiative forcing is a measure for quantifying the impact and is defined as the change in net radiation at the TOA with a positive value indicating a warming and a negative value indicating a cooling effect. For this research, the focus is on the effect of the predicted aerosol in the shortwave part of the spectrum. The results from the three model runs are used to estimate the solar direct radiative effect (DRE) and the anthropogenic direct radiative forcing.

As discussed previously, the DRE is the radiative forcing in the shortwave due to the direct effect of both anthropogenic and natural aerosols combined. The DRE is calculated for each of the simulations conducted in this work. In order to determine the DRE, a fourth control simulation was conducted for 2007 without any aerosol present in the atmosphere. The DRE is then calculated as the difference in the net clearsky shortwave flux ($F_{sw}^{(TOA)}$) between the simulation of interest and the simulation without aerosol present (Equation 1.4). For the assimilation runs, the ensemble members are used to determine the uncertainty in the calculated DRE. The results for the control, AOD/ANG assimilation and VERT assimilation are shown in Figure 7.1 . In the control simulation (Figure 7.1a), negative DRE values are observed in most locations with exceptions over the Sahara desert and Antarctica. As discussed previously, positive values can occur over bright surfaces including desert sand and ice. Globally averaged, the control DRE is -1.91 W/m^2. The AOD and angstrom assimilation has negative DRE values with high latitude regions as the exception (Figure 7.1b). The decrease in dust explains the change from positive to negative DRE over the Sahara since dust has an absorbing component. Additionally, the increase in AOD from the control to the AOD/ANG assimilation explains the increase in magnitude of the DRE. The hemispheric difference in AOD observed in the AOD/ANG assimilation is also reflected in the higher DRE values observed in the Northern hemisphere. The globally averaged DRE for the AOD/ANG assimilation is -5.2(±0.51) W/m^2. The VERT assimilation shows similar patterns in DRE to the AOD/ANG assimilation with some differences found over ocean (larger negative forcing). The globally averaged DRE for the VERT assimilation is

-7.2(±0.94) W/m^2. The increase in AOD from the AOD/ANG to the VERT assimilation run is reflected in the increase in magnitude of the DRE. The AOD/ANG estimate of the DRE is consistent with values reported in the literature while the control value is on the low end and the VERT assimilation is on the upper end of reported estimates [70] [84] [93].

In addition to the DRE, estimating the anthropogenic contribution to the direct radiative forcing is important since only anthropogenic aerosol can be considered as an external cause of climate change. The results from the analysis of the anthropogenic contribution to AOD were used in conjunction with the DRE estimates to determine an anthropogenic direct RF value for each simulation. For aerosol that is dominantly scattering and follows the single scattering approximation, the radiative forcing scales with the optical depth. The single scattering albedo, the fraction of extinction due to scattering, is shown in Figure 7.2 for the control, AOD/ANG assimilation and the VERT assimilation, respectively. For all simulations, the single scattering albedo is greater than 0.9 in most locations, with exceptions over parts of Africa and southeast Asia (≈0.85). Assuming the single scattering approximation is valid, the anthropogenic radiative forcing can be calculated by multiplying the DRE by the fraction of AOD that is anthropogenic, grid point by grid point. For the assimilation runs, the DRE ensemble spread and the uncertainty in the anthropogenic AOD were used to calculate bounds on the anthropogenic RF estimate. The anthropogenic direct RF results for the control, AOD/ANG assimilation and VERT assimilation are shown in Figure 7.3. For the control simulation, the anthropogenic RF is mostly over land and negative over most locations with an average anthropogenic direct RF of -0.77 W/m^2. For the AOD/ANG assimilation, the anthropogenic RF mostly exists in the northern hemisphere and is mostly negative with an average aerosol direct RF of -2.3(±0.64) W/m^2. The VERT assimilation results show a similar pattern to the AOD/ANG assimilation, however, the magnitude is greater with a globally averaged aerosol direct RF of -3.2(±0.7) W/m^2. All three simulations predict a negative globally averaged shortwave DRE and anthropogenic direct RF, indicating a cooling influence of the predicted aerosol.

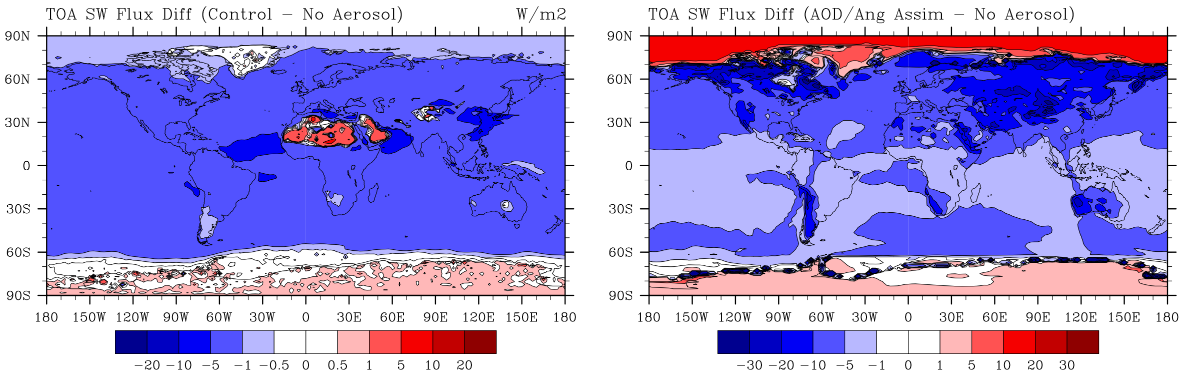

(a) Control

(b) AOD/ANG

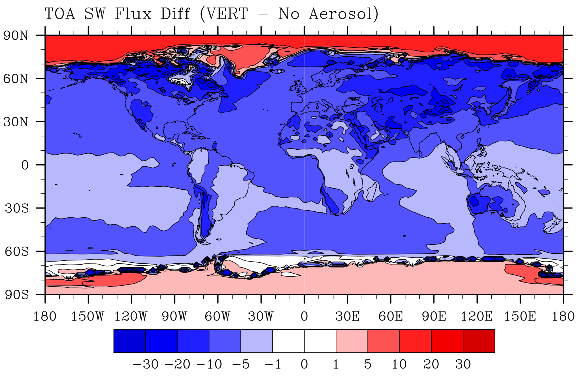

(c) VERT

Figure 7.1: The average 2007 solar direct radiative effect (DRE) for the a) control b) AOD and angstrom assimilation and c) AOD and angstrom assimilation with vertical adjustment. Results are shown in W/m^2 with blue regions having a negative radiative forcing and red regions having a positive radiative forcing.

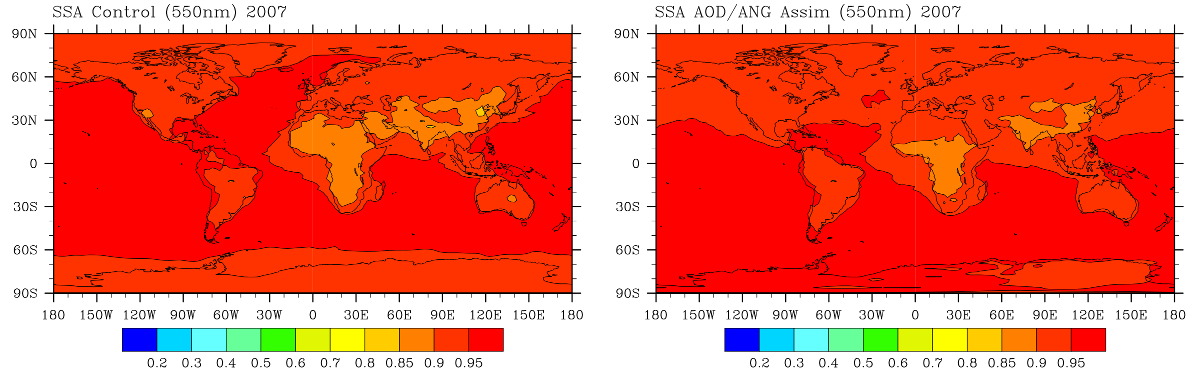

(a) Control (b) AOD/ANG

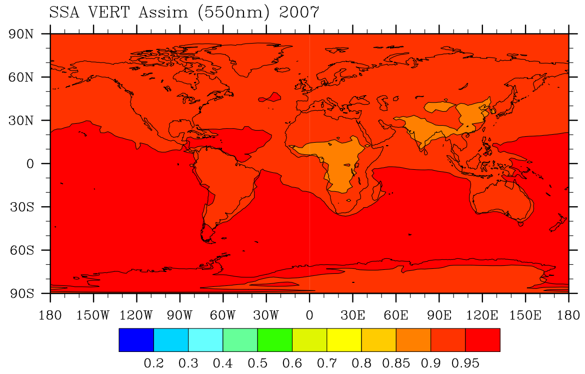

(c) VERT

Figure 7.2: The average 2007 single scattering albedo (0.55μm) (ω) for the a) control b) AOD and angstrom assimilation and c) AOD and angstrom assimilation with vertical adjustment. The single scattering albedo represents the fraction of extinction due to scattering.

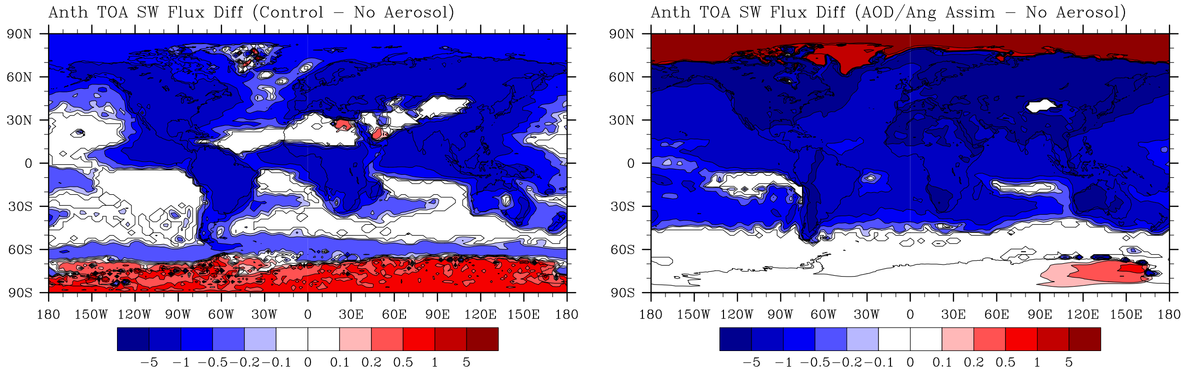

(a) Control

(b) AOD/ANG

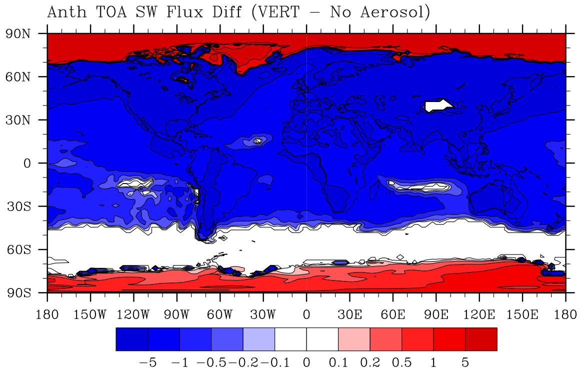

(c) VERT

Figure 7.3: The average 2007 anthropogenic direct aerosol radiative forcing for the a) control b) AOD and angstrom assimilation and c) AOD and angstrom assimilation with vertical adjustment. Results are shown in W/m^2 with blue regions having a negative radiative forcing and red regions having a positive radiative forcing.

Chapter 8

Conclusion

8.1 Summary of Findings

There were two goals associated with this research: 1) predict global aerosol fields with reduced uncertainty using data assimilation, a technique that uses observations to constrain model predictions and 2) investigate aerosol sources, lifetime and shortwave radiative forcing using the predicted aerosol fields. Two new aerosol assimilations that make use of an Ensemble Kalman Filter were presented as part of this work with the first assimilation making a joint adjustment in the amount of atmospheric aerosol as well as the relative contribution of fine and coarse aerosol. The assimilation was conducted using NCAR's CAM model and observations from NASA's MODIS and AERONET instruments. The amount and relative size of aerosol were identified as key parameters in radiative forcing estimates through an investigation of aerosols and their effect on outgoing shortwave radiation. Additionally, it was confirmed through principle component analysis that the amount and relative size of fine and coarse aerosol are independent pieces of information contained in MODIS spectral radiances. The second assimilation presented as part of this work is similar to the first with the addition of a vertical redistribution of coarse aerosol using extinction profile observations from NASA's CALIPSO satellite. Strong correlations were found between the model-predicted coarse aerosol profiles and the corresponding extinction profiles, leading to the vertical redistribution of coarse aerosol only. Studies have shown that aerosol lifetime and vertical profile are tightly coupled, therefore, vertical adjustments were expected to further reduce uncertainty, especially in coarse aerosol predictions. The presented assimilations were run for the year 2007.

The effectiveness of the aerosol assimilations were demonstrated by comparing predicted aerosol optical depth (AOD), angstrom exponent, and AOD fine aerosol contribution fields to control run predictions as well as observations from MODIS and AERONET. Control run comparisons to MODIS observations revealed a persistent negative bias in AOD predictions, indicating an under-prediction of the amount of atmospheric aerosol. The globally averaged AOD for the year 2007 predicted by the control run was 0.086(±0.06) while the globally averaged observed AOD by MODIS was 0.161(±0.09). The negative bias decreased in the assimilation runs with globally averaged AOD values for the year 2007 of 0.115(±0.05) and 0.140(±0.05) for the amount and size assimilation and the vertical assimilation, respectively. Average AOD values from the three simulations were found to be statistically different, indicating that the presented assimilations had a statistically significant effect on predicted AOD. In addition to increased predictions in AOD, the assimilation runs were able to better capture spatial and temporal variations in aerosol with the highest AOD values observed in the Northern Hemisphere spring through summertime. Both positive and negative biases were observed in the control run predictions of over-ocean angstrom exponents with positive biases indicating an over-prediction of fine aerosol and negative biases indicating an over-prediction of coarse aerosol. Over-ocean averaged angstrom exponent predictions from the control run are 0.65(±0.35) while the size and amount and vertical assimilation predictions are 0.68 (±0.15) and 0.66 (±0.15), respectively. This is compared to globally averaged MODIS observations of 0.65(±0.30). While it is difficult to determine improvements in angstrom exponent predictions based on the global average, clear reductions in regional biases were observed. Clear differences were also found between the two assimilation runs in regions dominated by coarse aerosol, especially the dusty Sahara, with higher AOD values and lower angstrom exponents in the vertical assimilation. This difference indicates an increase in the presence of atmospheric coarse aerosol in the vertical assimilation.

Assimilation results were also compared to ground-based AERONET observations by site category, including desert dust, biomass burning, rural, industrial pollution, polluted marine, and dirty pollution. While the rural sites had statistically similar averaged AOD values across simulations, improvements were found for the other site categories in the assimilation runs with higher average AOD values and greater temporal variability. With respect to the amount of AOD due to fine aerosol, the greatest reduction in bias was observed for polluted marine sites with the assimilations predicting a smaller fine aerosol contribution than the control simulation. This result is encouraging given that the size-related observations used in the assimilation were concentrated over ocean regions and, therefore, the marine sites should be most affected. Additionally, the positive bias in fine aerosol contribution predicted at dusty sites was reduced the most in the vertical assimilation. This is expected since dust is mostly coarse in size and the vertical assimilation adjusted the profile of coarse aerosol only. In summary, the comparison of the new aerosol assimilation results to the control run and observations revealed a decrease in the bias of predicted AOD and fine aerosol contributions to AOD with temporal and spatial variations in line with observations.

In addition to assessing the performance of the assimilation systems, the predicted aerosol fields were used to investigate the anthropogenic aerosol contribution to AOD, aerosol lifetime and aerosol radiative forcing. Since only anthropogenic aerosol can be considered an external cause of climate change, it is necessary to quantify the anthropogenic contribution for radiative forcing calculations. Globally averaged, the anthropogenic contribution to AOD was 38.8% for the control simulation, 47.6% for the amount and size assimilation and 49.5% from the vertical assimilation. These results are comparable to previously published anthropogenic AOD percentages which range from 41 to 72% [84]. Additionally, aerosol loss processes and lifetime were analyzed. The dominant loss processes were condensational growth for nucleation mode aerosol (fine, $<0.1\mu$m), activation and wet deposition for accumulation mode aerosol (fine, 0.1-1μm), and dry deposition and activation for coarse mode aerosol ($>1\mu$m). The longest aerosol lifetimes were found in the vertical assimilation with most aerosol species showing better comparison to reported AEROCOM lifetimes, except for sulfate. In particular, the lifetimes of coarse mode dust and sea salt increased in the vertical adjustment assimilation, reducing the negative aerosol optical depth bias, especially in dusty regions. The predicted sulfate lifetime was double the reported AEROCOM value and may be the cause of some positive AOD bias regions in the Northern hemisphere predicted in the model runs.

The solar direct radiative forcing (DRE) was calculated using the predicted aerosol fields with the DRE including the effects of both anthropogenic and natural aerosol. Uncertainties in DRE for the assimilation runs were determined using the 60 member ensemble spread. Globally averaged DRE values were -1.9W/m^2, -5.2($\pm$0.51)W/m^2, and -7.2($\pm$0.94)W/m^2, for the control, amount and size and vertical assimilation, respectively. The predicted DRE from the amount and size assimilation compared the best to previously published estimates. Additionally, the calculated anthropogenic contribution to AOD was used in conjunction with the DRE estimates to calculate anthropogenic radiative forcing estimates with predicted values of -0.77, -2.3($\pm$0.64) and -3.2($\pm$0.7)W/m^2 for the control, amount and size assimilation and vertical assimilation, respectively. Again, the spread in the ensemble members was used to determine the uncertainty in the assimilation run anthropogenic RF estimates. All results indicate a cooling influence by the predicted aerosol with an increased cooling influence in the assimilation runs.

8.2 Next Steps and Future Research

The next step for this research is to further investigate aerosol radiative forcing using the assimilated aerosol fields. The DRE and the anthropogenic direct radiative forcing were quantified for the presented aerosol assimilations. As previously discussed, it is also expected that changes to the amount of aerosol, size and vertical profile will effect aerosol-cloud interactions. This was confirmed in observed differences between the assimilation and control run such as changes in aerosol number concentration, increased aerosol activation, and changes in cloud cover. The next step will be to quantify the aerosol first indirect effect. A new release of NCAR's CAM model that includes aerosol-cloud interactions related to the first indirect effect and provides the ability to use prescribed modal aerosol is expected to be available soon. This will allow the insertion of the predicted modal aerosol fields from this work into the new version of CAM in order to quantify the aerosol first indirect effect.

The predicted aerosol fields from this work can also be useful in investigating other physical processes that are related to aerosol amount, size and vertical profile. Given that cloud-aerosol interactions are important for precipitation, an investigation of changes to the hydrological cycle can be conducted. Additionally, spatial differences in aerosol radiative forcing have been shown to affect atmospheric dynamics including shifts in the Intertropical Convergence Zone (ITCZ) and altering the strength of the Hadley circulation [3]. Assimilated aerosol fields could be used to investigate impacts on dynamics.

Future steps can also be taken with respect to aerosol assimilation, a relatively new area of research. A next step would be the direct assimilation of MODIS radiances which would be an improvement upon AOD assimilation. Retrieving AOD from spectral radiances is an underdetermined problem as discussed previously. As a result, additional and less accurate statistical information is introduced in the retrieval process. The additional uncertainty introduced by the a priori assumptions inherent in retrievals regarding aerosol microphysical and optical properties can be avoided by using the directly-measured satellite radiances as the observations in the assimilation procedure. As demonstrated in the MODIS independent information analysis, the radiances could be used in a similar manner to the AOD and angstrom exponent scalings used in this work. An aerosol radiance assimilation would require coupling CAM with an accurate radiative transfer model, such as MODTRAN, and quantifying the surface reflectance properties in order to accurately simulate model radiances for comparison with observations.

Bibliography

[1] H. Abdul-Razzak and S.J. Ghan. A parameterization of aerosol activation 2. multiple aerosol types. *Journal of Geophysical Research-Atmospheres*, 105 (D5):6837–6844, 2000.

[2] A.S. Ackerman, O.B. Toon, J.P. Taylor, D.W. Johnson, P.V. Hobbs, and R.J. Ferek. Effects of aerosols on cloud albedo: Evaluation of twomey's parameterization of cloud susceptibility using measurements of ship tracks. *Journal of Atmospheric Science*, 57:2684–2695, 2000.

[3] R.J. Allen and S.C. Sherwood. The impact of natural versus anthropogenic aerosols on atmospheric circulation in the community atmsophere model. *Climate Dynamics*, 36:1959–1978, 2011.

[4] J. Anderson. An ensemble adjustment kalman filter for data assimilation. *Monthly Weather Review*, 129:2884–2903, 2001.

[5] J. Anderson, T. Hoar, K. Raeder, H. Liu, N. Collins, R. Torn, and A. Avellano. The data assimilation research testbed: A community facility. *Bulletin of the American Meteorological Society*, (1283-1296), September 2009.

[6] M.O. Andreae. Smoking rain clouds over the amazon. *Science*, 303(1337), 2004.

[7] A.F. Arellano, K. Raeder, J.L. Anderson, P.G. Hess, L.K. Emmons, D.P. Edwards, G.G. Pfister, T.L. Campos, and G.W. Sachse. Evaluating model performance of an ensemble-based chemical data assimilation system during intex-b field mission. *Atmospheric Chemistry and Physics*, 7:5695–5710, 2007.

[8] Y.J. Balkanski, D.J. Jacob, and G.M. Gardner. Transport and residence times of tropospheric aerosols inferred from a global three-dimensional simulation of 210pb. *Journal of Geophysical Research*, 98(D11):20573–20586, November 1993.

[9] M.C. Barth, P.J. Rasch, J.T. Kiehl, C.M. Benkovitz, and S.E. Schwartz. Sulfur chemistry in the national center for atmospheric research community climate model: Description, evaluation, features and sensitivity to aqueous chemistry. *Journal of Geophysical Research*, 105:1387–1415, 2000.

[10] N. Bellouin, O. Boucher, J. Haywood, and M. Shekar Reddy. Global estimate of aerosol direct radiative forcing from satellite measurements. *Nature*, 438:1138–1141, 2005.

[11] A. Berk, G.P. Anderson, P.K. Acharya, L.S. Bernstein, L. Muratov, J. Lee, M. Fox, S.M. Adler-Golden, J.H. Chetwynd, M.L. Hoke, and R.B. Lockwood. Modtran5: 2006 update. In *Proceedings of SPIE*, volume 6233, page 62331F, 2006.

[12] A. Berk, L.S. Bernstein, and D.C. Robertson. Modtran: A moderate resolution model for lowtran. Scientific report, Spectral Sciences, Inc., 1987.

[13] G. Burgers, P. Jan Van Leeuwen, and G. Evensen. Analysis scheme in the ensemble kalman filter. *Monthly Weather Review*, 126:1719–1724, 1998.

[14] R.J. Charlson, S.E. Schwartz, J.M. Hales, R.D. Cess, Jr J.A. Coakley, J.E. Hanson, and D.J. Hoffman. Climate forcing by anthropogenic aerosols. *Science*, 255:423–430, 1992.

[15] P. Chylke and J. Wong. Effect of absorbing aerosols on global radiation budget. *Geophysical Research Letter*, 22(8):929, 1995.

[16] W.D. Collins, P.J. Rasch, B.E. Eaton, B.V. Khattatov, J.F. Lamarque, and C.S. Zender. Simulating aerosols using a chemical transport model with assimilation of satellite aerosol retrievals: Methodology for indoex. *Journal of Geophysical Research*, 106:7313–7336, 2001.

[17] C. Cox and W. Munk. Measurement of the roughness of the sea surface from photographs of the sun's glitter. *Journal of the Optical Society of America*, 14:838–850, 1954.

[18] P.M. Cox, P.P. Harris, C. Huntingford, R.A. Betts, M. Collins, C.D. Jones, T.E. Jupp, J.A. Marengo, and C.A. Nobre. Increasing risk of amazonian drought due to decreasing air pollution. *Nature*, 453(7192):212–U7, May 2008.

[19] R.C. Easter, S.J. Ghan, Y. Zhang, R.D. Saylor, E.G. Chapman, N.S. Laulainen, H. Abdul-Razzak, L.R. Leung, X. Bian, and R.A. Zaveri. Mirage: Model description and evaluation of aerosols and trace gases. *Journal of Geophysical Research*, 109(D20210), 2004.

[20] J.E. Penner et al. Aerosols, their direct and indirect effects. in: Climate change 2001: The scientific basis. contribution of working group i to the third assessment report of the intergovernmental panel on climate change. Technical Report 289-348, Cambridge, United Kingdom and New York, NY, USA, 2001.

[21] L.K. Emmons et al. Description and evaluation of the model for ozone and related chemical tracers, version 4 (mozart-4). *Geoscience Model Development*, 3:43–67, 2010.

[22] G. Evensen. Sequential data assimilation with a nonlinear quasi-geostrophic model using monte-carlo methods to forecast error statistics. *Journal of Geophysical Research*, 99(C5):10143–10162, 1994.

[23] G. Evensen. The ensemble kalman filter: Theoretical formulation and practical implementation. *Ocean Dynamics*, 53:343–367, 2003.

[24] G. Feingold, W.L. Eberhard, D.E. Veron, and M. Previdi. First measurements of the twomey indirect effect using ground-based remote sensors. *Geophysical Research Letter*, 30(6)(1287), 2003.

[25] R.J. Ferek, D.A. Hegg, P.V. Hobbs, P.A. Durkee, and K.E. Nielsen. Measurements of ship-induced cloud tracks off the washington coast. *Journal of Geophysical Research*, 103:23199–23206, 1998.

[26] G. Gaspari and S.E. Cohn. Construction of correlation functions in two and three dimensions. *Q.J.R. Meteorol. Soc.*, 125:723–757, 1999.

[27] S.J. Ghan and R.A. Zaveri. Parameterization of optical properties for hydrated internally mixed aerosol. *Journal of Geophysical Research*, 112(D10201), 2007.

[28] F. Giorgi and W.L. Chameides. Rainout lifetimes of highly soluble aerosols and gases as inferred from simulations with a general circulation model. *Journal of Geophysical Research*, 91:14,367–14376, 1986.

[29] T.M. Hamill and J.S. Whitaker. Distance-dependent filtering of background error covariance estimates in an ensemble kalman filter. *Monthly Weather Review*, 129:2776–2790, 2001.

[30] J.M. Haywood and K.P. Shine. Multi-spectral calculations of the direct radiative forcing of tropospheric sulphate and soot aerosol using a column model. *Q.J.R. Meteorol. Soc.*, 123:1907–1930, 1997.

[31] M. Hess, P. Koepke, and I. Schult. Optical properties of aerosols and clouds: the software package opac. *Bulletin of the American Meteorological Society*, 79:831–844, 1998.

[32] B.N. Holben, T.F. Eck, I. Slutsker, D. Tanre, J.P. Buis, A. Setzer, E. Vermote, J.A. Reagan, Y.J. Kaufman, T. Nakajima, F. Lavenu, I. Jankowiak, and A. Smirnov. Aeronet-a federated instrument network and data archive for aerosol characterization. *Remote Sensing of Environment*, 66:1–16, 1998.

[33] L. Horowitz, S. Walters, D. Mauzerall, L. Emmons, P. Rasch, C. Granier, X. Tie, J.F. Lamarque, M. Schulz, G. Tyndall, J. Orlando, and G. Brasseur. A global simulation of tropospheric ozone and related tracers: Description and evaluation of mozart, version 2. *Journal of Geophysical Research*, 108:4784, 2003.

[34] C.A. Hostetler, Z. Liu, J. Reagan, M. Vaughan, D. Winker, M. Osborn, W.H. Hunt, K.A. Powell, and C. Trepte. Caliop algorithm theorectical basis document. Technical Report PC-SCI-201, NASA Langley Research Center, Hampton, VA, 2006.

[35] P.L. Houtekamer and H.L. Mitchell. A sequential ensemble kalman filter for atmospheric data assimilation. *Monthly Weather Review*, 129:123–137, 2001.

[36] P.L. Houtekamer and H.L. Mitchell. Ensemble kalman filtering. *Q.J.R. Meteorol. Soc.*, 131:3269–3289, 2006.

[37] Platnick Hubanks, King and Pincus. Modis atmosphere l3 gridded product algorithm theoretical bases document. Technical Report ATBD-MOD-30, NASA, 2008.

[38] B.R. Hunt, E.J. Kostelich, and I. Szunyogh. Efficient data assimilation for spatiotemporal chaos: A local ensemble transform kalman filter. *Physica D*, 230:112–126, 2007.

[39] M. Iacono, J. Delamere, E. Mlawer, M. Shephard, S. Clough, and W.D. Collins. Radiative forcing by long-lived greenhouse gases: Calculations with the aer radiative transfer models. *Journal of Geophysical Research*, 2008.

[40] S. Joussaume. Three-dimensional simulation of the atmospheric cycle of desert dust particles using a general circulation model. *Journal of Geophysical Research*, 95:1909–1941, 1990.

[41] E. Kalnay. *Atmospheric Modeling, Data Assimilation and Predictibility.* Cambridge University Press, 2003.

[42] E. Kalnay, M. Kanamitsu, R. Kistler, W.D. Collins, D. Deaven, L. Gandin, M. Iredell, S. Saha, G. White, and J. Woollen. The ncep/ncar 40-year reanalysis project. *Bulletin of the American Meteorological Society*, 1996.

[43] Y.J. Kaufman, O. Boucher, D. Tanre, M. Chin, L.A. Remer, and T. Takemura. Aerosol anthropogenic component estimated from satellite data. *Geophysical Research Letter*, 32(17, L17804), September 2005.

[44] Y.J. Kaufman, N. Gobron, B. Pinty, J. Widlowski, and M.M. Verstraete. Relationship between surface reflectance in the visible and mid-ir used in modis aerosol algorithm - theory. *Geophysical Research Letter*, 29(23, 2116), 2002.

[45] Y.J. Kaufman, B.N. Holben, D. Tanre, I. Slutsker, A. Smirnov, and T.F. Eck. Will aerosol measurements from terra and aqua polar orbiting satellites represent the daily aerosol abundance and properties? *Geophysical Research Letter*, 27(23):3861–3864, 2000.

[46] Y.J. Kaufman, A. Smirnov, B.N. Holben, and O. Dubovik. Baseline maritime aerosol: methodology to derive the optical thickness and scattering properties. *Geophysical Research Letter*, 28(17):3251–3254, September 2001.

[47] Y.J. Kaufman, A. Wald, L. Lorraine, B. Gao, R. Li, and L. Flynn. Remote sensing of aerosol over the continents with the aid of a 2.2um channel. *IEEE Transactions on Geoscience and Remote Sensing*, 35:1286–1298, 1997.

[48] M.D. King, Y.J. Kaufman, W.P. Menzel, and D. Tanre. Remote-sensing of cloud, aerosol, and water-vapor properties from the moderate resolution imaging spectroradiometer (modis). *IEEE Transactions on Geoscience and Remote Sensing*, 30(1):2–27, 1992.

[49] S. Kinne, M. Schulz, C. Textor, S. Guibert, Y. Balkanski, S.E. Bauer, T. Berntsen, T.F. Berglen, O. Boucher, M. Chin, W. Collins, F. Dentener, T. Diehl, R. Easter, J. Feichter, D. Fillmore, S. Ghan, P. Ginoux, S. Gong, A. Grini, J. Hendricks, M. Herzog, L. Horowitz, I. Isaksen, T. Iversen, A. Kirkevag, S. Kloster, D. Koch, J.E. Kristjansson, M. Krol, A. Lauer, J.F. Lamarque, G. Lesins, X. Liu, U. Lohmann, V. Montanaro, G. Myhre, J.E. Penner, G. Pitari, S. Reddy, O. Seland, P. Stier, T. Takemura, and X. Tie. An aerocom initial assessment - optical properties in aerosol component modules of global models. *Atmospheric Chemistry and Physics*, 6:1815–1834, 2006.

[50] R. Kistler, E. Kalnay, W.D. Collins, S. Saha, G. White, J. Woollen, M. Chelliah, W. Ebisuzaki, M. Kanamitsu, V. Kousky, H. van del Dool, R. Jenne, and M. Fiorino. The ncep-ncar 50-year reanalysis: Monthly means cd-rom and documentation. *Bulletin of the American Meteorological Society*, 82(2), February 2001.

[51] C. Kittaka, D.M. Winker, M.A. Vaughan, A. Omar, and L.A. Remer. Intercomparison of column aerosol optical depths from calipso and modis-aqua. *Atmospheric Measurement Techniques*, 4(2):131–141, 2011.

[52] P. Koepke. Effective reflectance of oceanic whitecaps. *Applied Optics*, 23:1816–1824, 1984.

[53] G. Kopp and J.L. Lean. A new, lower value of total solar irradiance: Evidence and climate significane. *Geophysical Research Letter*, 38, 2011.

[54] J.H. Kroll, N.L. Ng, S.M. Murphy, R.C. Flagan, and J.H. Seinfeld. Secondary organic aerosol formation from isoprene photooxidation. *Environmental Science and Technology*, 40(6):1869–1877, 2006.

[55] J.F. Lamarque, T.C. Bond, V. Eyring, C. Granier, A. Heil, Z. Klimont, D. Lee, C. Liousse, A. Mieville, B. Owen, M.G. Schultz, D. Shindell, S.J. Smith, E. Stehfest, J. Van Aardenne, O.R. Cooper, M. Kainuma, N. Mahowald, J.R. McConnell, V. Naik, K. Riahi, and D.P. van Vuuren. Historical (1850-2000) gridded anthropogenic and biomass burning emissions of reactive gases and aerosols: methodology and application. *Atmospheric Chemistry and Physics*, 10:7017–7039, 2010.

[56] R.C. Levy, L.A. Remer, and O. Dubovik. Global aerosol optical properties and application to moderate resolution imaging spectroradiometer aerosol retrieval over land. *Journal of Geophysical Research*, 112(D13210), 2007.

[57] Y.B. Lim and P.J. Ziemann. Products and mechanism of secondary organic aerosol formation from reactions of n-alkanes and oh radicals in the presence of nox. *Environmental Science and Technology*, 39(23):9229–9236, 2005.

[58] K.N. Liou. *An Introduction to Atmospheric Radiation*, volume 84 of *International Geophysics Series*. Elsevier, 2002.

[59] U. Lohmann and J. Feichter. Global indirect aerosol effects: a review. *Atmospheric Chemistry and Physics*, 5:715–737, 2005.

[60] U. Lohmann, J. Feichter, C. Chuang, and J.E. Penner. Predicting the number of cloud droplets in the echam gcm. *Journal of Geophysical Research*, 104(9169-9198), 1999.

[61] N.M. Mahowald, D.R. Muhs, S. Levis, P.J. Rasch, M. Yoshioka, C.S. Zender, and C. Luo. Change in atmospheric mineral aerosols in response to climate: Last glacial period, preindustrial, modern and doubles carbon dioxide climates. *Journal of Geophysical Research-Atmospheres*, 111 (D10), 2006.

[62] N.M. Mahowald, M. Yoshioka, W.D. Collins, A.J. Conley, D.W. Fillmore, and D.B. Coleman. Climate response and radiative forcing from mineral aerosols during the last glacial maximum, pre-industrial, current and doubled-carbon dioxide climates. *Geophysical Research Letter*, 33 (20), 2006.

[63] E.M. Martensson, E.D. Nilsson, G. deLeeuw, L.H. Cohen, and H.C. Hansson. Laboratory simulations and parameterization of the primary marine aerosol production. *Journal of Geophysical Research-Atmospheres*, 108 (D9), 2003.

[64] M. Mircea, M.C. Facchini, S. Decesari, F. Cavalli, L. Emblico, S. Fuzzi, A. Vestin, J. Rissler, E. Swietlicki, G. Frank, M.O. Andreae, W. Maenhaut, Y. Rudich, and P. Artaxo. Importance of the organic aerosol fraction for modeling aerosol hygroscopic growth and activation: a case study in the amazon basin. *Atmospheric Chemistry and Physics*, 5:3111–3126, 2005.

[65] E. Mlawer, S. Taubman, P. Brown, M. Iacono, and S. Clough. Radiative transfer for inhomogeneous atmospheres: Rrtm, a validated correlated-k model for the longwave. *Journal of Geophysical Research*, 102:16663–16682, 1997.

[66] R.B. Neale, J.H. Richter, A.J. Conley, S. Park, P.H. Lauritzen, A. Gettelman, and D.L. Williamson. Description of the ncar community atmosphere model (cam 4.0). Technical Report TN-485+STR, National Center for Atmospheric Research, Boulder, CO, April 2010.

[67] N.L. Ng, P.S. Chhabra, A.W.H. Chan, J.D. Surratt, J.H. Kroll, A.J. Kwan, D.C. McCabe, A. Sorooshian, S.M. Murphy, N.F. Dalleska, R.C. Flagan, and J.H. Seinfeld. Effect of nox level on secondary organic aerosol (soa) formation from the photooxidation of terpenes. *Atmospheric Chemistry and Physics*, 7:5159–5174, 2007.

[68] J.R. Odum, T.P.W. Jungkamp, R.J. Griffin, H.J.L. Forstner, R.C. Flagan, and J.H. Seinfeld. Aromatics, reformulated gasoline, and atmospheric organic aerosol formation. *Environmental Science and Technology*, 31(7):1890–1897, 1997.

[69] A.H. Omar, J.-G. Won, D.M. Winker, S.-C. Yoon, O. Dubovik, and M.P. McCormick. Development of global aerosol models using cluster analysis of aerosol robotic network (aeronet) measurements. *Journal of Geophysical Research*, 110(D10S14), 2005.

[70] F. Patadia and E.-S. Yang. Does dust change the clear sky top of atmosphere shortwae flux over high surface reflectance regions? *Geophysical Research Letter*, 36(L15825), 2009.

[71] J.E. Penner, X. Dong, and Y. Chen. Observational evidence of a change in radiative forcing due to the indirect aerosol effect. *Nature*, 427:231–234, 2004.

[72] R.E. Petrie. Localization in the ensemble kalman filter. Master's thesis, University of Reading, 2008.

[73] V. Ramanathan and G. Carmichael. Global and regional climate changes due to black carbon. *Nature*, 1:221–227, 2008.

[74] V. Ramanathan, P.J. Crutzen, J. Lelieveld, A.P. Mitra, D. Althausen, J. Anderson, M.O. Andreae, W. Cantrell, G.R. Cass, C.E. Chung, and A.D. Clarke et al. Indian ocean experiment: An integrated analysis of the climate forcing and effects of the great indo-asian haze. *Journal of Geophysical Research*, 106(D22):28371–28398, November 2001.

[75] P.J. Rasch, M.C. Barth, J.T. Kiehl, S.E. Schwartz, and C.M. Benkovitz. A description of the global sulfur cycle and its controlling processes in the national center for atmospheric research community climate model, version 3. *Journal of Geophysical Research*, 105:1367–1385, 2000.

[76] J.S. Reid, P.V. Hobbs, A.L. Rangno, and D.A. Hegg. Relationships between cloud droplet effective radius, liquid water content, and droplet concentration for warm clouds in brazil embedded in biomass smoke. *Journal of Geophysical Research*, 104:6145–6153, 1999.

[77] L.A. Remer, Y.J. Kaufman, D. Tanre, S. Mattoo, D.A. Chu, J.V. Martins, R.R. Li, C. Ichoku, R. Levy, R.G. Kleidman, T.F. Eck, E. Vermote, and B.N. Holben. The modis aerosol algorithm, products and validation. *Journal of the Atmospheric Sciences*, 62:947–973, April 2005.

[78] L.A. Remer, D. Tanre, Y.J. Kaufman, R. Levy, and S. Mattoo. Algorithm for remote sensing of tropospheric aerosol from modis: Collection 005, product id mod04/myd04. Technical Report ATBD-MOD-96, NASA - Goddard Space Flight Center, 2006.

[79] R.R. Rogers and M.K. Yau. *A Short Course in Cloud Physics*, volume 113 of *International Series in Natural Philosophy*. Butterworth-Heinemann, 1976.

[80] L.D. Rotstayn and U. Lohmann. Tropical rainfall trends and the indirect aerosol effect. *Journal of Climate*, 15(15):2103–2116, August 2002.

[81] V.V. Salomonson, W.L. Barnes, P.W. Maymon, H.E. Montgomery, and H. Ostrow. Modis: Advanced facility instrument for studies of the earth as a system. *IEEE Geoscience and Remote Sensing*, 27:145–153, 1989.

[82] J.H. Seinfeld and S.N. Pandis. *Atmospheric Chemistry and Physics. From Air Pollution to Climate Change.* John Wiley and Sons, Inc., 1997.

[83] T.T. Sekiyama, T.Y. Tanaka, A. Shimizu, and T. Miyoshi. Data assimilation of calipso aerosol observations. *Atmospheric Chemistry and Physics*, 10:39–49, 2010.

[84] S. Solomon, D. Qin, M. Manning, Z. Chen, M. Marquis, K.B. Averyt, M. Tignor, and H.L. Miller. Climate change 2007: The physical science basis. Technical report, Intergovernmental Panel on Climate Change, 2007.

[85] I. Szunyogh, E.J. Kostelich, G. Gyarmati, E. Kalnay, B.R. Hunt, E. Ott, E. Satterfield, and J.A. Yorke. A local ensemble transform kalman filter data assimilation system for the ncep global model. *Tellus*, 60A:113–130, 2008.

[86] I. Szunyogh, E.J. Kostelich, G. Gyarmati, D.J. Patil, B.R. Hunt, E. Kalnay, E. Ott, and J.A. Yorke. Assessing a local ensemble kalman filter: perfect model experiments with the national centers for environmental predction global model. *Tellus Series A - Dynamic Meteorology and Oceanography*, 57(4):528–545, 2005.

[87] O. Talagrand. Assimilation of observations, an introduction. *Journal of Meteorological Society of Japan*, 75(1B):191–209, 1997.

[88] D. Tanre, Y.J. Kaufman, B.N. Holben, B. Chatenet, A. Karnieli, F. Lavenu, L. Blarel, O. Dubovik, L.A. Remer, and A. Smirnov. Climatology of dust aerosol size distribution and optical properties derived from remotely sensed data in the solar spectrum. *Journal of Geophysical Research*, 106(18,205-18,217), 2001.

[89] I. Tegen and A.A. Lacis. Modeling of particle size distribution and its influence on the radiative properties of mineral dust aerosol. *Journal of Geophysical Research*, 101(D14):19237–19244, August 1996.

[90] I. Tegen, M. Werner, S.P. Harrison, and K.E. Kohfeld. Relative importance of climate and land use in determining present and future global soil dust emission. *Geophysical Research Letter*, 31(5), 2004.

[91] C. Textor, M. Schulz, G. Guibert, S. Kinne, Y.J. Balkanski, S. Bauer, T. Berntsen, T. Berglen, O. Boucher, and M. Chin et al. The effect of harmonized emissions on aerosol properties in global models - an aerocom experiment. *Atmospheric Chemistry and Physics*, 7:4489–4501, 2007.

[92] C. Textor, M. Schulz, S. Guibert, S. Kinne, Y. Balkanski, S. Bauer, T. Berntsen, T. Berglen, O. Boucher, M. Chin, F. Dentener, T. Diehl, R. Easter, H. Feichter, D. Fillmore, S.J. Ghan, P. Ginoux, S. Gong, J.E. Kristjansson, M. Krol, A. Lauer, J.F. Lamarque, X. Liu, V. Montanaro, G. Myhre, J.E. Penner, G. Pitari, S. Reddy, O. Seland, P. Stier, T. Takemura, and X. Tie. Analysis and quantification of the diversities of aerosol life cycles in aerocom. *Atmospheric Chemistry and Physics*, 6:1777–1813, May 2006.

[93] G.E. Thomas, N. Chalmers, B. Harris, R.G. Grainger, and E.J. Highwood. Regional and monthly and clear-sky aerosol direct radiative effect (and forcing) derived from the globaerosol-aatsr satellite aerosol product. *Atmospheric Chemistry and Physics*, 12:18459–18497, 2012.

[94] X. Tie, G. Brasseur, L. Emmons, L. Horowitz, and D. Kinnison. Effects of aerosols on tropospheric oxidants: A global model study. *Journal of Geophysical Research-Atmospheres*, 106 (D19)(22931-22964), 2001.

[95] S.A. Twomey. Aerosols, clouds and radiation. *Atmospheric Environment*, 25A:2435–2442, 1991.

[96] M. Vaughan, S. Young, D. Winker, K. Powell, A. Omar, Z. Liu, Y. Hu, and C. Hostetler. Fully automated analysis of space-based lidar data: an overview of the calipso retrieval algorithms and data products. *Proceedings of SPIE International Society of Optical Engineering*, 5575:16–30, 2004.

[97] H. Vehkamaki, M. Kulmala, I. Napari, K.E.J. Lehtinen, C. Timmreck, M. Noppel, and A. Laaksonen. An improved parameterization for sulfuric acid-water nucleation rates for tropospheric and stratospheric conditions. *Journal of Geophysical Research*, 107(D22)(4622), 2002.

[98] C. Weaver, A. Da Silva, M. Chin, P. Ginoux, O. Dubovik, D. Flittner, A. Zia, L.A. Remer, B.N. Holben, and W. Gregg. Direct insertion of modis radiances in a global aerosol transport model. *Journal of the Atmospheric Sciences*, 64(3):808–826, 2007.

[99] J.S. Whitaker and T.M. Hamill. Ensemble data assimilation without perturbed observations. *Monthly Weather Review*, 130:1913–1924, 2002.

[100] J.S. Whitaker, T.M. Hamill, X. Wei, Y. Song, and Z. Toth. Ensemble data assimilation with the ncep global forecast system. *Monthly Weather Review*, 136:463–482, 2008.

[101] E.R. Whitby and P.H. McMurry. Modal aerosol dynamics modeling. *Aerosol Science and Technology*, 27(6):673–688, December 1997.

[102] D.M. Winker, J. Pelon, and M. Patrick McCormick. The calipso mission: Spaceborne lidar for observation of aerosols and clouds. In Upendra N. Singh, Toshikasu Itabe, and Zhishen Liu, editors, *Lidar Remote Sensing for Industry and Environment Monitoring III*, volume 4893. SPIE, 2003.

[103] M. Yoshioka, N.M. Mahowald, A.J. Conley, W.D. Collins, D.W. Fillmore, C.S. Zender, and D.B. Coleman. Impact of desert dust radiative forcing on sahel precipitation: Relative importance of dust compared to sea surface temperature variations, vegetation changes, and greenhouse gas warming. *Journal of Climate*, 20 (8), 2007.

[104] S.A. Young, M.A. Vaughan, and D. Winker. Adaptive methods for retrieving extinction profiles from space applied to calipso lidar data. In *Proceedings of the 21st International Laser Radar Conference*, pages 743–746, Quebec City, Canada, 2002.

[105] S.A. Young, M.A. Vaughan, and D. Winker. Adaptive algorithms for the fully-automated retrieval of cloud and aerosol extinction profiles from calipso lidar data. In IEEE International, editor, *IEEE Geoscience and Remote Sensing Symposium*, volume 3, pages 1517–1519, 2003.

[106] Hongbin Yu, R.E. Dickinson, and M. Chin. Annual cycle of global distributions of aerosol optical depth from integration of modis retrievals and gocart model simulations. *Journal of Geophysical Research*, 108(D3)(4128), 2003.

[107] L.M. Zhang, S.L. Gong, J. Padro, and L. Barrie. A size-segregated particle dry deposition scheme for an atmospheric aerosol module. *Atmospheric Environment*, 35 (3):549–560, 2001.